



**Maynooth  
University**

National University  
of Ireland Maynooth

# High Fidelity Modelling of Motorcycle Dynamics

by

Thomas G. O'Kane

A thesis presented on application for the degree of

Doctor of Philosophy

in the

Faculty of Science & Engineering

National University of Ireland, Maynooth

Head of Department: Prof. Ronan Farrell

Supervisor: Prof. John V. Ringwood

Department of Electronic Engineering

June 2018

# Contents

<b>Abstract</b>	<b>xxx</b>
<b>Acknowledgements</b>	<b>xxxii</b>
<b>Declaration</b>	<b>xxxiv</b>
	<b>xxxv</b>
<b>1 Introduction</b>	<b>1</b>
1.1 Introductory remarks . . . . .	1
1.2 Motivation . . . . .	1
1.3 Novelty of research . . . . .	2
1.4 Thesis layout . . . . .	3
<b>2 Literature Review</b>	<b>6</b>
2.1 Equations of motion for a Whipple bicycle . . . . .	7
2.2 State of the art multibody models . . . . .	11
2.2.1 The SL 2001 model . . . . .	12
2.2.2 The CL 2002 model . . . . .	13
2.2.3 Comparison of multibody models . . . . .	13
2.3 Tyre model time line . . . . .	14
2.3.1 Tyre forces and moments, dynamic response . . . . .	18
<b>3 Multibody System Modelling</b>	<b>19</b>
3.1 Reference frames . . . . .	19
3.2 Vector notation . . . . .	20

3.3	Generalised co-ordinates and speeds . . . . .	21
3.4	Partial angular velocities and velocities . . . . .	21
3.5	The model . . . . .	22
3.6	Newton's Equations . . . . .	23
3.7	Lagrange's equations . . . . .	26
3.8	Kane's equations . . . . .	29
3.8.1	Partial velocities . . . . .	30
3.8.2	Kane's Equations . . . . .	31
3.8.3	Active forces . . . . .	31
3.8.4	Inertial forces . . . . .	32
3.8.5	Equate the active and inertial forces . . . . .	32
3.9	Conclusion . . . . .	33
<b>4</b>	<b>The Motorcycle Model</b>	<b>34</b>
4.1	Introduction . . . . .	34
4.2	Constraints and degrees of freedom . . . . .	34
4.3	Generalised co-ordinates and generalised speeds . . . . .	37
4.4	Reference frames . . . . .	38
4.4.1	Transformations between reference frames . . . . .	40
4.4.2	The angle $\xi$ between reference frames $F$ and $G$ . . . . .	41
4.4.3	The front wheel camber angle $\gamma_1$ and kinematic steering angle $\delta'$ . . . . .	43
4.5	Forces and moments in the model . . . . .	44
4.5.1	Suspension forces in the model . . . . .	45
4.5.2	The effect of chain tension . . . . .	49
4.5.3	Crankshaft rotation . . . . .	50
4.5.4	Wheel rotation . . . . .	50
4.5.5	Drag . . . . .	51
4.6	Rider body position . . . . .	55
4.7	Engine Torque . . . . .	62
4.8	Main frame position in terms of the state variables . . . . .	64
4.8.1	Frame pitch angle $\mu = q_{14}$ as a function of $q_1 \dots q_{13}$ . . . . .	67

---

4.8.2	Frame $x$ position $q_{15}$ as a function of $q_1 \dots q_{11}$ . . . . .	75
4.8.3	Frame $z$ position $q_{16}$ as a function of $q_1 \dots q_{11}$ . . . . .	76
4.8.4	Wheelbase $q_{18}$ as a function of $q_1 \dots q_{11}$ . . . . .	78
4.8.5	Trail $q_{19}$ as a function of $q_1 \dots q_{11}$ . . . . .	80
4.8.6	Frame yaw angle $q_{13}$ as a function of $q_1 \dots q_{11}$ . . . . .	81
4.8.7	Frame $y$ position $q_{17}$ as a function of $q_1 \dots q_{11}$ . . . . .	85
4.8.8	Concluding remarks on the main frame position . . . . .	86
4.9	Sampling rate . . . . .	88
4.10	Modelling procedure . . . . .	89
4.10.1	Velocity and acceleration expressions for the key points . . . . .	90
4.10.2	Kane's Equations . . . . .	99
4.11	The state output matrix, $C$ . . . . .	106
4.12	Controlling the model . . . . .	107
4.13	Crash avoidance . . . . .	110
4.13.1	Traction control . . . . .	111
4.13.2	Anti-lock braking . . . . .	112
4.14	Model computational performance . . . . .	115
<b>5</b>	<b>The Tyre Model</b> . . . . .	<b>116</b>
5.1	Introduction . . . . .	116
5.2	Tyre characteristics and terminology . . . . .	117
5.2.1	Grip . . . . .	118
5.2.2	Tyre radius . . . . .	119
5.2.3	Vertical force $F_z$ . . . . .	120
5.2.4	Longitudinal force $F_x$ . . . . .	120
5.2.5	Lateral force $F_y$ . . . . .	121
5.2.6	Camber thrust force . . . . .	122
5.2.7	Pneumatic trail $t$ . . . . .	123
5.2.8	Overturning moment $M_x$ . . . . .	123
5.2.9	Rolling resistance moment $M_y$ . . . . .	124
5.2.10	Aligning moment $M_z$ . . . . .	124
5.2.11	Longitudinal slip . . . . .	124

---

5.2.12	Lateral slip . . . . .	125
5.2.13	Stiffness . . . . .	126
5.2.14	Turn slip . . . . .	126
5.2.15	Ply-steer . . . . .	127
5.2.16	Dynamic behaviour . . . . .	127
5.3	The Magic Formula tyre model . . . . .	131
5.3.1	The sine formula . . . . .	132
5.3.2	The cosine formula . . . . .	133
5.3.3	Magic Formula inputs and outputs . . . . .	134
5.4	Magic Formula parameters . . . . .	135
5.4.1	Refining the tyre parameters . . . . .	136
5.5	Tyre profile . . . . .	143
<b>6</b>	<b>Sensing and Data Logging</b>	<b>152</b>
6.1	Introduction . . . . .	152
6.2	Data logging hardware overview . . . . .	154
6.3	The Controller Area Network (CAN) bus . . . . .	154
6.4	The data logger . . . . .	156
6.5	The sensor interface module . . . . .	158
6.5.1	Analog channels . . . . .	158
6.5.2	Digital channels . . . . .	159
6.6	Recorded channels . . . . .	159
6.6.1	Engine speed . . . . .	160
6.6.2	Throttle position . . . . .	161
6.6.3	Gear position . . . . .	162
6.6.4	The inertial measurement unit . . . . .	163
6.6.5	Front wheel speed . . . . .	167
6.6.6	Rear wheel speed . . . . .	169
6.6.7	Front suspension position . . . . .	170
6.6.8	Rear suspension position . . . . .	172
6.6.9	Steering angle . . . . .	175
6.6.10	Brake pressures . . . . .	175

---

6.6.11	Calculating wheel torques . . . . .	176
6.6.12	GPS . . . . .	176
6.7	Coast-down testing . . . . .	177
6.8	Data formatting . . . . .	178
<b>7</b>	<b>Model Validation and Analysis</b>	<b>179</b>
7.1	Introduction . . . . .	179
7.2	Coast-down test . . . . .	179
7.3	Race circuit tests . . . . .	181
7.3.1	Preliminary validation in Mondello Park . . . . .	182
7.3.2	Testing at race speed in Nutts Corner . . . . .	183
7.4	Turning behaviour . . . . .	190
7.4.1	Steady state turning . . . . .	190
7.4.2	Roll angle change . . . . .	191
7.5	Turning radius . . . . .	192
7.6	The effect of changing the slip angle . . . . .	195
7.7	Tracking the bike position . . . . .	196
7.8	Root locus analysis . . . . .	196
<b>8</b>	<b>Application Examples</b>	<b>202</b>
8.1	Estimation of unmeasurable quantities . . . . .	202
8.2	Evaluating parameter changes . . . . .	206
<b>9</b>	<b>Conclusions</b>	<b>209</b>
9.1	Introduction . . . . .	209
9.2	The model . . . . .	209
9.3	Utility of the model . . . . .	211
9.4	Future work . . . . .	212
	<b>Appendices</b>	<b>220</b>
<b>A</b>	<b>Magic Formula Equations</b>	<b>221</b>
A.1	Longitudinal force $F_x$ . . . . .	221

A.1.1	Longitudinal force (pure longitudinal slip, $\kappa \neq 0$ , $\alpha = 0$ ) . . . . .	222
A.1.2	Longitudinal force (combined slip, $\kappa \neq 0$ , $\alpha \neq 0$ ) . . . . .	224
A.2	Lateral force $F_y$ . . . . .	225
A.2.1	Lateral force (pure side slip, $\kappa = 0$ , $\alpha \neq 0$ ) . . . . .	225
A.2.2	Lateral force (combined slip, $\kappa \neq 0$ , $\alpha \neq 0$ ) . . . . .	228
A.3	Overturning moment $M_x$ . . . . .	229
A.4	Rolling resistance moment $M_y$ . . . . .	230
A.5	Aligning moment $M_z$ . . . . .	231
A.6	Relaxation behaviour . . . . .	234

# List of Figures

3.1	Vector convention shown in two reference frames . . . . .	19
3.2	An inverted pendulum with spring and damper . . . . .	22
4.1	Bike model degrees of freedom . . . . .	35
4.2	Key points and bodies in the model . . . . .	35
4.3	Generalised co-ordinates in the $x, z$ plane . . . . .	38
4.4	Bike reference frames shown in $x, z$ plane . . . . .	40
4.5	Bike reference frames in three dimensions . . . . .	40
4.6	Vectors $f_1$ and $g_1$ . . . . .	42
4.7	Front wheel camber angle $\gamma_1$ and kinematic steering angle $\delta'$ . . .	43
4.8	Front fork spring force vs. fork position. Swing-arm spring torque (showing non-linearity due to bump rubber) vs. swing-arm angle.	47
4.9	Front fork damping force vs. fork speed. Swing-arm damping torque vs. swing-arm angle and shock absorber speed. . . . .	48
4.10	Drive chain forces and torques . . . . .	49
4.11	Tyre longitudinal slip forces in freewheel, modelled and curve fitted	52
4.12	Tyre longitudinal shear force vs. acceleration for different wheel inertial moments and bike mass . . . . .	53
4.13	Freewheel coast-down test. Road speed, measured and simulated by the model . . . . .	55
4.14	Tyre contact patch shape at various camber angles . . . . .	55
4.15	Cross-section of the motorcycle at high roll angle . . . . .	56
4.16	Cross-correlation of IMU data with engine speed . . . . .	58
4.17	Accelerometer signals from track test . . . . .	59

4.18	Amplitude spectrum of $Y$ accelerometer signal from 36.4 to 36.65 seconds . . . . .	60
4.19	Vector diagram of cornering acceleration . . . . .	61
4.20	Engine torque, wide open throttle and fully closed . . . . .	63
4.21	Percentage of engine torque vs. throttle position (typical) . . . . .	64
4.22	Engine torque map . . . . .	64
4.23	Measured steering angle versus camber angle . . . . .	66
4.24	Bike dimensions in $x, z$ plane . . . . .	67
4.25	Rear tyre dimensions . . . . .	67
4.26	Linearisation notation . . . . .	71
4.27	Frame pitch angle as a function of $q_1, q_2, q_3, q_4, q_9$ and $q_{11}$ . . . . .	74
4.28	Frame X position from rear tyre contact point as a function of $q_1, q_2, q_3, q_4, q_9$ and $q_{11}$ . . . . .	76
4.29	Frame Z position from rear tyre contact point as a function of $q_1, q_2, q_3, q_4, q_9$ and $q_{11}$ . . . . .	78
4.30	Front wheel trail . . . . .	81
4.31	Frame yaw angle as a function of $q_1, q_2, q_3, q_4, q_9$ and $q_{11}$ . . . . .	85
4.32	Frame Y position from rear tyre contact point as a function of $q_1, q_2, q_3, q_4, q_9$ and $q_{11}$ . . . . .	86
4.33	The effect of different sampling rates . . . . .	88
4.34	The key points of the bike model . . . . .	90
4.35	Wheel angular velocity with and without Kalman filter . . . . .	109
4.36	The bike model with steering torque controller and Kalman filter . . . . .	110
4.37	Inertial path compared to GPS path . . . . .	110
4.38	Traction control strategy . . . . .	111
4.39	Anti-lock braking strategy . . . . .	112
4.40	Crash avoidance strategies . . . . .	114
5.1	Forces and moments acting on a tyre in the Pacejka co-ordinate system . . . . .	117
5.2	$F_x, F_y, M_x$ and $M_z$ vs. longitudinal slip $\kappa$ and lateral slip $\alpha$ . . . . .	117
5.3	Hysteresis in a viscoelastic material . . . . .	118

---

5.4	Viscoelastic material slipping across an indented surface . . . . .	119
5.5	Tyre radius . . . . .	120
5.6	Slip and camber angle comparison for bikes and cars . . . . .	122
5.7	The effect of camber thrust on lateral force . . . . .	123
5.8	Slip angle . . . . .	125
5.9	The curve produced by the sine formula . . . . .	132
5.10	$F_y$ and $M_z$ versus slip angle $\alpha$ with $\kappa = 0$ . . . . .	133
5.11	The curve produced by the cosine formula . . . . .	134
5.12	The Magic Formula inputs and outputs . . . . .	135
5.13	Comparison of front and rear tyre character . . . . .	139
5.14	Steering angle vs. roll angle using initial set of tyre parameters .	140
5.15	Optimisation of front tyre $p_{Dy1}$ . . . . .	141
5.16	Steering angle vs. roll angle in Nutts Corner using adjusted set of tyre parameters . . . . .	143
5.17	Steering angle vs. roll angle in Mondello Park using adjusted set of tyre parameters . . . . .	143
5.18	Card template on front tyre . . . . .	144
5.19	Transferring tyre profile tangent points to graph paper . . . . .	146
5.20	Tyre profile semicircle and semi-ellipse . . . . .	146
5.21	Tyre profile measurements and fitted functions . . . . .	148
5.22	Tyre Y co-ordinate versus camber . . . . .	149
5.23	Tyre Z co-ordinate versus camber . . . . .	150
5.24	Tyre profile measurements and polynomials in $\gamma$ . . . . .	150
6.1	Data logger and sensor interface unit . . . . .	154
6.2	Configuring a CAN channel . . . . .	156
6.3	Data logger (right) and sensor interface unit (left) installation . .	157
6.4	CBR600RR crankshaft trigger wheel, bottom right (12 pulses per revolution). The back-torque limiting clutch is also shown. . . . .	161
6.5	Engine speed channel setting . . . . .	161
6.6	The 2D gear speed assistant . . . . .	163
6.7	Orientation of IMU axes. Figure courtesy of 2D Datarecording .	164

---

6.8	IMU mounting bracket . . . . .	164
6.9	Preparation for IMU mounting . . . . .	164
6.10	The IMU mounted on a Sorbothane pad . . . . .	165
6.11	The IMU final mounting arrangement . . . . .	165
6.12	Aluminium epoxy filler in the instrument mounting bracket . . . . .	166
6.13	IMU and front suspension stroke sensor . . . . .	166
6.14	Front wheel speed sensor ring from later model . . . . .	167
6.15	Front wheel speed sensor mounting bracket (sheet metal) . . . . .	168
6.16	Front wheel speed sensor . . . . .	168
6.17	Front wheel speed channel setting . . . . .	169
6.18	Rear wheel speed and rear brake pressure sensors . . . . .	170
6.19	3D printed brackets . . . . .	171
6.20	Front suspension stroke sensor mounted on left-hand fork leg. Steering and front brake pressure sensors are also shown . . . . .	171
6.21	Rear suspension stroke sensor . . . . .	173
6.22	Rear stroke sensor geometry . . . . .	173
6.23	The Unit Pro-link rear suspension system . . . . .	174
6.24	Steering sensor in place on the steering damper . . . . .	175
6.25	Front brake pressure sensor . . . . .	176
6.26	The GPS Antenna mounted on the tail unit . . . . .	177
6.27	Coast-down test speeds . . . . .	177
7.1	Freewheel coast-down speeds and suspension positions, measured and modelled. . . . .	180
7.2	4 <sup>th</sup> gear coast-down speeds and suspension positions, measured and modelled. . . . .	181
7.3	Estimated and recorded suspension data for one lap of Mon- dello Park . . . . .	182
7.4	Estimated and recorded suspension data for one lap of Nutts Corner	184
7.5	Estimated and recorded wheel angular velocity . . . . .	185
7.6	Estimated and recorded rate gyro data . . . . .	186

---

7.7	Google Earth map of Mondello Park circuit, showing elevation change . . . . .	187
7.8	Nutts Corner race circuit, Antrim, showing two lap GPS trace . .	188
7.9	Google Earth map of Nutts Corner circuit, showing elevation change	189
7.10	Yaw rate, steering torque and steering angle vs. road speed at 45° roll angle . . . . .	190
7.11	Roll angle driven from 0 to 50° at 20 m/s . . . . .	191
7.12	Balanced turning . . . . .	192
7.13	Turning radius . . . . .	193
7.14	The effect of changes in slip angle . . . . .	195
7.15	3D map of bike trajectory for two laps, with zoomed inset . . . .	196
7.16	Training data used to build the $K_{in}$ matrix . . . . .	198
7.17	Testing the tyre lateral force generated by the trained system . .	199
7.18	Root locus with bike upright for road speed from 3 to 60 $m/s$ . .	200
7.19	Root locus at 50 $m/s$ , with roll angle from 0 to 50° . . . . .	201
8.1	Roll angle, tyre lateral shear force (actual and normalised) and slip angle. Data from Nutts Corner with initial tyre parameter set. . .	203
8.2	Roll angle, tyre lateral shear force (actual and normalised) and slip angle. Data from Nutts Corner with modified tyre parameter set.	204
8.3	Roll angle, tyre lateral shear force (actual and normalised) and slip angle. Data from Mondello Park with final tyre parameter set. . .	205
8.4	Histogram of rear tyre normal force . . . . .	207
8.5	Histogram of rear tyre slip ratio . . . . .	208
8.6	Histogram of normalised front tyre lateral force . . . . .	208

# List of Tables

2.1	Model degrees of freedom compared . . . . .	14
3.1	Reference frame vector relationship . . . . .	23
3.2	Partial velocities . . . . .	30
4.1	Key points in the the multi-body system . . . . .	36
4.2	Degrees of freedom and constraints . . . . .	36
4.3	Generalised co-ordinates . . . . .	38
4.4	Reference frame transformations . . . . .	41
4.5	Generalised co-ords describing main frame position . . . . .	65
4.6	Main frame position and orientation . . . . .	91
4.7	Mean absolute value of state variables during one lap . . . . .	102
4.8	Mean absolute value of inputs during one lap . . . . .	102
4.9	Input vector $u_{in}$ . . . . .	103
4.10	Non-zero values in the C matrix, indexed by row and column . . .	107
4.11	Operating system and compiler specifications . . . . .	115
5.1	Non-zero parameters for front tyre $F_x$ . No data for 120/70 tyre . .	137
5.2	Non-zero parameters for front tyre $F_y$ . . . . .	137
5.3	Non-zero parameters for rear tyre $F_x$ . No data for 180/55 tyre . .	138
5.4	Non-zero parameters for rear tyre $F_y$ . . . . .	138
5.5	Modified $F_y$ tyre parameters . . . . .	141
5.6	Measured tyre profile tangent points . . . . .	145
5.7	Front tyre profile, measured and fitted . . . . .	145
5.8	Rear tyre profile, measured and fitted . . . . .	147

5.9	Front tyre profile polynomial coefficients . . . . .	150
5.10	Rear tyre profile polynomial coefficients . . . . .	151
6.1	Gear ratios (number of teeth) . . . . .	162

# List of Notations

The list of notations contains a large number of symbols so it is arranged in the following sections:

- Motorcycle model
- Tyre model
- Tyre model, MF-Tyre / MF-Swift parameters
- Other symbols

These sections are followed by a list of abbreviations.

## Motorcycle model

- $\delta$  Steering angle. Alias for generalised co-ord.  $q_{11}$ , page 37
- $\delta'$  Kinematic steering angle, page 40
- $\gamma$  Motorcycle roll angle. Alias for generalised co-ord.  $q_9$ , page 37
- $\gamma_1$  Front tyre camber angle, page 40
- $\omega$  Vector of non-linear terms, page 106
- $\psi$  Motorcycle yaw angle. Alias for generalised co-ord.  $q_{10}$ , page 37
- $\rho$  Density of air, page 54
- $\varepsilon$  Steering head angle, page 40
- $\xi$  Angle of reference frame  $F$  to ground plane, page 40

- $A$  Frontal area of bike and rider, page 54
- $A$  Reference frame: main frame, engine and rider etc., page 35
- $A$  System  $A$  matrix, page 106
- $A'$  Abridged system  $A$  matrix, page 106
- $a_c$  Centripetal acceleration, page 61
- $a_r$  Resultant of centripetal and gravitational acceleration, page 61
- $a_x$  X acceleration measured by IMU, page 56
- $a_y$  Y acceleration measured by IMU, page 56
- $a_z$  Z acceleration measured by IMU, page 56
- $B$  Reference frame: swing-arm, brakes etc., page 35
- $B$  System  $B$  matrix, page 106
- $B'$  Abridged system  $B$  matrix, page 106
- $B_{x,z}$  Co-ordinates of swing-arm mass centre. See Fig. 4.24, page 67
- $C$  Reference frame: fork unsprung mass, brakes etc., page 35
- $C$  State output matrix, page 106
- $C_d$  Aerodynamic drag coefficient, page 54
- $C_{x,z}$  Co-ordinates of body  $C$  mass centre. See Fig. 4.24, page 67
- $D$  Reference frame: rear wheel and tyre, page 35
- $F$  Reference frame: fork upper, controls and rider's forearms, page 35
- $F_n$  Linearised coefficients for main frame roll angle, page 91
- $F_r$  Kane's equations, active forces, page 100
- $F_r^*$  Kane's equations, inertial forces, page 100

- $F_{drag}$  Aerodynamic drag force, page 102
- $F_{fork}$  Front suspension force, page 102
- $F_{fwx}$  Front wheel  $x$  force, page 102
- $F_{fwy}$  Front wheel  $y$  force, page 102
- $F_{fwz}$  Front wheel  $z$  force, page 102
- $F_{lift}$  Aerodynamic lift force, page 102
- $F_{rwx}$  Rear wheel  $x$  force, page 102
- $F_{rwy}$  Rear wheel  $y$  force, page 102
- $F_{rwx}$  Rear wheel  $x$  force, page 102
- $F_{rwx}$  Rear wheel  $x$  force, page 102
- $F_{x,z}$  Co-ordinates of body  $F$  mass centre, page 67
- $G$  Reference frame: front wheel and tyre, page 35
- $g$  Acceleration due to gravity, page 102
- $G_n$  Linearised coefficients for main frame yaw angle, page 91
- $H$  Point: steering head point, page 35
- $H_n$  Linearised coefficients for main frame pitch angle, page 91
- $H_{x,z}$  Co-ordinates of steering head. See Fig. 4.24, page 67
- $J_n$  Linearised coefficients for main frame  $x$  displacement, page 91
- $K_n$  Linearised coefficients for main frame  $z$  displacement, page 91
- $K_s$  Coefficient of longitudinal tyre shear force, page 53
- $L_n$  Linearised coefficients for main frame  $y$  displacement, page 91
- $M_M$  Mass of the motorcycle and rider, page 57
- $M_n$  Mass of body  $n$ , page 57

$N$	Reference frame: ground plane must be included as a body, page 35
$P$	Point: swing-arm pivot, page 35
$P_{x,z}$	Co-ordinates of body $A$ mass centre. See Fig. 4.24, page 67
$Q$	Point: upper limit of front axle, page 35
$q_1$	Generalised co-ordinate: front suspension extension, page 37
$q_2$	Generalised co-ordinate: swing-arm angle relative to the main frame, page 37
$q_3$	Generalised co-ordinate: front tyre vertical deflection, page 37
$q_4$	Generalised co-ordinate: rear tyre vertical deflection, page 37
$q_5$	Generalised co-ordinate: front wheel rotation angle, page 37
$q_6$	Generalised co-ordinate: rear wheel rotation angle, page 37
$q_7$	Generalised co-ordinate: X co-ordinate on the ground plane, alias $x$ , page 37
$q_8$	Generalised co-ordinate: Y co-ordinate on the ground plane, alias $y$ , page 37
$q_9$	Generalised co-ordinate: motorcycle roll angle, alias $\gamma$ , page 37
$q_{10}$	Generalised co-ordinate: motorcycle yaw angle, alias $\psi$ , page 37
$q_{11}$	Generalised co-ordinate: steering angle, alias $\delta$ , page 37
$q_{12}$	Main frame roll angle, page 65
$q_{13}$	Main frame yaw angle, page 65
$q_{14}$	Main frame pitch angle, page 65
$q_{15}$	Main frame $x$ position, page 65
$q_{16}$	Main frame $z$ position, page 65
$q_{17}$	Main frame $y$ position, page 65
$q_{18}$	Wheelbase, page 65

- $q_{19}$  Trail, page 65
- $Q_{x,z}$  Co-ordinates of point  $Q$ . See Fig. 4.24, page 67
- $R$  Coefficient matrix for system non-linear terms, page 106
- $R$  Point: aerodynamic centre of pressure, page 35
- $R'$  Abridged coefficient matrix for system non-linear terms, page 106
- $R_a$  Swing-arm length. See Fig. 4.24, page 67
- $S$  Point: front tyre contact point, page 35
- $T$  Point: rear tyre contact point, page 35
- $T'_{Fz}$  Modified Z co-ordinate of front tyre contact patch. See Fig. 4.25, page 67
- $T'_{Rz}$  Modified Z co-ordinate of rear tyre contact patch. See Fig. 4.25, page 67
- $T_{df}$  Front wheel drag torque, page 55
- $T_{dr}$  Rear wheel drag torque, page 55
- $T_{fwx}$  Front wheel  $x$  torque, page 102
- $T_{fwy}$  Front wheel  $y$  torque, page 102
- $T_{fwz}$  Front wheel  $z$  torque, page 102
- $T_{Fy}$  Y co-ordinate of front tyre contact patch., page 67
- $T_{Fz}$  Z co-ordinate of front tyre contact patch., page 67
- $T_{mfx}$  Main frame  $x$  torque, page 102
- $T_{mfy}$  Main frame  $y$  torque, page 102
- $T_{mfz}$  Main frame  $z$  torque, page 102
- $T_{rwx}$  Rear wheel  $x$  torque, page 102
- $T_{rwy}$  Rear wheel  $y$  torque, page 102

- $T_{rwz}$  Rear wheel  $z$  torque, page 102
- $T_{Ry}$  Y co-ordinate of rear tyre contact patch., page 67
- $T_{Rz}$  Z co-ordinate of rear tyre contact patch., page 67
- $T_{say}$  Swing-arm  $y$  torque, page 102
- $T_{steer}$  Steering torque, page 102
- $U$  Point: front pneumatic trail point, page 35
- $u_1$  Generalised speed: front suspension speed, page 37
- $u_2$  Generalised speed: swing-arm angular velocity relative to the main frame, page 37
- $u_3$  Generalised speed: front tyre vertical deflection speed, page 37
- $u_4$  Generalised speed: rear tyre vertical deflection speed, page 37
- $u_5$  Generalised speed: front wheel angular velocity, page 37
- $u_6$  Generalised speed: rear wheel angular velocity, page 37
- $u_7$  Generalised speed: X speed on the ground plane, alias  $x$ , page 37
- $u_8$  Generalised speed: Y speed on the ground plane, alias  $y$ , page 37
- $u_9$  Generalised speed: motorcycle roll rate, page 37
- $u_{10}$  Generalised speed: motorcycle yaw rate, page 37
- $u_{11}$  Generalised speed: steering rate, page 37
- $u_{in}$  System input vector, page 106
- $V$  Point: rear pneumatic trail point, page 35
- $v$  Velocity of the bike, page 54
- $x$  X co-ordinate on the ground plane. Alias for generalised co-ord.  $q_7$ , page 37

---

$y$  Y co-ordinate on the ground plane. Alias for generalised co-ord.  $q_8$ , page 37

**Tyre model**

$df_z$  Vertical force increment, page 221

$dp_i$  Inflation pressure increment, page 221

$F_x$  Force exerted on the tyre by the ground in the  $x$  direction, page 120

$F_y$  Force exerted on the tyre by the ground in the  $y$  direction, page 121

$F_z$  Force exerted on the tyre by the ground in the  $z$  direction, page 120

$F_{z0}$  Nominal vertical force, page 221

$F'_{z0}$  Scaled, nominal vertical force, page 221

$K_{x\kappa}$  Longitudinal slip stiffness, page 126

$K_{y\alpha}$  Cornering stiffness, page 126

$M_x$  Overturning moment, page 123

$M_y$  Rolling resistance moment, page 124

$M_z$  Aligning (or self-aligning) moment, page 124

$P$  Inflation pressure, page 221

$P_0$  Nominal inflation pressure, page 221

$R_0$  Unloaded, or free, tyre radius, page 120

$R_e$  Effective rolling radius, page 120

$R_l$  Loaded tyre radius, page 120

$V_0$  Reference velocity, page 230

$V_x$  Forward velocity of the wheel, page 120

$V_{sx}$  Longitudinal slip velocity of the wheel, page 125

- $V_{sy}$  Lateral slip velocity, page 126
- $\alpha$  Side slip angle, page 126
- $\alpha^*$  Arctan of slip angle. Used to denote lateral slip, page 126
- $\delta_x$  Relaxation length for longitudinal force, page 127
- $\delta_y$  Relaxation length for lateral force, page 127
- $\Omega$  Angular velocity of wheel, page 125
- $\Omega_0$  Angular velocity of a free rolling wheel, page 120
- $\varepsilon_x$  Small quantity to avoid singularity, page 222
- $\varepsilon_y$  Small quantity to avoid singularity, page 226

**Tyre model, MF-Tire / MF-Swift Parameters**

- $p_{cfx1}$  Tyre overall longitudinal stiffness vertical deflection dependency linear term, page 234
- $p_{cfx2}$  Tyre overall longitudinal stiffness vertical deflection dependency quadratic term, page 234
- $p_{cfx3}$  Tyre overall longitudinal stiffness pressure dependency, page 234
- $p_{cfy1}$  Tyre overall lateral stiffness vertical deflection dependency linear term, page 234
- $p_{cfy2}$  Tyre overall lateral stiffness vertical deflection dependency quadratic term, page 234
- $p_{cfy3}$  Tyre overall lateral stiffness pressure dependency, page 234
- $p_{Cx1}$  Shape factor for longitudinal force, page 222
- $p_{Cy1}$  Shape factor for lateral force, page 226
- $p_{Dx1}$  Longitudinal friction,  $\mu_x$ , at nominal  $F_z$ , page 222

- 
- $p_{Dx2}$  Variation of longitudinal friction,  $\mu_x$ , with load,  $F_z$ , page 222
- $p_{Dx3}$  Variation of longitudinal friction,  $\mu_x$ , with camber,  $\gamma$ , page 222
- $p_{Dy1}$  Lateral friction,  $\mu_y$ , at nominal  $F_z$ , page 226
- $p_{Dy2}$  Variation of lateral friction,  $\mu_y$ , with load,  $F_z$ , page 226
- $p_{Dy3}$  Variation of lateral friction,  $\mu_y$ , with squared camber,  $\gamma^2$ , page 226
- $p_{Ex1}$  Longitudinal curvature at nominal  $F_z$ , page 222
- $p_{Ex2}$  Variation of longitudinal curvature with load,  $F_z$ , page 222
- $p_{Ex3}$  Variation of longitudinal curvature with load squared,  $F_z^2$ , page 222
- $p_{Ex4}$  Factor in longitudinal curvature while driving, page 222
- $p_{Ey1}$  Lateral curvature at nominal  $F_z$ , page 226
- $p_{Ey2}$  Variation of lateral curvature with load  $F_z$ , page 226
- $p_{Ey3}$  Zero order camber dependency of curvature, page 226
- $p_{Ey4}$  Variation of lateral curvature with camber,  $\gamma$ , page 226
- $p_{Ey5}$  Camber curvature coefficient, page 226
- $p_{Hx1}$  Horizontal shift,  $S_{Hx}$ , at nominal  $F_z$ , page 222
- $p_{Hx2}$  Variation of horizontal shift,  $S_{Hx}$ , with load,  $F_z$ , page 222
- $p_{Hy1}$  Horizontal shift,  $S_{Hy}$ , at nominal  $F_z$ , page 226
- $p_{Hy2}$  Variation of horizontal shift,  $S_{Hy}$ , with load,  $F_z$ , page 226
- $p_{Kx1}$  Longitudinal slip stiffness at nominal  $F_z$ , page 222
- $p_{Kx2}$  Variation of longitudinal slip stiffness with load,  $F_z$ , page 222
- $p_{Kx3}$  Exponent in longitudinal slip stiffness with load,  $F_z$ , page 222
- $p_{Ky1}$  Maximum value of stiffness,  $\frac{K_{y\alpha}}{F_{z0}}$ , page 226

- 
- $p_{Ky2}$  Load at which  $K_{y\alpha}$  reaches maximum value, page 226
- $p_{Ky3}$  Variation of  $\frac{K_{y\alpha}}{F_{z0}}$  with camber, page 226
- $p_{Ky4}$  Peak stiffness variation with camber squared, page 226
- $p_{Ky5}$  Lateral stiffness dependency on camber, page 226
- $p_{Ky6}$  Camber stiffness factor, page 226
- $p_{Ky7}$  Load dependency of camber stiffness factor, page 226
- $p_{px1}$  Linear pressure effect on longitudinal slip stiffness, page 222
- $p_{px2}$  Quadratic pressure effect on longitudinal slip stiffness, page 222
- $p_{px3}$  Linear pressure effect on longitudinal friction, page 222
- $p_{px4}$  Quadratic pressure effect on longitudinal friction, page 222
- $p_{py1}$  Pressure effect on cornering stiffness magnitude, page 226
- $p_{py2}$  Pressure effect on location of cornering stiffness peak, page 226
- $p_{py3}$  Linear pressure effect on lateral friction, page 226
- $p_{py4}$  Quadratic pressure effect on lateral friction, page 226
- $p_{py5}$  Influence of inflation pressure on camber stiffness, page 226
- $p_{pz1}$  Linear pressure effect on pneumatic trail, page 232
- $p_{pz2}$  Influence of inflation pressure on residual aligning moment, page 232
- $p_{Vx1}$  Vertical shift at nominal  $F_z$ , page 222
- $p_{Vx2}$  Variation of vertical shift with load,  $F_z$ , page 222
- $p_{Vy1}$  Vertical shift in  $\frac{S_{Vy}}{F_z}$  at nominal load,  $F_{z0}$ , page 226
- $p_{Vy2}$  Variation of shift in  $\frac{S_{Vy}}{F_z}$  with load,  $F_z$ , page 226
- $p_{Vy3}$  Variation of shift in  $\frac{S_{Vy}}{F_z}$  with camber,  $\gamma$ , page 226

- $q_{Vy4}$  Variation of shift in  $\frac{S_{Vy}}{F_z}$  with camber and load, page 226
- $q_{Bz10}$  Slope factor  $B_r$  of residual torque  $M_{zr}$ , page 232
- $q_{Bz1}$  Slope factor for pneumatic trail  $B_t$  at nominal load  $F_{z0}$ , page 232
- $q_{Bz2}$  Variation of slope factor for pneumatic trail  $B_t$  with load, page 232
- $q_{Bz3}$  Variation of slope factor for pneumatic trail  $B_t$  with load squared, page 232
- $q_{Bz4}$  Variation of slope factor for pneumatic trail  $B_t$  with camber, page 232
- $q_{Bz5}$  Variation of slope factor for pneumatic trail  $B_t$  with absolute camber, page 232
- $q_{Bz9}$  Slope factor  $B_r$  of residual torque  $M_{zr}$ , page 232
- $q_{Cz1}$  Shape factor for  $C_t$  for pneumatic trail, page 232
- $q_{Dz10}$  Variation of  $D_r$  with camber squared, page 232
- $q_{Dz11}$  Variation of  $D_r$  with camber squared and load, page 232
- $q_{Dz1}$  Peak pneumatic trail  $D_t$ , page 232
- $q_{Dz2}$  Variation of peak pneumatic trail  $D_t$  with load, page 232
- $q_{Dz3}$  Variation of peak pneumatic trail  $D_t$  with camber, page 232
- $q_{Dz4}$  Variation of peak pneumatic trail  $D_t$  with camber squared, page 232
- $q_{Dz6}$  Peak residual torque  $D_r$ , page 232
- $q_{Dz7}$  Variation of  $D_r$  with load, page 232
- $q_{Dz8}$  Variation of  $D_r$  with camber, page 232
- $q_{Dz9}$  Variation of  $D_r$  with camber and load, page 232
- $q_{Ez1}$  Pneumatic trail curvature  $E_t$  at nominal load  $F_{z0}$ , page 232
- $q_{Ez2}$  Variation of pneumatic trail curvature  $E_t$  with load, page 232

- $q_{Ez3}$  Variation of pneumatic trail curvature  $E_t$  with load squared, page 232
- $q_{Ez4}$  Variation of pneumatic trail curvature  $E_t$  with sign of  $\alpha_t$ , page 232
- $q_{Ez5}$  Variation of  $E_t$  with camber and sign of  $\alpha_t$ , page 232
- $q_{Hz1}$  Pneumatic trail horizontal shift  $S_{ht}$  at  $F_z0$ , page 232
- $q_{Hz2}$  Variation of  $S_{ht}$  with load, page 232
- $q_{Hz3}$  Variation of  $S_{ht}$  with camber, page 232
- $q_{Hz4}$  Variation of  $S_{ht}$  with camber and load, page 232
- $q_{sx12}$  Camber squared induced overturning moment, page 230
- $q_{sx13}$  Lateral force induced overturning moment, page 230
- $q_{sx14}$  Lateral force induced overturning moment with camber, page 230
- $q_{sy1}$  Rolling resistance moment coefficient, page 230
- $q_{sy2}$  Rolling resistance moment dependence on  $F_x$ , page 230
- $q_{sy3}$  Rolling resistance moment dependence on speed  $V_x$ , page 230
- $q_{sy4}$  Rolling resistance moment dependence on  $V_x^4$ , page 230
- $q_{sy5}$  Rolling resistance moment dependence on  $\gamma^2$ , page 230
- $q_{sy6}$  Rolling resistance moment dependence on  $\gamma^2$  and load  $F_z$ , page 230
- $q_{sy7}$  Rolling resistance moment dependence on load, page 230
- $q_{sy8}$  Rolling resistance moment dependence on inflation pressure, page 230
- $r_{Bx1}$  Slope factor for combined slip  $F_x$  reduction, page 224
- $r_{Bx2}$  Variation of slope  $F_x$  reduction with  $\kappa$ , page 224
- $r_{Bx3}$  Influence of camber on stiffness for  $F_x$  combined slip, page 224
- $r_{By1}$  Slope factor for combined slip  $F_y$  reduction, page 228

- 
- $r_{By2}$  Variation of slope  $F_y$  reduction with slip angle,  $\alpha$ , page 228  
 $r_{By3}$  Shift term for  $\alpha$  in slope  $F_y$  reduction, page 228  
 $r_{By4}$  Influence of camber on stiffness of  $F_y$  combined slip, page 228  
 $r_{Cx1}$  Shape factor for combined slip  $F_x$  reduction, page 224  
 $r_{Cy1}$  Shape factor for combined slip  $F_y$  reduction, page 228  
 $r_{Ex1}$  Curvature factor of combined slip  $F_x$ , page 224  
 $r_{Ex2}$  Curvature factor of combined slip  $F_x$  with load, page 224  
 $r_{Ey1}$  Curvature factor of combined slip  $F_y$ , page 228  
 $r_{Ey2}$  Curvature factor of combined slip  $F_y$  with load, page 228  
 $r_{Hx1}$  Shift factor for combined slip  $F_x$  reduction, page 224  
 $r_{Hy1}$  Shift factor for combined slip  $F_y$  reduction, page 228  
 $r_{Hy2}$  Shift factor for combined slip  $F_y$  reduction with load, page 228  
 $r_{Vy1}$   $\kappa$  induced side force  $\frac{S_{Vy\kappa}}{\mu_y F_z}$  at  $F_{z0}$ , page 228  
 $r_{Vy2}$  Variation of  $\frac{S_{Vy\kappa}}{\mu_y F_z}$  with load,  $F_z$ , page 228  
 $r_{Vy3}$  Variation of  $\frac{S_{Vy\kappa}}{\mu_y F_z}$  with camber,  $\gamma$ , page 228  
 $r_{Vy4}$  Variation of  $\frac{S_{Vy\kappa}}{\mu_y F_z}$  with slip angle,  $\alpha$ , page 228  
 $r_{Vy5}$  Variation of  $\frac{S_{Vy\kappa}}{\mu_y F_z}$  with slip ratio,  $\kappa$ , page 228  
 $r_{Vy6}$  Variation of  $\frac{S_{Vy\kappa}}{\mu_y F_z}$  with  $\arctan(\kappa)$ , page 228  
 $s_{sz1}$  Nominal value of  $\frac{s}{R_0}$ : effect of  $F_x$  on  $M_z$ , page 232  
 $s_{sz2}$  Variation of  $\frac{s}{R_0}$  with  $\frac{F_y}{F_{z0}}$ , page 232  
 $s_{sz3}$  Variation of  $\frac{s}{R_0}$  with camber, page 232  
 $s_{sz4}$  Variation of  $\frac{s}{R_0}$  with load and camber, page 232

- $\lambda_r$  Scale factor of offset of residual torque, page 232
- $\lambda_s$  Scale factor of moment arm of  $F_x$ , page 232
- $\lambda_t$  Scale factor of peak of pneumatic trail, page 232
- $\lambda_{\mu x}$  Scale factor of  $F_x$  peak friction coefficient, page 222
- $\lambda_{\mu y}$  Scale factor of  $F_y$  peak friction coefficient, page 226
- $\lambda_{Cx}$  Scale factor of  $F_x$  shape factor, page 222
- $\lambda_{Cy}$  Scale factor of  $F_y$  shape factor, page 226
- $\lambda_{Ex}$  Scale factor of  $F_x$  curvature factor, page 222
- $\lambda_{Ey}$  Scale factor of  $F_y$  curvature factor, page 226
- $\lambda_{Fz0}$  Scale factor of nominal load,  $F_{z0}$ , page 221
- $\lambda_{Hx}$  Scale factor of  $F_x$  horizontal shift, page 222
- $\lambda_{Hy}$  Scale factor of  $F_y$  horizontal shift, page 226
- $\lambda_{Ky\alpha}$  Scale factor of cornering stiffness, page 226
- $\lambda_{Ky\alpha}$  Scale factor of cornering stiffness, page 232
- $\lambda_{Ky\gamma}$  Scale factor of camber stiffness, page 226
- $\lambda_{Kz\gamma}$  Scale factor of camber stiffness, page 232
- $\lambda_{Mx}$  Scale factor for overturning moment, page 230
- $\lambda_{My}$  Scale factor for rolling resistance moment, page 230
- $\lambda_{Vx}$  Scale factor of  $F_x$  vertical shift, page 222
- $\lambda_{Vy\kappa}$  Scale factor of  $\kappa$  induced ply-steer, page 228
- $\lambda_{Vy}$  Scale factor of  $F_y$  vertical shift, page 226
- $\lambda_{x\alpha}$  Scale factor of  $\alpha$  influence on  $F_x$ , page 224

$\lambda_{y\kappa}$  Scale factor of  $\kappa$  influence on  $F_y$ , page 228

$\zeta_{1\dots 8}$  Turn slip parameters ( = 1 when turn slip is not used), page 222

### Other symbols

$d$  Inverted pendulum model, damping constant, page 23

$F_C$  Inverted pendulum model, horizontal force on cart, page 23

$F_P$  Inverted pendulum model, horizontal force on pendulum, page 23

$I_P$  Inverted pendulum model, moment of inertia of pendulum, page 23

$k$  Inverted pendulum model, spring constant, page 23

$L$  Inverted pendulum model, length of pendulum, page 23

$M_C$  Inverted pendulum model, mass of cart, page 23

$M_P$  Inverted pendulum model, mass of pendulum, page 23

$\hat{n}_r$  Inverted pendulum model, vectors defining the  $N$  reference frame, page 23

$N$  Inverted pendulum model, Newtonian reference frame, page 23

$\hat{p}_r$  Inverted pendulum model, vectors defining the  $P$  reference frame, page 23

$P$  Inverted pendulum model, pendulum reference frame, page 23

$q_1$  Inverted pendulum model, horizontal position of cart, page 23

$q_2$  Inverted pendulum model, angular position of pendulum, page 23

$u_1$  Inverted pendulum model, horizontal velocity of cart, page 23

$u_2$  Inverted pendulum model, angular velocity of pendulum, page 23

## Abbreviations

**ABS** anti-lock braking system

**ADC** analog to digital converter

**BHP** brake horsepower

**CAD** computer-aided design

**CAL** Cornell Aeronautical Laboratory Inc.

**CAN** Controller Area Network

**CSV** comma-separated value

**DFT** Discrete Fourier Transform

**ECU** engine control unit

**GIS** geographic information system

**GPS** Global Positioning System

**IMU** inertial measurement unit

**ODE** ordinary differential equation

**PI** proportional-integral

**PID** proportional-integral-derivative

**rpm** revolutions per minute

**TC** traction control

# Abstract

Modern racing and high performance road motorcycles have begun to use ever more sophisticated control systems to improve performance and safety. Traction control, anti-wheelie control, engine brake control and in the case of road bikes, anti-lock braking are now ubiquitous. Electronically adjustable suspension damping is becoming ever more common. At the time of writing, no manufacturer uses a high fidelity real time model of the motorcycle and tyres in their control strategies. The use of such a model would assist in integrating separate strategies into an overall vehicle stability strategy. Furthermore, the development of racing and high performance road motorcycles has traditionally depended more on experience and testing than on modelling and simulation. One reason for this has been the lack of availability of a high fidelity motorcycle model suitable for the task. The development of general multibody simulation software such as MSC Adams has been driven primarily by the four wheel world and is much more suited to cars than motorcycles. Simplified or over-linearised models lack the required fidelity.

A new high fidelity multibody motorcycle model for use in real time is proposed. It is an eleven degree of freedom model and the equations of motion are formulated using Kane's equations. Kane's method has been chosen over other methodologies as it scales well to complex systems and lends itself to automated numerical computation in a way that other methods do not. There are few linear relationships in the mechanism of a motorcycle, but many relationships are very nearly linear. This fact is used to simplify the model while maintaining fidelity and this contributes to lowering the computation cost. The tyre model is the widely used Magic Formula model, developed by Pacejka and others. The motorcycle model estimates data which is not directly measurable, such as tyre shear

---

forces and slip angles.

A motorcycle was instrumented and data was recorded during various tests, including coast-down testing and some very competitive laps of a race circuit by a professional motorcycle racer and test rider. The data from the coast-down tests was used to estimate aerodynamic and engine drag parameters. The model was validated against the race track test data with satisfactory results. Tyre model parameters were not available for the tyres used in testing, so a method was developed to estimate the tyre parameters which predict lateral force. The behaviour of the model was analysed by applying various test functions and root locus analysis was carried out to investigate the system modes.

The utility of the model for motorcycle development and set-up was investigated and a method was developed whereby motorcycle parameters may be optimised with respect to certain performance criteria. This method may be used to explore directions for future development and also to optimise settings for racing.

# Acknowledgements

I would like to express my sincere gratitude to my supervisor, Prof. John Ringwood, for his advice, encouragement and patience during the course of this research and thesis preparation.

Sincere thanks are also due to the staff and postgrads in the Department of Electronic Engineering for their help and encouragement over the years, especially Ann Dempsey and Joanne Bredin. I am very grateful also to the library staff who 3D printed many components essential to this project.

I am indebted to Jeremy McWilliams who rode my instrumented motorcycle at Nutts Corner race circuit in Northern Ireland. Despite my assurance that a moderately fast pace would suffice, Jeremy provided me with data recorded at close to the limit of the bike's performance. Like most professional racers, Jeremy downplays personal risk, but I am conscious of it and very grateful.

This research was generously assisted by 2D Debus & Diebold Meßsysteme GmbH (2D Datarecording), Karlsruhe, Germany, who provided the data logger, hardware, sensors and data recording software. The support of the company, and especially Dirk Debus, is gratefully acknowledged.

Thanks also to Seán O'Kane for his assistance in processing the Global Positioning System (GPS) data and his use of the geographic information system (GIS) to produce the track map used in Chapter 6.

Generous assistance was also provided by Öhlins Racing AB, Upplands Väsby, Sweden, in the form of suspension and steering components. Special thanks to Graeme Irvine of Öhlins Racing for suspension set-up and calibration, and unfailing encouragement.

Sincere thanks also to Neil Spalding of Sigma Performance, Tunbridge Wells,

---

England, who provided a back-torque limiting clutch for the bike, giving a significant improvement in performance and safety when testing on track.

Finally, I want to thank my friends and mentors Warren Willing and Mike Sinclair for the knowledge, inspiration and encouragement they so generously provided.

# Declaration

I hereby certify that this material, which I now submit for assessment on the programme of study leading to the award of Doctor of Philosophy in Electronic Engineering is entirely my own work and has not been taken from the work of others save and to the extent that such work has been cited and acknowledged within the text of my work.

Signed: \_\_\_\_\_

ID No. 13250093

Date:

To my parents, my children Seán and Aoife and my brothers Declan and J.J.

This work is a result of their love, support and sacrifices.

# Chapter 1

## Introduction

### 1.1 Introductory remarks

In many fields, there is a gap between research and engineering, and the field of single track vehicles is no exception. The gap is arguably less in racing than in the motorcycle industry as a whole, but much work remains to be done to bridge it. The four wheel world has done somewhat better in this regard. Driven by advertising, the F1 racing series has embraced modelling and simulation in a way that motorcycle racing is now just beginning to do. Development of commercial multibody modelling software, such as MSC Adams, has been led by the demands of F1 and the car industry, and this is therefore not an ideal solution for modelling motorcycles. In any case, the use of high level software tools does not always imply a good understanding of the underlying physics. This thesis is an attempt to understand what makes motorcycles and tyres behave the way they do when pushed to the limit of their performance, while laying the foundation for the engineering tools needed to exploit that knowledge.

### 1.2 Motivation

Not long after I began to work in motorcycle racing, I got to know Peter Williams, who was long retired from a successful motorcycle racing career. Peter was renowned for his engineering approach to racing and at the time I met him,

he was working as an engineer for Cosworth. We talked a lot about how motorcycles worked and what the future might hold in terms of our understanding. At that time I was involved in the early stages of data recording and Peter was very optimistic about where that might lead. We looked forward to the day when it would be possible to model the entire system and drive the model with real data. I remember that Peter was pessimistic about the obstacles, but he might contend that I was naïvely optimistic. Nevertheless, the ambition to solve that problem never left me.

As I continued to work with motorcycles, data recording and engineering tools provided more insight into what was happening on track. However, there remained a great many unknowns, and it was necessary to supplement the data with mental imagery to fill in the blank spaces. My ambition for this project is to shrink those areas of ‘terra incognita’, while probably at the same time raising new questions.

On a more general note, single track vehicles have, in my opinion, been somewhat neglected and even underestimated in the wider field of vehicle dynamics. Knowledge has been advanced by a relatively small number of people who were ‘bitten by the bug’ in one way or another. So, a further motivation is to help show what a fascinating field of study this is.

## 1.3 Novelty of research

Previous multibody motorcycle models have mainly used Lagrange’s equations to formulate the equations of motion. These require differentiation of scalar functions of kinetic and potential energy, and are inefficient and cumbersome when dealing with complex systems. Developed in the 1960s, Kane’s method of formulating the equations of motion is a relatively recent development that is not yet in widespread use in the field of vehicle dynamics. It is an elegant means of developing the equations of motion for a multibody system that lends itself well to numerical computation. [1]

Many previous multibody models lose fidelity due to linearisation. In this

model, care has been taken to linearise only those relationships that are very close to being linear over their operating range. These are the relationships between the position and orientation of the main frame and most, but not all, of the state variables. Suspension forces, which are substantially non-linear, though treated as linear by many other models, are moved to the input of the system, using the Hammerstein model architecture.

The structure of the model is designed to be computationally efficient so that it can run in real time, and may therefore be used as an observer in an embedded control system.

## 1.4 Thesis layout

The thesis is organised in four sections. These are itemised below, followed by a brief description of each chapter to assist the reader in navigating the thesis.

- Introduction
  - Chapter 1: Introduction.
  - Chapter 2: Literature Review.
- Methodology
  - Chapter 3: Multibody System Modelling.
  - Chapter 4: The Motorcycle Model.
  - Chapter 5: The Tyre Model.
- Validation
  - Chapter 6: Sensing and Data Logging.
  - Chapter 7: Model Validation and Analysis.
- Utility
  - Chapter 8: Application Examples.
  - Chapter 9: Conclusions.

**Chapter 2: Literature Review.** This chapter presents a brief history of research in the field of bicycle and motorcycle dynamic modelling, and then focuses on the current state of the art. The chapter also provides a summary of the history of tyre models.

**Chapter 3: Multibody System Modelling.** There are a number of methods for deriving the equations of motion for a multibody system. In this chapter, the Newton-Euler, Lagrange and Kane's method are used to derive the model for a simple system, and the pros and cons of each method are analysed, so as to choose the method to be used for the motorcycle model.

**Chapter 4: The Motorcycle Model.** This is the chapter that deals with the main subject of the thesis, that is to construct the multibody model of the motorcycle. It begins by explaining the principles and terminology needed to build the model, and goes on to examine the forces and moments that determine the behaviour of a motorcycle. The linearisation of certain aspects of the model is then covered before the actual modelling procedure is explained. This is followed by an explanation of how the model is controlled, and the chapter finishes with a section on strategies such as traction control (TC) and anti-lock braking system (ABS) which are implemented to prevent the model from crashing in certain circumstances.

**Chapter 5: The Tyre Model.** The chapter begins by explaining tyre characteristics and terminology. The Magic Formula tyre model is explained and a set of Magic Formula parameters is constructed for the tyres used in testing. The procedure for measuring the tyre profile as a function of camber angle is explained.

**Chapter 6: Sensing and Data Logging.** The chapter begins with an overview of the data logging system and a detailed explanation of the hardware modules. A description of how the 2D Datarecording system handles analog and digital channels is given, followed by an in depth description of each recorded channel.

Each sensor and its application is discussed, and issues such as mounting, calibration and vibration are covered. The procedures for track and coast-down testing are also explained.

**Chapter 7: Model Validation and Analysis.** The chapter begins by simulating the two coast-down tests outlined in Chapter 6 and comparing the estimated and recorded data. The same is done for the data recorded on the race track, and the location of the bike estimated by the model is compared to the GPS data. Test inputs are applied to the model and the system behaviour is analysed. Finally, root locus analysis of the model is performed.

**Chapter 8: Application Examples.** This chapter gives a practical example of how the model can be used to evaluate parameter changes before they are applied to the bike. A single parameter change is evaluated using a number of criteria.

**Chapter 9: Conclusions.** This chapter discusses the conclusions arising from the thesis.

**Appendix A: Magic Formula Equations.** This appendix contains the equations for the MF-Tyre MF-Swift 6.2 tyre model, which is the model used in the thesis and the latest version of the Magic Formula tyre model at the time of writing.

# Chapter 2

## Literature Review

This chapter presents a brief history of research in the field of bicycle and motorcycle dynamic modelling, and then focuses on the current state of the art. Although the thesis does not concern itself with extending the field of tyre modelling, a brief history of that field is also presented, so as to explain the rationale for choosing the tyre model. As in many fields, the literature on the development of bicycle and motorcycle dynamic models is extremely varied. In developing the structure of this chapter, the 2007 article by Meijaard et al. [2] was very useful. As well as providing a benchmark model for studying controlled and uncontrolled stability of a bicycle, the authors provide a history of bicycle dynamics studies up to that point in time, extending the earlier work of Hand, 1988 [3], and grouping the literature into three categories. This classification is adopted here and a fourth category is added.

Category (a) comprises ‘qualitative discussions of stability’. These are articles and books that discuss handling and stability without detailed equations. This group is not considered here. In category (b), ‘simplified analyses that use dynamics’, Meijaard et al. [2] include models that have either simplified geometry and or mass distribution, no steering dynamics because the steering is fully controlled by the rider, or mathematically simplified models. While some individual articles are mentioned because they made a significant contribution to the literature, this category as a whole is not discussed because it has little direct relevance. Group (c), ‘equations of motion for a Whipple bicycle’ contains models that have enough

complexity to predict hands-free stability and this category covers a good deal of relevant literature. A fourth category (d), ‘state of the art multibody models’ is added here.

Before, discussing category (c), two early works on the subject deserve mention. In 1869, W. J. M. Rankine [4] made fundamental observations on the steering and leaning of velocipedes, and is mentioned here because his work contained the earliest known mention of counter-steering. In 1896, Archibald Sharp [5] used a greatly simplified model to calculate the torque needed to execute a steady turn. Like many pioneering works, his description includes some assumptions that were later challenged. Nevertheless, his work is of engineering, and not merely historical, interest.

## 2.1 Equations of motion for a Whipple bicycle

The models in this category are capable of self-stability and allow uncontrolled steering dynamics. They are discussed mainly in chronological order. The first to formally derive a fully general set of equations for the bicycle model was Francis John Welsh Whipple in his 1899 paper [6]. Whipple’s model is still relevant today and modified versions of his model feature in articles throughout this chapter. Whipple’s bicycle is made up of a front and rear frame, hinged at an inclined steering head. The wheels are modelled by holonomic constraints in the vertical direction and by non-holonomic constraints in the lateral and longitudinal directions. He analysed the speed ranges for which the bicycle was self-stable, i.e. with the rider’s hands off the handlebar, and for which it could be stabilised by the rider applying a steering torque or moving their centre of mass. He also proposed the name ‘back trail’ for the distance from the point of intersection of the steering axis with the road to the rear tyre contact point. At around the same time, the French mathematician, Emmanuel Carvallo [7] [8] developed a bicycle model. Although Carvallo’s model is not dissimilar to Whipple’s, apparently both men were unaware of each other’s work. Some authors, for example Schwab and Meijaard [9] refer to this bicycle model as the Carvallo-Whipple model. After the

pioneering work of Whipple and Carvallo, there was a lengthy hiatus, and it was not until Sharp published his seminal paper in 1971 [10] that the field began to move forward significantly.

In the meantime, in their 1948 book [11], Timoshenko and Young reproduced a point-mass model originally published by Bouasse in 1910 [12]. As a simplified model which lacks the ability to self-steer, it belongs in category (b). Nevertheless it helps to illustrate some key features of bicycle behaviour and is therefore useful up to a point. As in all models of this era, the contact between the wheels and the road is regarded as a constraint. In their 1996 article [13], Limebeer and Sharp resolve the Timoshenko-Young model into a point-mass specialisation of the Whipple model. In doing this, many simplifying assumptions must be made. Nevertheless, the authors state that under certain conditions, simple Timoshenko-Young type models have been applied to sophisticated machine models with some success.

Sharp's 1971 article [10] has been one of the most influential on bicycle and motorcycle dynamics. In it, he predicted and named three important modes, 'capsize', 'weave' and 'wobble'. The paper is also remarkable in being among the first to treat the tyre as a force and moment producing component, rather than a constraint. It was also the start of a process that led to the Sharp and Limebeer 2001 model [14], which is discussed in more detail in Section 2.2. Sharp's motorcycle consists of a front and rear frame hinged on an inclined steering axis. A linear steering damper is included. The rear frame is made up of the motorcycle frame, engine, petrol tank, swing-arm, rear wheel, etc. and the rider is rigidly attached to the rear frame. The front frame consists of the front fork, handlebars, front wheel, etc. The model has four degrees of freedom; yaw, roll, steer and lateral motion. The wheels are rigid discs, making point contact with the smooth, level road surface, and there is no longitudinal slip. The tyres produce steady state forces and moments that are linearly related to camber and side slip. The lag due to the tyre relaxation property is modelled by a first order differential equation. The bike moves at a constant forward speed. Both aerodynamic forces and tyre pneumatic trail are considered to be negligible, as is the minute amount

of pitch induced by small steering angles. The equations of motion are derived using Lagrange's equations\*, and neglecting second and higher order terms means that only small perturbations from straight line running are considered, and the model becomes linear.

Sharp carried out a stability analysis by calculating the eigenvalues for a range of constant forward road speeds. At low speed, the capsize mode is a non-oscillatory divergent instability where the motorcycle falls over on its side. The weave mode involves motion in roll, yaw and steer. It is oscillatory with a frequency increasing from about 0.2 Hz at a forward speed of approximately 1.5 m/s to about 3.4 Hz at approximately 48.8 m/s. It is unstable up to about 6 m/s, is well damped in the medium speed range and moderately so at high speed. In wobble mode, the front frame oscillates relative to the rear frame about the steering axis with a natural frequency of around 9 Hz [10]. The natural frequency is almost independent of forward speed. It is well damped at low and medium speeds and only moderately so at high speed. Moreover, Sharp found that the degree of damping for wobble is strongly dependent on the tyre relaxation length and the damping of the weave mode is only moderately dependent. The article by Limebeer and Sharp, 2006 [13] cites a survey by Juden, 1988 [15] that suggests that wobble may occur over a wide range of frequencies, but is often close to the rotation frequency of the front wheel. Limebeer and Sharp suggest that forcing from wheel or tyre non-uniformity may be an added influence.

Sharp's article analyses the case where the steering angle degree of freedom is removed, and also a case which excludes tyre sideslip, but the results of these configurations are not of interest here. He also investigated the model sensitivity to various parameters. Some parameter changes may bring both advantages and disadvantages. For example, he found that wobble was stabilised by increasing the steering damping, but at the expense of amplifying weave. Making the steering head steeper improved low and medium speed behaviour at the expense of high speed behaviour. He found that other design changes brought advantages with no disadvantage, provided that the steering damper is suitably adjusted.

---

\* Lagrange's equations are examined in Section 3.7.

Among these were lowering the rear frame mass centre or moving it forward, or increasing the rear wheel rotational inertia. These advantages are valid within the limitations of the model. In 1974, Sharp [16] expanded his model to allow torsional flexibility in the rear frame. The rear wheel was allowed to twist relative to the rear frame about a longitudinal axis, restrained by a linear spring and damper.

Tyre models evolved from non-slipping wheels into components that generate forces and moments. Early models concerned themselves with constant speeds and small perturbations about the straight-running condition but, partly due to advances in computing power, modern models handle the non-linear differential equations that are needed to describe the vehicle at high camber angles. In 1974, aerodynamic effects began to be included and Cooper [17] used Sharp's model and wind-tunnel data to analyse the influence of aerodynamic effects on stability.

One of the first computer simulations of a nonlinear bicycle model was carried out in 1973 by Douglas Roland [18] at Cornell Aeronautical Laboratory Inc. (CAL) in a research program sponsored by the Schwinn Bicycle Company. The purpose of the simulation was to study the effects of design parameter variations on stability and control. The model has eight degrees of freedom: six for the main frame, including the rider, one for rider lean and one for steering. The model includes tyre side forces, due to lean and sideslip angles, and gyroscopic effects for the rotating wheels. Among the forty four design parameters are the radial stiffness of the tyres. The dynamic equations are integrated using a modified Runge-Kutta procedure, and outputs included translational and angular positions, velocities, accelerations and tyre force components. A second phase included the development of the first computer graphics program to present animations of the bicycle and rider [19].

Prior to the independent work of Sharp and Alstead in 1980 [20], and Spierings in 1981 [21] there was a discrepancy between experimental results and theoretical predictions of the wobble mode. In those articles, torsional compliance about a longitudinal axis was introduced between the front wheel and the main frame, and this turned out to be the missing detail that allowed agreement between the

theoretical and measured results.

Koenen was one of the first to analyse the effect of perturbations about the steady cornering condition in his articles with Pacejka in 1980 [22] and 1981 [23] and in his 1983 PhD. thesis [24]. In the PhD. thesis, he considers a motorcycle in three conditions. In the ‘nominal’ conditions, the motorcycle with the rider has zero roll angle and zero forward speed. In the ‘stationary’ conditions, the motorcycle with rider is in straight running or steady-state cornering, and in the ‘non-stationary’ condition, there are infinitesimal perturbations from the stationary condition. The nominal condition serves as the starting point for the calculations, the stationary situation is described by a set of non-linear algebraic equations, and the non-stationary condition is described by a set of linear differential equations. He draws a distinction between ‘symmetrical dynamics’, which are the longitudinal dynamics including suspension dynamics, and ‘anti-symmetrical dynamics’, which are lateral dynamics. Koenen [24] noted that, in cornering, the symmetric vibration modes of pitch, bounce and wheel hop interact with the anti-symmetric modes such as weave and wobble.

Koenen’s full model [24] consists of the following bodies; the main frame assembly, the upper part of the rider’s body, the front and rear wheels and the front and rear unsprung masses. Additionally, the mass of the front frame is divided into upper and lower masses; the lower part can twist about a longitudinal axis with respect to the main frame, while the upper part cannot. He devised a unique and helpful method of illustrating the motorcycle in various modes of oscillation and included many root loci plots to illustrate the sensitivity of the model to parameter variations. The tyre model is discussed in Section 2.3.

## 2.2 State of the art multibody models

Two models are considered in this category. The Sharp and Limebeer 2001 model [14] is abbreviated as ‘SL 2001’ and the Cossalter and Lot 2002 model [25] is abbreviated as ‘CL 2002’. These models are described individually, and then compared. The tyre models are discussed in detail in Section 2.3.

### 2.2.1 The SL 2001 model

Sharp extended his model in 1994 [26] and this was the forerunner to Sharp and Limebeer's SL 2001 model. [14] The authors analyse the motions arising from small perturbations about the straight running condition as per Sharp, 1971 [10], and also about an equilibrium cornering condition. The equilibrium cornering condition was first analysed by Koenen [24], extending his previous work with Pacejka [22] and [23]. In the SL 2001 model, a description of longitudinal tyre force is avoided by constraining the wheels to rotate without longitudinal slip. One effect of this assumption is to alter the rotational speed of the wheels and therefore the magnitude of the gyroscopic torques, but this effect is taken into account. The wheels are treated as discs which can be deflected in the direction from the contact point towards the wheel centre. This deflection is subject to a spring force in the radial direction due to tyre deflection. The tyres are rigid in the lateral direction relative to the wheel. Relaxation behaviour is modelled by a first order lag equation that relates the lateral force and aligning torque to the sideslip and camber angles. Tyre forces and moments are generated by Koenen's tyre model [24], which is discussed in Section 2.3. As a motorcycle leans over, the tyre contact patch moves laterally with respect to the wheel centre plane, giving rise to an overturning moment. Disc wheels with infinitesimal thickness do not inherently create this moment, so it is added separately. The authors control the vehicle speed using a proportional-integral (PI) controller that uses the speed error to produce a rear wheel torque. Roll angle is controlled by a proportional-integral-derivative (PID) controller that uses camber error to produce a steering torque. They note that the controller gains are critical to the stability of the model. The authors found that the controllers needed re-tuning for each camber angle. Suspension limit stops are included at each end, modelled as fifth powers of displacement from stop contact. [27] This model has been used in further work such as the study of burst oscillations by Evangelou et al. [28]

### 2.2.2 The CL 2002 model

Cossalter and Lot [25] built an 11 degree of freedom non-linear multibody dynamic model and developed an original tyre model, which is discussed in Section 2.3. The motorcycle is described by a set of 45 co-ordinates. Because it has eleven degrees of freedom, a set of  $45 - 11 = 34$  constraint equations are needed. The multibody model is implemented in Fortran code with a view to real time simulation. The Fortran code is generated using Maple<sup>®</sup> to perform the symbolic calculations. The equations of motion are obtained using Lagrange's equations. Together, the Lagrange, constraint and tyre equations form a set of 85 second order differential-algebraic simultaneous equations, where the unknowns are 51 generalised co-ordinates and 34 Lagrange multipliers.

In the appendix, Cossalter and Lot illustrate the non-linear nature of the suspension spring and damping curves used in the model, but no mention is made of the extreme non-linearities that are encountered at the limits of suspension travel. These are particularly relevant when the motorcycle is being ridden close to the performance limit as they introduce steps in spring rate and force.

### 2.2.3 Comparison of multibody models

Table 2.1 lists the degrees of freedom in the SL 2001 and CL 2002 models. The SL 2001 model has two more degrees of freedom than the CL 2002 model, namely, fork twist about a longitudinal axis and rider upper body rotation, also about a longitudinal axis. The SL 2001 model is implemented in AutoSim, which can generate a C or Fortran simulation and data files containing bike parameters and simulation run control parameters. [14] AutoSim is a language used to describe general multi-body systems and is based on Kane's equations. It provides a level of abstraction from the equations of motion, using commands such as 'add body', 'add speed constraint', etc. The CL 2002 model is implemented in Fortran and is sold commercially as 'FastBike'. [25] The equations of motion are formulated using Lagrange's equations.

When introducing the SL 2001 model, [14] Sharp and Limebeer use Koenen's

	SL 2001	CL 2002
Front wheel rotation angle	✓	✓
Rear wheel rotation angle	✓	✓
Front suspension travel	✓	✓
Rear suspension travel	✓	✓
Yaw angle	✓	✓
Roll angle	✓	✓
Pitch angle	✓	✓
Steering angle	✓	✓
X position	✓	✓
Y position	✓	✓
Z position	✓	✓
Front tyre vertical deflection		
Rear tyre vertical deflection		
Fork twist	✓	
Rider upper body rotation, X	✓	

Table 2.1: Model degrees of freedom compared

tyre model, and in a later implementation, Sharp et al. [27] use the Magic Formula tyre model. Cossalter and Lot [25] do not provide great detail about the character of the forces and moments in their tyre model but say that by taking the deflection of the contact patch into account, the model represents an improvement over previous ones. The tyre forces are applied at the contact point. The authors also derive an expression for longitudinal relaxation length.

## 2.3 Tyre model time line

This section provides background and a brief summary of the history of tyre models, and then discusses the models used in Section 2.2 in some detail. For an explanation of tyre characteristics and terms, such as longitudinal or lateral slip stiffness etc. refer to Section 5.2. The term ‘sideslip angle’ is often abbreviated to ‘slip angle’ and both terms may be used here. One of the main differences between early and modern bicycle models is that the tyre went from being treated as a constraint to being a force and moment-producing entity.

Since study of the pneumatic tyre began, a wide variety of approaches have been adopted with regard to modelling. These range from empirical methods that

use regression techniques to fit test data to a set of formulas, to complex finite element physical models that describe the tyre in great detail. Simple physical models have long been used to approximate the compliance of the tyre tread rubber, belt and carcass. One of these is the brush model, originated by Fromm in his 1941 paper [29], and translated to English by the National Advisory Council for Aeronautics (NACA). It consists of a row of elastic bristles extending radially from the wheel, which represent elements of the tread. Fromm refers to these as rubber lugs, and each element acts independently of its neighbours. When the wheel rolls freely, without torque, sideslip, camber or turning, the elements remain un-deflected. Otherwise, lateral and longitudinal forces are generated in each element, depending on the extent and direction of its deflection.

Another simplified mechanical model is represented by a string following the circumference of the wheel, that is kept under tension by a uniform outward radial force. The string is flattened where it contacts the flat road surface and may move elastically in the axial direction. Movement in the circumferential direction is represented by the deflection of independent tread elements similar to those of the brush model, though they are constrained to move only in that direction. Lateral and longitudinal forces are generated by the axial deflection of the string and the circumferential deflection of the tread elements respectively.

The tyre model adopted by Koenen [24] consists of a thin disc which is flexible in the radial direction, subject to a spring force. The model produces a lateral force in response to sideslip, camber angle and turnslip, an aligning moment in response to those same inputs, and an overturning moment in response to camber angle. Although turnslip is included in the model, Koenen found it to be negligible. Longitudinal force due to longitudinal slip is disregarded. Lateral force and aligning moment due to sideslip are lagged to simulate the relaxation property of the tyre. Other forces and moments are assumed to be instantaneous. Cornering or sideslip stiffness, i.e. the rate of change of lateral force with respect to slip angle, is treated as being linear, with no saturation. Therefore, it is accurate only at relatively small slip angles. The cornering stiffness decays linearly with increasing camber magnitude and is linearly dependent on load. Lateral force

due to camber, on the other hand, is treated as non-linear with respect to camber angle and is approximated by a parabola. It too is assumed to be linearly dependent on load. The aligning moment is made up of lateral force components due to sideslip and camber acting through the pneumatic trail. As mentioned previously, the contribution of turnslip is considered negligible. The pneumatic trail, and likewise the aligning moment due to sideslip, decrease linearly with respect to the slip angle magnitude and are proportional to the square root of the nominal load ratio  $F_z/F_{z0}$ . The aligning moment due to camber has a parabolic dependence on the camber angle in accordance with data obtained by Sakai [30], and is proportional to the nominal load ratio to the power of  $5/2$ .

Due to the lack of experimental data, Koenen derives the non-stationary tyre behaviour from the taut string theory, introduced above. First order differential equations for slip angle-dependent lateral force and aligning moment are derived. These are distance rather than time dependent, with the relaxation length being the response distance constant. Koenen cites Segel and Wilson [31] in stating that about 80% of the camber-dependent lateral force lags the input, with the remaining 20% of the response being instantaneous. The lagged component is attributed to the lateral displacement of the string where it contacts the road, while the instantaneous part is due to the lateral component of the tyre radial force. With regard to aligning torque, the part due to slip angle is assumed to be lagged, while the part due to camber angle is assumed to be instantaneous.

The SL 2001 multibody model which is discussed in Section 2.2, adopts the tyre model used by Koenen [24] and described above. This is done for the purpose of reproducing Koenen's motorcycle model results and it is acknowledged by the authors that the Magic Formula<sup>†</sup> tyre model has more recently been applied to motorcycle tyres with the possibility of improving on previous methods. Subsequently, Sharp et al. [27] use the SL 2001 multibody model in conjunction with the Magic Formula tyre model

The tyre model used by Cossalter and Lot [25] considers the lateral and longitudinal slip stiffness to be linear, with no saturation. Therefore, the model is

---

<sup>†</sup> The Magic Formula tyre model is discussed later in this section.

accurate only in the linear range, i.e. at relatively low levels of longitudinal or lateral slip. The rolling resistance moment,  $M_y$  and aligning moment  $M_z$  are likewise considered to be linear with respect to normal load, slip angle and camber. The overturning moment  $M_x$  is zero because the tyre forces are applied at the actual tyre contact point, taking into account the deflection of the tyre and contact patch migration due to camber angle. When modelling tyres, the lag due to the tyre relaxation property is typically modelled by a first order differential equation. In the paper, the authors show how this lag equation may be formulated, and an expression is derived for the longitudinal relaxation length in terms of the longitudinal slip stiffness, rotational stiffness of the tyre and the effective rolling radius. Cossalter and Lot treat the pneumatic trail as constant, while Sharp, Limebeer and Pacejka treat it as decreasing with slip angle magnitude.

The best known empirical tyre model is the Magic Formula model. The first Magic Formula tyre model by Bakker et al. [32] and [33], is known as the ‘Monte Carlo’ version due to the conference at which the 1989 paper was presented. A later, 1993, version by Pacejka and Bakker [34] is known as ‘Version 3’ of the Magic Formula. These early versions modelled the tyre in steady state conditions only, but it was known that in reality, the generation of lateral force is not instantaneous but subject to a lag. It was shown by Loeb et al. 1990 [35] that the tyre must roll a certain distance, the ‘relaxation length’ for the tyre to deflect sufficiently to generate lateral force. In 1997, Pacejka and Besselink [36] extended the Magic Formula model by introducing longitudinal and lateral transient responses. This model is referred to as the ‘Delft Tyre ’97’ version. The Magic Formula model was originally developed around car tyres and was not accurate at large camber angles, so in 1998, De Vries and Pacejka adapted the Magic Formula model to be more versatile and cover the larger camber angle range needed for motorcycle tyres [37]. Further improvements to the Magic Formula model for motorcycle tyres were made by Tezuka et al., 2001 [38] and by Pacejka, 2006 [39].

The Dutch organisation for applied research TNO has turned the Magic Formula into commercial software under the name ‘Delft-Tire’. They have implemented the Magic Formula tyre model in a software package known as ‘MF-

Tire / MF-Swift', which has become an industry standard. MF-Tire / MF-Swift interfaces to Adams MSC, DADS (Dynamic Analysis and Design System) and Matlab, and has been adopted by major tyre manufacturers such as Michelin.

### 2.3.1 Tyre forces and moments, dynamic response

Tyre lateral force  $F_y$  is generated due to sideslip, camber and turnslip. Koenen [24] found the contribution of turnslip to be negligible. The literature is unanimous in that the lateral force due to side slip is subject to a lag that depends on the distance rolled by the tyre. The distance constant is known as the relaxation length. Because the aligning moment due to sideslip depends directly on the lateral force, this too is lagged. Segel and Wilson, 1976 [31] examined the different camber force generating mechanisms experimentally and found that about 80% of lateral force lags the input while 20% is instantaneous. Koenen [24] uses the stretched string model and states that the lateral displacement of the equatorial line lags the camber input while the lateral component of the tyre radial force responds instantaneously. Weir and Zellner, 1978 [40] showed that while the lag of lateral tyre force  $F_y$  due to side slip significantly affected the lateral dynamics of the vehicle, the lag of  $F_y$  due to camber had no such effect and was unimportant. This result was used when creating tyre models in later studies, such as Sharp, 1994 [26]. Pacejka [39] takes into account the transient response of the lateral force  $F_y$  and aligning moment  $M_z$  to changes in slip and camber angles. He disregards the non-lagging part of the response. The overturning moment  $M_x$  is assumed to respond instantaneously to camber changes.

# Chapter 3

## Multibody System Modelling

The first step in building a dynamic model is to formulate the equations of motion. In this chapter, three methods for deriving the equations of motion of a multibody system are examined, using Newton's, Lagrange's and Kane's equations. The pros and cons of each method are evaluated and one is chosen to derive the equations for the motorcycle model. The chapter begins with an explanation of reference frames and the vector notation used here and throughout the thesis. The concept of generalised co-ordinates and generalised speeds is introduced.

### 3.1 Reference frames

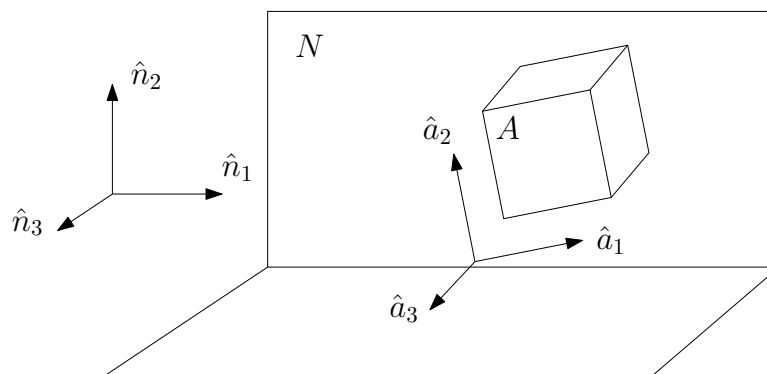


Figure 3.1: Vector convention shown in two reference frames

In a multibody system, the positions, velocities and accelerations of the bodies and points are vector quantities, and therefore must be expressed in a particular

reference frame. The terms ‘reference frame’ and ‘rigid body’ may be used interchangeably. Every rigid body may serve as a reference frame and every reference frame may be regarded as a massless rigid body [41]. Reference frames should not be confused with co-ordinate systems, as many co-ordinate systems may co-exist in a given reference frame, though in this thesis, one Cartesian co-ordinate system is used for each reference frame. Reference frames, like rigid bodies, are denoted by upper case letters, and the axes of the Cartesian co-ordinate system used within each reference frame use the same letter in lower case. This is shown in Fig. 3.1, where the axes of the  $N$  and  $A$  reference frames are indicated by three orthogonal unit vectors. The notation  $\vec{v}$  is used to denote vectors in general and  $\hat{v}$  denotes a unit vector.

The right-hand Cartesian co-ordinate system as used by Kane and Levinson 1985 [41] is adopted and is shown in Fig. 3.1. Rotation about these vectors also obeys the right hand rule, so that when a vector is grasped in the right hand with the thumb pointing in the positive direction, the fingers point in the direction of positive rotation. In this thesis, the inertial or global reference frame is denoted by  $N$ . The reference frames in the motorcycle model are explained in Section 4.4.

## 3.2 Vector notation

Roman letters are used for translational vectors and Greek letters for vectors representing angular motion. The letter  $r$  denotes relative position,  $v$  is translational velocity,  $a$  is translational acceleration,  $\omega$  is angular velocity and  $\alpha$  is angular acceleration. A left-hand superscript indicates the reference frame. For velocities and accelerations, a right-hand superscript indicates the body or point in question. Note that while a body may have angular motion, a point may not. For example,  ${}^N\vec{\omega}^P$  is the angular velocity of body  $P$  in the  $N$  reference frame, and  ${}^M\vec{a}^P$  is the translational acceleration of the point or body  $P$  in some reference frame  $M$ . In the case of relative positions, a right-hand superscript denotes the beginning and end of the vector, so  ${}^M\vec{r}^{AP}$  is the vector from point  $A$  to point  $P$

expressed in the  $M$  reference frame.

### 3.3 Generalised co-ordinates and speeds

Huston, 1990 [1] defines the co-ordinates of a multibody system as “the parameters (for example orientation angles or translation variables) needed to define the configuration of the system”. “When the co-ordinates are chosen such that there is one co-ordinate for each degree of freedom, they are called generalised co-ordinates”. Generalised co-ordinates are denoted by the letter  $q$ . Kane and Levinson 1985, [41] define generalised speeds as follows:

$$u_r := \sum_{s=1}^n Y_{rs} \dot{q}_s + Z_r \quad (r = 1, \dots, n) \quad (3.1)$$

where  $Y_{rs}$  and  $Z_r$  are functions of the generalised co-ordinates  $q_1, \dots, q_n$  and time  $t$ . These functions must be chosen such that Eqns. (3.1) can be solved uniquely for  $q_1, \dots, q_n$ . Eqns. (3.1) are called kinematical differential equations. Some authors, such as Roithmayr and Hodges 2016 [42] refer to generalised speeds as ‘motion variables’. In the simplest case, and in this thesis, each generalised speed is simply the first derivative with respect to time of the corresponding generalised co-ordinate, i.e.

$$u_r = \dot{q}_r \quad (r = 1, \dots, n)$$

The generalised co-ordinates of the system in this chapter are  $q_1$  and  $q_2$ , and the generalised speeds are  $u_1$  and  $u_2$ .

### 3.4 Partial angular velocities and velocities

Kane’s method uses the concept of ‘partial velocities’. If  ${}^M\vec{\omega}^A$  and  ${}^M\vec{v}^A$  are the angular and translational velocity respectively of body  $A$  in reference frame  $M$ ,

then they can be expressed uniquely as:

$$M\vec{\omega}^A = \sum_{r=1}^n M\vec{\omega}_r^A u_r + M\vec{\omega}_t^A$$

$$M\vec{v}^A = \sum_{r=1}^n M\vec{v}_r^A u_r + M\vec{v}_t^A$$

where  $M\vec{\omega}_r^A$ ,  $M\vec{v}_r^A$ ,  $M\vec{\omega}_t^A$  and  $M\vec{v}_t^A$  for  $(r = 1, \dots, n)$  are functions of  $q_1, \dots, q_n$  and time  $t$ . The vector  $M\vec{\omega}_r^A$  is called the  $r^{\text{th}}$  *partial angular velocity* of  $A$  in  $M$ , and  $M\vec{v}_r^A$  is the  $r^{\text{th}}$  *partial velocity* of  $A$  in  $M$ . When speaking of partial angular velocities and or partial velocities, the adjectives ‘holonomic’ and ‘non-holonomic’ can generally be omitted without loss of clarity [41].

### 3.5 The model

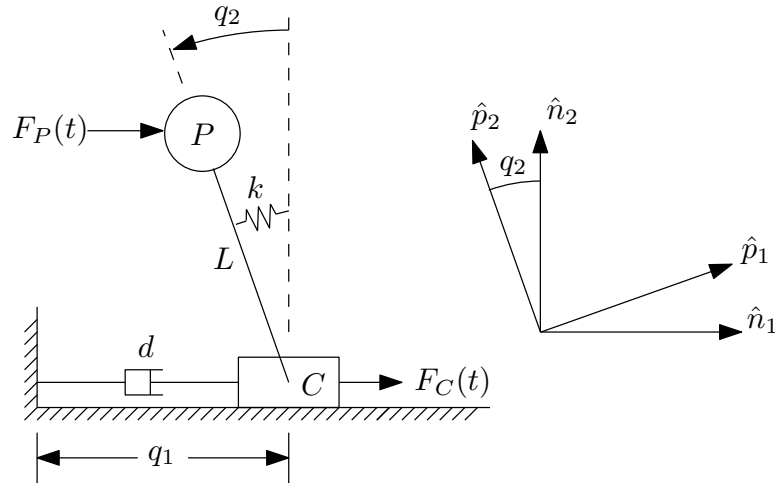


Figure 3.2: An inverted pendulum with spring and damper

An inverted pendulum is often used as an analogue for a motorcycle leaning over, so it seems an appropriate model to use in this context. The model is shown in Fig. 3.2. The pendulum  $P$  has mass  $M_P$  and its moment of inertia is  $I_P$ . The base of the pendulum is hinged at the centre of mass of a cart  $C$ , which has mass  $M_C$  and is free to slide on a frictionless surface. The horizontal position of the cart is  $q_1$  and the speed is  $u_1$ . The pendulum angle to the vertical is  $q_2$  and its angular velocity is  $u_2$ . The dimensions  $q_1$  and  $q_2$  are the generalised co-

ordinates, and the generalised speeds are  $u_1$  and  $u_2$ . A damper resists the lateral motion of the cart, and a spring attached between the pendulum and the cart forces the pendulum towards the vertical. Two reference frames are used: the global, or inertial, reference frame  $N$  and the reference frame  $P$ , which is aligned with the pendulum. The angle between the reference frames is  $q_2$ . The reference frame vectors are related as shown in the following equations, where  $c_2$  and  $s_2$  are shorthand for  $\cos q_2$  and  $\sin q_2$  respectively. Vectors  $\hat{n}_3$  and  $\hat{p}_3$  are collinear and point out of the page. When differentiating vector expressions, it is important to remember that while all  $\hat{n}$  vectors and  $\hat{p}_3$  are time invariant,  $\hat{p}_1$  and  $\hat{p}_2$  are functions of time.

$$\begin{aligned}\hat{p}_1 &= c_2\hat{n}_1 + s_2\hat{n}_2 \\ \hat{p}_2 &= -s_2\hat{n}_1 + c_2\hat{n}_2 \\ \hat{p}_3 &= \hat{n}_3\end{aligned}$$

It is useful to express this relationship in a table, as shown in Table 3.1. The expressions for  $\hat{n}_1$ ,  $\hat{n}_2$  and  $\hat{n}_3$  in terms of  $\hat{p}_1$ ,  $\hat{p}_2$  and  $\hat{p}_3$  can easily be found by multiplying the table entries in the relevant column with the corresponding  $\hat{p}$  unit vectors, and adding the results. The dot product of any pair of  $\hat{n}$  and  $\hat{p}$  unit vectors is the corresponding table entry.

	$\hat{n}_1$	$\hat{n}_2$	$\hat{n}_3$
$\hat{p}_1$	$c_2$	$s_2$	$0$
$\hat{p}_2$	$-s_2$	$c_2$	$0$
$\hat{p}_3$	$0$	$0$	$1$

Table 3.1: Reference frame vector relationship

## 3.6 Newton's Equations

The following forces act on the cart:

- The applied force is  $F_C\hat{n}_1$
- The inertia of the cart resists acceleration with the force  $-M_C\ddot{q}_1\hat{n}_1$

- The damping force is  $-d\dot{q}_1\hat{n}_1$
- The rotational inertia of the pendulum resists angular acceleration with a torque  $\vec{\tau} = -I_P\ddot{q}_2\hat{p}_3$ , which acts on the cart through the lever  $-L\hat{p}_2$ . Torque  $\vec{\tau} = \vec{r} \times \vec{F}$ , so the equation  $-I_P\ddot{q}_2\hat{p}_3 = -L\hat{p}_2 \times \vec{F}$  is satisfied when  $\vec{F} = -\frac{1}{L}I_P\ddot{q}_2\hat{p}_1$ . In the  $N$  reference frame, this force is  $-\frac{1}{L}I_P\ddot{q}_2c_2\hat{n}_1 - \frac{1}{L}I_P\ddot{q}_2s_2\hat{n}_2$ .
- The spring resists angular displacement with a torque  $\vec{\tau} = -kq_2\hat{p}_3$ , which acts on the cart through the lever  $-L\hat{p}_2$ . Torque  $\vec{\tau} = \vec{r} \times \vec{F}$ , so the equation  $-kq_2\hat{p}_3 = -L\hat{p}_2 \times \vec{F}$  is satisfied when  $\vec{F} = -\frac{k}{L}q_2\hat{p}_1$ . In the  $N$  reference frame, this force is  $-\frac{k}{L}q_2c_2\hat{n}_1 - \frac{k}{L}q_2s_2\hat{n}_2$ .
- Let  $F_T$  be the tension or compression force in the pendulum rod which exerts a force on the cart  $F_T\hat{p}_2 = -F_Ts_2\hat{n}_1 + F_Tc_2\hat{n}_2$

The following forces act on the pendulum:

- The applied force  $F_P\hat{n}_1$
- The inertia of the pendulum resists acceleration with the force  $-M_P\ddot{x}_p\hat{n}_1 - M_P\ddot{y}_p\hat{n}_2$ , where  $\ddot{x}_p$  and  $\ddot{y}_p$  are the horizontal and vertical acceleration of the pendulum.
- The force due to gravitational acceleration is  $-M_Pg\hat{n}_2$
- The rotational inertia gives rise to a force on the pendulum which is equal and opposite to that exerted on the cart, that is  $\frac{1}{L}I_P\ddot{q}_2c_2\hat{n}_1 + \frac{1}{L}I_P\ddot{q}_2s_2\hat{n}_2$ .
- The spring force exerted on the pendulum is equal and opposite that exerted on the cart, i.e.  $\frac{k}{L}q_2c_2\hat{n}_1 + \frac{k}{L}q_2s_2\hat{n}_2$
- The tension or compression force in the pendulum rod exerts a force on the pendulum bob of  $-F_T\hat{p}_2 = F_Ts_2\hat{n}_1 - F_Tc_2\hat{n}_2$

The position of the pendulum is given by:

$$x_p = q_1 - Ls_2 \quad y_p = Lc_2$$

The velocity is:

$$\dot{x}_p = \dot{q}_1 - L\dot{q}_2 c_2 \quad \dot{y}_p = -L\dot{q}_2 s_2$$

And the acceleration is:

$$\ddot{x}_p = \ddot{q}_1 - L\ddot{q}_2 c_2 + L\dot{q}_2^2 s_2 \quad \ddot{y}_p = -L\ddot{q}_2 s_2 - L\dot{q}_2^2 c_2$$

The forces acting on the pendulum in the  $x$  direction are analysed using Newton's second law.

$$\begin{aligned} \sum F_x &= 0 \\ F_P - M_P \ddot{x}_p + \frac{1}{L} I_P \ddot{q}_2 c_2 + \frac{k}{L} q_2 c_2 + F_T s_2 &= 0 \\ F_P - M_P (\ddot{q}_1 - L\ddot{q}_2 c_2 + L\dot{q}_2^2 s_2) + \frac{1}{L} I_P \ddot{q}_2 c_2 + \frac{k}{L} q_2 c_2 + F_T s_2 &= 0 \\ F_P - M_P \ddot{q}_1 + M_P L \ddot{q}_2 c_2 - M_P L \dot{q}_2^2 s_2 + \frac{1}{L} I_P \ddot{q}_2 c_2 + \frac{k}{L} q_2 c_2 + F_T s_2 &= 0 \end{aligned} \quad (3.2)$$

Likewise in the  $y$  direction:

$$\begin{aligned} \sum F_y &= 0 \\ -M_P \ddot{y}_p - M_P g + \frac{1}{L} I_P \ddot{q}_2 s_2 + \frac{k}{L} q_2 s_2 - F_T c_2 &= 0 \\ -M_P (-L\ddot{q}_2 s_2 - L\dot{q}_2^2 c_2) - M_P g + \frac{1}{L} I_P \ddot{q}_2 s_2 + \frac{k}{L} q_2 s_2 - F_T c_2 &= 0 \\ M_P L \ddot{q}_2 s_2 + M_P L \dot{q}_2^2 c_2 - M_P g + \frac{1}{L} I_P \ddot{q}_2 s_2 + \frac{k}{L} q_2 s_2 - F_T c_2 &= 0 \end{aligned} \quad (3.3)$$

The cart accelerates only in the horizontal direction so it is described by one equation:

$$\begin{aligned} \sum F_x &= 0 \\ F_C - M_C \ddot{q}_1 - d\dot{q}_1 - \frac{1}{L} I_P \ddot{q}_2 c_2 - \frac{k}{L} q_2 c_2 - F_T s_2 &= 0 \end{aligned} \quad (3.4)$$

By summing Eqns. (3.2) and (3.4), the unknown  $F_T$  is eliminated and the first equation of motion is found.

$$F_P + F_C - (M_P + M_C)\ddot{q}_1 + M_P L \ddot{q}_2 c_2 - M_P L \dot{q}_2^2 s_2 - d\dot{q}_1 = 0 \quad (3.5)$$

The second equation of motion is obtained by multiplying Eqn. (3.2) by  $c_2$  and multiplying Eqn. (3.3) by  $s_2$  to get:

$$\begin{aligned} c_2(F_P - M_P \ddot{q}_1 + M_P L \ddot{q}_2 c_2 - M_P L \dot{q}_2^2 s_2 + \frac{1}{L} I_P \ddot{q}_2 c_2 + \frac{k}{L} q_2 c_2) + F_T s_2 c_2 &= 0 \\ s_2(M_P L \ddot{q}_2 s_2 + M_P L \dot{q}_2^2 c_2 - M_P g + \frac{1}{L} I_P \ddot{q}_2 s_2 + \frac{k}{L} q_2 s_2) - F_T c_2 s_2 &= 0 \end{aligned}$$

Summing these equations gives the second equation of motion:

$$-M_P L c_2 \ddot{q}_1 + M_P L^2 \ddot{q}_2 + I_P \ddot{q}_2 + F_P L c_2 - M_P g L s_2 + k q_2 = 0 \quad (3.6)$$

Substituting  $u_1 = \dot{q}_1$  and  $u_2 = \dot{q}_2$  into Eqns. (3.5) and (3.6), the equations of motion become:

$$\begin{aligned} (M_P + M_C) \dot{u}_1 - M_P L c_2 \dot{u}_2 &= -M_P L s_2 u_2^2 - d u_1 + F_C + F_P \\ M_P L c_2 \dot{u}_1 - (M_P L^2 + I_P) \dot{u}_2 &= k q_2 + F_P L c_2 - M_P g L s_2 \end{aligned} \quad (3.7)$$

## 3.7 Lagrange's equations

The procedure for using Lagrange's equation is as follows.

1. Find K, the kinetic energy of the system.
2. Find U, the potential energy of the system.
3. Evaluate the Lagrangian equation for each generalised co-ordinate,  $q_1$  and  $q_2$ .

The linear velocity of the pendulum centre of mass is:

$$v_P = (\dot{q}_1 - L \dot{q}_2 c_2) \hat{n}_1 - L \dot{q}_2 s_2 \hat{n}_2$$

and the square of the magnitude is:

$$\begin{aligned} v_P^2 &= (\dot{q}_1 - L\dot{q}_2c_2)^2 + (-L\dot{q}_2s_2)^2 \\ &= \dot{q}_1^2 + L^2\dot{q}_2^2 - 2L\dot{q}_1\dot{q}_2c_2 \end{aligned}$$

The kinetic energy is given by:

$$\begin{aligned} K &= \frac{1}{2}M_C\dot{q}_1^2 + \frac{1}{2}M_Pv_P^2 + \frac{1}{2}I_P\dot{q}_2^2 \\ &= \frac{1}{2}M_C\dot{q}_1^2 + \frac{1}{2}M_P(\dot{q}_1^2 + L^2\dot{q}_2^2 - 2L\dot{q}_1\dot{q}_2c_2) + \frac{1}{2}I_P\dot{q}_2^2 \end{aligned}$$

The potential energy is given by:

$$U = \frac{1}{2}kq_2^2 + M_PgLc_2$$

The damping and external forces are non-conservative\* so they enter the Lagrangian as generalised forces.

$$\begin{aligned} \delta W^{nc} &= \sum_i^N f_i^{nc} \cdot \delta R_i = \sum_{j=1}^N Q_j \delta \xi_j \\ &= (-d\dot{q}_1 + F_C + F_P)\delta q_1 + (-F_PLc_2)\delta q_2 \end{aligned}$$

so

$$Q_{q_1} = -d\dot{q}_1 + F_C + F_P \quad Q_{q_2} = -F_PLc_2$$

The Lagrangian is:

$$\begin{aligned} \mathcal{L} &= K - U \\ &= \frac{1}{2}M_C\dot{q}_1^2 + \frac{1}{2}M_P(\dot{q}_1^2 + L^2\dot{q}_2^2 - 2L\dot{q}_1\dot{q}_2c_2) + \frac{1}{2}I_P\dot{q}_2^2 - \frac{1}{2}kq_2^2 - M_PgLc_2 \end{aligned}$$

---

\* If the work done by an external force is stored as some form of potential energy, then the force is conservative, otherwise it is non-conservative.

The following derivatives need to be evaluate for the Lagrange equations:

$$\begin{aligned}\frac{\delta \mathcal{L}}{\delta q_1} &= 0 \\ \frac{\delta \mathcal{L}}{\delta \dot{q}_1} &= M_C \dot{q}_1 + M_P \dot{q}_1 - M_P \dot{q}_2 L c_2 \\ \frac{d}{dt} \left( \frac{\delta \mathcal{L}}{\delta \dot{q}_1} \right) &= M_C \ddot{q}_1 + M_P \ddot{q}_1 - M_P \ddot{q}_2 L c_2 + M_P \dot{q}_2^2 L s_2 \\ \frac{\delta \mathcal{L}}{\delta q_2} &= g M_P L s_2 + M_P \dot{q}_2 \dot{q}_1 L s_2 - k q_2 \\ \frac{\delta \mathcal{L}}{\delta \dot{q}_2} &= I_P \dot{q}_2 + L^2 M_P \dot{q}_2 - M_P \dot{q}_1 L c_2 \\ \frac{d}{dt} \left( \frac{\delta \mathcal{L}}{\delta \dot{q}_2} \right) &= I_P \ddot{q}_2 + L^2 M_P \ddot{q}_2 - M_P \ddot{q}_1 L c_2 + M_P \dot{q}_2 \dot{q}_1 L s_2\end{aligned}$$

Lagrange's equation for the first generalised co-ordinate  $q_1$

$$\frac{d}{dt} \left( \frac{\delta \mathcal{L}}{\delta \dot{q}_1} \right) - \frac{\delta \mathcal{L}}{\delta q_1} = Q_{q_1}$$

yields the first equation of motion:

$$M_C \ddot{q}_1 + M_P \ddot{q}_1 - M_P \ddot{q}_2 L c_2 + M_P \dot{q}_2^2 L s_2 = -d u_1 + F_C + F_P$$

and the equation for the second generalised co-ordinate  $q_2$

$$\frac{d}{dt} \left( \frac{\delta \mathcal{L}}{\delta \dot{q}_2} \right) - \frac{\delta \mathcal{L}}{\delta q_2} = Q_{q_2}$$

gives the second equation of motion:

$$I_P \ddot{q}_2 + L^2 M_P \ddot{q}_2 - M_P \ddot{q}_1 L c_2 + M_P \dot{q}_2 \dot{q}_1 L s_2 - (g M_P L s_2 + M_P \dot{q}_2 \dot{q}_1 L s_2 - k q_2) = -F_P L c_2$$

Substituting  $u_1 = \dot{q}_1$  and  $u_2 = \dot{q}_2$  and re-arranging, produces the same equations of motion given in Eqns. (3.7)

$$\begin{aligned}(M_C + M_P) \dot{u}_1 - M_P L c_2 \dot{u}_2 &= -M_P L s_2 u_2^2 - d u_1 + F_C + F_P \\ M_P L c_2 \dot{u}_1 - (M_P L^2 + I_P) \dot{u}_2 &= k q_2 + F_P L c_2 - M_P g L s_2\end{aligned}$$

### 3.8 Kane's equations

This method was developed in the early 1960s by Thomas R. Kane and was originally known as “Lagrange’s form of d’Alembert’s principle”. [1] It has also been called the “principle of virtual power”. The principle states that the sum of the generalised active and inertia forces for each generalised co-ordinate, or alternately each generalised speed, is zero. That is,

$$F_r + F_r^* = 0 \quad r = 1, \dots, n$$

where  $F_r$  are the active forces and  $F_r^*$  are the inertia forces. The procedure for using Kane’s method is as follows.

1. Define the important points.
2. Select generalised co-ordinates and generalised speeds.
3. Derive velocity and acceleration expressions for the important points.
4. Construct the partial velocity table.
5. Calculate active forces  $F_r$  and inertia forces  $F_r^*$ , and set  $F_r + F_r^* = 0$ .

The important points in the mechanism are the mass centres of the cart  $C$  and pendulum  $P$  as shown in Fig. 3.2. The generalised co-ordinates are  $q_1$  and  $q_2$  and the generalised speeds are  $u_1 = \dot{q}_1$  and  $u_2 = \dot{q}_2$ . The velocities and angular velocities of the bodies are as follows:

$$\begin{aligned} {}^N\vec{\omega}^C &= 0 \\ {}^N\vec{\omega}^P &= u_2\hat{n}_3 \\ {}^N\vec{v}^C &= u_1\hat{n}_1 \\ {}^N\vec{v}^P &= {}^N\vec{v}^C + {}^N\vec{\omega}^P \times {}^N\vec{r}^{CP} \\ &= u_1\hat{n}_1 + u_2\hat{n}_3 \times L\hat{p}_2 \\ &= u_1\hat{n}_1 - u_2L(c_2\hat{n}_1 + s_2\hat{n}_2) \end{aligned}$$

$u_r$	${}^N\vec{\omega}_r^C$	${}^N\vec{v}_r^C$	${}^N\vec{\omega}_r^P$	${}^N\vec{v}_r^P$
$r = 1$	0	$\hat{n}_1$	0	$\hat{n}_1$
$r = 2$	0	0	$\hat{n}_3$	$-L(c_2\hat{n}_1 + s_2\hat{n}_2)$

Table 3.2: Partial velocities

Acceleration expressions are therefore:

$${}^N\vec{\alpha}^C = 0$$

$${}^N\vec{\alpha}^P = \dot{u}_2\hat{n}_3$$

$${}^N\vec{a}^C = \dot{u}_1\hat{n}_1$$

$${}^N\vec{a}^P = \dot{u}_1\hat{n}_1 - \dot{u}_2L(c_2\hat{n}_1 + s_2\hat{n}_2) - u_2^2L(c_2\hat{n}_2 - s_2\hat{n}_1)$$

### 3.8.1 Partial velocities

Kane's equations use partial velocities and partial angular velocities, which are defined as follows. For a certain system, let  $q_1 \dots q_n$  and  $u_1 \dots u_n$  be generalised co-ordinates and generalised speeds respectively. The angular velocity of a body in the system may be expressed uniquely as

$$\omega = \sum_{r=1}^n \omega_r u_r + \omega_t$$

and the velocity may be expressed uniquely as

$$v = \sum_{r=1}^n v_r u_r + v_t$$

The vectors  $\omega_r$  and  $v_r$  are called the  $r^{\text{th}}$  partial angular velocity and  $r^{\text{th}}$  partial velocity of the body, respectively. The  $r^{\text{th}}$  partial angular velocity of body  $P$  in reference frame  $N$  is expressed as  ${}^N\vec{\omega}_r^P$ . The partial velocities for the current system are derived from the velocity expressions above and are shown in Table 3.2.

### 3.8.2 Kane's Equations

The final step in Kane's method is to construct the set of equations for the generalised active force  $F_r$  and for the generalised inertial force  $F_r^*$ . Equating these produces the equations of motion for the system.

$$F_r^* = F_r$$

The generalised active force  $F_r$  (for two bodies, A and B) is given by:

$$F_r = \sum_r \left( \vec{F}_A \cdot {}^N \vec{v}_r^A + \vec{T}_A \cdot {}^N \vec{\omega}_r^A + \vec{F}_B \cdot {}^N \vec{v}_r^B + \vec{T}_B \cdot {}^N \vec{\omega}_r^B \right) \quad (3.8)$$

where  $F$  and  $T$  denote force and torque respectively. The generalised inertial force  $F_r^*$  is given by:

$$F_r^* = \sum_r \left( -M_A {}^N \vec{a}^A \cdot {}^N \vec{v}_r^A - \left( {}^N \vec{\alpha}^A \cdot \vec{I}_A + {}^N \vec{\omega}^A \times \vec{I}_A \cdot {}^N \vec{\omega}^A \right) \cdot {}^N \vec{\omega}_r^A \right. \\ \left. - M_B {}^N \vec{a}^B \cdot {}^N \vec{v}_r^B - \left( {}^N \vec{\alpha}^B \cdot \vec{I}_B + {}^N \vec{\omega}^B \times \vec{I}_B \cdot {}^N \vec{\omega}^B \right) \cdot {}^N \vec{\omega}_r^B \right) \quad (3.9)$$

### 3.8.3 Active forces

Let  $\vec{F}'_C$  and  $\vec{T}'_C$  be the total active force and torque on the cart and let  $\vec{F}'_P$  and  $\vec{T}'_P$  be the total active force and torque on the pendulum.

$$\vec{F}'_C = F_C \hat{n}_1 - du_1 \hat{n}_1$$

$$\vec{F}'_P = -M_P g \hat{n}_2 + F_P \hat{n}_1$$

$$\vec{T}'_C = K q_2 \hat{n}_3$$

$$\vec{T}'_P = -K q_2 \hat{n}_3$$

so

$$\begin{aligned} F_1 &= \vec{F}'_C \cdot {}^N \vec{v}_1^C + \vec{T}'_C \cdot {}^N \vec{\omega}_1^C + \vec{F}'_P \cdot {}^N \vec{v}_1^P + \vec{T}'_P \cdot {}^N \vec{\omega}_1^P \\ &= F_C + F_P - du_1 \end{aligned} \quad (3.10)$$

$$\begin{aligned} F_2 &= \vec{F}'_C \cdot {}^N \vec{v}_2^C + \vec{T}'_C \cdot {}^N \vec{\omega}_2^C + \vec{F}'_P \cdot {}^N \vec{v}_2^P + \vec{T}'_P \cdot {}^N \vec{\omega}_2^P \\ &= M_P g L s_2 - F_P L c_2 - k q_2 \end{aligned} \quad (3.11)$$

### 3.8.4 Inertial forces

$$\begin{aligned} F_1^* &= -M_C {}^N \vec{a}^C \cdot {}^N \vec{v}_1^C - \left( {}^N \vec{\alpha}^C \cdot \vec{I}_C + {}^N \vec{\omega}^C \times \vec{I}_C \cdot {}^N \vec{\omega}^C \right) \cdot {}^N \vec{\omega}_1^C \\ &\quad - M_P {}^N \vec{a}^P \cdot {}^N \vec{v}_1^P - \left( {}^N \vec{\alpha}^P \cdot \vec{I}_P + {}^N \vec{\omega}^P \times \vec{I}_P \cdot {}^N \vec{\omega}^P \right) \cdot {}^N \vec{\omega}_1^P \\ &= -(M_C + M_P) \dot{u}_1 + M_P L c_2 \dot{u}_2 - M_P L s_2 u_2^2 \end{aligned} \quad (3.12)$$

$$\begin{aligned} F_2^* &= -M_C {}^N \vec{a}^C \cdot {}^N \vec{v}_2^C - \left( {}^N \vec{\alpha}^C \cdot \vec{I}_C + {}^N \vec{\omega}^C \times \vec{I}_C \cdot {}^N \vec{\omega}^C \right) \cdot {}^N \vec{\omega}_2^C \\ &\quad - M_P {}^N \vec{a}^P \cdot {}^N \vec{v}_2^P - \left( {}^N \vec{\alpha}^P \cdot \vec{I}_P + {}^N \vec{\omega}^P \times \vec{I}_P \cdot {}^N \vec{\omega}^P \right) \cdot {}^N \vec{\omega}_2^P \\ &= M_P L c_2 \dot{u}_1 - (M_P L^2 + I_P) \dot{u}_2 \end{aligned} \quad (3.13)$$

### 3.8.5 Equate the active and inertial forces

Equating the active forces in Eqns. (3.10) and (3.11) with the inertial forces in Eqns. (3.12) and (3.13) as follows,

$$F_1 = F_1^*$$

$$F_2 = F_2^*$$

results in the same equations of motion given in Eqns. (3.7).

$$\begin{aligned} (M_C + M_P) \dot{u}_1 - M_P L c_2 \dot{u}_2 &= -M_P L s_2 u_2^2 - du_1 + F_C + F_P \\ M_P L c_2 \dot{u}_1 - (M_P L^2 + I_P) \dot{u}_2 &= k q_2 + F_P L c_2 - M_P g L s_2 \end{aligned}$$

## 3.9 Conclusion

Clearly, all three methods produce the equations of motion for the system, but they differ in ease of use. Of the three methods, Newton's equations are the only ones that require the explicit calculation of the constraint forces and torques between the bodies. Even for quite simple systems, these can be tricky to visualise and formulate, and this requirement adds unnecessary complexity to the calculations. Furthermore, expressions for  $x_p$  and  $y_p$  had to be introduced in order to represent the angular motion of the pendulum as translational quantities, and the first and second derivatives of these expressions had to be found.

While Lagrange's equations avoid these problems, they require differentiation of scalar functions of kinetic and potential energy. For smaller systems such as the current example, this is not a big problem, but it becomes inefficient when dealing with more complex systems.

Kane's equations avoid the disadvantages of both Newton's and Lagrange's equations, while offering a well structured method that scales well to larger and more complex systems. The calculations above validate the views of Case [43] and Huston [1] that Kane's method lends itself to automated numerical computation in a way that Newton's and Lagrange's equations do not. A further advantage of Kane's method is that the equations are of vector rather than scalar quantities. By keeping the values in vector form, velocities and accelerations may easily be expressed in any reference frame, global or local. It was for these reasons that Kane's method was chosen for use in the motorcycle models.

# Chapter 4

## The Motorcycle Model

This chapter covers the main subject of the thesis; the motorcycle multibody model. In Chapter 3, reference frames, vector notation, generalised co-ordinates and speeds were introduced. In this chapter, they are applied to the task of building the multibody model.

### 4.1 Introduction

The motorcycle is represented as a multibody system with eleven degree of freedom. A multibody system is a set of interconnected rigid or flexible bodies that may undergo rotational and translational motion. The current model consists of rigid bodies, and because the bodies do not form a closed loop, it is classified as an ‘open chain’ or ‘open tree’ structure [1]. The displacements, velocities and accelerations in the model are represented by vectors, and every vector must be specified in a particular reference frame, as described in Section 4.4.

### 4.2 Constraints and degrees of freedom

Huston, 1990 [1] defines constraint equations as follows: “If the motion of the system is restricted so that there are relations between the co-ordinates that must be satisfied during the motion, these are called constraint equations”. The number of degrees of freedom in a multibody system depends on the number

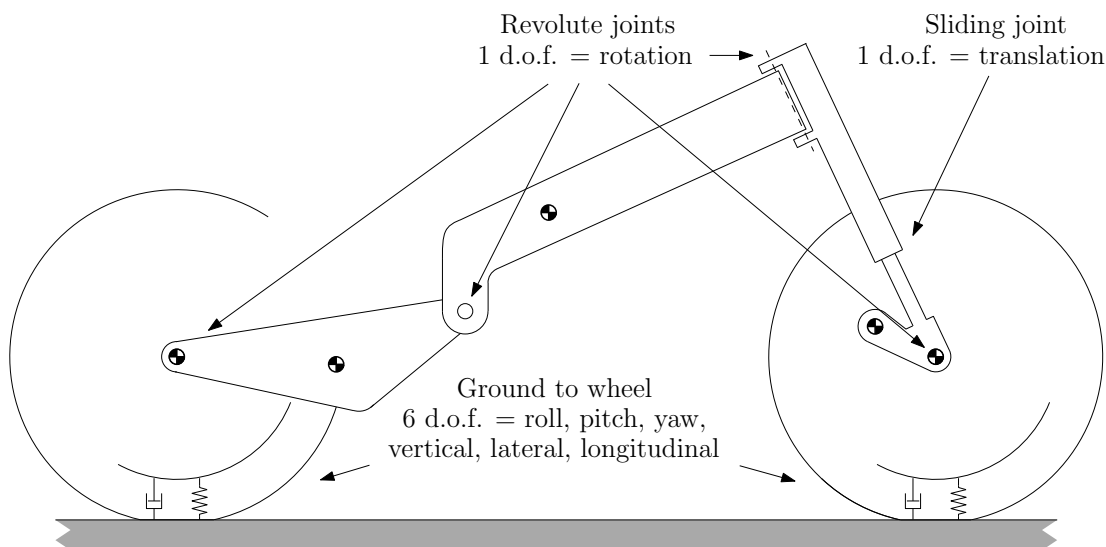


Figure 4.1: Bike model degrees of freedom

of bodies and constraints. The degrees of freedom in the motorcycle model are shown in Fig. 4.1. The rigid bodies and other key points are designated by the capital letters. They are shown in Fig. 4.2 and listed in Table 4.1.

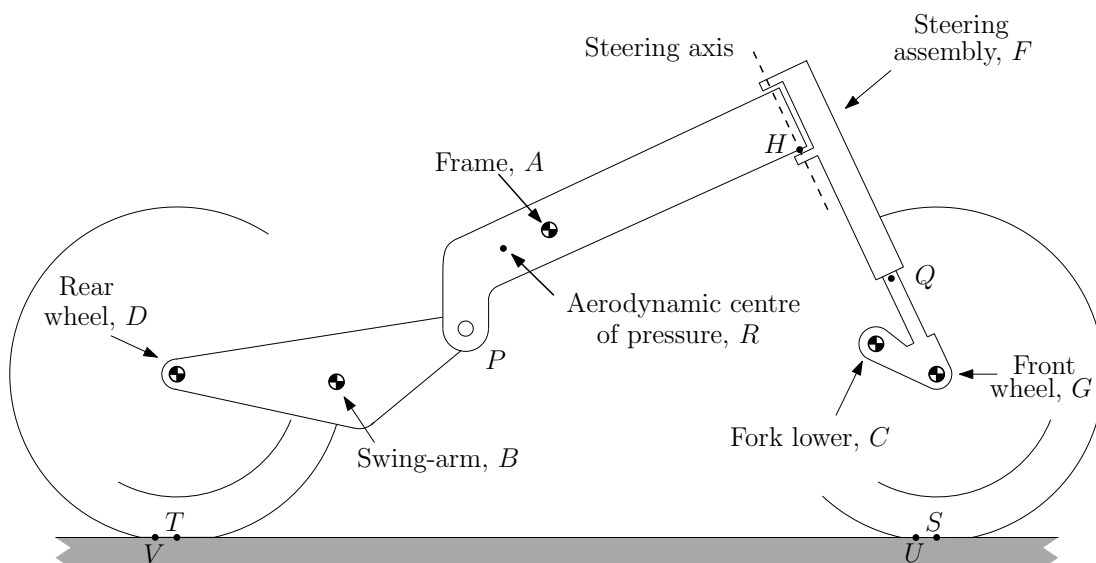


Figure 4.2: Key points and bodies in the model

A free floating or unconstrained body has six degrees of freedom; translation in the  $x$ ,  $y$  and  $z$  directions and rotation in roll, pitch and yaw. Likewise, each joint starts out with six degrees of freedom and each constraint placed on the joint removes one degree of freedom, so the number of degrees of freedom in a

\* For the purpose of defining the degrees of freedom, the ground plane must be counted as a body.

Point	Name
<i>A</i>	Main frame centre of mass
<i>B</i>	Swing-arm centre of mass
<i>C</i>	Fork lower centre of mass
<i>D</i>	Rear wheel centre of mass
<i>F</i>	Steering assembly centre of mass
<i>G</i>	Front wheel centre of mass
<i>H</i>	Steering head point
<i>N</i>	Ground plane*
<i>P</i>	Swing-arm pivot
<i>Q</i>	Upper limit of front axle travel
<i>R</i>	Aerodynamic centre of pressure
<i>S</i>	Front tyre contact point
<i>T</i>	Rear tyre contact point
<i>U</i>	Front pneumatic trail point
<i>V</i>	Rear pneumatic trail point

Table 4.1: Key points in the the multi-body system

Joint	Degrees of freedom	Constraints
N - G	vert, lat, long, roll, pitch, yaw	0
N - D	vert, lat, long, roll, pitch, yaw	0
G - C	revolute	5
D - B	revolute	5
C - F	translational	5
F - A	revolute	5
B - A	revolute	5
Total		25

Table 4.2: Degrees of freedom and constraints

joint is equal to six minus the number of constraints. Table 4.2. lists the degrees of freedom and constraints in each joint. In total, there are 25 constraints. The Gruebler equation calculates the total number of degrees of freedom in the system:

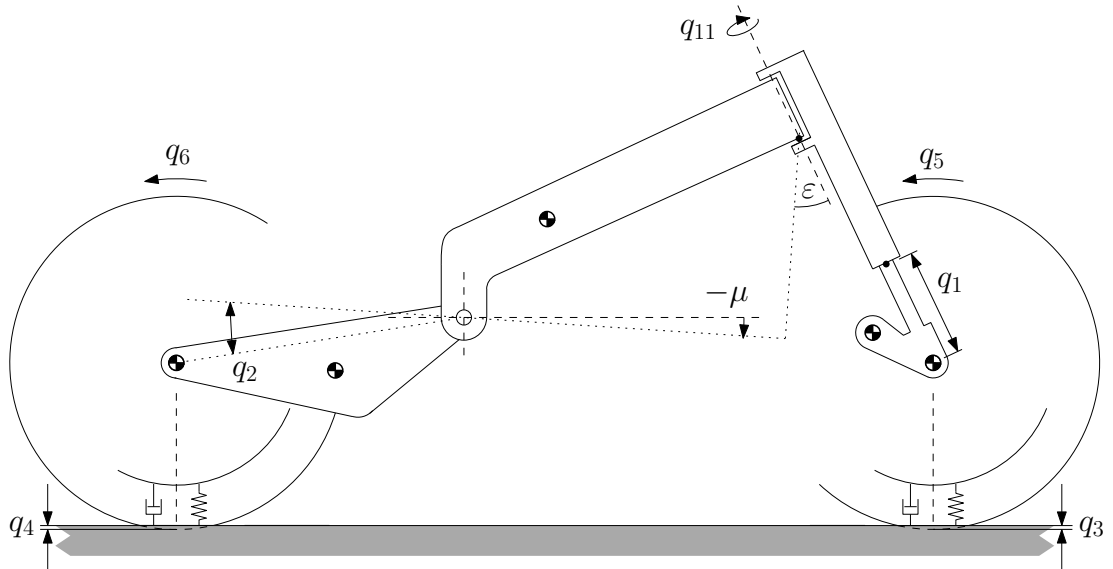
$$\begin{aligned}\text{Total d.o.f.} &= 6 \times (\text{number of bodies} - 1) - \text{number of constraints} \\ &= 6(7 - 1) - 25 \\ &= 11\end{aligned}$$

### 4.3 Generalised co-ordinates and generalised speeds

The eleven generalised co-ordinates that are state variables in the motorcycle model are listed in Table 4.3. It is sometimes convenient to use symbols to refer to certain generalised co-ordinates, especially for readers who are familiar with other literature in the field. For example, Pacejka [44] and Cossalter [25] both use  $\delta$  to represent steering angle and Pacejka uses  $\gamma$  for camber. Fig. 4.3 shows the generalised co-ordinates that can be viewed in the  $x - z$  plane. The  $x$  and  $y$  co-ordinates on the ground plane,  $q_7$  and  $q_8$  and the bike yaw angle  $q_{10}$  are not shown. It can be seen that the axis convention dictates that the generalised co-ordinates representing wheel rotation are opposite to the usual rotation direction. The generalised co-ordinate  $q_1$  is the distance between the front axle centre and the axle position with the front suspension fully compressed. Fig. 4.3 shows one other important dimension,  $\mu$ , the pitch angle of the main frame relative to the ground plane.

G.C.	Symbol	Description
$q_1$		Front suspension extension
$q_2$		Swing-arm angle relative to the main frame
$q_3$		Front tyre vertical deflection
$q_4$		Rear tyre vertical deflection
$q_5$		Front wheel rotation angle
$q_6$		Rear wheel rotation angle
$q_7$	$x$	X co-ordinate on the ground plane
$q_8$	$y$	Y co-ordinate on the ground plane
$q_9$	$\gamma$	Motorcycle roll angle
$q_{10}$	$\psi$	Motorcycle yaw angle
$q_{11}$	$\delta$	Steering angle

Table 4.3: Generalised co-ordinates

Figure 4.3: Generalised co-ordinates in the  $x, z$  plane

## 4.4 Reference frames

A number of reference frames are used in the model, as shown in Figs. 4.4 and 4.5, and they are denoted by capital letters. Each reference frame has its own Cartesian co-ordinate system. The unit vectors along the Cartesian axes use the reference frame letter in lower case with the ‘hat’ symbol ‘ $\hat{\cdot}$ ’. The inertial or global reference frame is  $N$ . Fig. 4.4 shows the reference frames that are aligned with the centre plane of the motorcycle. The symbol  $\odot$  denotes a vector pointing out of the page and  $\otimes$  denotes the centre of mass of a rigid body. Reference

frames  $A$  and  $B$  are aligned with the main frame and swing-arm respectively. Reference frame  $E$  is oriented so that  $\hat{e}_2$  is parallel to the steering axis. Reference frame  $M$  is oriented so that  $\hat{m}_1$  and  $\hat{m}_3$  lie on the ground plane. Fig. 4.5. shows that  $\hat{m}_1$  is collinear with  $\hat{d}_1$  of the rear wheel reference frame  $D$ . The yaw angle of the bike,  $\psi$ , is defined as the angle between  $\hat{n}_1$  and  $\hat{m}_1$ , and is positive when the bike is rotated to the left. The longitudinal dot-dashed line in Fig. 4.5 is the ground centre-line where the bike centre plane intersects the ground plane. The angle between these two planes is the roll angle,  $\gamma$ .

Local reference frames are associated with bodies  $A$ ,  $B$ ,  $D$ ,  $F$  and  $G$ , which are described in Table 4.1. Reference frame  $D$  is the rear wheel reference frame and is equivalent to reference frame  $M$  rotated by the camber angle  $\gamma$  about  $\hat{m}_1$ . Reference frame  $A$  is the local reference frame of the main frame of the bike. The vectors  $\hat{a}_3$  and  $\hat{d}_3$  are parallel, and the angle between vectors  $\hat{a}_1$  and  $\hat{d}_1$  is  $\mu$ , the pitch angle of the main frame, which increases in the direction that lifts the front of the bike. The angle  $\mu$  is shown in Fig. 4.3. Reference frame  $B$  is the local reference frame of the swing-arm. Vector  $\hat{b}_3$  is parallel to  $\hat{a}_3$  and the generalised co-ordinate  $q_2$  is the angle between vectors  $\hat{b}_1$  and  $\hat{a}_1$ , with  $q_2$  increasing in the direction that lifts the front of the swing-arm.

The  $E$  reference frame is not associated with any of the rigid bodies, but is an intermediate reference frame between  $A$  and the steering assembly reference frame  $F$ . The angle between  $\hat{a}_1$  and  $\hat{e}_1$  is the steering head angle  $\varepsilon$ . The steering assembly consists of the front fork, the handlebars and the rider's hands and forearms. Vector  $\hat{e}_2$  is parallel to the steering axis, as is  $\hat{f}_2$ . Reference frame  $F$  is  $E$  rotated about  $\hat{e}_2$  by the steering angle  $q_{11} = \delta$ .

Reference frames  $A$  and  $B$  are shown in Fig. 4.4 and all other reference frames are shown in Fig. 4.5. The steering angle is  $\delta$ , and the steering angle projected onto the road surface, is  $\delta'$ . This is known as the kinematic steering angle. The camber angle of the front wheel relative to the ground plane is  $\gamma_1$ . The steering caster angle  $\varepsilon$  is defined as the angle between vectors  $\hat{a}_2$  and  $\hat{e}_2$ .

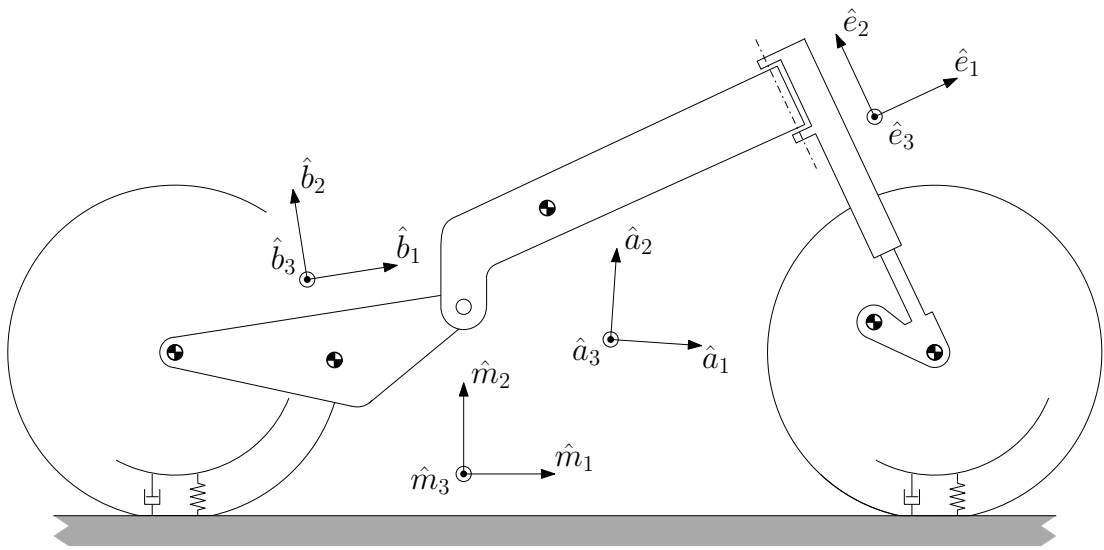
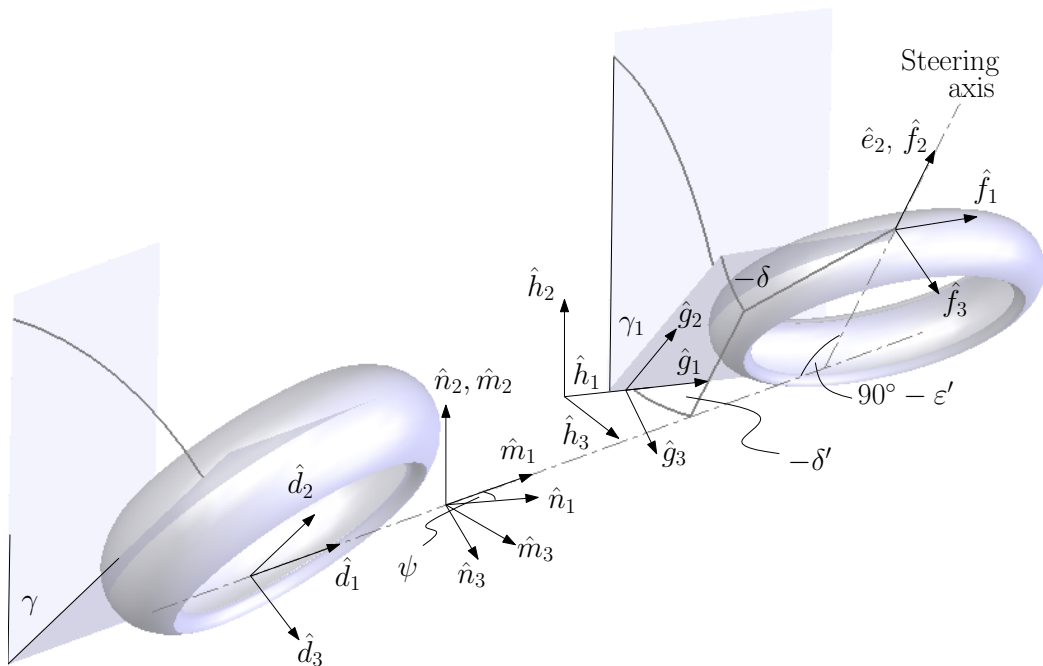
Figure 4.4: Bike reference frames shown in  $x, z$  plane

Figure 4.5: Bike reference frames in three dimensions

#### 4.4.1 Transformations between reference frames

Table 4.4 shows the transformations between reference frames, beginning with the inertial reference frame  $N$  and following sequentially through the bike, linking all reference frames. The transformations are in terms of generalised co-ordinates  $q_2$ ,  $q_9$ ,  $q_{10}$  and  $q_{11}$ , the main frame pitch angle  $\mu$ , the steering head angle  $\varepsilon$ , the kinematic steering angle  $\delta'$  and the front wheel camber angle  $\gamma_1$ . Table 4.4 introduces

	$\hat{n}_1$	$\hat{n}_2$	$\hat{n}_3$		$\hat{m}_1$	$\hat{m}_2$	$\hat{m}_3$		$\hat{d}_1$	$\hat{d}_2$	$\hat{d}_3$
$\hat{m}_1$	$c_{10}$	0	$-s_{10}$	$\hat{d}_1$	1	0	0	$\hat{a}_1$	$c_\mu$	$s_\mu$	0
$\hat{m}_2$	0	1	0	$\hat{d}_2$	0	$c_9$	$s_9$	$\hat{a}_2$	$-s_\mu$	$c_\mu$	0
$\hat{m}_3$	$s_{10}$	0	$c_{10}$	$\hat{d}_3$	0	$-s_9$	$c_9$	$\hat{a}_3$	0	0	1
	$\hat{a}_1$	$\hat{a}_2$	$\hat{a}_3$		$\hat{a}_1$	$\hat{a}_2$	$\hat{a}_3$		$\hat{e}_1$	$\hat{e}_2$	$\hat{e}_3$
$\hat{b}_1$	$c_2$	$s_2$	0	$\hat{e}_1$	$c_\varepsilon$	$s_\varepsilon$	0	$\hat{f}_1$	$c_{11}$	0	$-s_{11}$
$\hat{b}_2$	$-s_2$	$c_2$	0	$\hat{e}_2$	$-s_\varepsilon$	$c_\varepsilon$	0	$\hat{f}_2$	0	1	0
$\hat{b}_3$	0	0	1	$\hat{e}_3$	0	0	1	$\hat{f}_3$	$s_{11}$	0	$c_{11}$
	$\hat{f}_1$	$\hat{f}_2$	$\hat{f}_3$		$\hat{g}_1$	$\hat{g}_2$	$\hat{g}_3$		$\hat{h}_1$	$\hat{h}_2$	$\hat{h}_3$
$\hat{g}_1$	$c_\xi$	$-s_\xi$	0	$\hat{h}_1$	1	0	0	$\hat{m}_1$	$c_{\delta'}$	0	$s_{\delta'}$
$\hat{g}_2$	$s_\xi$	$c_\xi$	0	$\hat{h}_2$	0	$c_{\gamma_1}$	$-s_{\gamma_1}$	$\hat{m}_2$	0	1	0
$\hat{g}_3$	0	0	1	$\hat{h}_3$	0	$s_{\gamma_1}$	$c_{\gamma_1}$	$\hat{m}_3$	$-s_{\delta'}$	0	$c_{\delta'}$

Table 4.4: Reference frame transformations

one new symbol,  $\xi$ . This is the angle through which reference frame  $F$  must be rotated about  $\hat{f}_3$  in order for  $\hat{f}_1$  to be parallel to the ground plane. The relative positions of the bodies, and therefore the reference frames, depend on the generalised co-ordinates and the geometry of the motorcycle, so all transformations between reference frames must be expressed in terms of these. Therefore, expressions must be found for  $\mu$ ,  $\xi$ ,  $\gamma_1$  and  $\delta'$  in terms of the generalised co-ordinates. Expressions for  $\xi$ ,  $\gamma_1$  and  $\delta'$  are derived in the following sections and  $\mu$  is derived in Section 4.8.1.

#### 4.4.2 The angle $\xi$ between reference frames $F$ and $G$

Given the reference frame  $F$ , we want to find  $\hat{g}_1$  whose components are given by  $\hat{g}_1 = (g_{1,1}, g_{1,2}, g_{1,3})$ . Because  $\hat{g}_1$  lies on the ground plane,  $g_{1,2} = 0$ . The magnitude of  $\hat{g}_1$  is unity so

$$\begin{aligned}
 g_{1,1}^2 + g_{1,3}^2 &= 1 \\
 \implies g_{1,3} &= \sqrt{1 - g_{1,1}^2}
 \end{aligned}$$

$\hat{g}_1$  and  $\hat{f}_3$  are orthogonal so their dot product is zero

$$\begin{aligned}\hat{g}_1 \cdot \hat{f}_3 &= 0 \\ \implies f_{3,1}g_{1,1} + f_{3,2}g_{1,2} + f_{3,3}g_{1,3} &= 0\end{aligned}$$

But  $\hat{g}_1$  lies on the ground plane so  $g_{1,2} = 0$ , therefore

$$\begin{aligned}f_{3,1}g_{1,1} + f_{3,3}g_{1,3} &= 0 \\ f_{3,1}g_{1,1} + f_{3,3}\sqrt{1 - g_{1,1}^2} &= 0 \\ \implies g_{1,1} &= \pm \sqrt{\frac{f_{3,3}^2}{f_{3,1}^2 + f_{3,3}^2}} \quad + \text{ gives the correct orientation}\end{aligned}$$

Next,  $g_{1,3}$  is found

$$\begin{aligned}f_{3,1}g_{1,1} + f_{3,3}g_{1,3} &= 0 \\ \implies g_{1,3} &= -\frac{f_{3,1}g_{1,1}}{f_{3,3}}\end{aligned}$$

The relationship between  $\hat{f}_1$  and  $\hat{g}_1$  is shown in Fig. 4.6. The rotation angle  $\xi$  is found by calculating the distance  $d$  between the vectors.

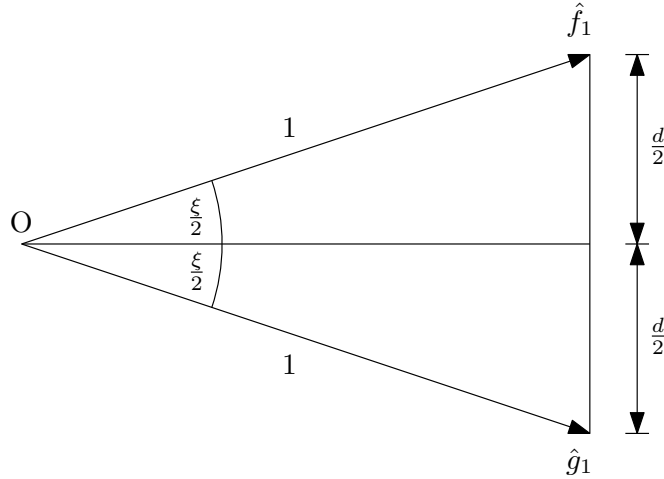


Figure 4.6: Vectors  $f_1$  and  $g_1$

The camber angle of the front wheel,  $\gamma_1$  is found in a similar way to  $\xi$ . Reference frame  $H$  is created by rotating the  $G$  reference frame about  $\hat{g}_1$  until  $\hat{g}_3$  lies

on the ground plane. For small steering angles

$$\begin{aligned}\xi &= \varepsilon + \mu \\ c_\xi &= \cos(\varepsilon + \mu) = c_\varepsilon c_\mu - s_\varepsilon s_\mu \\ s_\xi &= \sin(\varepsilon + \mu) = s_\varepsilon c_\mu + c_\varepsilon s_\mu\end{aligned}$$

#### 4.4.3 The front wheel camber angle $\gamma_1$ and kinematic steering angle $\delta'$

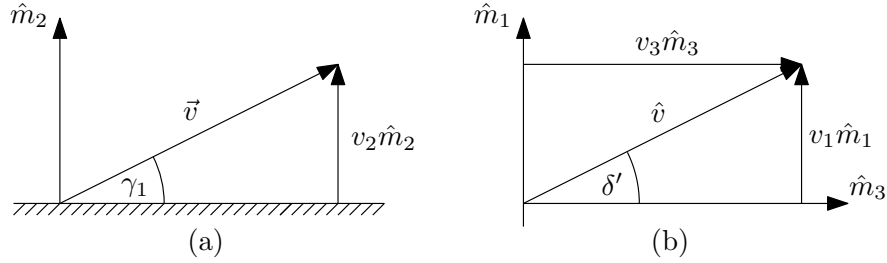


Figure 4.7: Front wheel camber angle  $\gamma_1$  and kinematic steering angle  $\delta'$

The vector  $\hat{f}_3$  is the unit vector that points to the right along the front axle. Converting this vector to the  $M$  reference frame using the transformations in Table 4.4 results in the vector:

$$\begin{aligned}\vec{v} &= v_1 \hat{m}_1 + v_2 \hat{m}_2 + v_3 \hat{m}_3 \\ &= \sin \delta \cos(\varepsilon + \mu) \hat{m}_1 \\ &\quad + (-\cos \delta \sin \gamma + \cos \gamma \sin \delta \sin(\varepsilon + \mu)) \hat{m}_2 \\ &\quad + \cos \gamma \cos \delta + \sin \gamma \sin \delta \sin(\varepsilon + \mu) \hat{m}_3\end{aligned}\tag{4.1}$$

The unit vector  $\vec{v}$  is at an angle of  $\gamma_1$  to the ground plane, as shown in Fig. 4.7 (a), and the vertical component,  $v_2$ , is the coefficient of  $\hat{m}_2$  in Eqn. (4.1). If the wheel has positive camber angle, then  $v_2$  will be negative, so the sign of  $v_2$  is opposite to that of the camber angle. This results in the equation:

$$\begin{aligned}\sin \gamma_1 &= \cos \delta \sin \gamma - \cos \gamma \sin \delta \sin(\varepsilon + \mu) \\ \gamma_1 &= \arcsin(\cos \delta \sin \gamma - \cos \gamma \sin \delta \sin(\varepsilon + \mu))^\dagger\end{aligned}$$

Eqn. (4.1) also provides the expression for the kinematic steering angle  $\delta'$ . Fig. 4.7 (b) is the projection of vector  $\vec{v}$ , the front axle, onto the ground plane. The Kinematic steering angle is the angle that  $\vec{v}$  makes with  $\hat{m}_3$ , which is the angle of the front axle with no steering angle applied.

$$\tan \delta' = \frac{v_1}{v_3} = \frac{\sin \delta \cos(\epsilon + \mu)}{\cos \gamma \cos \delta + \sin \gamma \sin \delta \sin(\epsilon + \mu)}$$

$$\delta' = \arctan \frac{\sin \delta \cos(\epsilon + \mu)}{\cos \gamma \cos \delta + \sin \gamma \sin \delta \sin(\epsilon + \mu)}^\dagger$$

## 4.5 Forces and moments in the model

Before explaining the modelling procedure, it is necessary to explain how forces and moments are handled in the model. Inertial forces and moments arise due to acceleration and angular acceleration of the masses. All other forces and moments are termed ‘active’, and Kane’s method treats these separately. The active forces and moments in the model are as follows:

- Front wheel torque
- Rear wheel torque
- Steering torque
- Forces due to gravitational acceleration
- Crankshaft gyroscopic moments
- Front suspension spring and damping force
- Rear suspension spring and damping torque
- Aerodynamic forces
- Torque arising from drive chain tension

---

<sup>†</sup> Note that when the bike is leaned to the right,  $\gamma$  is positive and when the bike is steered to the right,  $\delta$  and  $\sin \delta$  are negative.

- Tyre forces
- Wheel gyroscopic moments

The first three are rider inputs and these, along with forces due to gravity and crankshaft gyroscopic moments, are the inputs that do not depend on the system state. Of the other forces and moments, only the wheel gyroscopic moments are substantially linear, and these are handled within the system  $A$  matrix.

The tyre, suspension, aerodynamic and chain forces are non-linear, and linearising them to the extent that they could be included in the  $A$  matrix would reduce the fidelity of the model to an unacceptable extent. It was decided instead to treat the system as a Hammerstein model, that is, a linear model with a non-linear stage at the input. This approach has some advantages. One is simplicity; the non-linear forces and moments are calculated and simply placed in the input vector. The non-linear input blocks are modular and, for example, a simple spring and damper front suspension model could easily be replaced by an active suspension system. One disadvantage is that important elements of the system dynamics are no longer represented in the system  $A$  matrix. Of course this presents an issue when performing analysis using the root locus technique, for example. It will be shown, however, that this issue can be overcome and root locus analysis can be carried out in the normal way.

### 4.5.1 Suspension forces in the model

Vehicle suspension units usually consist of a spring and damper. In suspension models, the travel and speed of the suspension unit are typically chosen as state variables. Models are often simplified, and spring and damping forces are treated as being proportional to the travel and speed respectively. The constants of proportionality are the spring and damping constants and they reside naturally in the system  $A$  matrix.

Physical systems are not usually so simple. The spring is usually compressed to some extent at zero suspension travel. This is called preload and it can make up a significant proportion of the total spring force. So-called top-out springs

modify the force close to zero suspension travel, and bottom-out springs and gas pressure may introduce non-linearity close to full travel. Furthermore, the relationship between wheel travel and suspension unit travel is often non-linear.

The non-linearity of the spring and damping forces may be handled in the model in a number of different ways. As already mentioned, they may be approximated by using spring and damping constants. A closer approximation to the spring force may be achieved using the formula  $F = k(x + p) = kx + kp$ , where  $x$  is the suspension travel,  $p$  is the preload and  $k$  is the spring constant. In this case, the constant  $k$  would be in the  $A$  matrix and  $kp$  would be in the input matrix  $B$  or the input vector  $u$ . This is unavoidably less tidy and is still a relatively poor approximation. To achieve the best possible approximation of the spring force, the constants  $k$  and  $p$  may be scheduled depending on the system state, so that they describe a straight line that is tangential to the actual force curve at the current operating point. This would also work for the damping force.

The approach that has been taken is to move the suspension forces to the input vector  $u$ . This is not ideal from a conceptual viewpoint because the spring and damping forces are not really system inputs, and it moves the suspension dynamics outside the  $A$  matrix; a fact that must be taken into account when analysing the system. However, it has the advantages of simplicity and modularity. The suspension forces are calculated as functions of the state variables and stored during initialisation. It is a then simple matter within the main program loop to look them up and place them in the input vector. Another advantage of dealing with the suspension forces as external inputs is that the suspension units can be treated as separate modules. This makes it easier to incorporate different models for the suspension units without having to re-model the whole system. One could even replace them with devices that are more complex than springs and dampers, such as actuators, as used in ‘active’ suspension systems.

Because dynamic models are not available for the front and rear suspension systems, they are treated statically. The damping forces used in the model are assumed to have been measured at a constant damper speed, and no transient behaviour of the suspension unit is included. The front suspension is the simpler

of the two because the suspension travel and the wheel travel  $q_1$  are one and the same. Likewise the suspension speed and the rate of change of wheel travel  $u_1$ . In this case, a vector of values for wheel travel  $q_1$  is used to generate a corresponding vector containing spring force, and a vector of values for  $u_1$  is used to generate a corresponding vector of damping forces. The front suspension system imparts equal and opposite forces to the front suspension upper and lower bodies,  $F$  and  $C$ . The front suspension forces due to spring and damper are shown in the upper plots of Fig. 4.8 and 4.9.

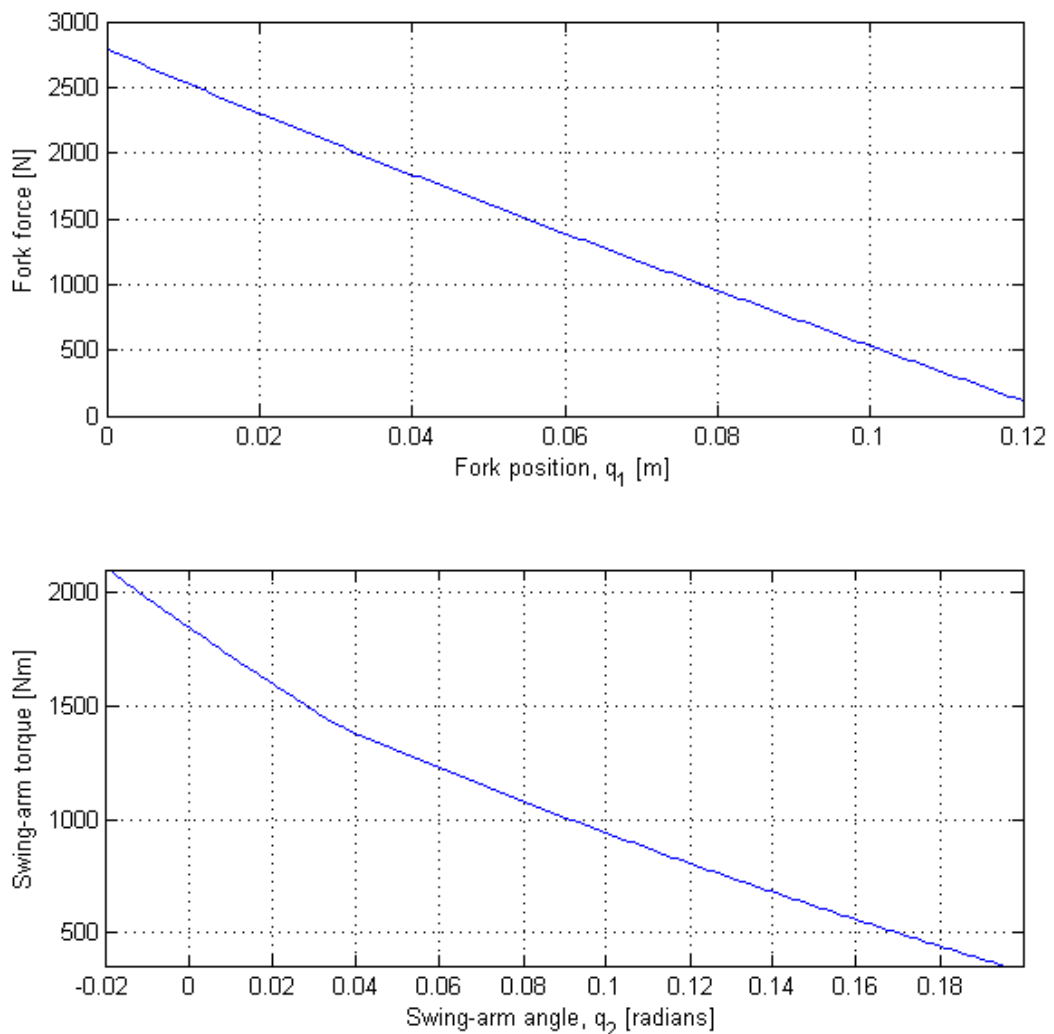


Figure 4.8: Front fork spring force vs. fork position. Swing-arm spring torque (showing non-linearity due to bump rubber) vs. swing-arm angle.

Rear wheel travel is represented by the swing-arm angle  $q_2$ , and instead of a force, the rear suspension imparts an equal and opposite torque to the main frame and swing-arm bodies  $A$  and  $B$ . The relationship between swing-arm angle  $q_2$  and

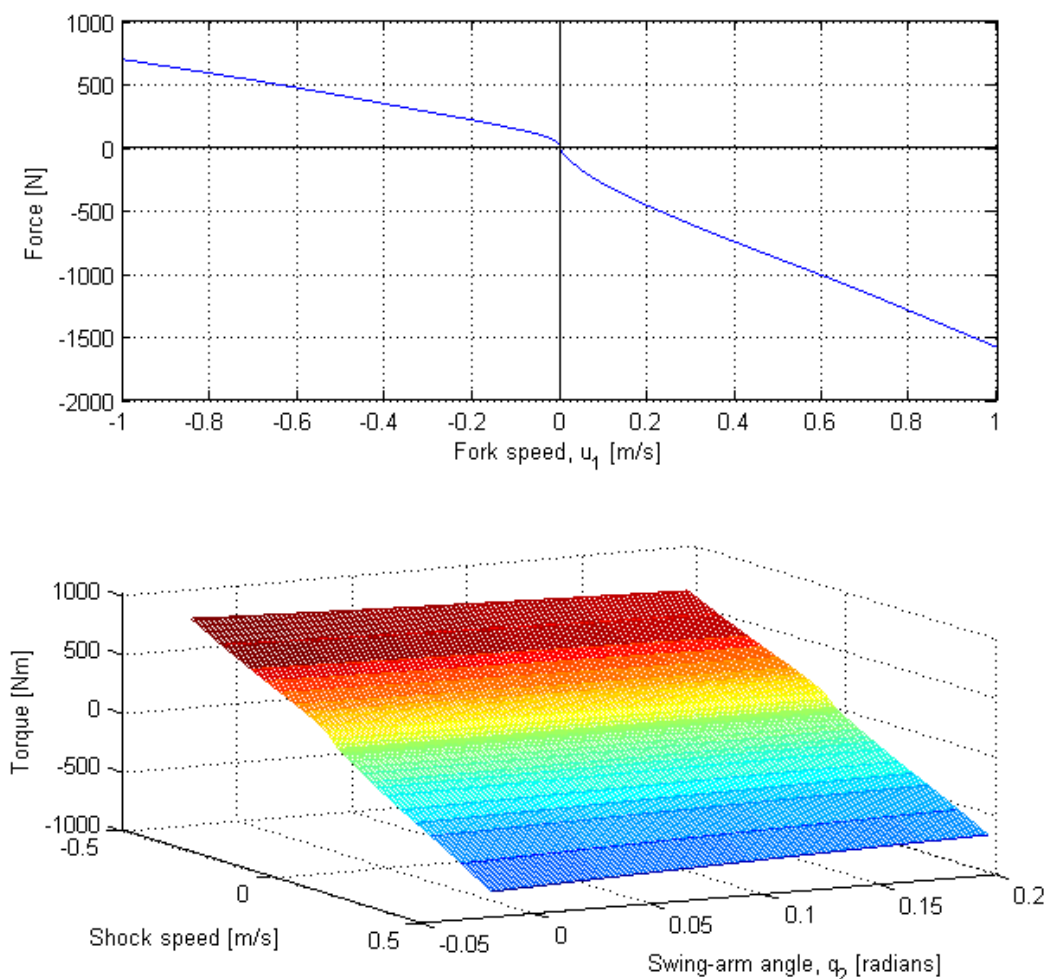


Figure 4.9: Front fork damping force vs. fork speed. Swing-arm damping torque vs. swing-arm angle and shock absorber speed.

the suspension unit travel is governed by a mechanical linkage. The term ‘lever ratio’ will be used here as the ratio of the shock absorber speed to the tangential speed of the rear axle. This is also the ratio of the tangential force at the rear axle to the shock absorber force. Generally, the lever ratio is not constant but depends on  $q_2$ , so a vector of lever ratios is generated from a corresponding vector of  $q_2$  values. From the  $q_2$  and lever ratio vectors, another vector is calculated for torque arising from the spring force. These three vectors are stored for use in the main program loop.

The torque due to rear damping force depends not only on the swing-arm angle  $q_2$  but on its angular velocity  $u_2$ . Therefore a two-dimensional table is needed. Ideally, a table would be generated giving the damping torque in terms of  $q_2$  and  $u_2$ , but unfortunately this is not easy to achieve. Suspension manufacturers pro-

vide tables of damping force as a function of the suspension unit speed. Because the lever ratio depends on the swing-arm position  $q_2$ , it is not possible to have a vector of  $u_2$  values that correspond to the damping table indices at all values of  $q_2$ . A table of damping-related torques is generated, therefore, using  $q_2$  and suspension unit speed as indices. In the main program loop, the procedure is as follows. First the lever ratio is calculated for the current value of  $q_2$ . Then the suspension unit speed is calculated from  $u_2$  and the lever ratio. Using  $q_2$  and suspension speed as indices, the damping-related swing-arm torque is interpolated from the table. The swing-arm torques due to the spring and damping forces are added and placed in the input vector. The rear suspension torques due to spring and damper are shown in the lower plots of Fig. 4.8 and 4.9.

#### 4.5.2 The effect of chain tension

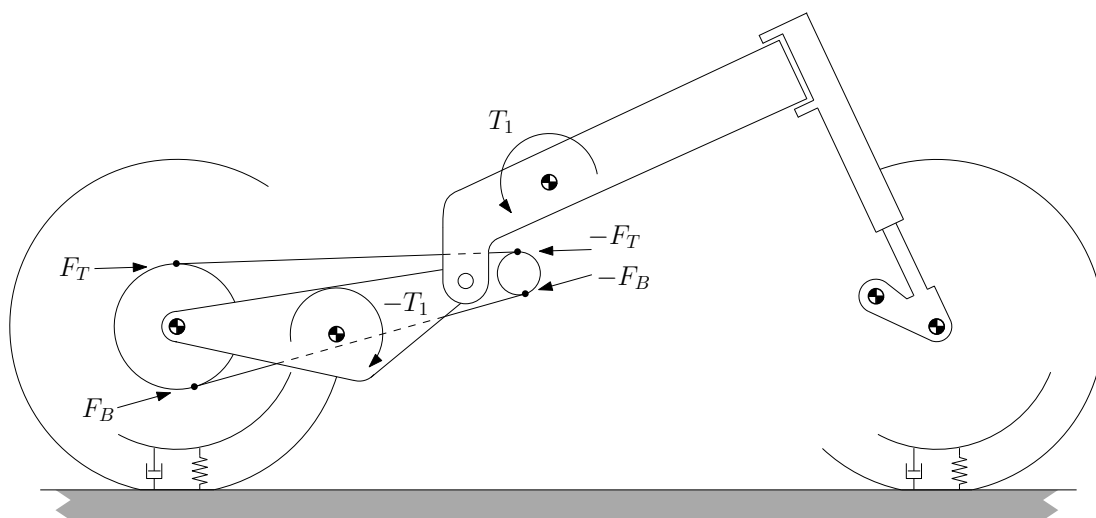


Figure 4.10: Drive chain forces and torques

Figure 4.10 shows the upper and lower chain runs that transmit torque from one sprocket to the other. When engine torque is positive, only the upper chain run is in tension, and equal and opposite forces of magnitude  $F_T$  are applied tangentially to the upper part of the sprockets. These tangent points are marked by dots. When the engine torque is negative, only the lower chain run is in tension, and equal and opposite forces of magnitude  $F_B$  are applied at the lower tangent points of the sprockets. At any given angle of the swing-arm relative to

the main frame, even though the chain is moving and the sprockets are rotating, the tangent points are fixed relative to the main frame and swing-arm, and the chain force acts as though it were applied to the frame and swing-arm at those points. The equal and opposite forces are analogous to equal and opposite torques applied to the frame and swing-arm, where the torque is the chain force multiplied by the perpendicular distance from the chain run to the swing-arm pivot. As the dimensions from the pivot to the upper and lower chain runs are a function of  $q_2$ , they can be calculated and stored during the initialisation phase, and values are scheduled as needed in the main program loop. In Section 4.5.1, it was explained how and why the suspension spring and damping forces are treated as inputs and placed in the input vector  $u$ . The torques on the frame and swing-arm due to chain tension are treated in the same way.

### 4.5.3 Crankshaft rotation

Crankshaft rotation affects the main frame in two ways. It imparts an inertial torque in the  $Y$  direction proportional to its angular acceleration, and gyroscopic torque in the  $X$  and  $Z$  directions, proportional to its angular velocity. Both are proportional to the  $Y$  moment of inertia of the crankshaft. Because these torques depend on engine speed and its rate of change, which are not state variables, they are applied in the input vector  $u$ .

### 4.5.4 Wheel rotation

Like the crankshaft, the wheels generate inertial torque in the local  $Y$  direction and gyroscopic torque in the local  $X$  and  $Z$  directions, and these are proportional to the  $Y$  moment of inertia of the wheel. The inertial torque due to angular acceleration of the wheel about the axle is treated the same as any other inertial torque in the system. The gyroscopic torque is applied to the wheel within the equations of motion and so is represented in the system  $A$  matrix. An additional effect of wheel rotation is that the rotational inertia of the wheels gives rise to longitudinal tyre shear forces. These are dealt with in Section 4.5.5.

### 4.5.5 Drag

The coast-down tests, as described in Section 6.7, provide measurements that allow drag to be separated by source; engine, aerodynamic, tyres and other factors. Section 4.7 describes how engine negative torque is differentiated from the overall drag. Here, aerodynamic drag and longitudinal tyre force will be separated from other remaining sources of drag. In the freewheel coast-down test, road speed was measured as the bike decelerated from high speed due to drag. A second order polynomial for acceleration in terms of road speed  $v$ , as shown in Eqn. (4.2), was fitted to the data, and this is shown in Fig. 6.27, overlaid on the recorded data.

$$a = pv^2 + qv + r \quad (4.2)$$

$$p = -932.95 \times 10^{-6} \quad q = -2.91 \times 10^{-3} \quad r = -189.67 \times 10^{-3}$$

If the total mass of the bike and rider is  $m$ , then the drag force is:

$$F = ma = mpv^2 + mqv + mr \quad (4.3)$$

Eqn. (4.3) gives the inertial force calculated from the negative acceleration and bike mass, but it does not take into account the fact that the wheels, which have rotational inertia, are also being forced to decelerate. The negative angular acceleration of the wheels implies that there are torques acting to slow the wheels, and these are created by longitudinal shear forces at the tyre contact patches, which act in the positive  $X$  direction. It seems somewhat counterintuitive that when the bike is freewheeling, the forces at the tyre contact patches act in the direction to accelerate the bike, but it makes more sense to think of them as the effect of wheel inertia opposing deceleration. Fig. 4.11 shows these shear forces generated by the model, plotted against road speed. Second order polynomials in road speed are a very good fit to the force data and are shown also. Being second order polynomials in road speed means that they are in a similar form to Eqn. (4.2), which is an expression for acceleration. Given that they involve a change in angular acceleration of the wheels, there is a good chance that the shear

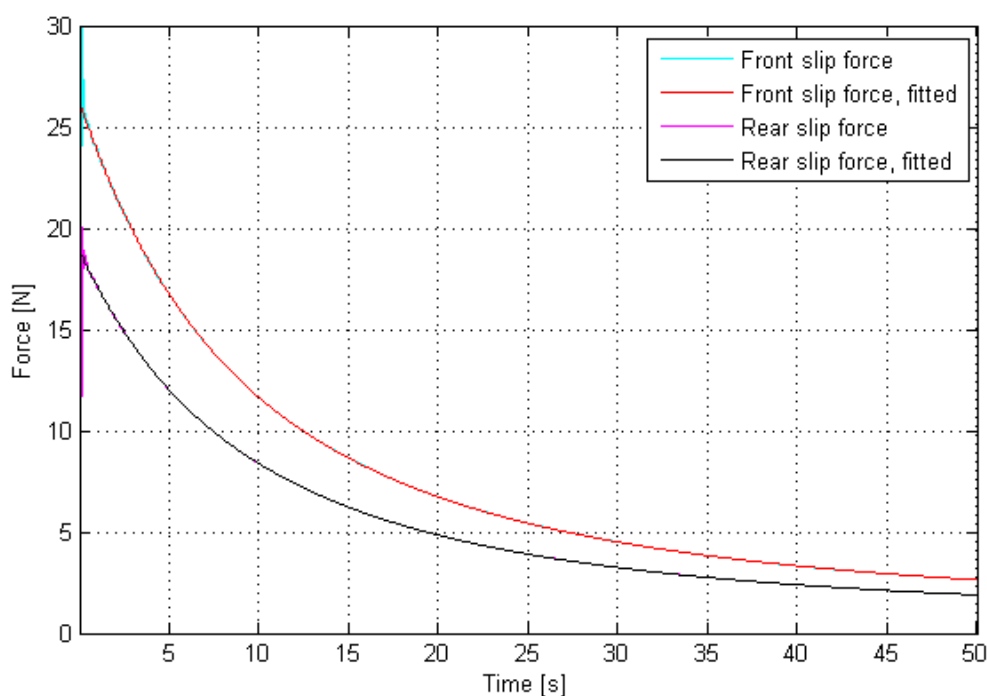


Figure 4.11: Tyre longitudinal slip forces in freewheel, modelled and curve fitted

forces are proportional to the  $Y$  moment of inertia of the wheels. In order to test both these hypotheses, the fitted polynomials for shear force in Fig. 4.11 were plotted against longitudinal acceleration,  ${}^M\vec{a}_1^A$ . The upper plot in Fig. 4.12 shows the shear force for the front and rear tyres versus longitudinal acceleration and clearly, the relationship is linear. In the second plot, the  $Y$  moments of inertia of the wheels have been doubled and the vertical scale for force is doubled, likewise. It is clear that the shear force has doubled and is therefore proportional to the  $Y$  moment of inertia of the wheel. Plot three in Fig. 4.12 shows the situation when the mass of the bike is doubled. The bike decelerates from a lower initial rate, but the slopes of the lines are very similar to the upper plot where the bike mass is normal. This means that while the shear force is proportional to acceleration and the moment of inertia of the wheel, it is largely independent of vertical load, so the  $K_s$  constants need to be calculated only once for a given bike and tyre set. The equation for longitudinal shear force due to the acceleration of the wheels may be written as:

$$F = K_s I a$$

The slopes in the upper plot are  $-5.377$  and  $-6.395$ , and the moments of inertia  $I$  are  $0.484 \text{ kg.m}^2$  and  $0.638 \text{ kg.m}^2$  for the front and rear tyres respectively, resulting in constants  $K_s$  of  $-11.11$  and  $-10.02$  respectively. Eqn. (4.3) may now be

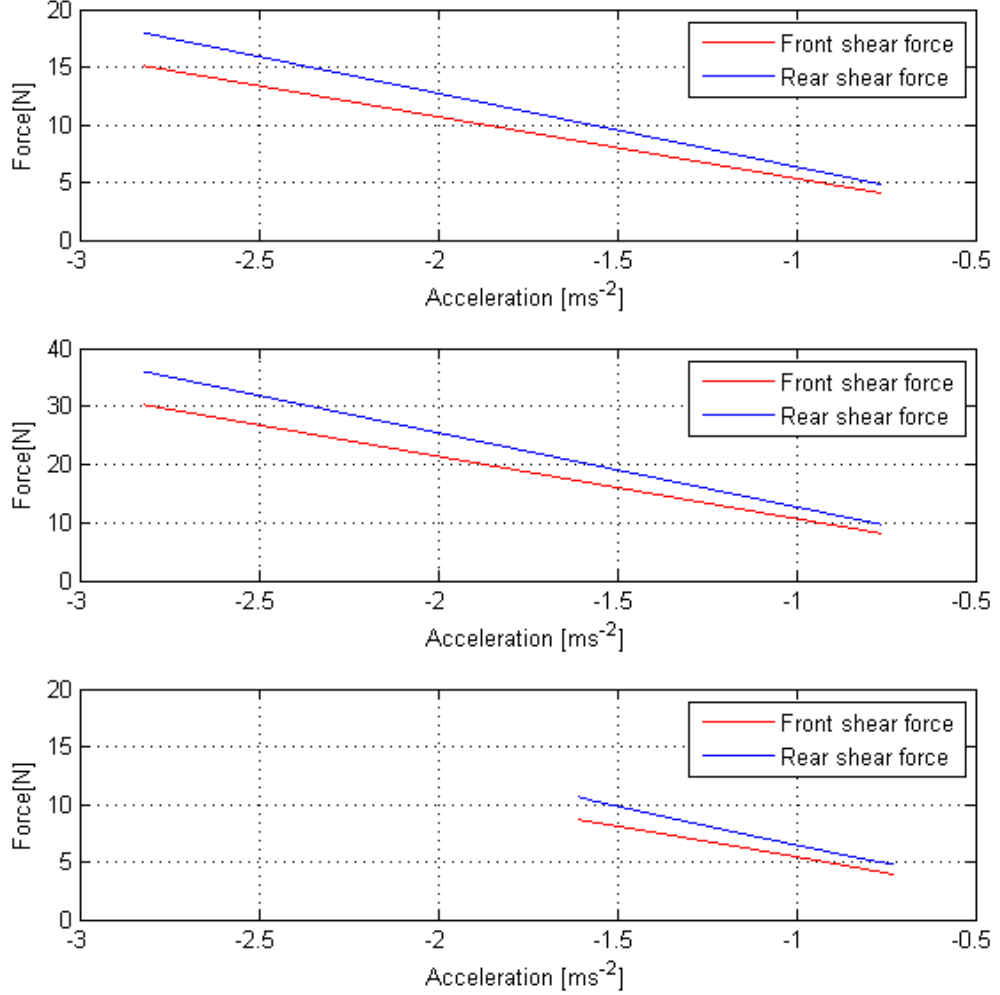


Figure 4.12: Tyre longitudinal shear force vs. acceleration for different wheel inertial moments and bike mass

modified by adding the shear forces as follows:

$$F = mpv^2 + mqv + mr + K_{sf}I_f a + K_{sr}I_r a \quad (4.4)$$

where the subscripts  $f$  and  $r$  refer to the front and rear wheels. The shear forces are converted to torques by multiplying by the tyre rolling radii, and the torques are applied to the wheels in the model. The equation for aerodynamic drag force

is:

$$F = \frac{1}{2}\rho v^2 C_d A \quad (4.5)$$

Equating the aerodynamic force with the  $v^2$  term in Eqn. (4.4) gives:

$$\frac{1}{2}\rho v^2 C_d A = mpv^2 \quad (4.6)$$

The coast-down tests were carried out at an air temperature of  $10^\circ\text{C}$  and a pressure of  $1004\text{ mb}$ , giving an air density of  $\rho = 1.235\text{ kg.m}^{-3}$ . The mass of the bike and rider is  $270\text{ kg}$ . Substituting physical values into Eqn. (4.6), and negating  $p$  because  $F$  in Eqn. (4.5) is implicitly negative, gives:

$$C_d A = 0.4078$$

This would be satisfied by a frontal area of  $A \approx 0.8\text{ m}^2$  and a drag coefficient of  $C_d \approx 0.5$ , which are reasonable for the semi-prone riding position used. It is not really necessary to separate  $C_d$  and  $A$  for the purposes of the model. The force in Eqn. (4.6) is applied to the centre of pressure in the model in the negative  $X$  direction. With the terms for aerodynamic and tyre force in Eqn. (4.4) evaluated, the remaining terms are  $mqv + mr$ . Substituting physical values gives the equation for remaining force; call it  $F_r$ :

$$\begin{aligned} F_r &= mqv + mr \\ &= -0.7857v - 51.2 \end{aligned} \quad (4.7)$$

This force is presumed to be due to mechanical drag, which results in front and rear wheel drag torque.  $F_r$  was divided in the ratio of  $9 : 1$  and converted to front and rear drag torques  $T_{df}$  and  $T_{dr}$  using the front and rear tyre radii,  $T_{fz}$  and  $T_{rz}$

as follows:

$$T_{df} = 0.1F_r T_{fz}$$

$$T_{dr} = 0.9F_r T_{rz}$$

These torques are applied to the wheels in the model. The measured road speed from the freewheel coast-down test is shown in Fig. 4.13 along with the road speed predicted by the model.

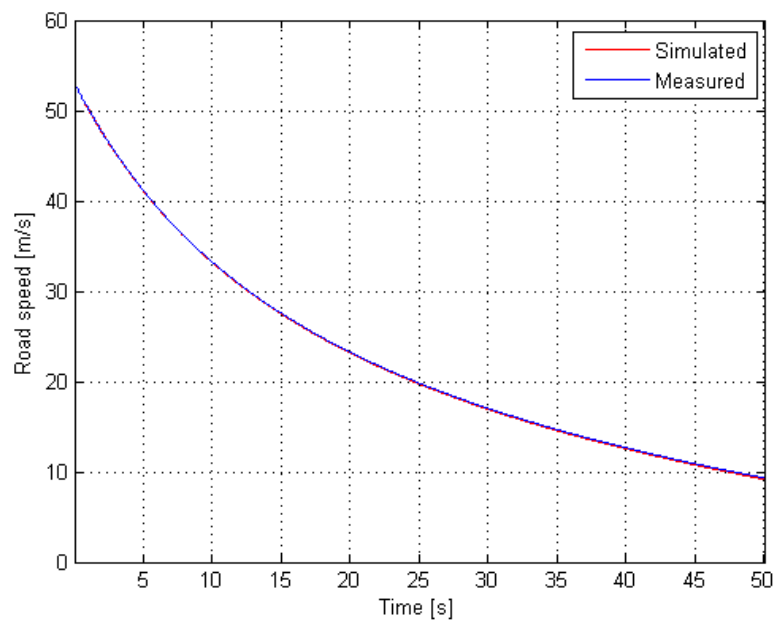


Figure 4.13: Freewheel coast-down test. Road speed, measured and simulated by the model

## 4.6 Rider body position

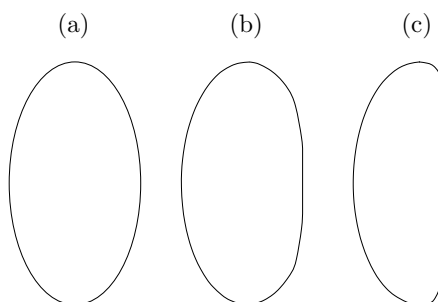


Figure 4.14: Tyre contact patch shape at various camber angles

As the rider leans the bike over, the tyre contact patches migrate towards the edge of the tyres. Up to the point where the contact patch reaches the edge of the tyre, the shape and area remain more or less unchanged, as shown in Fig. 4.14 (a). At a certain camber angle, the contact patch reaches the edge of the tread and begins to change shape, as shown in (b). Any further increase in camber results in further distortion of the contact patch shape and a progressive reduction in contact area as shown in (c), so in order to maintain contact patch area, the rider must limit the roll angle of the motorcycle. On the other hand, to achieve the highest possible road speed, the centre of mass of the motorcycle and rider must move as far as possible towards the inside of the turn by achieving the highest possible roll angle. These competing requirements are optimised if the rider's centre of mass is shifted as far as possible from the central plane of the bike, towards the inside of the turn, so that the roll angle of the combined mass centre exceeds that of the bike to the greatest extent possible.

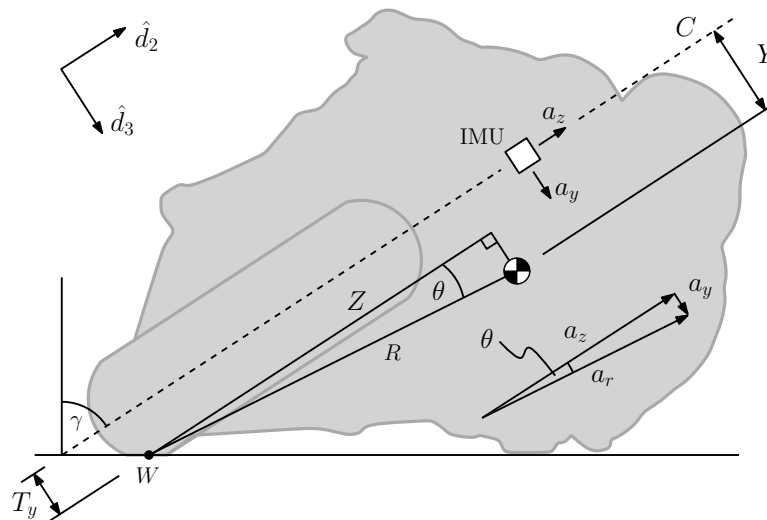


Figure 4.15: Cross-section of the motorcycle at high roll angle

Fig. 4.15 shows the silhouette of a motorcycle leaning over. It can be visualised as a cross-section of the bike and rider at the position of the combined centre of mass, which is indicated by the symbol  $\oplus$ . The point  $W$  indicates where the line of the wheelbase, i.e. the line joining the front and rear tyre contact points, intersects the page. The dashed line,  $C$ , marks the central plane of the motorcycle, with the roll angle denoted by  $\gamma$ . Line  $Z$  is parallel to  $C$  and passes

through the wheelbase line. Line  $R$  passes through the combined mass centre and the wheelbase, so it is collinear with the resultant acceleration vector due to centripetal and gravitational acceleration,  $a_r$ . This line is at an angle  $\theta$  to line  $Z$ . The inertial measurement unit (IMU) is shown, along with the measured accelerations  $a_y$  and  $a_z$ . The inset vector diagram shows that  $\theta$ , and therefore the lateral offset  $Y$ , of the combined centre of mass, may be calculated from the accelerometer measurements as follows:

$$\tan \theta = \frac{a_y}{a_z} = \frac{Y - T_y}{Z}$$

$$Y = T_y + Z \frac{a_y}{a_z} \quad (4.8)$$

where  $T_y$  is the lateral offset due to the combined front and rear tyre profiles, and  $Z$  is the vertical height of the combined mass centre above the wheelbase line in the  $D$  reference frame. The lateral offset of the combined mass centre is:

$$Y = \frac{M_A A_y + M_B B_y + M_C C_y + M_D D_y + M_F F_y + M_G G_y}{M_M} \quad (4.9)$$

$M_M$  is the total mass of the motorcycle and rider. But the lateral offsets of all bodies other than  $A$  are assumed to be zero, so:

$$Y = \frac{M_A A_y}{M_M} \quad (4.10)$$

Combining Eqns. (4.8) and (4.10) gives:

$$T_y + Z \frac{a_y}{a_z} = \frac{M_A A_y}{M_M} \quad \text{or}$$

$$A_y = \frac{M_M}{M_A} \left( T_y + Z \frac{a_y}{a_z} \right) \quad (4.11)$$

$A_y$  is the lateral offset of the mass centre of body  $A$ , caused by the rider's weight shifting towards the inside or the corner.  $Z$  is calculated in a similar way to  $Y$

in Eqn. (4.9):

$$Z = \frac{M_A A_z + M_B B_z + M_C C_z + M_D D_z + M_F F_z + M_G G_z}{M_M}$$

where  $A_z$ , etc. are the vertical heights of the masses above the wheelbase line in reference frame  $D$ .

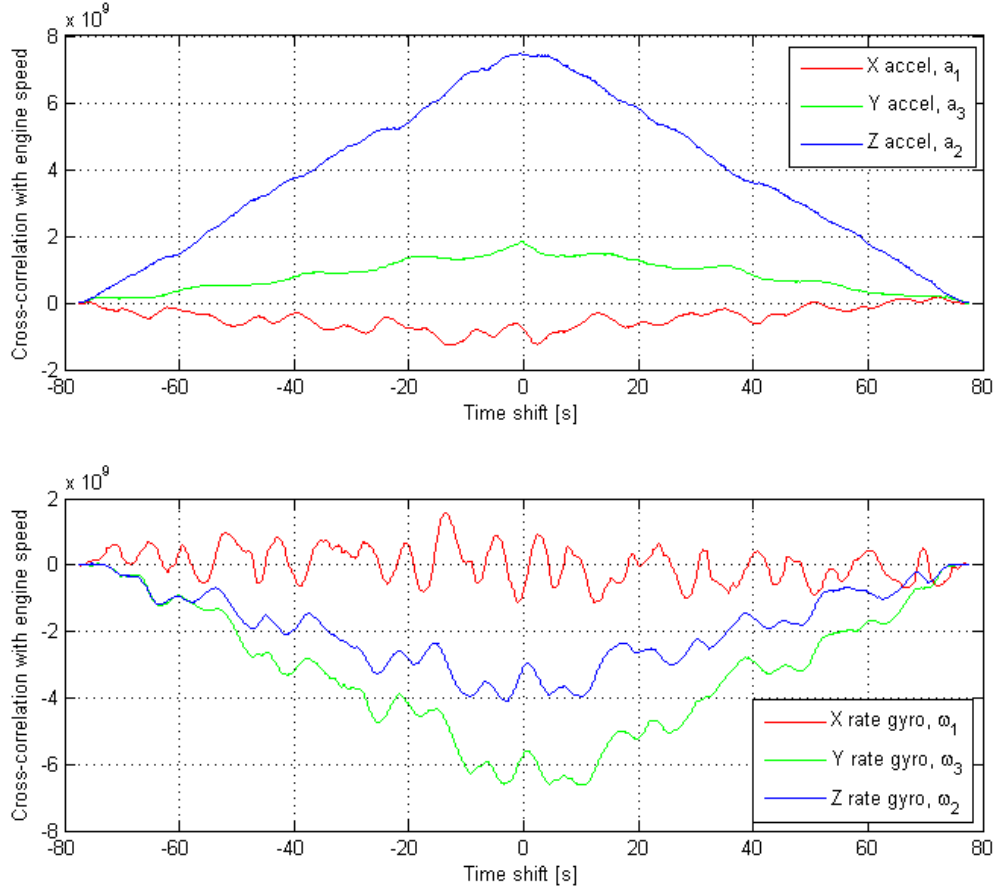


Figure 4.16: Cross-correlation of IMU data with engine speed

Unfortunately, the data recorded from the IMU accelerometers was sub-optimal. Fig. 4.16 shows the non-normalised cross-correlation of the IMU accelerometer and rate gyro signals with engine speed. Clearly, engine speed is present in all accelerometer signals to a large degree, with the  $Z$  accelerometer being the worst.

The  $Y$  and  $Z$  accelerometer data is shown in Fig. 4.17, along with engine speed and throttle position in the third plot. The  $Y$  accelerometer data would be expected to lie in the approximate range of  $\pm 3 \text{ ms}^{-2}$ . In certain sections, it

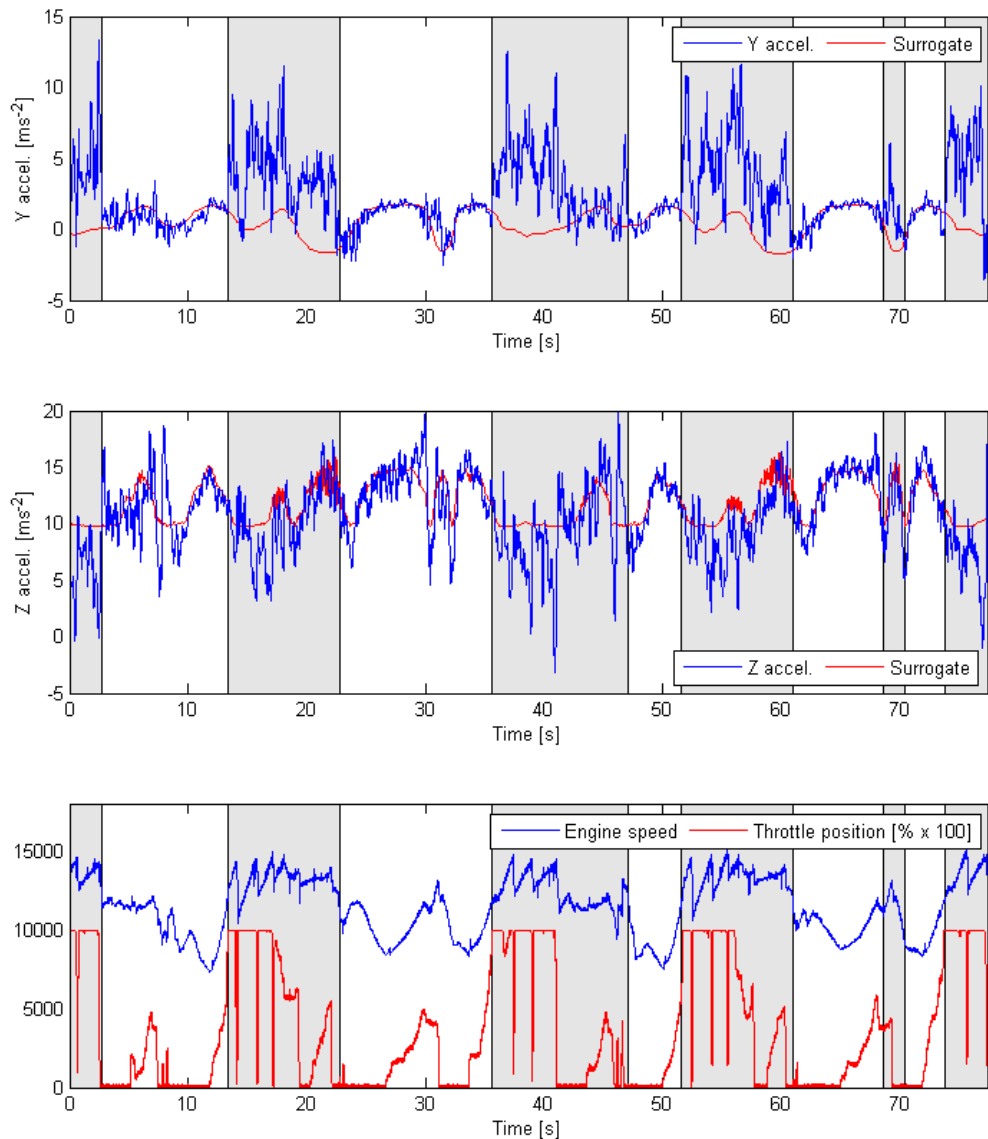


Figure 4.17: Accelerometer signals from track test

appears to behave well, but in others, it contains much higher values. These sections are shaded, and it can be seen that the bad data corresponds to parts of the track where the engine speed is high. It seems likely that in spite of the precautions explained in Section 6.6.4, the bracket on which the IMU is mounted resonates at high engine speed. The  $Z$  accelerometer, which cross-correlation shows to contain the most engine speed information, should not experience acceleration values that are continuously less than  $9.81 \text{ m s}^{-2}$ . Values lower than this are to be expected for short durations when cresting a hill or during direction changes, as seen in Fig. 4.17 at around 30 and 70 seconds. It would be expected

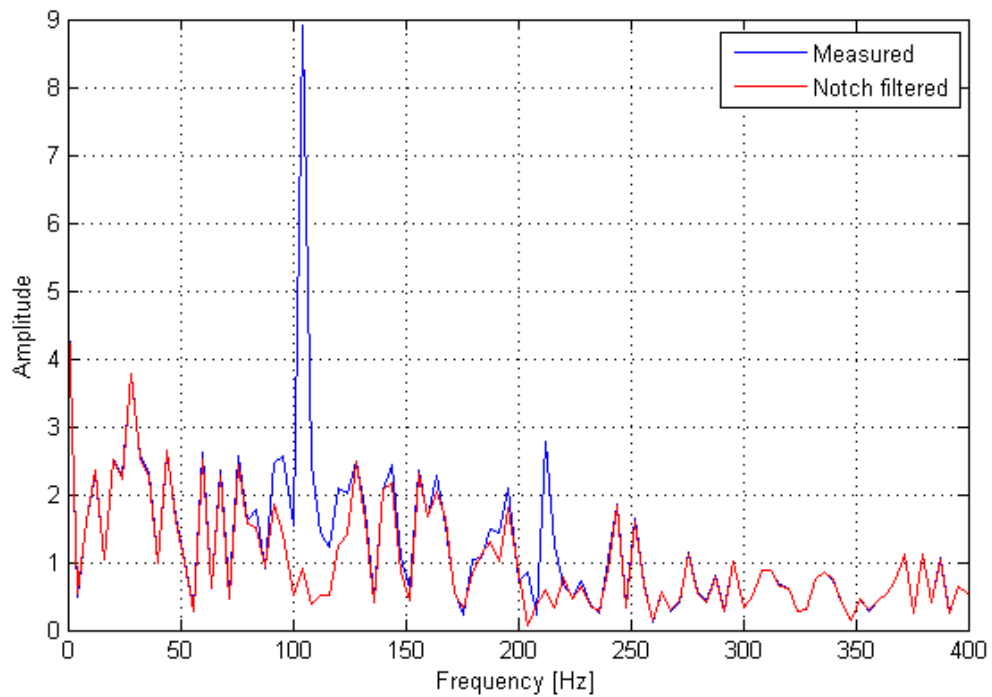


Figure 4.18: Amplitude spectrum of  $Y$  accelerometer signal from 36.4 to 36.65 seconds

that when the bike is upright, the average value would vary a little above and below that value due to bumps. In fact, in the shaded areas, the  $Z$  acceleration is unrealistically low for long periods.

Fig. 4.18 shows the amplitude spectrum of a Discrete Fourier Transform (DFT) of the  $Y$  accelerometer data in a 0.25 second window, starting at time 36.4 seconds. The mean engine speed in this window is 12,670 revolutions per minute (rpm), or 211.2 Hz. It can be seen that the harmonic at half engine speed is more significant than the fundamental frequency. Two notch filters were used, whose coefficients vary with engine speed, one at the fundamental frequency and one at half that frequency. The amplitude spectrum of the filtered data is shown in Fig. 4.18, and it is clear that the filters remove the peaks, as designed. Unfortunately, cross-correlation of the notch filtered signals with engine speed show no perceptible difference to the unfiltered versions. The reason can be surmised by looking at the time series data in Fig. 4.17. The errors in the IMU signals in the shaded areas show a large low frequency component, and this is the frequency range that contains the dynamic behaviour of the motorcycle.

Unfortunately therefore, the recorded data for  $a_y$  and  $a_z$  is not useable to determine  $A_y$  in Eqn. (4.11), and it was impossible to repeat the track test with a better IMU mounting arrangement, so a ‘Plan B’ is needed. It was decided to simulate the accelerations  $a_y$  and  $a_z$  by creating surrogate channels. The lateral displacement of the rider’s body is related to roll angle, so scaled roll angle data was overlaid on the  $Y$  acceleration signal and the scaling factor adjusted while checking the areas of ‘good’ data to determine the optimal match. The result was the surrogate channel for lateral acceleration:

$$a'_y = 1.9 q_9$$

and this is shown in the first plot in Fig. 4.17. The surrogate channel for

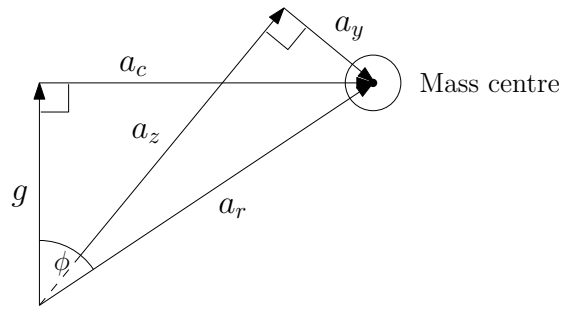


Figure 4.19: Vector diagram of cornering acceleration

$a_z$  is calculated as follows, using the vector diagram in Fig. 4.19. The circle represents the centre of mass for the combined bike and rider,  $a_y$  and  $a_z$  are the  $Y$  and  $Z$  accelerations measured by the IMU,  $a_c$  is centripetal acceleration,  $g$  is gravitational acceleration,  $a_r$  is the resultant of centripetal and gravitational acceleration,  $v$  is the road speed of the bike and  $\omega$  is the angular velocity of the bike. Then:

$$\begin{aligned} a_c &= v\omega \\ \phi &= \arctan \frac{a_c}{g} \\ a_r &= \frac{g}{\cos \phi} \\ a'_z &= \sqrt{a_r^2 - a_y^2} \end{aligned}$$

This calculation assumes that the angular acceleration of the bike is entirely due to cornering, and that there is no local rotation due to sliding. This is not ideal but it is part of a work-around for sub-optimal data. The surrogate channel  $a'_z$  is shown in the second plot in Fig. 4.17. It can be seen that  $a'_z$  is a good fit for  $a_z$  in the areas of ‘good’ data. There is some noise on the yaw rate  $\omega$ , and this appears on  $a'_z$ , but the measured  $a_z$  channel will contain noise due to road irregularity, even when the IMU is optimally mounted.

## 4.7 Engine Torque

Engine torque is a function of engine speed and throttle position. The CBR600RR has been raced extensively and many companies have measured the engine power at wide open throttle so it was not difficult to obtain this data. Power is typically measured in kilowatts (kW) or brake horsepower (BHP), with ‘brake’ referring to the dynamometer which applies a load to the engine in order to measure the power. It is proportional to torque multiplied by engine speed. Output torque from the engine is made up of the torque created by the combustion process and negative torque, which is created by frictional and pumping losses. Negative torque depends on engine speed. This negative torque was measured by coast-down testing, which is measuring the deceleration of the bike under the influence of various drag forces. Two coast-down tests were performed as described in Section 6.7. In one test, the throttle was closed at maximum engine speed<sup>‡</sup> in 4<sup>th</sup> gear the bike was allowed to slow down to 3,000 rpm. In the second test, the bike was allowed to freewheel with the clutch disengaged over a similar speed range.

Engine frictional torque was estimated from the 4<sup>th</sup> gear test data. First, the aerodynamic, tyre and other drag parameters were set, as explained in Section 4.5.5, so that the model behaviour matches the freewheel coast-down test. It was initially assumed that engine drag torque is proportional to engine speed, so a hypothetical torque character at closed throttle was constructed by making an initial estimate of torque values at 4,000 and 15,500 rpm. These engine speeds

---

<sup>‡</sup> The throttle was closed when the engine speed limiter began to activate.

are the lowest and highest in the full throttle torque table. Torque values between these engine speeds were interpolated. The 4<sup>th</sup> gear coast-down test was then modelled, and the low and high speed torque values were adjusted until the modelled engine speed optimally matched the actual engine speed. The upper plot in Fig. 7.2 shows the match that was obtained, so the assumption that drag torque is proportional to engine speed is validated. Fig. 4.20 shows the resulting

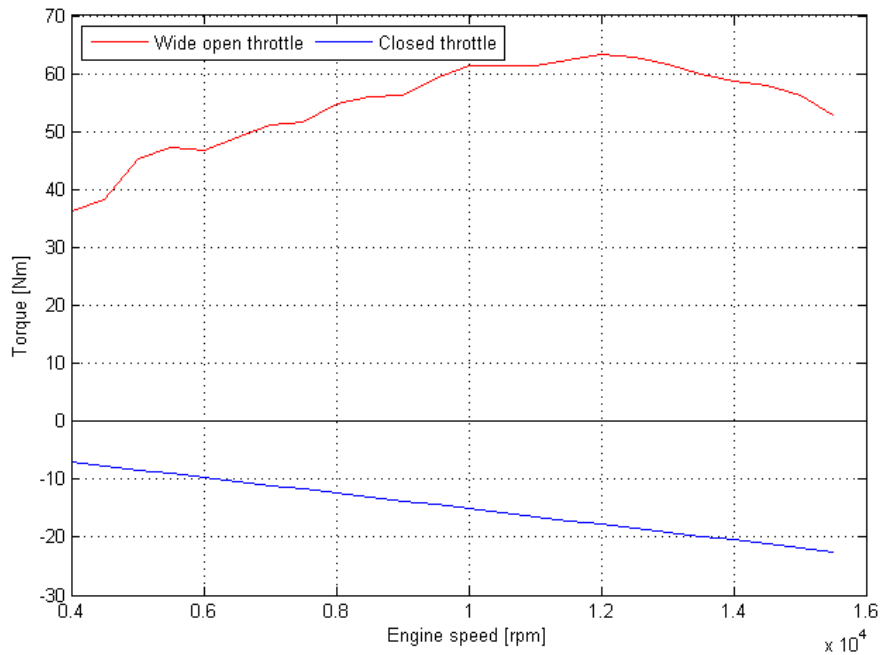


Figure 4.20: Engine torque, wide open throttle and fully closed

negative torque at closed throttle along with the wide open throttle torque curve.

With the wide open throttle and fully closed throttle torque curves established, what remains is to estimate the part throttle torque. No direct information was available on the relationship between throttle position and torque for the CBR600RR, so a typical characteristic curve from vehicle dynamics company OptimumG [45] was selected, and is shown in Fig. 4.21. Using this curve, the part throttle torque table was interpolated and this is shown in Fig. 4.22. Torque values in the model are interpolated from the torque table using engine speed and throttle position as indices.

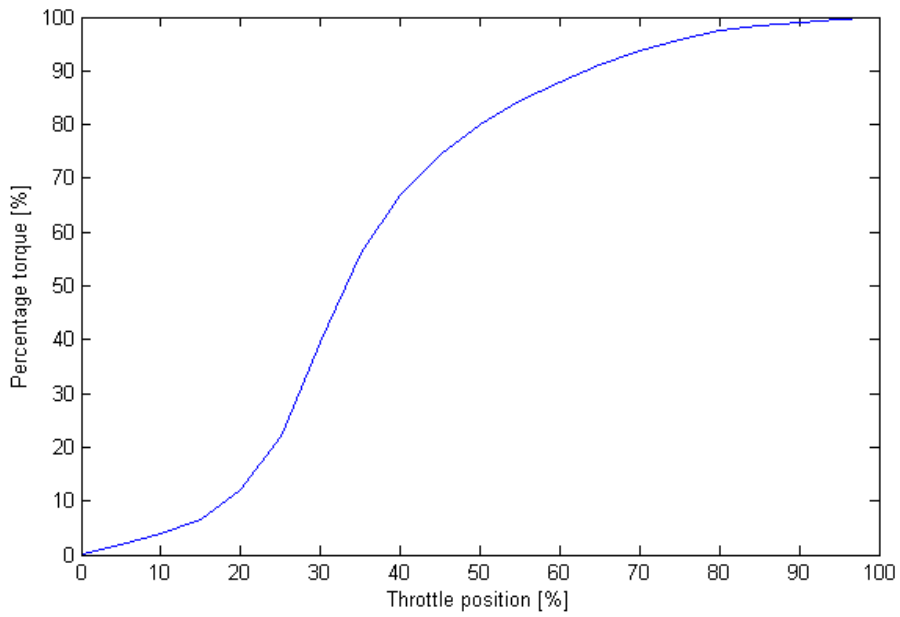


Figure 4.21: Percentage of engine torque vs. throttle position (typical)

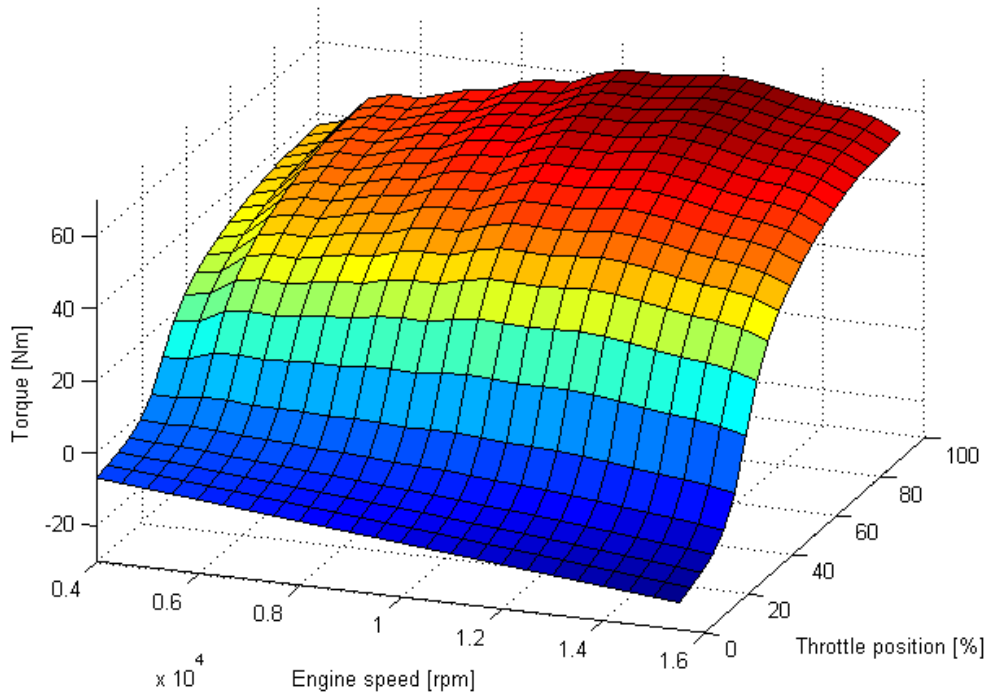


Figure 4.22: Engine torque map

## 4.8 Main frame position in terms of the state variables

In order to perform the multi-body analysis, the positions and orientations of the bodies must be found in terms of the state variables, i.e. the generalised co-

ordinates  $q_1, \dots, q_{11}$ , which are listed in Table. 4.3. The main frame,  $A$ , is chosen as the ‘primary body’, and its position and orientation are found as functions of the state variables. The position of the main frame is calculated relative to the rear tyre contact point with the ground plane, so to find its true position, the generalised co-ordinates  $q_7$  and  $q_8$ , the  $X$  and  $Y$  co-ordinates of the bike, must be included. The positions and orientations of the other bodies may then be found relative to the main frame. The generalised co-ordinates describing the position and orientation of the main frame are shown in Table 4.5. The table includes two extra generalised co-ordinates,  $q_{18}$  and  $q_{19}$ , which represent the wheelbase and trail respectively. These need to be calculated as intermediate steps in calculating  $q_{13}$  and  $q_{17}$ , and are useful model outputs in their own right.

Generalised co-ord	Description
$q_{12}$	Main frame roll angle
$q_{13}$	Main frame yaw angle
$q_{14}$	Main frame pitch angle
$q_{15}$	Main frame $x$ position
$q_{16}$	Main frame $z$ position
$q_{17}$	Main frame $y$ position
$q_{18}$	Wheelbase
$q_{19}$	Trail

Table 4.5: Generalised co-ords describing main frame position

In examining the frame position and orientation, the range of the state variables is important. Some, like suspension positions, have clearly defined limits, while others do not. Fig. 4.23 plots steering angle versus roll angle for two laps of Nutts Corner race track. The range of steering angle at maximum roll is within  $\pm 3^\circ$ , even on the slowest corner, which stands out from the others on the right of the plot. The plot is approximately cross shaped with most of the higher steering angles occurring close to the upright position as the rider counter-steers. In the following sections, a roll angle range of  $\pm 60^\circ$  and steering angle range of  $\pm 10^\circ$  are used, so as to take into account situations outside the range of race track testing, though it is noted that at normal road or racing speeds, high roll and steering angles never occur simultaneously. One interesting feature of Fig. 4.23 is that it

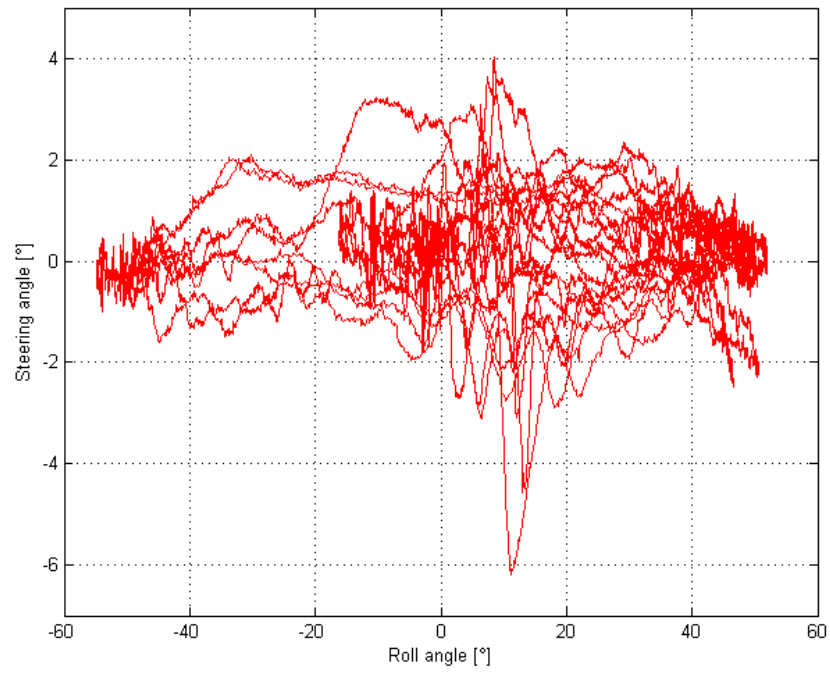


Figure 4.23: Measured steering angle versus camber angle

shows the consistency of a good rider. In many places, the traces from both laps are virtually identical. This consistency is one factor that allows the best riders to stay close to the performance limit.

4.8.1 Frame pitch angle  $\mu = q_{14}$  as a function of  $q_1 \dots q_{13}$

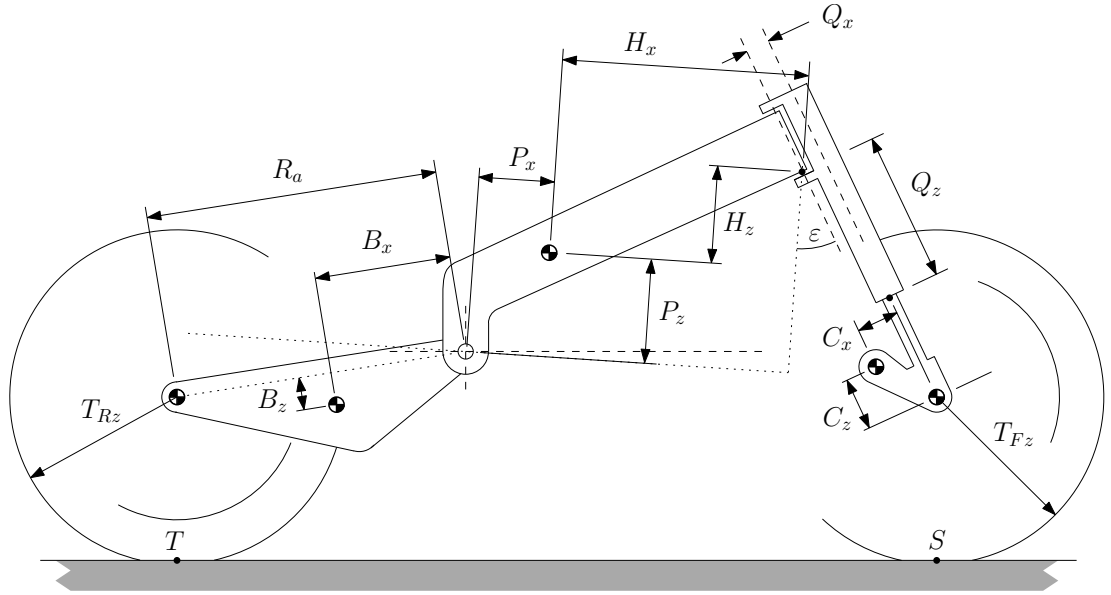


Figure 4.24: Bike dimensions in  $x, z$  plane

The vector path from the rear tyre point  $A$  in Fig. 4.25 to the equivalent front tyre point is given by the following expression:

$$T'_{Rz} \hat{d}_2 + R_a \hat{b}_1 + (P_x + H_x) \hat{a}_1 + (P_z + H_z) \hat{a}_2 + Q_x \hat{f}_1 - (-Q_z + q_1) \hat{f}_2 - T'_{Fz} \hat{g}_2 \quad (4.12)$$

$T'_{Rz}$  and the equivalent dimension for the front tyre,  $T'_{Fz}$  are easy to calculate

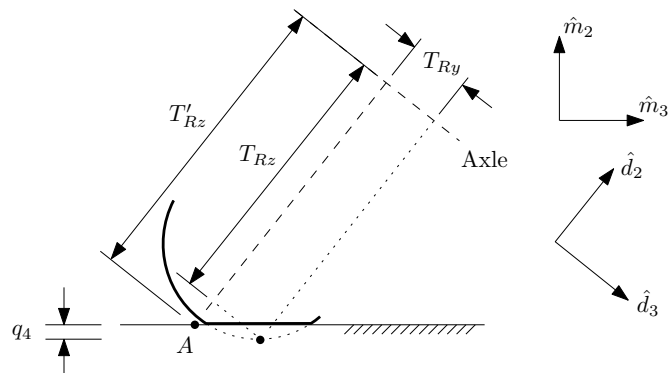


Figure 4.25: Rear tyre dimensions

geometrically:

$$\begin{aligned} T'_{Rz} &= T_{Rz} + T_{Ry} \tan \gamma - \frac{q_4}{\cos \gamma} \\ T'_{Fz} &= T_{Fz} + T_{Fy} \tan \gamma_1 - \frac{q_3}{\cos \gamma_1} \end{aligned} \quad (4.13)$$

Referring to Table 4.4, the reference frame conversions to the  $D$  reference frame are as follows

$$\begin{bmatrix} \hat{a}_1 \\ \hat{a}_2 \\ \hat{a}_3 \end{bmatrix} = \begin{bmatrix} c_\mu & s_\mu & 0 \\ -s_\mu & c_\mu & 0 \\ 0 & 0 & 1 \end{bmatrix} \begin{bmatrix} \hat{d}_1 \\ \hat{d}_2 \\ \hat{d}_3 \end{bmatrix}$$

$$\begin{bmatrix} \hat{b}_1 \\ \hat{b}_2 \\ \hat{b}_3 \end{bmatrix} = \begin{bmatrix} c_2 & s_2 & 0 \\ -s_2 & c_2 & 0 \\ 0 & 0 & 1 \end{bmatrix} \begin{bmatrix} \hat{a}_1 \\ \hat{a}_2 \\ \hat{a}_3 \end{bmatrix} = \begin{bmatrix} c_2 c_\mu - s_2 s_\mu & s_2 c_\mu + c_2 s_\mu & 0 \\ -s_2 c_\mu - c_2 s_\mu & c_2 c_\mu - s_2 s_\mu & 0 \\ 0 & 0 & 1 \end{bmatrix} \begin{bmatrix} \hat{d}_1 \\ \hat{d}_2 \\ \hat{d}_3 \end{bmatrix}$$

$$\begin{bmatrix} \hat{e}_1 \\ \hat{e}_2 \\ \hat{e}_3 \end{bmatrix} = \begin{bmatrix} c_\varepsilon & s_\varepsilon & 0 \\ -s_\varepsilon & c_\varepsilon & 0 \\ 0 & 0 & 1 \end{bmatrix} \begin{bmatrix} \hat{a}_1 \\ \hat{a}_2 \\ \hat{a}_3 \end{bmatrix} = \begin{bmatrix} c_\mu c_\varepsilon - s_\mu s_\varepsilon & s_\mu c_\varepsilon + c_\mu s_\varepsilon & 0 \\ -s_\mu c_\varepsilon - c_\mu s_\varepsilon & c_\mu c_\varepsilon - s_\mu s_\varepsilon & 0 \\ 0 & 0 & 1 \end{bmatrix} \begin{bmatrix} \hat{d}_1 \\ \hat{d}_2 \\ \hat{d}_3 \end{bmatrix}$$

$$\begin{bmatrix} \hat{f}_1 \\ \hat{f}_2 \\ \hat{f}_3 \end{bmatrix} = \begin{bmatrix} c_{11} & 0 & -s_{11} \\ 0 & 1 & 0 \\ s_{11} & 0 & c_{11} \end{bmatrix} \begin{bmatrix} \hat{e}_1 \\ \hat{e}_2 \\ \hat{e}_3 \end{bmatrix} = \begin{bmatrix} c_{11}(c_\mu c_\varepsilon - s_\mu s_\varepsilon) & c_{11}(s_\mu c_\varepsilon + c_\mu s_\varepsilon) & -s_{11} \\ -s_\mu c_\varepsilon - c_\mu s_\varepsilon & c_\mu c_\varepsilon - s_\mu s_\varepsilon & 0 \\ s_{11}(c_\mu c_\varepsilon - s_\mu s_\varepsilon) & s_{11}(s_\mu c_\varepsilon + c_\mu s_\varepsilon) & c_{11} \end{bmatrix} \begin{bmatrix} \hat{d}_1 \\ \hat{d}_2 \\ \hat{d}_3 \end{bmatrix}$$

$$\begin{bmatrix} \hat{m}_1 \\ \hat{m}_2 \\ \hat{m}_3 \end{bmatrix} = \begin{bmatrix} 1 & 0 & 0 \\ 0 & c_9 & -s_9 \\ 0 & s_9 & c_9 \end{bmatrix} \begin{bmatrix} \hat{d}_1 \\ \hat{d}_2 \\ \hat{d}_3 \end{bmatrix}$$

$$\begin{bmatrix} \hat{h}_1 \\ \hat{h}_2 \\ \hat{h}_3 \end{bmatrix} = \begin{bmatrix} c_{\delta'} & 0 & -s_{\delta'} \\ 0 & 1 & 0 \\ s_{\delta'} & 0 & c_{\delta'} \end{bmatrix} \begin{bmatrix} \hat{m}_1 \\ \hat{m}_2 \\ \hat{m}_3 \end{bmatrix} = \begin{bmatrix} c_{\delta'} & -s_9 s_{\delta'} & -c_9 s_{\delta'} \\ 0 & c_9 & -s_9 \\ s_{\delta'} & s_9 c_{\delta'} & c_9 c_{\delta'} \end{bmatrix} \begin{bmatrix} \hat{d}_1 \\ \hat{d}_2 \\ \hat{d}_3 \end{bmatrix}$$

$$\begin{bmatrix} \hat{g}_1 \\ \hat{g}_2 \\ \hat{g}_3 \end{bmatrix} = \begin{bmatrix} 1 & 0 & 0 \\ 0 & c_{\gamma_1} & s_{\gamma_1} \\ 0 & -s_{\gamma_1} & c_{\gamma_1} \end{bmatrix} \begin{bmatrix} \hat{h}_1 \\ \hat{h}_2 \\ \hat{h}_3 \end{bmatrix} = \begin{bmatrix} c_{\delta'} & -s_9 s_{\delta'} & -c_9 s_{\delta'} \\ s_{\gamma_1} s_{\delta'} & c_9 c_{\gamma_1} + s_9 c_{\delta'} s_{\gamma_1} & c_9 c_{\delta'} s_{\gamma_1} - s_9 c_{\gamma_1} \\ c_{\gamma_1} s_{\delta'} & s_9 c_{\gamma_1} c_{\delta'} - c_9 s_{\gamma_1} & c_9 c_{\gamma_1} c_{\delta'} + s_9 s_{\gamma_1} \end{bmatrix} \begin{bmatrix} \hat{d}_1 \\ \hat{d}_2 \\ \hat{d}_3 \end{bmatrix}$$

The vectors in Eqn. (4.12) will be converted to the  $D$  reference frame using the conversion matrices above, and the  $\hat{d}_2$  vector components will be summed to zero. The  $\hat{d}_1$  and  $\hat{d}_3$  vectors are disregarded. The most convenient way to do this is to zero the  $\hat{d}_1$  and  $\hat{d}_3$  vector components in the conversion matrices before substituting them into Eqn. (4.12). Eliminating the first and third columns in the conversion matrices results in the following conversions:

$$\begin{bmatrix} \hat{a}_1 \\ \hat{a}_2 \\ \hat{a}_3 \end{bmatrix} = \begin{bmatrix} 0 & s_\mu & 0 \\ 0 & c_\mu & 0 \\ 0 & 0 & 0 \end{bmatrix} \begin{bmatrix} \hat{d}_1 \\ \hat{d}_2 \\ \hat{d}_3 \end{bmatrix}$$

$$\begin{bmatrix} \hat{b}_1 \\ \hat{b}_2 \\ \hat{b}_3 \end{bmatrix} = \begin{bmatrix} 0 & s_2 c_\mu + c_2 s_\mu & 0 \\ 0 & c_2 c_\mu - s_2 s_\mu & 0 \\ 0 & 0 & 0 \end{bmatrix} \begin{bmatrix} \hat{d}_1 \\ \hat{d}_2 \\ \hat{d}_3 \end{bmatrix}$$

$$\begin{bmatrix} \hat{f}_1 \\ \hat{f}_2 \\ \hat{f}_3 \end{bmatrix} = \begin{bmatrix} 0 & c_{11}(s_\mu c_\varepsilon + c_\mu s_\varepsilon) & 0 \\ 0 & c_\mu c_\varepsilon - s_\mu s_\varepsilon & 0 \\ 0 & s_{11}(s_\mu c_\varepsilon + c_\mu s_\varepsilon) & 0 \end{bmatrix} \begin{bmatrix} \hat{d}_1 \\ \hat{d}_2 \\ \hat{d}_3 \end{bmatrix}$$

$$\begin{bmatrix} \hat{g}_1 \\ \hat{g}_2 \\ \hat{g}_3 \end{bmatrix} = \begin{bmatrix} 0 & -s_9 s_{\delta'} & 0 \\ 0 & c_9 c_{\gamma_1} + s_9 c_{\delta'} s_{\gamma_1} & 0 \\ 0 & s_9 c_{\gamma_1} c_{\delta'} - c_9 s_{\gamma_1} & 0 \end{bmatrix} \begin{bmatrix} \hat{d}_1 \\ \hat{d}_2 \\ \hat{d}_3 \end{bmatrix}$$

The  $\hat{d}_2$  components of the vectors in Eqn. (4.12) are therefore:

$$\hat{a}_1 = s_\mu \hat{d}_2 \quad (4.14)$$

$$\hat{a}_2 = c_\mu \hat{d}_2 \quad (4.15)$$

$$\hat{b}_1 = (s_2 c_\mu + c_2 s_\mu) \hat{d}_2 \quad (4.16)$$

$$\hat{f}_1 = c_{11} (s_\mu c_\epsilon + c_\mu s_\epsilon) \hat{d}_2$$

$$\hat{f}_2 = (c_\mu c_\epsilon - s_\mu s_\epsilon) \hat{d}_2$$

$$\hat{g}_2 = (c_9 c_{\gamma_1} + s_9 c_{\delta'} s_{\gamma_1}) \hat{d}_2$$

Also,

$$\delta' \approx \arctan \left( \frac{\cos(\epsilon + \mu) \tan \delta}{c_9} \right)$$

Substituting the above values into Eqn. (4.12) and setting it equal to zero, and dividing by  $\hat{d}_2$  gives:

$$\begin{aligned} & R_a \sin(\mu + q_2) + c_\delta Q_x (c_\epsilon s_\mu + c_\mu s_\epsilon) + (Q_z - q_1) (c_\epsilon c_\mu - s_\mu s_\epsilon) + s_\mu (H_x + P_x) \\ & + c_\mu (H_z + P_z) + T'_{Rz} - T'_{Fz} \left( \frac{s_{\gamma_1} s_9}{\sqrt{c_\epsilon^2 \tan^2 \delta \sec^2 q_9 + 1}} + c_{\gamma_1} c_9 \right) = 0 \end{aligned}$$

The expression in brackets at the end is the extent to which  $T'_{Fz}$  is altered by the fact that the front and rear wheel cambers angles are not exactly the same. As the steering angle  $\delta$  is typically low at road speeds, it can be assumed that the wheels have approximately the same camber, i.e.  $\gamma_1 \approx q_9$  and  $\tan^2 \delta \approx 0$ , so the

bracketed expressions becomes 1. The equation becomes:

$$\begin{aligned} & c_\mu(R_a s_2 + H_z + P_z + c_\epsilon(Q_z - q_1) + Q_x c_\delta s_\epsilon) \\ & + s_\mu(R_a c_2 + H_x + P_x + c_\epsilon c_\delta Q_x - s_\epsilon(Q_z - q_1)) \\ & + T'_{Rz} - T'_{Fz} = 0 \end{aligned}$$

Next,  $\mu$  lies in the approximate range of  $\pm 5^\circ$ ,<sup>§</sup> so  $s_\mu \approx \mu$  and  $c_\mu \approx 1$ . Making these substitutions, gives the final equation for  $\mu$ .

$$\mu = \frac{-R_a s_2 - H_z - P_z - c_\epsilon(Q_z - q_1) - Q_x c_\delta s_\epsilon - T'_{Rz} + T'_{Fz}}{R_a c_2 + H_x + P_x + c_\epsilon c_\delta Q_x - s_\epsilon(Q_z - q_1)}$$

Substituting Eqns. (4.13) gives:

$$q_{14} = \mu = \frac{-R_a s_2 - H_z - P_z - c_\epsilon(Q_z - q_1) - Q_x c_\delta s_\epsilon + T'_{Fz} - T'_{Rz} + \tan q_9(T_{Fy} - T_{Ry}) + \frac{q_4 - q_3}{c_9}}{R_a c_2 + H_x + P_x + c_\epsilon c_\delta Q_x - s_\epsilon(Q_z - q_1)} \quad (4.17)$$

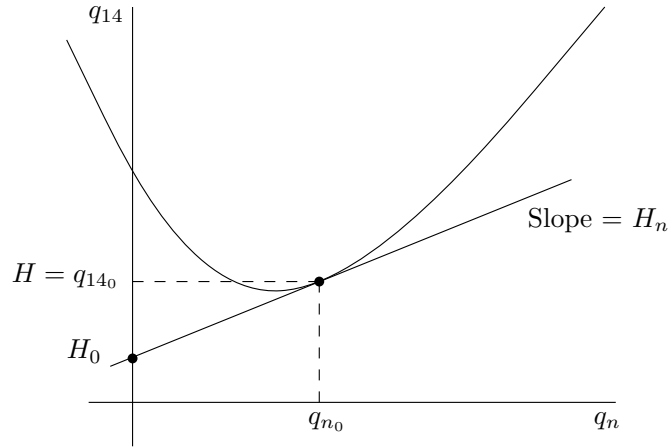


Figure 4.26: Linearisation notation

The pitch angle  $q_{14}$  is expanded about the linearisation point  $(q_{1_0}, q_{2_0}, q_{3_0}, q_{4_0}, q_{9_0}, q_{11_0})$  by performing a first order Taylor series expansion for each variable. Performing the expansion for  $q_1$  about  $q_{1_0}$  while setting  $q_2 = q_{2_0}, \dots, q_{11} = q_{11_0}$  results in an

<sup>§</sup> If the range of  $\mu$  is not centred close to 0, a rotational transformation may be applied to the dimensions of the main frame to change its ‘base’ angle.

equation of the form

$$q_{14} = H + H_1(q_1 - q_{1_0})$$

Doing the same for  $q_2$  results in

$$q_{14} = H + H_2(q_2 - q_{2_0})$$

Likewise for all the other variables.  $H$  is the value of  $q_{16}$  at the linearisation point and so is the offset common to the Taylor series expansions for each variable. Combining all the individual Taylor series expansions gives an overall approximation for  $q_{14}$ . The constant  $H$  appears only once, because it is the overall offset.

$$\begin{aligned} q_{14} = & H + H_1(q_1 - q_{1_0}) + H_2(q_2 - q_{2_0}) + H_3(q_3 - q_{3_0}) + H_4(q_4 - q_{4_0}) \\ & + H_9(q_9 - q_{9_0}) + H_{11}(q_{11} - q_{11_0}) \end{aligned}$$

The pitch angle does not depend on the wheel rotation angles, the position of the bike on the ground plane or the yaw angle of the bike, so the state variables  $q_5$ ,  $q_6$ ,  $q_7$ ,  $q_8$  and  $q_{10}$  are not present. The expansions for  $q_3$ ,  $q_4$  and  $q_{11}$  are performed about zero so the equation becomes:

$$q_{14} = H + H_1(q_1 - q_{1_0}) + H_2(q_2 - q_{2_0}) + H_3q_3 + H_4q_4 + H_9(q_9 - q_{9_0}) + H_{11}q_{11}$$

If:

$$H_0 = H - H_1q_{1_0} - H_2q_{2_0} - H_9q_{9_0}$$

then:

$$q_{14} = H_0 + H_1q_1 + H_2q_2 + H_3q_3 + H_4q_4 + H_9q_9 + H_{11}q_{11} \quad (4.18)$$

where:

$$H = -\frac{R_a s_2 + c_\epsilon(Q_z - q_1) + \tan q_9(T_{Ry} - T_{Fy}) - T_{Fz} + H_z + P_z + Q_x c_{11} s_\epsilon + T_{Rz}}{W_0}$$

$$H_1 = \frac{c_\epsilon(R_a c_2 + H_x + P_x) + s_\epsilon(R_a s_2 + \tan q_9(T_{Ry} - T_{Fy}) - T_{Fz} + H_z + P_z + Q_x c_{11} s_\epsilon + T_{Rz}) + c_\epsilon^2 Q_x c_{11}}{W_0^2}$$

$$H_2 = \frac{R_a(-R_a - s_2(c_\epsilon(Q_z - q_1) - T_{Fz} + H_z + P_z + Q_x c_{11} s_\epsilon + T_{Rz}) - c_2(c_\epsilon Q_x c_{11} + H_x + s_\epsilon(q_1 - Q_z) + P_x) + \tan q_9(T_{Fy} - T_{Ry})s_2)}{W_0^2}$$

$$H_3 = -\frac{\sec q_9}{W_0}$$

$$H_4 = \frac{\sec q_9}{W_0}$$

$$H_9 = \frac{\sec^2 q_9(T_{Fy} - T_{Ry})}{W_0}$$

$$H_{11} = \frac{Q_x s_{11}(-c_\epsilon(R_a s_2 + \tan q_9(T_{Ry} - T_{Fy}) - T_{Fz} + H_z + P_z + T_{Rz}) + s_\epsilon(R_a c_2 + H_x + s_\epsilon(q_1 - Q_z) + P_x) + c_\epsilon^2(q_1 - Q_z))}{W_0^2}$$

$$W_0 = c_2 R_a + c_\epsilon c_{11} Q_x + H_x + P_x + s_\epsilon(q_1 - Q_z)$$

$W_0$  happens to be the wheelbase of the bike at the linearisation point, projected onto the  $\hat{d}_1, \hat{d}_2$  plane. Exact and linearised values of the pitch angle  $q_{16}$ , from Eqns. (4.17) and (4.18) are plotted in Fig. 4.27. In order to show the effectiveness of the linearisation process, all plots are with the bike at  $60^\circ$  roll angle and  $10^\circ$  steering angle except as stated in the last two plots.

## 4.8. Main frame position in terms of the state variables

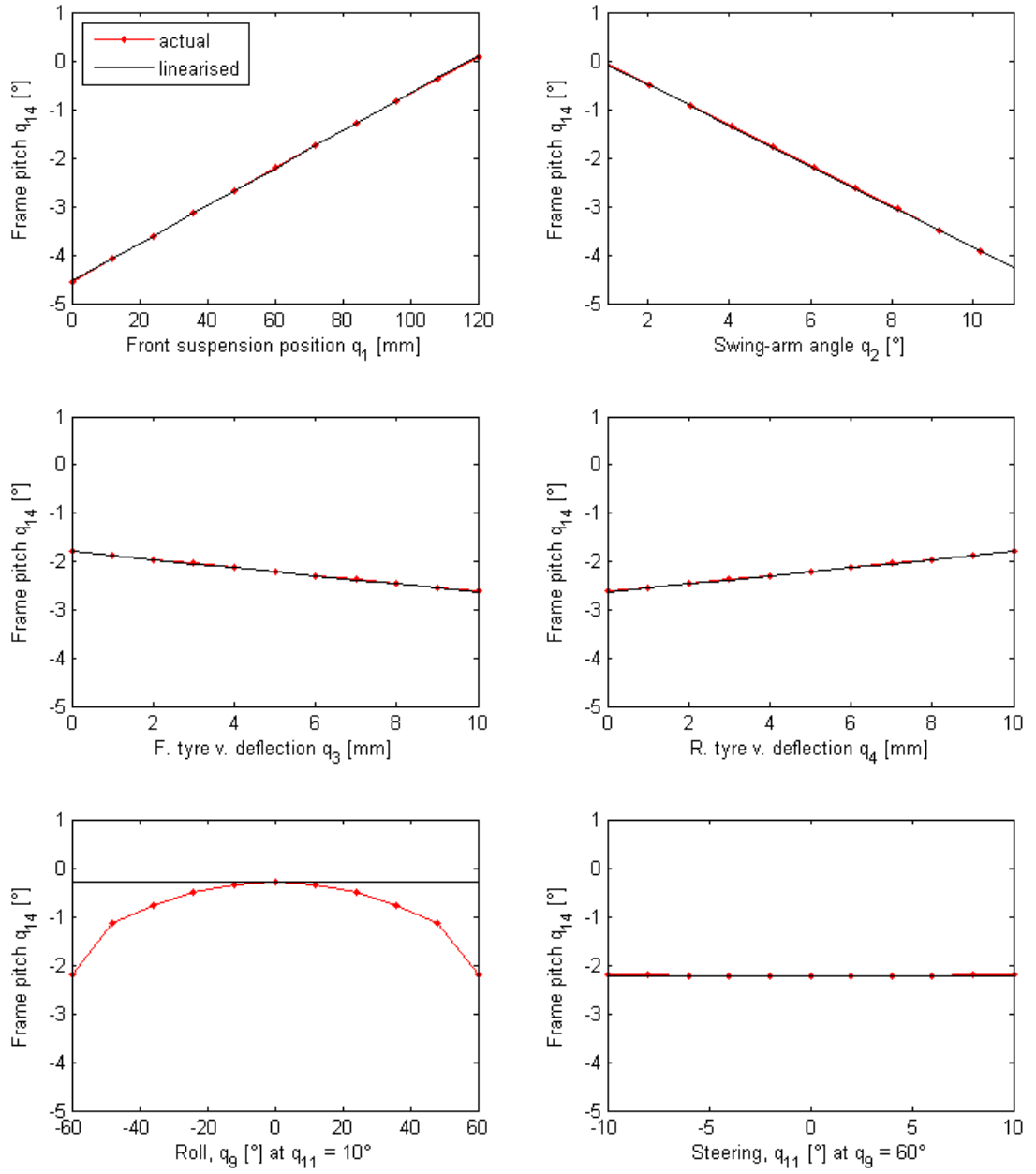


Figure 4.27: Frame pitch angle as a function of  $q_1$ ,  $q_2$ ,  $q_3$ ,  $q_4$ ,  $q_9$  and  $q_{11}$

$H_0, \dots, H_{11}$  have been introduced as the state variables coefficients in Eqn. (4.18), which is the linearised function for the pitch angle  $q_{14}$ . The other orientations and displacements of body  $A$  are described in a similar way in the following sections. Each orientation and displacement has its own set of coefficients and these are listed in Table 4.6.

### 4.8.2 Frame $x$ position $q_{15}$ as a function of $q_1 \dots q_{11}$

Expressions are needed for the  $x$  and  $y$  co-ordinates of the main frame mass centre in the  $D$  reference frame, relative to the rear tyre contact point. Using Eqn. (4.12), an expression may be written for the vector path from the rear contact point  $T$  to body  $A$ .

$$\vec{T}A = T'_{Rz}\hat{d}_2 + R_a\hat{b}_1 + P_x\hat{a}_1 + P_z\hat{a}_2 \quad (4.19)$$

This must be converted to the  $D$  reference frame, and all vector components except  $\hat{d}_1$  are then disregarded. The expressions for  $\hat{a}_1$ ,  $\hat{a}_2$  and  $\hat{b}_1$  in terms of  $\hat{d}_1$  from Eqns. (4.22), (4.23) and (4.24) are substituted, resulting in an expression for the  $x$  position:

$$\vec{T}A = R_a(c_2c_\mu - s_2s_\mu)\hat{d}_1 + P_xc_\mu\hat{d}_1 - P_zs_\mu\hat{d}_1$$

Using generalised co-ordinates, the magnitude is:

$$x = R_a(c_2c_{14} - s_2s_{14}) + P_xc_{14} - P_zs_{14} \quad (4.20)$$

This expression for  $x$  is linearised in the same way as  $q_{14}$  in Section 4.8.1. In fact,  $x$  is a function of  $q_{14}$  and the coefficients  $J$ ,  $J_1$ ,  $J_2$ ,  $J_3$ ,  $J_4$ ,  $J_9$  and  $J_{11}$  are considerably more complex than the  $H$  coefficients of  $q_{14}$ . For that reason, they are not reproduced here, but Fig. 4.28 shows the actual and linearised character of  $x$  in terms of  $q_1$ ,  $q_2$ ,  $q_3$ ,  $q_4$ ,  $q_9$  and  $q_{11}$ . As  $x$  is being regarded in the local  $D$  reference frame, the other state variables are irrelevant.

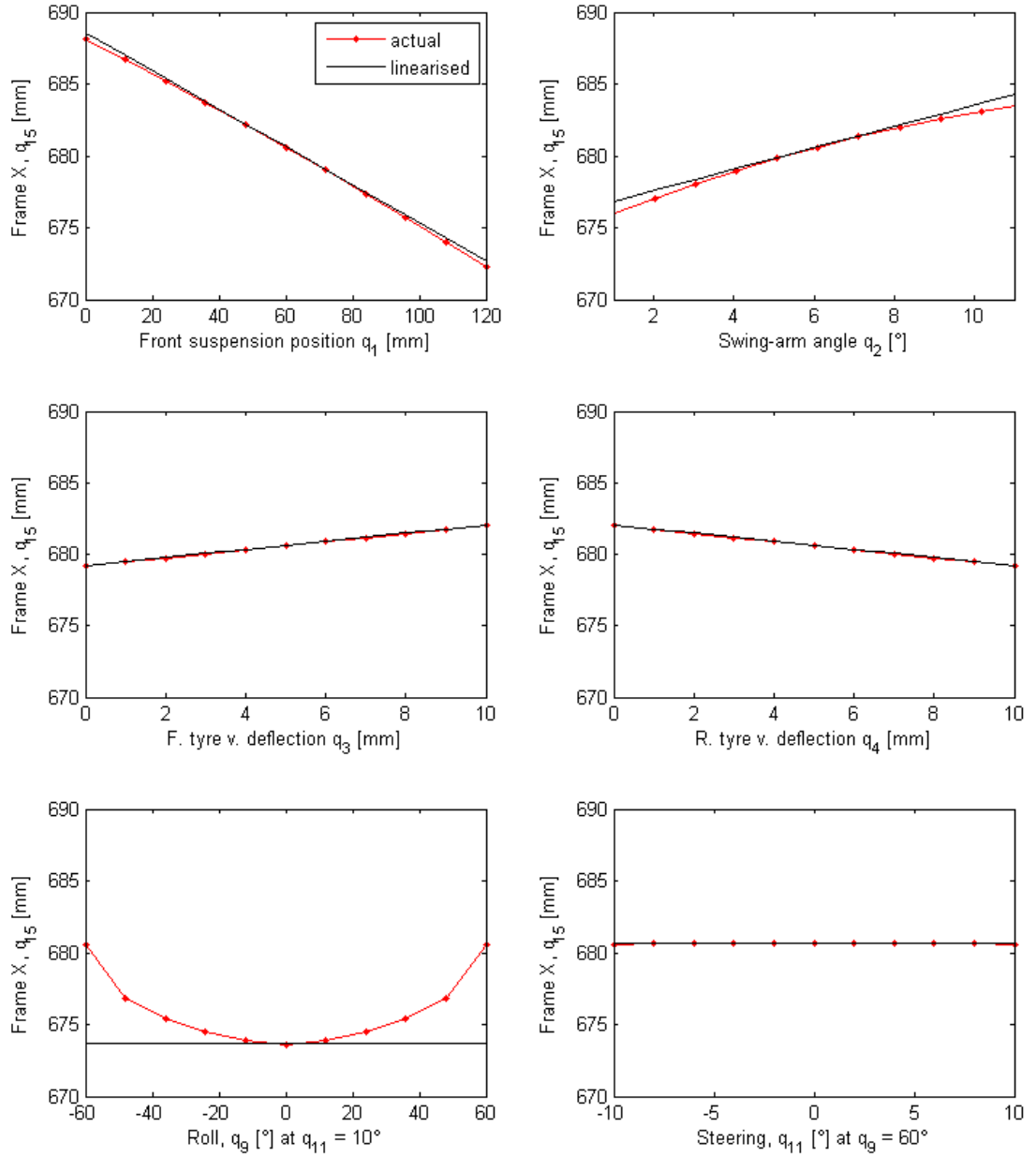


Figure 4.28: Frame X position from rear tyre contact point as a function of  $q_1$ ,  $q_2$ ,  $q_3$ ,  $q_4$ ,  $q_9$  and  $q_{11}$

### 4.8.3 Frame $z$ position $q_{16}$ as a function of $q_1 \dots q_{11}$

The procedure to find the  $z$  co-ordinate of the main frame mass centre in the  $D$  reference frame begins with Eqn. (4.19). All unit vectors are converted to the  $D$  reference frame and only the  $\hat{d}_2$  components are used. The expressions for  $\hat{a}_1$ ,  $\hat{a}_2$  and  $\hat{b}_1$  in terms of  $\hat{d}_2$  from Eqns. (4.14), (4.15) and (4.16) are substituted,

resulting in an expression for the  $z$  position:

$$\vec{z} = T'_{Rz} \hat{d}_2 + R_a(s_2 c_\mu + c_2 s_\mu) \hat{d}_2 + P_x s_\mu \hat{d}_2 + P_z c_\mu \hat{d}_2$$

Expanding  $T'_{Rz}$  according to Eqn. (4.13), and using generalised co-ordinates, the magnitude is:

$$z = T_{Rz} + T_{Ry} \tan q_9 - \frac{q_4}{c_9} + R_a(s_2 c_{14} + c_2 s_{14}) + P_x s_{14} + P_z c_{14} \quad (4.21)$$

The expression for  $z$  is linearised using the same procedure as before. The  $K$  coefficients are complex and are not shown here, but Fig. 4.29 shows the actual and linearised behaviour.

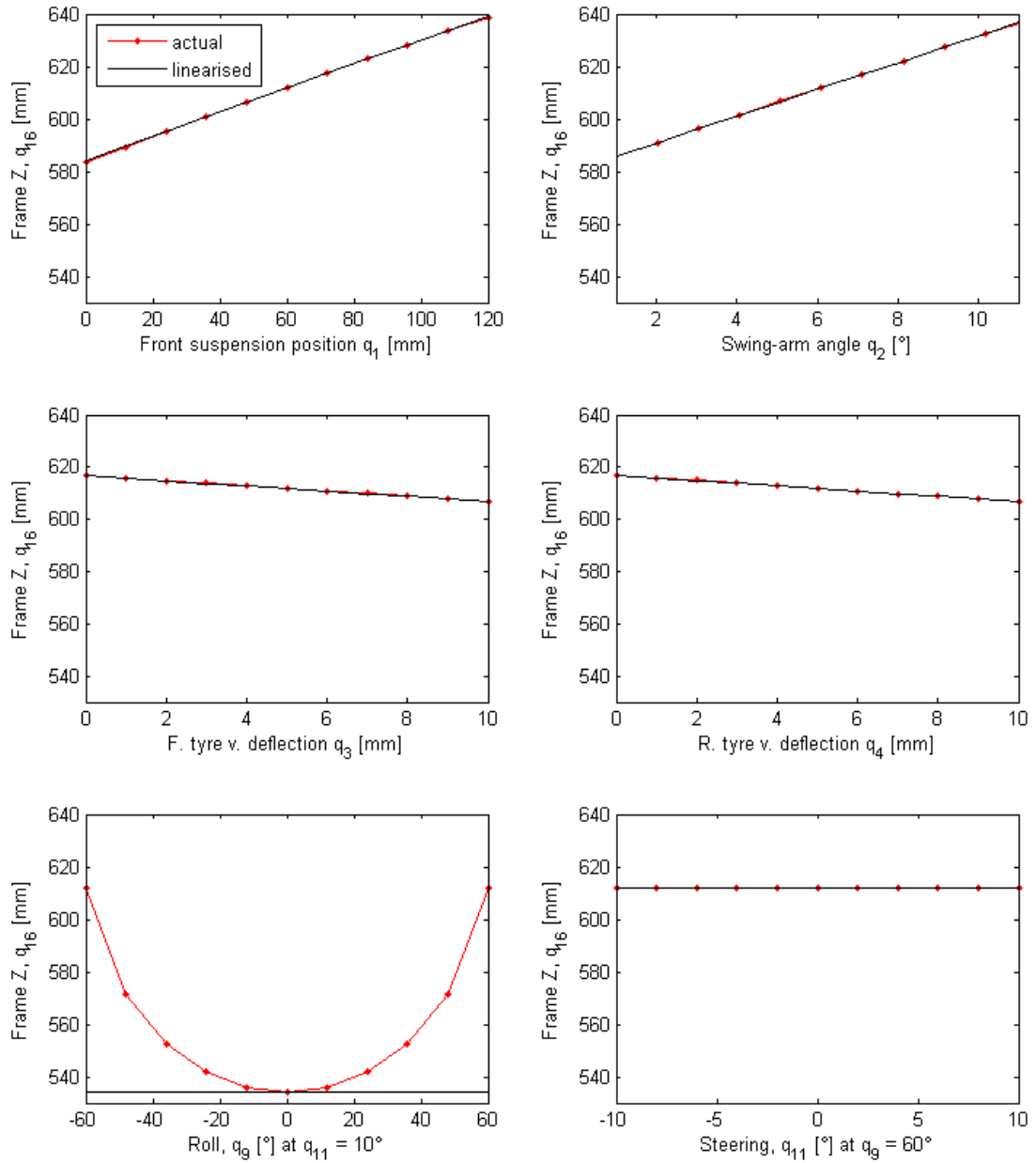


Figure 4.29: Frame Z position from rear tyre contact point as a function of  $q_1$ ,  $q_2$ ,  $q_3$ ,  $q_4$ ,  $q_9$  and  $q_{11}$

#### 4.8.4 Wheelbase $q_{18}$ as a function of $q_1 \dots q_{11}$

In Section 4.8.1, the vector path from the rear tyre contact point to the front was given in Eqns. (4.12) and (4.13), which are shown again below. To find the frame pitch angle, only the vertical  $\hat{d}_2$  component was considered. To calculate

the wheelbase, only the longitudinal  $\hat{d}_1$  component will be used.

$$T'_{Rz}\hat{d}_2 + R_a\hat{b}_1 + (P_x + H_x)\hat{a}_1 + (P_z + H_z)\hat{a}_2 + Q_x\hat{f}_1 - (-Q_z + q_1)\hat{f}_2 - T'_{Fz}\hat{g}_2 \quad (4.12)$$

$$\begin{aligned} T'_{Rz} &= T_{Rz} + T_{Ry} \tan \gamma - \frac{q_4}{\cos \gamma} \\ T'_{Fz} &= T_{Fz} + T_{Fy} \tan \gamma_1 - \frac{q_3}{\cos \gamma_1} \end{aligned} \quad (4.13)$$

and the vector transformations are the same as in Section 4.8.1. Eliminating the second and third columns in the conversion matrices results in the following conversions:

$$\begin{bmatrix} \hat{a}_1 \\ \hat{a}_2 \\ \hat{a}_3 \end{bmatrix} = \begin{bmatrix} c_\mu & 0 & 0 \\ -s_\mu & 0 & 0 \\ 0 & 0 & 0 \end{bmatrix} \begin{bmatrix} \hat{d}_1 \\ \hat{d}_2 \\ \hat{d}_3 \end{bmatrix}$$

$$\begin{bmatrix} \hat{b}_1 \\ \hat{b}_2 \\ \hat{b}_3 \end{bmatrix} = \begin{bmatrix} c_2c_\mu - s_2s_\mu & 0 & 0 \\ -s_2c_\mu - c_2s_\mu & 0 & 0 \\ 0 & 0 & 0 \end{bmatrix} \begin{bmatrix} \hat{d}_1 \\ \hat{d}_2 \\ \hat{d}_3 \end{bmatrix}$$

$$\begin{bmatrix} \hat{f}_1 \\ \hat{f}_2 \\ \hat{f}_3 \end{bmatrix} = \begin{bmatrix} c_{11}(c_\mu c_\varepsilon - s_\mu s_\varepsilon) & 0 & 0 \\ -s_\mu c_\varepsilon - c_\mu s_\varepsilon & 0 & 0 \\ -s_{11}(s_\mu s_\varepsilon - c_\mu c_\varepsilon) & 0 & 0 \end{bmatrix} \begin{bmatrix} \hat{d}_1 \\ \hat{d}_2 \\ \hat{d}_3 \end{bmatrix}$$

$$\begin{bmatrix} \hat{g}_1 \\ \hat{g}_2 \\ \hat{g}_3 \end{bmatrix} = \begin{bmatrix} c_{\delta'} & 0 & 0 \\ s_{\gamma_1} s_{\delta'} & 0 & 0 \\ c_{\gamma_1} s_{\delta'} & 0 & 0 \end{bmatrix} \begin{bmatrix} \hat{d}_1 \\ \hat{d}_2 \\ \hat{d}_3 \end{bmatrix}$$

The  $\hat{d}_1$  components of the vectors in Eqn. (4.12) are therefore:

$$\hat{a}_1 = c_\mu \hat{d}_1 \quad (4.22)$$

$$\hat{a}_2 = -s_\mu \hat{d}_1 \quad (4.23)$$

$$\hat{b}_1 = (c_2 c_\mu - s_2 s_\mu) \hat{d}_1 \quad (4.24)$$

$$\hat{f}_1 = c_{11}(c_\mu c_\varepsilon - s_\mu s_\varepsilon) \hat{d}_1$$

$$\hat{f}_2 = (-s_\mu c_\varepsilon - c_\mu s_\varepsilon) \hat{d}_1$$

$$\hat{g}_2 = s_{\gamma_1} s_{\delta'} \hat{d}_1$$

These values are substituted into Eqn. (4.12) to give an expression for the vector from the rear contact point to the front:

$$\begin{aligned} \vec{W} = & (R_a(c_2 c_\mu - s_2 s_\mu) + (P_x + H_x)c_\mu - (P_z + H_z)s_\mu \\ & + Q_x c_{11}(c_\mu c_\varepsilon - s_\mu s_\varepsilon) + (-Q_z + q_1)(s_\mu c_\varepsilon + c_\mu s_\varepsilon)) \hat{d}_1 \end{aligned}$$

The magnitude of  $\vec{W}$  is the wheelbase length and is shown here in terms of the generalised co-ordinates:

$$\begin{aligned} q_{18} = & R_a(c_2 c_{14} - s_2 s_{14}) + (P_x + H_x)c_{14} - (P_z + H_z)s_{14} \\ & + Q_x c_{11}(c_{14} c_\varepsilon - s_{14} s_\varepsilon) + (-Q_z + q_1)(s_{14} c_\varepsilon + c_{14} s_\varepsilon) \end{aligned}$$

#### 4.8.5 Trail $q_{19}$ as a function of $q_1 \dots q_{11}$

The following expression for trail in the front wheel reference frame  $G$  may be found from Fig. 4.30:

$$\begin{aligned} q_{19} = & \frac{T_{Fz} \sin(\mu + \varepsilon) - Q_x}{\cos(\mu + \varepsilon)} \quad \mu = q_{14} \\ = & \frac{T_{Fz}(s_{14} c_\varepsilon + c_{14} s_\varepsilon) - Q_x}{c_{14} c_\varepsilon - s_{14} s_\varepsilon} \end{aligned} \quad (4.25)$$

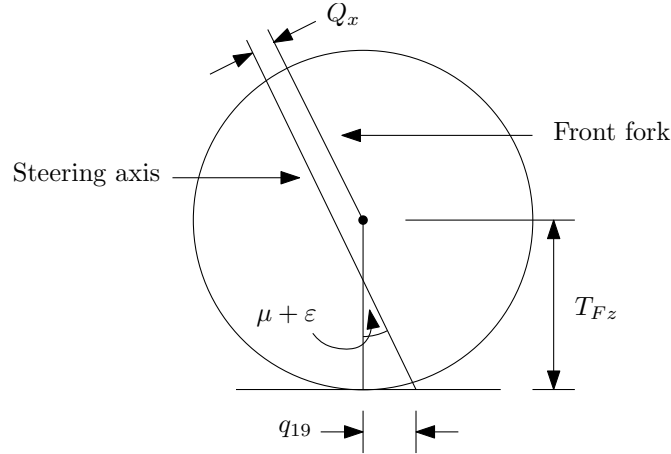


Figure 4.30: Front wheel trail

The pitch angle  $\mu = q_{14}$  is typically<sup>¶</sup> in the  $\pm 5^\circ$  range so the following approximations may be made:

$$s_{14} = q_{14} \quad c_{14} = 1$$

The resulting equation for  $q_{19}$  is:

$$q_{19} = \frac{T_{Fz}(q_{14}c_\varepsilon + s_\varepsilon) - Q_x}{c_\varepsilon - q_{14}s_\varepsilon}$$

#### 4.8.6 Frame yaw angle $q_{13}$ as a function of $q_1 \dots q_{11}$

The first step in calculating yaw angle is to find the lateral offset of the front contact point. Once again, the starting point is the vector path from the rear tyre contact point to the front, in Eqns. (4.12) and (4.13). These are shown again below. To find the lateral offset, only the transverse component,  $\hat{d}_3$ , will be used.

$$T'_{Rz}\hat{d}_2 + R_a\hat{b}_1 + (P_x + H_x)\hat{a}_1 + (P_z + H_z)\hat{a}_2 + Q_x\hat{f}_1 - (-Q_z + q_1)\hat{f}_2 - T'_{Fz}\hat{g}_2 \quad (4.12)$$

<sup>¶</sup> If the range of  $\mu$  is not centred close to 0, a rotational transformation may be applied to the dimensions of the main frame to change its 'base' angle.

$$\begin{aligned}
 T'_{Rz} &= T_{Rz} + T_{Ry} \tan \gamma - \frac{q_4}{\cos \gamma} \\
 T'_{Fz} &= T_{Fz} + T_{Fy} \tan \gamma_1 - \frac{q_3}{\cos \gamma_1}
 \end{aligned}
 \tag{4.13}$$

and the vector transformations are the same as in Section 4.8.1. Eliminating the first and second columns in the conversion matrices results in the following conversions:

$$\begin{bmatrix} \hat{a}_1 \\ \hat{a}_2 \\ \hat{a}_3 \end{bmatrix} = \begin{bmatrix} 0 & 0 & 0 \\ 0 & 0 & 0 \\ 0 & 0 & 1 \end{bmatrix} \begin{bmatrix} \hat{d}_1 \\ \hat{d}_2 \\ \hat{d}_3 \end{bmatrix}$$

$$\begin{bmatrix} \hat{b}_1 \\ \hat{b}_2 \\ \hat{b}_3 \end{bmatrix} = \begin{bmatrix} 0 & 0 & 0 \\ 0 & 0 & 0 \\ 0 & 0 & 1 \end{bmatrix} \begin{bmatrix} \hat{d}_1 \\ \hat{d}_2 \\ \hat{d}_3 \end{bmatrix}$$

$$\begin{bmatrix} \hat{f}_1 \\ \hat{f}_2 \\ \hat{f}_3 \end{bmatrix} = \begin{bmatrix} 0 & 0 & -s_{11} \\ 0 & 0 & 0 \\ 0 & 0 & c_{11} \end{bmatrix} \begin{bmatrix} \hat{d}_1 \\ \hat{d}_2 \\ \hat{d}_3 \end{bmatrix}$$

$$\begin{bmatrix} \hat{g}_1 \\ \hat{g}_2 \\ \hat{g}_3 \end{bmatrix} = \begin{bmatrix} 0 & 0 & -c_9 s_{\delta'} \\ 0 & 0 & c_9 c_{\delta'} s_{\gamma_1} - s_9 c_{\gamma_1} \\ 0 & 0 & c_9 c_{\gamma_1} c_{\delta'} + s_9 s_{\gamma_1} \end{bmatrix} \begin{bmatrix} \hat{d}_1 \\ \hat{d}_2 \\ \hat{d}_3 \end{bmatrix}$$

The  $\hat{d}_3$  components of the vectors in Eqn. (4.12) are therefore:

$$\begin{aligned}\hat{a}_1 &= 0 \\ \hat{a}_2 &= 0 \\ \hat{b}_1 &= 0 \\ \hat{f}_1 &= -s_{11}\hat{d}_3 \\ \hat{f}_2 &= 0 \\ \hat{g}_2 &= (c_9c_{\delta'}s_{\gamma_1} - s_9c_{\gamma_1})\hat{d}_3\end{aligned}$$

These values are substituted into Eqn. (4.12) to give the vector for the lateral offset of the front tyre contact point relative to the rear.

$$\vec{y}'_1 = -Q_x s_{11} \hat{d}_3 - \left( T_{Fz} + T_{Fy} \tan \gamma_1 - \frac{q_3}{\cos \gamma_1} \right) (c_9 c_{\delta'} s_{\gamma_1} - s_9 c_{\gamma_1}) \hat{d}_3$$

Assuming that the camber angles of the front and rear tyres are very similar, i.e.  $\gamma_1 \approx \gamma = q_9$ , then:

$$\vec{y}'_1 = -Q_x s_{11} \hat{d}_3 + \left( T_{Fz} + T_{Fy} \tan q_9 - \frac{q_3}{c_9} \right) s_9 c_9 (1 - c_{\delta'}) \hat{d}_3$$

This is the offset of the front tyre contact point relative to the rear, so if the contact points remain in line, the movement of the front of the bike at the front contact point is the same distance in the opposite direction, or:

$$\vec{y}_1 = Q_x s_{11} \hat{d}_3 - \left( T_{Fz} + T_{Fy} \tan q_9 - \frac{q_3}{c_9} \right) s_9 c_9 (1 - c_{\delta'}) \hat{d}_3$$

At non-zero roll angle, the vertical contact patch deflection must also be taken into account. If the bike were lying on its right side, the lateral offset of the front axle relative to the rear would be  $q_3 - q_4$ . Taking roll angle into account, the

lateral offset becomes:

$$\vec{y}_2 = s_9(q_3 - q_4)\hat{d}_3$$

and the overall lateral displacement is:

$$\vec{y} = \vec{y}_1 + \vec{y}_2 = \left( Q_x s_{11} - \left( T_{Fz} + T_{Fy} \tan q_9 - \frac{q_3}{c_9} \right) s_9 c_9 (1 - c_{\delta'}) + s_9 (q_3 - q_4) \right) \hat{d}_3$$

The frame yaw angle  $q_{13}$  is:

$$q_{13} = \arctan \frac{y}{q_{18}} \approx \frac{y}{q_{18}} \quad \text{because the angle is small}$$

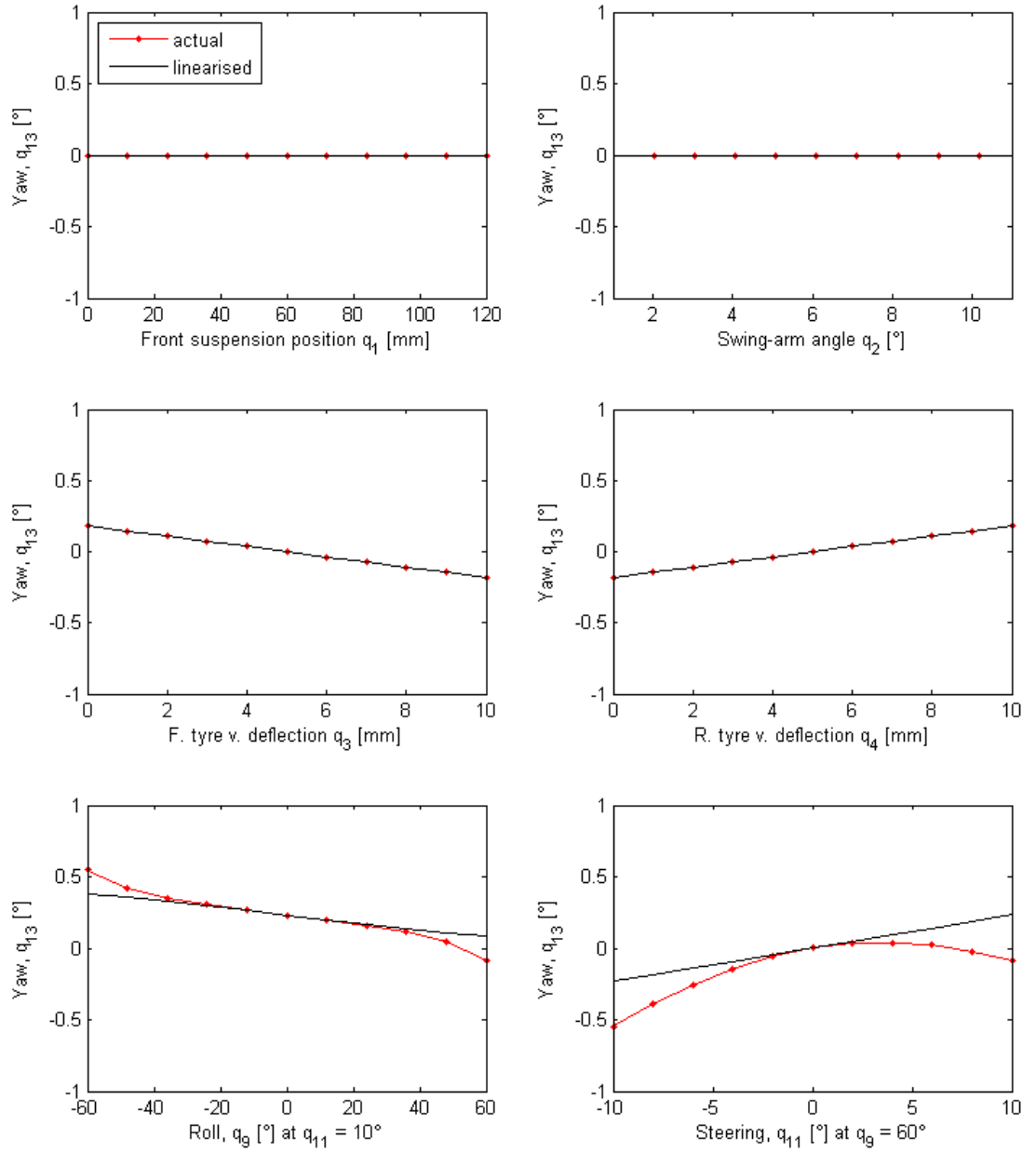


Figure 4.31: Frame yaw angle as a function of  $q_1$ ,  $q_2$ ,  $q_3$ ,  $q_4$ ,  $q_9$  and  $q_{11}$

#### 4.8.7 Frame $y$ position $q_{17}$ as a function of $q_1 \dots q_{11}$

The  $y$  co-ordinate of the main frame mass centre is simply the  $x$  co-ordinate multiplied by minus the yaw angle, plus the lateral offset due to deflection of the rear tyre contact patch. All of the components have already been calculated.

$$q_{17} = -q_{13} q_{15} + q_4 s_9$$

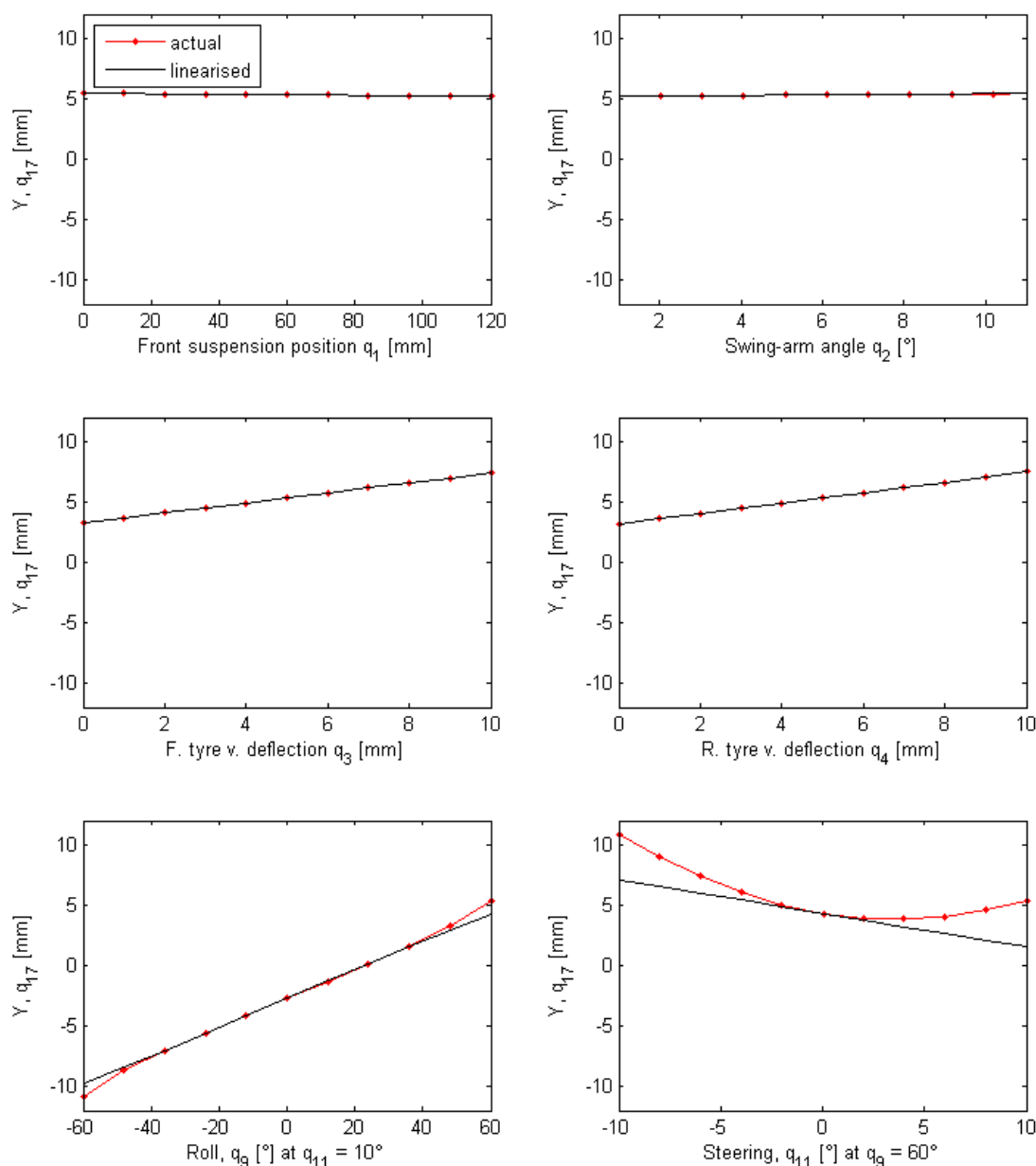


Figure 4.32: Frame Y position from rear tyre contact point as a function of  $q_1$ ,  $q_2$ ,  $q_3$ ,  $q_4$ ,  $q_9$  and  $q_{11}$

#### 4.8.8 Concluding remarks on the main frame position

In the previous sections, the orientation and position of the main frame has been expressed in terms of the relevant<sup>‡</sup> state variables, and the linearity of the relationship between each degree of freedom and each state variable was examined. The calculations have included the effects of tyre profile. In each case, linearisation has been carried out using a first order Taylor series expansion

<sup>‡</sup> Frame position and orientation is independent of many of the state variables.

about the middle of the working range of each state variable. The viability of linearising the relationships is examined by plotting the actual relationships along with the linearised version. It is clear from Figs. 4.27, 4.28 and 4.29 that roll angle cannot be linearised about a single linearisation point as the relationships between roll and each of  $\mu$ ,  $X$  and  $Z$  are highly non-linear. During initialisation, the linearisation constants must be calculated and stored for a range of roll angles and the values scheduled during run-time. This applies to all of the constants, and not just the ones related to roll angle.

Figs. 4.31 and 4.32 show that the yaw angle and  $Y$  position of body  $A$  are non-linear with respect to steering angle  $\delta$  ( $= q_{11}$ ). The graphs cover the range of roll angles  $\pm 60^\circ$  and steering angles  $\pm 10^\circ$  so as to show a range greater than would be expected for road and track conditions. Fig. 4.23 plots measured steering angle versus roll angle for two laps of Nutts Corner circuit. Even on a slow track with a minimum speed of less than 14 m/s, the steering angle is rarely outside the range  $\pm 4^\circ$ , and even less at high roll angles. Taking this into account, the non-linearity due to steering angle, as shown in Figs. 4.31 and 4.32 becomes acceptable, and the linearised functions for steering were used.

Because the linearisation constants are calculated locally in the  $D$  reference frame and then transformed to the  $N$  reference frame, they do not take into account roll and yaw of the  $D$  reference frame itself within the  $N$  reference frame. The roll aspect has been handled by calculating and storing the constants for a range of roll angles during initialisation, and then scheduling the values on each pass through the main program loop. Yaw is handled by calculating the  $G_{10}$  and  $H_{10}$  coefficients as follows:

$$G_{10} = c_9 \quad H_{10} = -s_9$$

So, if the bike is upright, then its pitch rate (the  $H$  coefficients) is unaffected by the global yaw rate  $u_{10}$ , but if it leaned over at  $90^\circ$  to the right, then its local pitch axis is aligned with the global yaw axis and it is pitching at minus the yaw rate. In the case of yaw, (the  $G$  coefficients), when the bike is upright, the local and global yaw axes coincide and the local and global yaw rates are the same,

but if the bike is again leaned over at  $90^\circ$  to the right, then the global yaw rate has no effect on the local yaw.

## 4.9 Sampling rate

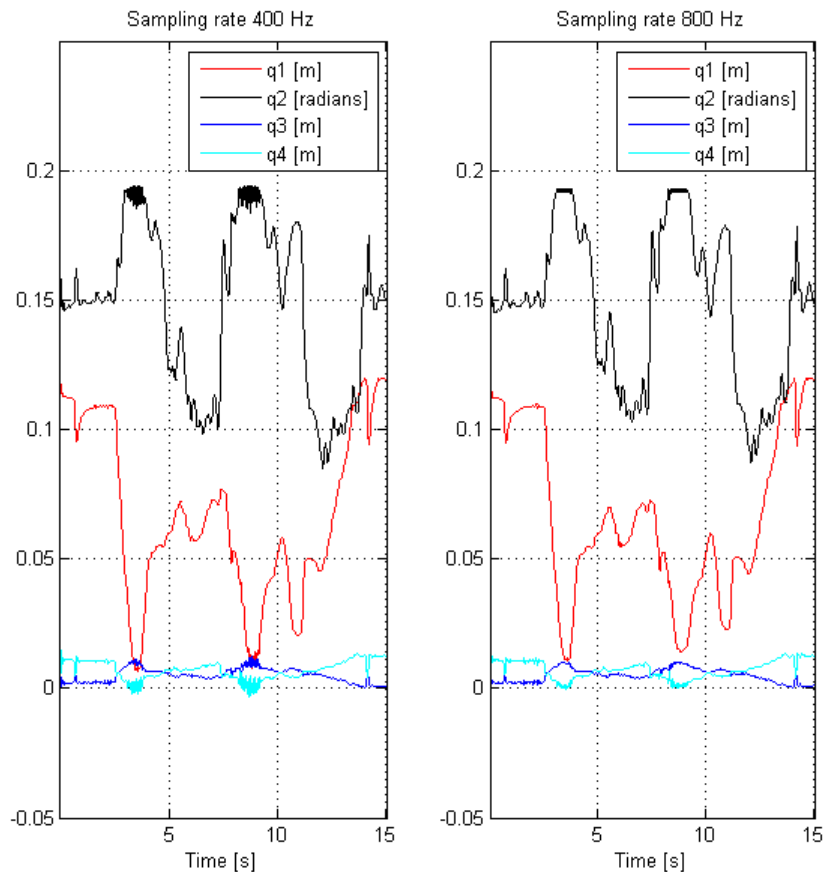


Figure 4.33: The effect of different sampling rates

Before beginning the modelling procedure, the sampling rate should be discussed. Every data channel was recorded at 800 Hz, and it was hoped to run the model at a lower rate by sub-sampling the recorded data. However, the magnitude of the largest real negative eigenvalue was 373.3, giving a Nyquist frequency of 746.6 Hz, so it was necessary to run the model at the full 800 Hz sampling rate. Fig. 4.33 shows the front suspension position  $q_1$ , swing-arm angle  $q_2$  and tyre deflections  $q_3$  and  $q_4$ . The left plot was obtained by running the model at 400 Hz and the right plot was obtained at 800 Hz. The limits of suspension travel are imposed by increasing the spring rates greatly, to mimic the effect of the rubber

bumpers which limit the physical travel. The effect of the lower sample rate can be seen on the swing-arm angle  $q_2$  where it enters the higher spring rate during top-out. The fast dynamics associated with the high spring rate cause the estimated rear suspension position to vibrate at high frequency, and this vibration is propagated to the tyre deflections, which also have fast dynamics due to high spring rates. The performance of the model when run at 800 Hz is acceptable. Using a variable sampling rate for the model was considered, based on monitoring the fastest system pole and ensuring that the Nyquist frequency was always exceeded. However, as explained in Section 4.5 the dynamic behaviour of the tyres and suspension is not included in the system  $A$  matrix, making it more difficult, though not impossible, to monitor the important fast poles when using recorded data.\*\* This limitation is easier to overcome for test functions as is done in Section 7.8 in order to perform root locus analysis.

## 4.10 Modelling procedure

The equations of motion are formulated using Kane's method, and the procedure may be summarised as follows:

1. Define the important points.
2. Select generalised co-ordinates and generalised speeds.
3. Derive velocity and acceleration expressions for the important points.
4. Construct a table of partial velocities.
5. Calculate active forces  $F_r$  and inertial forces  $F_r^*$ , and set  $F_r + F_r^* = 0$ , ( $r = 1, \dots, 11$ ).

The important points have been defined and are shown in Table 4.1. The generalised co-ordinates are shown in Table 4.3 and each generalised speed is the first

---

\*\* The same would apply to running the model in real-time in an embedded system.

time derivative of the corresponding generalised co-ordinate. i.e.

$$u_r = \dot{q}_r \quad (r = 1, \dots, 11)$$

The next step is to derive the velocity and acceleration expressions for the important points.

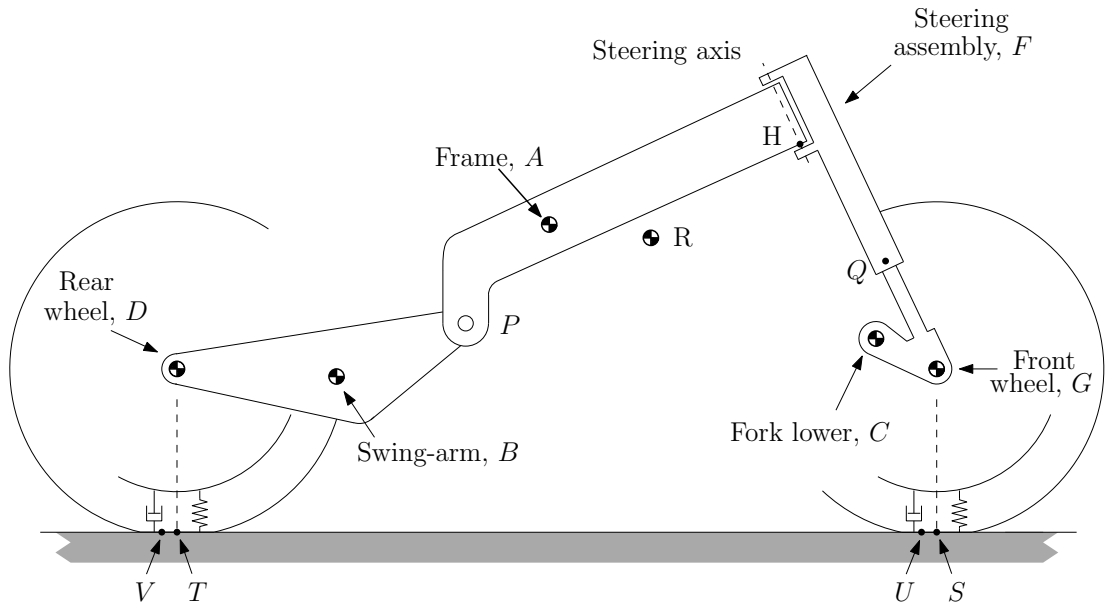


Figure 4.34: The key points of the bike model

#### 4.10.1 Velocity and acceleration expressions for the key points

The velocities of the key points are non-linear functions of the generalised speeds  $u_1, \dots, u_{11}$ , but importantly, most are very nearly linear over the range of motion of the motorcycle. The main frame  $A$  was chosen as the primary rigid body and expressions were derived to describe its motion in terms of the generalised speeds, i.e.

$$\begin{aligned} {}^N\vec{\omega}^A &= f_\omega(u_1, \dots, u_{11}) \\ {}^N\vec{v}^A &= f_v(u_1, \dots, u_{11}) \end{aligned} \quad (4.26)$$

Symbol	Coefficient	Description
$q_{12}$	F	Main frame roll angle
$q_{13}$	G	Main frame yaw angle
$q_{14}$	H	Main frame pitch angle
$q_{15}$	J	Main frame x position
$q_{16}$	K	Main frame z position
$q_{17}$	L	Main frame y position

Table 4.6: Main frame position and orientation

The first step in formulating  $f_\omega$  and  $f_v$  is to express the position and orientation of body  $A$  in terms of  $q_1, \dots, q_{11}$ . This is done first in the  $D$  reference frame. It is useful to introduce additional co-ordinates as shown in Table 4.6, and also a set of coefficients  $F, \dots, L$  such that the position and orientation of body  $A$  can be expressed in the  $D$  reference frame as linear functions of the generalised co-ordinates as follows:

$$\begin{aligned}
 q_{12} &= F_0 + F_1 q_1 + \dots + F_{11} q_{11} \\
 q_{13} &= G_0 + G_1 q_1 + \dots + G_{11} q_{11} \\
 q_{14} &= H_0 + H_1 q_1 + \dots + H_{11} q_{11} \\
 q_{15} &= J_0 + J_1 q_1 + \dots + J_{11} q_{11} \\
 q_{16} &= K_0 + K_1 q_1 + \dots + K_{11} q_{11} \\
 q_{17} &= L_0 + L_1 q_1 + \dots + L_{11} q_{11}
 \end{aligned} \tag{4.27}$$

Given that  $u_n = \dot{q}_n$  for all  $n$ , and by taking the first derivatives of Eqns. (4.27) it can be stated that the angular and translational velocities of body A are:

$$\begin{aligned}
{}^D\vec{\omega}^A &= u_{12}\hat{d}_1 + u_{13}\hat{d}_2 + u_{14}\hat{d}_3 \\
&= (F_1u_1 + \cdots + F_{11}u_{11})\hat{d}_1 \\
&\quad + (G_1u_1 + \cdots + G_{11}u_{11})\hat{d}_2 \\
&\quad + (H_1u_1 + \cdots + H_{11}u_{11})\hat{d}_3 \\
{}^D\vec{v}^A &= u_{15}\hat{d}_1 + u_{16}\hat{d}_2 + u_{17}\hat{d}_3 \\
&= (J_1u_1 + \cdots + J_{11}u_{11})\hat{d}_1 \\
&\quad + (K_1u_1 + \cdots + K_{11}u_{11})\hat{d}_2 \\
&\quad + (L_1u_1 + \cdots + L_{11}u_{11})\hat{d}_3
\end{aligned}$$

Taking the first two transformations in Table 4.4, let:

$$dm = \begin{bmatrix} 1 & 0 & 0 \\ 0 & c_9 & s_9 \\ 0 & -s_9 & c_9 \end{bmatrix}, \quad mn = \begin{bmatrix} c_{10} & 0 & -s_{10} \\ 0 & 1 & 0 \\ s_{10} & 0 & c_{10} \end{bmatrix}$$

Then Eqns. (4.26) become:

$$\begin{aligned}
{}^N\vec{\omega}^A &= {}^D\vec{\omega}^A \cdot dm \cdot mn \\
{}^N\vec{v}^A &= {}^D\vec{v}^A \cdot dm \cdot mn
\end{aligned} \tag{4.28}$$

The coefficients in Eqns. (4.27) are functions of the bike geometric parameters, and were derived in Section 4.8 by first deriving the actual expressions for  $q_{12}, \dots, q_{17}$  and then for each expression, applying a first order Taylor series expansion for each of the state variables that appear in those equations. The expansions were performed about the mid-point of the operating range of each state variable. The linearised expressions were validated by graphing them along with the actual non-linear expressions over the operating range. These plots are shown in Figs. 4.27, 4.28, 4.29, 4.31 and 4.32. Not every coefficient needs to be

calculated in this way, and many are zero. For example, the roll angle of the main frame depends only on  $q_9$ , so  $F_9 = 1$  and  $F_n = 0$  for other values of  $n$ . On inspecting the plots, it is clear that many of the parameters are camber dependent and this is partly due to the migration of the tyre contact points as the bike leans over. These parameters are calculated and stored during initialisation and then scheduled, based on camber angle. Note that, unless otherwise stated, the plots represent a roll angle of  $60^\circ$  and steering angle of  $10^\circ$ , the idea being to test linearity at the edge to the operating range at road and race track speeds. Unless otherwise stated, the front and rear contact patch deflections used in the plots are  $5 \text{ mm}$ .

Once the expressions for  ${}^N\vec{\omega}^A$  and  ${}^N\vec{v}^A$  have been found, the expressions for the other key points may be derived. For example, the co-ordinates of body  $A$  mass centre relative to the swing-arm pivot  $P$  in reference frame  $A$  are  $(a_x, a_y, a_z)$ . The vector from  $A$  to  $P$  is:

$${}^A\vec{r}^{AP} = -a_x\hat{a}_1 - a_z\hat{a}_2 - a_y\hat{a}_3$$

and using the transformation from  $A$  to  $D$ :

$${}^D\vec{r}^{AP} = {}^A\vec{r}^{AP} \cdot ad$$

Then the velocity of point  $P$  in reference frame  $D$  is:

$${}^D\vec{v}^P = {}^D\vec{v}^A + {}^D\vec{\omega}^A \times {}^D\vec{r}^{AP} \quad (4.29)$$

and the velocity in reference frame  $N$  is:

$${}^N\vec{v}^P = {}^D\vec{v}^P \cdot dm \cdot mn \quad (4.30)$$

Proceeding sequentially in this way, the velocity expression for every important point was found. Angular velocity expressions for the bodies are found in a similar way. For example, the angular velocity of the swing-arm is found as follows, remembering that  $u_2\hat{a}_3 = \dot{q}_2\hat{a}_3$  is the angular velocity of the swing-arm

relative to the main frame:

$$\begin{aligned} {}^D\vec{\omega}^B &= {}^D\vec{\omega}^A + \begin{bmatrix} 0 & 0 & u_2 \end{bmatrix} \cdot ad \\ {}^N\vec{\omega}^B &= {}^D\vec{\omega}^B \cdot dm \cdot mn \end{aligned}$$

It is easier to do the calculations in the  $D$  reference frame and then convert the result to the  $N$  reference frame. Differentiating the velocity and angular velocity expressions leads to expressions for acceleration. Note that the vectors  $\hat{d}_1$ ,  $\hat{d}_2$  and  $\hat{d}_3$  are themselves time dependent, so they are an integral part of the expressions to be differentiated. The sequence of calculations in the  $D$  reference frame is as follows:

Body A

$$\begin{aligned} {}^D\vec{\omega}^A &= F_9 u_9 \hat{d}_1 \\ &+ (G_3 u_3 + G_4 u_4 + G_{10} u_{10} + G_{11} u_{11}) \hat{d}_2 \\ &+ (H_1 u_1 + H_2 u_2 + H_3 u_3 + H_4 u_4 + H_{10} u_{10} + H_{11} u_{11}) \hat{d}_3 \\ {}^D\vec{v}^A &= (J_1 u_1 + J_2 u_2 + J_3 u_3 + J_4 u_4 + J_7 u_7 + J_8 u_8 + J_{11} u_{11}) \hat{d}_1 \\ &+ (K_1 u_1 + K_2 u_2 + K_3 u_3 + K_4 u_4 + K_7 u_7 + K_8 u_8 + K_{11} u_{11}) \hat{d}_2 \\ &+ (L_3 u_3 + L_4 u_4 + L_7 u_7 + L_8 u_8 + L_9 u_9 + L_{11} u_{11}) \hat{d}_3 \end{aligned}$$

Point P

$$\begin{aligned} {}^D\vec{r}^{AP} &= \begin{bmatrix} P_x & P_z & -P_y \end{bmatrix} \\ {}^D\vec{v}^P &= {}^D\vec{v}^A + {}^D\vec{\omega}^A \times {}^D\vec{r}^{AP} \end{aligned}$$

Point H

$$\begin{aligned} {}^D\vec{r}^{AH} &= \begin{bmatrix} H_x & H_z & -H_y \end{bmatrix} \\ {}^D\vec{v}^H &= {}^D\vec{v}^A + {}^D\vec{\omega}^A \times {}^D\vec{r}^{AH} \end{aligned}$$

Point R

$$D\vec{r}^{AR} = \begin{bmatrix} R_x & R_z & -R_y \end{bmatrix}$$

$$D\vec{v}^R = D\vec{v}^A + D\vec{\omega}^A \times D\vec{r}^{AR}$$

Body B

$$D\vec{r}^{PB} = \begin{bmatrix} B_x & B_z & 0 \end{bmatrix} \cdot ba \cdot ad$$

$$D\vec{\omega}^B = D\vec{\omega}^A + \begin{bmatrix} 0 & 0 & u_2 \end{bmatrix} \cdot ad$$

$$D\vec{v}^B = D\vec{v}^P + D\vec{\omega}^B \times D\vec{r}^{PB}$$

Body D

$$D\vec{r}^{PD} = \begin{bmatrix} R_a & 0 & 0 \end{bmatrix} \cdot ba \cdot ad$$

$$D\vec{\omega}^D = D\vec{\omega}^B + \begin{bmatrix} 0 & 0 & u_6 \end{bmatrix}$$

$$D\vec{v}^D = D\vec{v}^P + D\vec{\omega}^D \times D\vec{r}^{PD}$$

Body F

$$D\vec{r}^{HF} = \begin{bmatrix} F_x & F_z & 0 \end{bmatrix} \cdot fe \cdot ea \cdot ad$$

$$D\vec{\omega}^F = D\vec{\omega}^A + \begin{bmatrix} 0 & u_{11} & 0 \end{bmatrix} \cdot fe \cdot ea \cdot ad$$

$$D\vec{v}^F = D\vec{v}^H + D\vec{\omega}^F \times D\vec{r}^{HF}$$

Point Q

$$D\vec{r}^{HQ} = \begin{bmatrix} Q_x & Q_z & 0 \end{bmatrix} \cdot fe \cdot ea \cdot ad$$

$$D\vec{v}^Q = D\vec{v}^H + D\vec{\omega}^F \times D\vec{r}^{HQ}$$

Body G

$${}^D\vec{r}^{QG} = \begin{bmatrix} 0 & -q_1 & 0 \end{bmatrix} \cdot fe \cdot ea \cdot ad$$

$${}^D\vec{\omega}^G = {}^D\vec{\omega}^F + \begin{bmatrix} 0 & 0 & u_5 \end{bmatrix} \cdot fe \cdot ea \cdot ad$$

$${}^D\vec{v}^G = {}^D\vec{v}^Q + \begin{bmatrix} 0 & -u_1 & 0 \end{bmatrix} \cdot fe \cdot ea \cdot ad + {}^D\vec{\omega}^F \times {}^D\vec{r}^{QG}$$

Body C

$${}^D\vec{r}^{GC} = \begin{bmatrix} C_x & C_z & 0 \end{bmatrix} \cdot fe \cdot ea \cdot ad$$

$${}^D\vec{\omega}^C = {}^D\vec{\omega}^F$$

$${}^D\vec{v}^C = {}^D\vec{v}^G + {}^D\vec{\omega}^C \times {}^D\vec{r}^{GC}$$

Point S

$${}^D\vec{r}^{GS} = \begin{bmatrix} 0 & -T_{fz} & T_{fy} \end{bmatrix} \cdot gf \cdot fe \cdot ea \cdot ad + \begin{bmatrix} 0 & q_3 & 0 \end{bmatrix} \cdot hm \cdot md$$

$${}^F\vec{\omega}^F = {}^F\vec{\omega}^D \cdot da \cdot ae \cdot ef$$

$$\omega_S = \begin{bmatrix} {}^F\vec{\omega}_1^F & {}^F\vec{\omega}_2^F & 0 \end{bmatrix} \cdot fe \cdot ea \cdot ad$$

$${}^D\vec{v}^S = {}^D\vec{v}^G + \omega_S \times {}^D\vec{r}^{GS}$$

Point U

$${}^D\vec{r}^{SU} = \begin{bmatrix} -T_{pf} & 0 & 0 \end{bmatrix} \cdot hm \cdot md$$

$${}^H\vec{\omega}^F = {}^D\vec{\omega}^F \cdot dm \cdot mh$$

$$\omega_U = \begin{bmatrix} 0 & {}^H\vec{\omega}_2^F & 0 \end{bmatrix} \cdot hm \cdot md$$

$${}^D\vec{v}^U = {}^D\vec{v}^S + \omega_U \times {}^D\vec{r}^{SU}$$

Point T

$$\begin{aligned}
{}^D\vec{r}^{DT} &= \begin{bmatrix} 0 & -T_{rz} & T_{ry} \end{bmatrix} + \begin{bmatrix} 0 & q_4 & 0 \end{bmatrix} \cdot md \\
\omega_T &= \begin{bmatrix} {}^D\vec{\omega}_1^D & {}^D\vec{\omega}_2^D & 0 \end{bmatrix} \\
{}^D\vec{v}^T &= {}^D\vec{v}^D + \omega_T \times {}^D\vec{r}^{DT}
\end{aligned}$$

Point V

$$\begin{aligned}
{}^D\vec{r}^{TV} &= \begin{bmatrix} -T_{pr} & 0 & 0 \end{bmatrix} \\
{}^M\vec{\omega}^D &= {}^D\vec{\omega}^D \cdot dm \\
{}^D\vec{v}^V &= {}^D\vec{v}^T + \begin{bmatrix} 0 & {}^M\vec{\omega}_2^D & 0 \end{bmatrix} \times {}^D\vec{r}^{TV}
\end{aligned}$$

The angular velocity and velocity expressions for each body and point,  ${}^D\vec{\omega}^A$ ,  ${}^D\vec{v}^A$ , etc. are converted to the  $N$  reference frame using the transformations in Table 4.4 to get  ${}^N\vec{\omega}^A$ ,  ${}^N\vec{v}^A$  and so on. The partial velocities associated with each body and point are then found, as explained in Section 3.4. This is performed here for body  $A$  to show the procedure, but the expressions for the other bodies and points are too complex to include here and were calculated using Wolfram Mathematica<sup>®</sup>.

$$\begin{aligned}
{}^N\vec{\omega}^A &= {}^D\vec{\omega}^A \cdot dm \cdot mn \\
&= (F_9 u_9 c_{10} + s_{10}((G_3 u_3 + G_4 u_4 + G_{10} u_{10} + G_{11} u_{11}))s_9 \\
&\quad + (H_1 u_1 + H_2 u_2 + H_3 u_3 + H_4 u_4 + H_{10} u_{10} + H_{11} u_{11})c_9))\hat{n}_1 \\
&\quad + ((G_3 u_3 + G_4 u_4 + G_{10} u_{10} + G_{11} u_{11})c_9 \\
&\quad - (H_1 u_1 + H_2 u_2 + H_3 u_3 + H_4 u_4 + H_{10} u_{10} + H_{11} u_{11})s_9)\hat{n}_2 \\
&\quad + (c_{10}((G_3 u_3 + G_4 u_4 + G_{10} u_{10} + G_{11} u_{11}))s_9 \\
&\quad + (H_1 u_1 + H_2 u_2 + H_3 u_3 + H_4 u_4 + H_{10} u_{10} + H_{11} u_{11})c_9) - F_9 u_9 s_{10})\hat{n}_3
\end{aligned}$$

$$\begin{aligned}
{}^N\vec{v}^A &= D\vec{v}^A \cdot dm \cdot mn \\
&= ((J_1u_1 + J_2u_2 + J_3u_3 + J_4u_4 + J_7u_7 + J_8u_8 + J_{11}u_{11})c_{10} \\
&\quad + s_{10}((K_1u_1 + K_2u_2 + K_3u_3 + K_4u_4 + K_7u_7 + K_8u_8 + K_{11}u_{11})s_9 \\
&\quad + (L_3u_3 + L_4u_4 + L_7u_7 + L_8u_8 + L_9u_9 + L_{11}u_{11})c_9))\hat{n}_1 \\
&\quad + ((K_1u_1 + K_2u_2 + K_3u_3 + K_4u_4 + K_7u_7 + K_8u_8 + K_{11}u_{11})c_9 \\
&\quad - (L_3u_3 + L_4u_4 + L_7u_7 + L_8u_8 + L_9u_9 + L_{11}u_{11})s_9)\hat{n}_2 \\
&\quad + (c_{10}((K_1u_1 + K_2u_2 + K_3u_3 + K_4u_4 + K_7u_7 + K_8u_8 + K_{11}u_{11})s_9 \\
&\quad + (L_3u_3 + L_4u_4 + L_7u_7 + L_8u_8 + L_9u_9 + L_{11}u_{11})c_9) \\
&\quad - (J_1u_1 + J_2u_2 + J_3u_3 + J_4u_4 + J_7u_7 + J_8u_8 + J_{11}u_{11})s_{10})\hat{n}_3
\end{aligned}$$

The partial angular velocities are:

$$\begin{aligned}
{}^N\vec{\omega}_1^A &= H_1s_{10}c_9\hat{n}_1 - H_1s_9\hat{n}_2 + H_1c_9c_{10}\hat{n}_3 \\
{}^N\vec{\omega}_2^A &= H_2s_{10}c_9\hat{n}_1 - H_2s_9\hat{n}_2 + H_2c_9c_{10}\hat{n}_3 \\
{}^N\vec{\omega}_3^A &= (G_3s_9s_{10} + H_3s_{10}c_9)\hat{n}_1 + (G_3c_9 - H_3s_9)\hat{n}_2 + (G_3s_9c_{10} + H_3c_9c_{10})\hat{n}_3 \\
{}^N\vec{\omega}_4^A &= (G_4s_9s_{10} + H_4s_{10}c_9)\hat{n}_1 + (G_4c_9 - H_4s_9)\hat{n}_2 + (G_4s_9c_{10} + H_4c_9c_{10})\hat{n}_3 \\
{}^N\vec{\omega}_9^A &= F_9c_{10}\hat{n}_1 - F_9s_{10}\hat{n}_3 \\
{}^N\vec{\omega}_{10}^A &= (G_{10}s_9s_{10} + H_{10}s_{10}c_9)\hat{n}_1 + (G_{10}c_9 - H_{10}s_9)\hat{n}_2 + (G_{10}s_9c_{10} + H_{10}c_9c_{10})\hat{n}_3 \\
{}^N\vec{\omega}_{11}^A &= (G_{11}s_9s_{10} + H_{11}s_{10}c_9)\hat{n}_1 + (G_{11}c_9 - H_{11}s_9)\hat{n}_2 + (G_{11}s_9c_{10} + H_{11}c_9c_{10})\hat{n}_3
\end{aligned}$$

and the partial velocities are:

$${}^N\vec{v}_1^A = (J_1c_{10} + K_1s_9s_{10})\hat{n}_1 + K_1c_9\hat{n}_2 + (K_1s_9c_{10} - J_1s_{10})\hat{n}_3$$

$${}^N\vec{v}_2^A = (J_2c_{10} + K_2s_9s_{10})\hat{n}_1 + K_2c_9\hat{n}_2 + (K_2s_9c_{10} - J_2s_{10})\hat{n}_3$$

$$\begin{aligned} {}^N\vec{v}_3^A &= (J_3c_{10} + K_3s_9s_{10} + L_3s_{10}c_9)\hat{n}_1 + (K_3c_9 - L_3s_9)\hat{n}_2 \\ &\quad + (-J_3s_{10} + K_3s_9c_{10} + L_3c_9c_{10})\hat{n}_3 \end{aligned}$$

$$\begin{aligned} {}^N\vec{v}_4^A &= (J_4c_{10} + K_4s_9s_{10} + L_4s_{10}c_9)\hat{n}_1 + (K_4c_9 - L_4s_9)\hat{n}_2 \\ &\quad + (-J_4s_{10} + K_4s_9c_{10} + L_4c_9c_{10})\hat{n}_3 \end{aligned}$$

$$\begin{aligned} {}^N\vec{v}_7^A &= (J_7c_{10} + K_7s_9s_{10} + L_7s_{10}c_9)\hat{n}_1 + (K_7c_9 - L_7s_9)\hat{n}_2 \\ &\quad + (-J_7s_{10} + K_7s_9c_{10} + L_7c_9c_{10})\hat{n}_3 \end{aligned}$$

$$\begin{aligned} {}^N\vec{v}_8^A &= (J_8c_{10} + K_8s_9s_{10} + L_8s_{10}c_9)\hat{n}_1 + (K_8c_9 - L_8s_9)\hat{n}_2 \\ &\quad + (-J_8s_{10} + K_8s_9c_{10} + L_8c_9c_{10})\hat{n}_3 \end{aligned}$$

$${}^N\vec{v}_9^A = L_9s_{10}c_9\hat{n}_1 - L_9s_9\hat{n}_2 + L_9c_9c_{10}\hat{n}_3$$

$$\begin{aligned} {}^N\vec{v}_{11}^A &= (J_{11}c_{10} + K_{11}s_9s_{10} + L_{11}s_{10}c_9)\hat{n}_1 + (K_{11}c_9 - L_{11}s_9)\hat{n}_2 \\ &\quad + (-J_{11}s_{10} + K_{11}s_9c_{10} + L_{11}c_9c_{10})\hat{n}_3 \end{aligned}$$

## 4.10.2 Kane's Equations

The final step in formulating the equations of motion is to apply Kane's equations, which are as follows. The generalised active force  $F_r$  (for two bodies, A and B) is given by:

$$F_r = \sum_r \left( \vec{F}_A \cdot {}^N\vec{v}_r^A + \vec{T}_A \cdot {}^N\vec{\omega}_r^A + \vec{F}_B \cdot {}^N\vec{v}_r^B + \vec{T}_B \cdot {}^N\vec{\omega}_r^B \right)$$

where  $F$  and  $T$  denote force and torque respectively. The generalised inertial force  $F_r^*$  is given by:

$$\begin{aligned}
 F_r^* = \sum_r \left( \right. \\
 & - M_A {}^N \vec{a}^A \cdot {}^N \vec{v}_r^A - \left( {}^N \vec{\alpha}^A \cdot \vec{I}_A + {}^N \vec{\omega}^A \times \vec{I}_A \cdot {}^N \vec{\omega}^A \right) \cdot {}^N \vec{\omega}_r^A \\
 & \left. - M_B {}^N \vec{a}^B \cdot {}^N \vec{v}_r^B - \left( {}^N \vec{\alpha}^B \cdot \vec{I}_B + {}^N \vec{\omega}^B \times \vec{I}_B \cdot {}^N \vec{\omega}^B \right) \cdot {}^N \vec{\omega}_r^B \right) \quad (4.31)
 \end{aligned}$$

The components of Kane's equations are the velocities, partial velocities and accelerations, translational and angular, which have been derived. In this case,  $r = 1, \dots, 11$ . The active and inertial forces sum to zero

$$F_r + F_r^* = 0 \quad (4.32)$$

Eqn. (4.32) looks simple, but it is necessary to examine  $F_r$  and  $F_r^*$  to assess the importance of the terms. The mean absolute values of all state variables and inputs were calculated for a lap of the race track and are shown in Tables 4.7 and 4.8.  $F_r$  and  $F_r^*$  were evaluated for the input values in Table 4.8 and the generalised co-ordinate values  $q_1, \dots, q_{11}$  in Table 4.7 and are as follows:

$$\begin{aligned}
 F_1 = & 271.864 - 2.22 \times 10^{-16} u_1 + 1.11 \times 10^{-16} u_2 + 0.865 u_3 - 0.865 u_4 \\
 & + 1.159 u_9 - 2.938 u_{11}
 \end{aligned}$$

$$\begin{aligned}
F_1^* = & -79.6684\dot{u}_1 - 18.519\dot{u}_2 + 244.277\dot{u}_3 - 157.001\dot{u}_4 - 0.869316\dot{u}_5 - 0.93141\dot{u}_6 \\
& - 1.36377\dot{u}_9 + 0.0782136\dot{u}_{11} \\
& - 5.7152u_1^2 + 4.07721u_1u_2 + 83.6889u_1u_3 - 83.6889u_1u_4 \\
& - 0.213172u_2^2 - 7.20986u_2u_3 + 7.20986u_2u_4 \\
& - 84.7277u_3^2 + 169.455u_3u_4 + 192.419u_3u_9 - 38.7177u_3u_{10} + 3.24419u_3u_{11} \\
& - 84.7277u_4^2 - 51.5702u_4u_9 + 103.895u_4u_{10} - 3.24419u_4u_{11} \\
& + 201.484u_9^2 + 124.097u_9u_{10} - 21.5796u_9u_{11} \\
& - 0.423604u_{11}^2 - 9.04845u_{10}u_{11}
\end{aligned} \tag{4.33}$$

$F_1^*$  begins with a linear combination of the rates of change of the generalised speeds  $\dot{u}_1, \dots, \dot{u}_{11}$ .  $F_n^*$  are inertial forces, so these acceleration terms are to be expected. The rest of the expression is made up of a linear combination of products of generalised speeds. The magnitude of each of these terms must be examined with a view to simplifying the expression by discarding insignificant terms. The aim is to produce a model which is linear to the greatest extent possible without loss of fidelity, so only insignificant terms will be discarded. The generalised speeds from Table 4.7 are now substituted into Eqn. (4.33) to get Eqn. (4.34), which is arranged in the same order.

$$\begin{aligned}
F_1^* = & -79.6684\dot{u}_1 - 18.519\dot{u}_2 + 244.277\dot{u}_3 - 157.001\dot{u}_4 - 0.869316\dot{u}_5 - 0.93141\dot{u}_6 \\
& - 1.36377\dot{u}_9 + 0.0782136\dot{u}_{11} \\
& - 0.0083 + 0.0105 + 0.0391 - 0.0524 \\
& - 0.0010 - 0.0060 + 0.0080 \\
& - 0.0128 + 0.0341 + 0.7427 - 0.1159 + 0.0249 \\
& - 0.0228 - 0.2663 + 0.4161 - 0.0333 \\
& + 19.9284 + 9.5207 - 4.2409 \\
& - 0.1654 - 1.3793
\end{aligned} \tag{4.34}$$

The derivatives of the generalised speeds are accelerations associated with inertial forces and must be included. It is clear from Eqn. (4.34) that certain other terms,

especially those containing roll rate,  $u_9$ , are significant and these must also be included. The largest of these is  $u_9^2$ , which is the roll rate squared, and this is associated with the centripetal acceleration affecting the bodies as the roll angle changes. Centripetal acceleration  $a = r\omega^2$  where  $r$  is the radius and  $\omega$  is the angular velocity or roll rate. When the  $u_9^2$  term is excluded from the model, the estimated vertical position of the bike in fast direction changes is low compared to the measured value. The other term which is included in the model is the  $u_{10}u_{11}$  term, which has a value of  $-1.3793$  in Eqn. (4.34). When the expressions  $F_r$  and  $F_r^*$  are examined in the same way for other values of  $r$ , only the terms containing  $u_9$  and the  $u_{10}u_{11}$  term are significant.

n	$q_n$	$u_n$
1	0.076	0.038
2	0.137	0.068
3	0.005	0.012
4	0.008	0.016
5	2377.0	113.75
6	2356.4	110.13
7	167.80	29.26
8	59.55	11.10
9	0.493	0.314
10	3.128	0.244
11	0.028	0.625

Table 4.7: Mean absolute value of state variables during one lap

$u_{in_n}$	Input	Value	$u_{in_n}$	Input	Value	$u_{in_n}$	Input	Value
$u_{in_1}$	$F_{fwx}$	296.6	$u_{in_8}$	$F_{drag}$	330.9	$u_{in_{15}}$	$T_{fwy}$	73.8
$u_{in_2}$	$F_{fwy}$	833.7	$u_{in_9}$	$F_{fork}$	1225	$u_{in_{16}}$	$T_{fwz}$	7.7
$u_{in_3}$	$F_{fwz}$	1149.6	$u_{in_{10}}$	$T_{mfx}$	3.8	$u_{in_{17}}$	$T_{rwx}$	78.6
$u_{in_4}$	$F_{rwx}$	1011.5	$u_{in_{11}}$	$T_{mfy}$	670.2	$u_{in_{18}}$	$T_{rwy}$	299.4
$u_{in_5}$	$F_{rwy}$	832.5	$u_{in_{12}}$	$T_{mfz}$	7.6	$u_{in_{19}}$	$T_{rwz}$	21.8
$u_{in_6}$	$F_{rwz}$	1526.9	$u_{in_{13}}$	$T_{say}$	704.5	$u_{in_{20}}$	$T_{steer}$	102.0
$u_{in_7}$	$F_{lift}$	6.1	$u_{in_{14}}$	$T_{fwx}$	45.3	$u_{in_{21}}$	$g$	9.81

Table 4.8: Mean absolute value of inputs during one lap

$u_{in_n}$	Symbol	Description
$u_{in_1}$	$F_{fwx}$	Front wheel $x$ force
$u_{in_2}$	$F_{fwy}$	Front wheel $y$ force
$u_{in_3}$	$F_{f wz}$	Front wheel $z$ force
$u_{in_4}$	$F_{rwx}$	Rear wheel $x$ force
$u_{in_5}$	$F_{rwy}$	Rear wheel $y$ force
$u_{in_6}$	$F_{r wz}$	Rear wheel $z$ force
$u_{in_7}$	$F_{lift}$	Aerodynamic lift force
$u_{in_8}$	$F_{drag}$	Aerodynamic drag force
$u_{in_9}$	$F_{fork}$	Front suspension force
$u_{in_{10}}$	$T_{mf x}$	Main frame $x$ torque
$u_{in_{11}}$	$T_{mf y}$	Main frame $y$ torque
$u_{in_{12}}$	$T_{mf z}$	Main frame $z$ torque
$u_{in_{13}}$	$T_{say}$	Swing-arm $y$ torque
$u_{in_{14}}$	$T_{f wx}$	Front wheel $x$ torque
$u_{in_{15}}$	$T_{f wy}$	Front wheel $y$ torque
$u_{in_{16}}$	$T_{f wz}$	Front wheel $z$ torque
$u_{in_{17}}$	$T_{r wx}$	Rear wheel $x$ torque
$u_{in_{18}}$	$T_{r wy}$	Rear wheel $y$ torque
$u_{in_{19}}$	$T_{r wz}$	Rear wheel $z$ torque
$u_{in_{20}}$	$T_{steer}$	Steering torque
$u_{in_{21}}$	$g$	Acceleration due to gravity

Table 4.9: Input vector  $u_{in}$



containing  $\beta_{1,1} \dots \beta_{11,21}$ . So:

$$\begin{bmatrix} f_1 \\ \vdots \\ f_{11} \end{bmatrix} = \begin{bmatrix} \alpha_{1,1} & \dots & \alpha_{1,22} \\ \vdots & \ddots & \vdots \\ \alpha_{11,1} & \dots & \alpha_{11,22} \end{bmatrix} \begin{bmatrix} u_1 \\ q_1 \\ \vdots \\ u_{11} \\ q_{11} \end{bmatrix} \\ + \begin{bmatrix} \beta_{1,1} & \dots & \beta_{1,21} \\ \vdots & \ddots & \vdots \\ \beta_{11,1} & \dots & \beta_{11,21} \end{bmatrix} \begin{bmatrix} u_{in_1} \\ \vdots \\ u_{in_{21}} \end{bmatrix} + \begin{bmatrix} \gamma_{1,1} & \dots & \gamma_{1,4} \\ \vdots & \ddots & \vdots \\ \gamma_{11,1} & \dots & \beta_{11,4} \end{bmatrix} \begin{bmatrix} u_9^2 \\ u_9 u_{10} \\ u_9 u_{11} \\ u_{10} u_{11} \end{bmatrix}$$

or:

$$f = \alpha x + \beta u_{in} + \gamma w \quad (4.36)$$

Combining Eqns. (4.35) and (4.36) gives the equation:

$$\begin{aligned} \dot{u} &= -K^{-1}\alpha x - K^{-1}\beta u_{in} - K^{-1}\gamma w \\ &= A'x + B'u_{in} + R'w \end{aligned} \quad (4.37)$$

where  $A' = -K^{-1}\alpha$ ,  $B' = -K^{-1}\beta$  and  $R' = -K^{-1}\gamma$ . In order to create the state space matrices  $A$  and  $B$ , and the matrix  $R$ , rows must be added as shown, to

express  $\dot{q}_n = u_n$  for  $n = 1 \dots 11$ .

$$\begin{aligned}
 \begin{bmatrix} \dot{u}_1 \\ \dot{q}_1 \\ \vdots \\ \dot{u}_{11} \\ \dot{q}_{11} \end{bmatrix} &= \begin{bmatrix} A'_{1,1} & A'_{1,2} & \dots & A'_{1,22} \\ 1 & 0 & \dots & 0 \\ A'_{2,1} & A'_{2,2} & \dots & A'_{2,22} \\ \vdots & & \ddots & \vdots \\ A'_{11,1} & A'_{11,2} & \dots & A'_{11,22} \end{bmatrix} \begin{bmatrix} u_1 \\ q_1 \\ \vdots \\ u_{11} \\ q_{11} \end{bmatrix} \\
 &+ \begin{bmatrix} B'_{1,1} & \dots & B'_{1,21} \\ 0 & \dots & 0 \\ B'_{2,1} & \dots & B'_{2,21} \\ \vdots & \ddots & \vdots \\ B'_{11,1} & \dots & B'_{11,21} \end{bmatrix} \begin{bmatrix} u_{in_1} \\ u_{in_2} \\ u_{in_3} \\ \vdots \\ u_{in_{21}} \end{bmatrix} + \begin{bmatrix} R'_{1,1} & \dots & R'_{1,4} \\ 0 & \dots & 0 \\ R'_{2,1} & \dots & R'_{2,4} \\ \vdots & \ddots & \vdots \\ R'_{11,1} & \dots & R'_{11,4} \end{bmatrix} \begin{bmatrix} u_9^2 \\ u_9 u_{10} \\ u_9 u_{11} \\ u_{10} u_{11} \end{bmatrix}
 \end{aligned}$$

This is the continuous time state equation

$$\dot{x} = Ax + Bu_{in} + Rw \quad (4.38)$$

The matrices  $K$ ,  $\alpha$ ,  $\beta$  and  $\gamma$  are calculated symbolically in Mathematica<sup>®</sup>. Symbolic expressions for the tyre contact patch and axle velocities  ${}^H\vec{v}^S$ ,  ${}^M\vec{v}^T$ ,  ${}^H\vec{v}^G$  and  ${}^M\vec{v}^D$  are calculated similarly. These are used as inputs to the tyre model. Body  $A$  velocity and acceleration,  ${}^M\vec{v}^A$  and  ${}^M\vec{a}^A$  are also calculated. The velocity of body  $A$  provides road speed and the acceleration of body  $A$  is used in calculating the reactive shear forces at the tyre contact patches due to acceleration. These symbolic calculations need to be repeated only when the structure of the model changes in some way. Perl scripts convert the Mathematica<sup>®</sup> output files to Matlab and C code.

## 4.11 The state output matrix, $C$

The state output matrix  $C$  has eight rows, which are as follows:

1. Front suspension position,  $q_1$

2. Swing-arm angle,  $q_2$
3. Angular velocity about longitudinal axis in reference frame  $A$ ,  $\omega_1$
4. Angular velocity about vertical axis in reference frame  $A$ ,  $\omega_2$
5. Angular velocity about transverse axis in reference frame  $A$ ,  $\omega_3$
6. Front wheel angular velocity,  $u_5$
7. Rear wheel angular velocity,  $u_6$
8. Roll angle,  $q_9$

The non-zero entries in  $C$  are shown in Table 4.10. The estimated outputs of

	1	2	3	4	5	7	9	11	17	18	19	21
1		1										
2				1								
3					$G_3 s_{14}$	$G_4 s_{14}$			$F_9 c_{14}$		$G_{10} s_{14}$	$G_{11} s_{14}$
4					$G_3 c_{14}$	$G_4 c_{14}$			$-F_9 s_{14}$		$G_{10} c_{14}$	$G_{11} c_{14}$
5	$H_1$		$H_2$		$H_3$	$H_4$					$H_{10}$	$H_{11}$
6							1					
7								1				
8										1		

Table 4.10: Non-zero values in the C matrix, indexed by row and column

wheel speeds and rate gyro data are used in controlling the model when it is driven by recorded data.

## 4.12 Controlling the model

When the model is driven by test functions, two PID controllers are used; one for road speed and the other for roll angle. The speed controller varies rear wheel torque to control  ${}^M\vec{v}_1^A$ , the forward velocity of body  $A$  in the  $M$  reference frame. The roll angle controller varies steering torque to control  $q_9$ , the roll angle. The set points depend on the test function being used.

When the model is driven by recorded data, the road speed controller is not used, but instead, the speed is the result of wheel torques and the various drag

factors affecting the bike. It is very difficult to determine exactly all of the parameters affecting the speed, so this open loop method inevitably results in speed errors. It is important to reduce these errors as far as possible, because an error in speed causes further errors in angular velocity, lateral acceleration and so on. Therefore, a Kalman filter was added, as shown in Fig. 4.36, which uses the recorded data to produce optimal estimates for the wheel speeds. The equations are as follows:

$$\begin{aligned} s_k &= R + C_k P_k C_k^T \\ K_k &= A_k P_k C_k^T s_k^{-1} \\ \hat{x}_{k+1} &= A_k \hat{x}_k + B_k u_k + K_k (\hat{y}_k - C_k \hat{x}_k) \\ P_{k+1} &= A_k P_k A_k^T + Q - K_k C_k P_k A_k^T \end{aligned}$$

$K_k$  is the weighting coefficient matrix which weights the difference between the physical measurements  $\hat{y}_k$  and their estimates,  $C_k \hat{x}_k$ . Fig. 4.35 shows the recorded and estimated wheel angular velocities with and without the Kalman filter. The upper plots show the front wheel angular velocity and the lower plots show the rear.

The Kalman filter ensures that the road speed is optimally estimated, so if the estimated rates of change of orientation are also forced to match the recorded data, then the position and orientation of the model should match that of the real bike. Some drift in position and orientation is to be expected because any offset in the rate gyro data, however small, will result in a growing position error when the signal is integrated. This means, for example, that if the roll rate  $\omega_1$  alone was used to estimate the roll angle, then drift would occur because the estimated roll angle would depend wholly on the integrated rate gyro signal. However, roll angle depends on lateral acceleration, which in turn depends on road speed and angular velocity. The road speed has been corrected by the Kalman filter, and the  $\omega_2$  and  $\omega_3$  rate gyro signals depend on angular velocity. Because the angular velocity information is contained in the rate gyro signals themselves, and not their integrals, the angular velocity does not drift, and therefore lateral acceleration

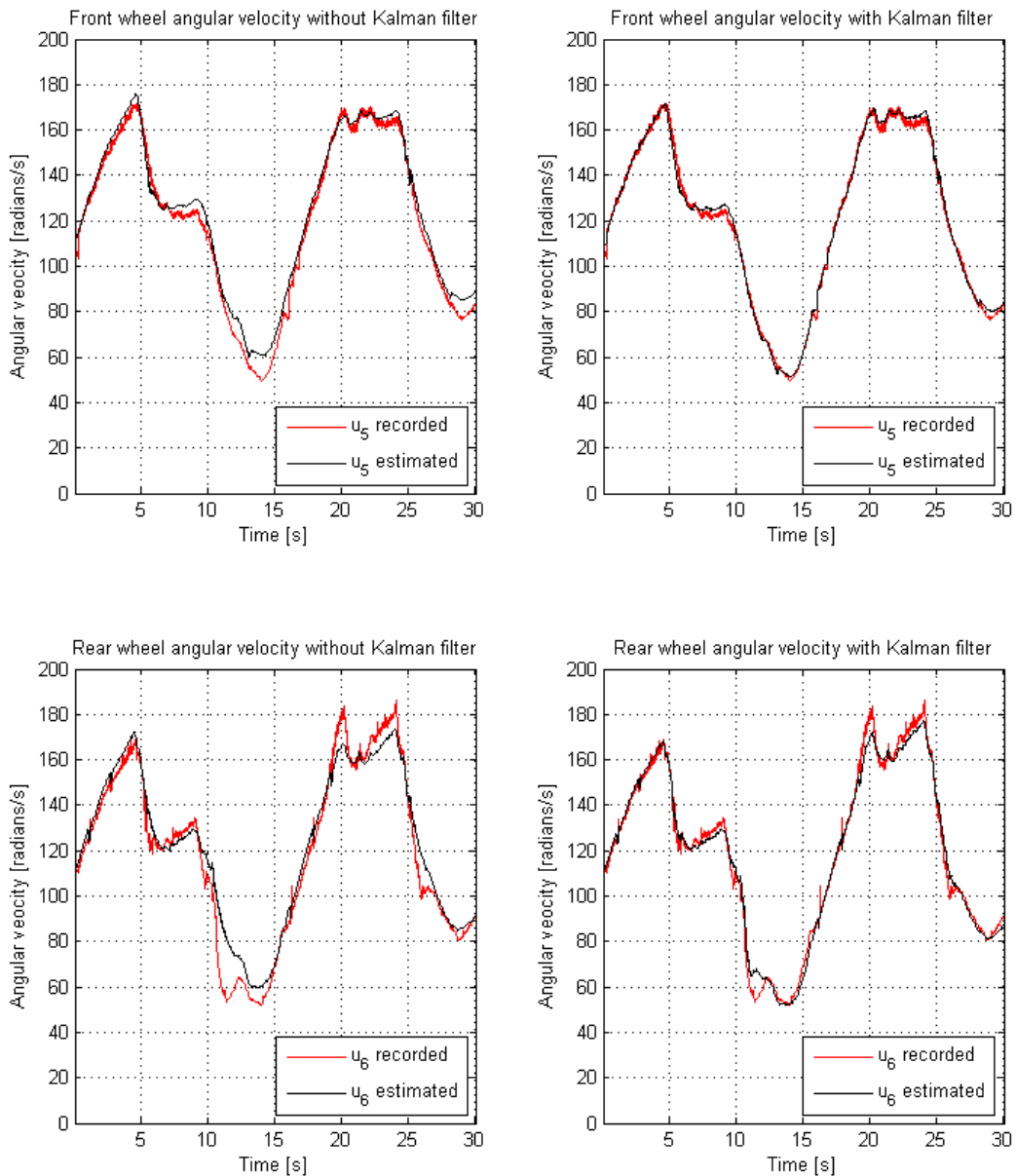


Figure 4.35: Wheel angular velocity with and without Kalman filter

and roll angle don't drift either. The gains  $g_2$  and  $g_3$  in Fig. 4.36 are lower than  $g_1$ . Fig. 4.16 shows the result of cross-correlation between the rate gyro data and engine speed. The rate gyro signal  $\omega_1$  is relatively uncorrelated with engine speed while  $\omega_2$  and  $\omega_3$  show a strong correlation, meaning that these signals contain a significant amount of engine speed data, picked up from engine vibration. It was found that increasing  $g_2$  or  $g_3$  introduced noise into the system, probably due to this issue. Although roll angle drift is absent, drift does occur in the position and yaw angle of the bike on the ground plane, as shown in Fig. 4.37. The map

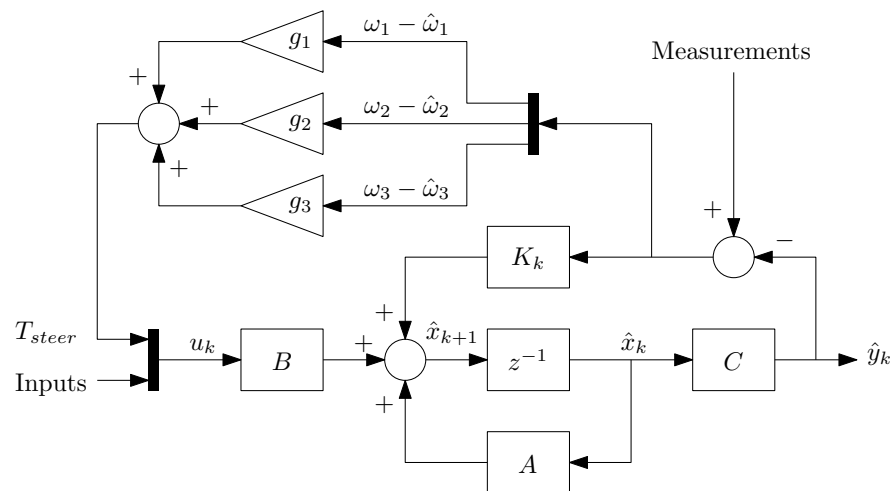


Figure 4.36: The bike model with steering torque controller and Kalman filter shows the measured GPS path and the path followed by the model for the same two consecutive laps.

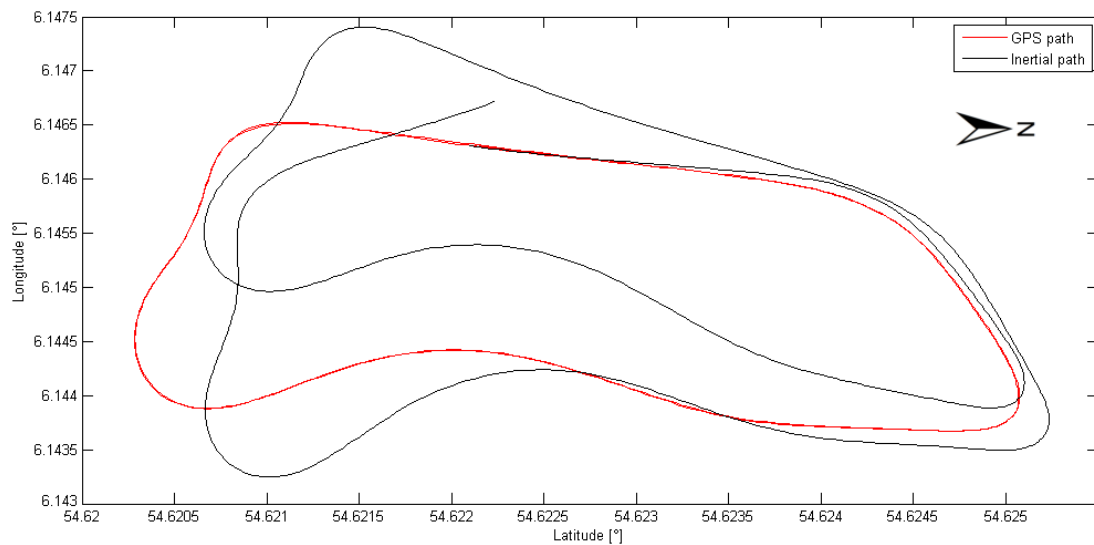


Figure 4.37: Inertial path compared to GPS path

## 4.13 Crash avoidance

If the data driving the model is recorded with the bike being ridden at the limit of grip, the model should run correctly provided that all motorcycle and tyre parameters are correct. Of course, correct parameters cannot be guaranteed, and it must be possible to experiment with parameters without the model crashing.

Strategies were devised to prevent the model from crashing when the grip limit is exceeded and the extent to which these strategies intervene can be monitored.

### 4.13.1 Traction control

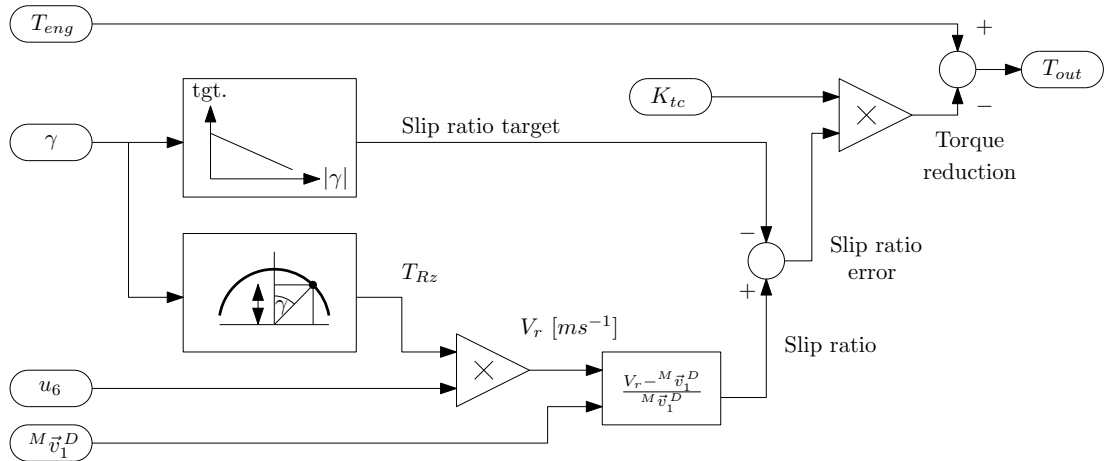


Figure 4.38: Traction control strategy

The TC strategy is illustrated in Fig. 4.38. The rear wheel angular velocity is converted to road speed in metres per second, using the roll angle and tyre profile data. This is converted to slip ratio by comparing it to the longitudinal speed of the rear axle. A slip ratio target is looked up from a table indexed by the absolute roll angle. This target represents the slip ratio below which the TC will not intervene. The target is subtracted from the slip ratio, giving a slip ratio error. Negative errors are ignored, and the error is scaled by a constant, which may be found empirically. This produces a torque reduction value which is then subtracted from the engine torque.

The result of the TC strategy can be seen in the fourth plot in Fig. 4.40. Throttle position and brake pressure are shown in the first plot. The rider opens the throttle just before 12 seconds and the rear wheel slip ratio becomes positive. At around 12.6 seconds, the slip ratio begins to exceed the slip ratio target and the strategy generates a TC slip ratio error signal, which is then multiplied by  $K_{tc}$  to generate the torque reduction. It can be seen that a spurious slip ratio error is caused by the gear change just before 16 seconds.

### 4.13.2 Anti-lock braking

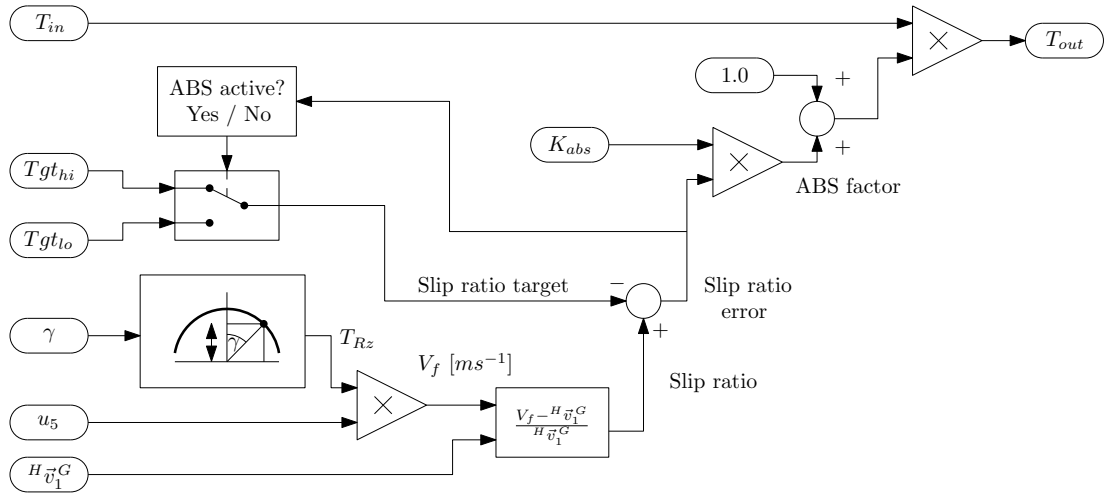


Figure 4.39: Anti-lock braking strategy

The ABS strategy is shown in Fig. 4.39 and most easily understood using a simple example. The slip ratio calculation is similar to the TC strategy, but only negative slip ratios are considered. If the forward speed of the front axle is  $H\vec{v}_1^G = 100 \text{ ms}^{-1}$  and the circumference of the tyre has a speed of  $90 \text{ ms}^{-1}$ , i.e. the wheel is under-rotating by 10%, then the slip ratio is  $-0.1$ . If the slip ratio target is  $-0.05$ , then the slip ratio error is  $-0.1 - (-0.05) = -0.05$ . Multiplying by the scaling factor  $K_{abs} = 2.0$  results in an ABS factor of  $-0.1$ . Adding 1.0 creates a multiplier of 0.9, so only 90% of the original braking torque is applied to the wheel. A circumferential speed of  $80 \text{ ms}^{-1}$  produces a slip ratio of  $-0.2$ , a slip ratio error of  $-0.15$ , an ABS factor of  $-0.3$  and a torque multiplier of 0.7.

ABS, especially on a motorcycle front wheel, differs from TC in one important regard. Whereas TC can moderate the slip to allow it to be more easily controlled by the rider, if a wheel begins to lock, it is crucial that the under-rotation be corrected immediately. Fig. 5.2 (a) shows the non-linear relationship between longitudinal force  $F_x$  and longitudinal slip  $\kappa$ . When the slip reaches the region past peak force, a reduction in torque to below that which initiated the locking is needed if the slip is to move back to the linear region. For this reason, separate slip targets are selected, depending on the current slip ratio error. If slip moves beyond the ‘normal’ target and the ABS becomes active, then slip must be brought to

a lower value, before the strategy reverts to the normal target. The front wheel may also under-rotate due to wheelies and this would generate a negative slip ratio and activate the strategy. This was avoided by disabling the ABS strategy when the front suspension is close to full extension.

The front ABS behaviour is shown in the second plot in Fig. 4.40. During the test run, no front wheel locking was experienced, so conservative slip ratio limits were set for illustration purposes. At just after 3 seconds, the ABS front slip limit is exceeded. The limit changes to a stricter value, and the slip ratio error is thereafter calculated relative to the new limit. The torque multiplier is then below unity, causing the front brake torque to be modulated. At around 4.6 seconds, the slip ratio no longer exceeds the limit, so the normal limit is selected and the torque multiplier returns to unity. It can be seen that the low negative value of front slip ratio just before 14 seconds does not activate the ABS strategy. This under-rotation of the front wheel at that point is caused by a wheelie, so the front suspension (not shown) is near full extension, and the TC strategy is disabled.

The rear ABS works in the same way, and is shown in the third plot in Fig. 4.40. At around 9 seconds, the negative rear wheel slip ratio reaches a very low value and the strategy is activated. However, the data in the upper plot shows that this is not caused by the rear brake. To avoid clutter, the gear position is not shown, but this under-rotation of the rear wheel is due to the clutch being released after two gear down-changes, while the front brake is applied heavily. The throttle blips at 8 seconds are evidence of this. Regardless of the cause, the ABS strategy works, but applies the torque modulation to an inactive rear brake.

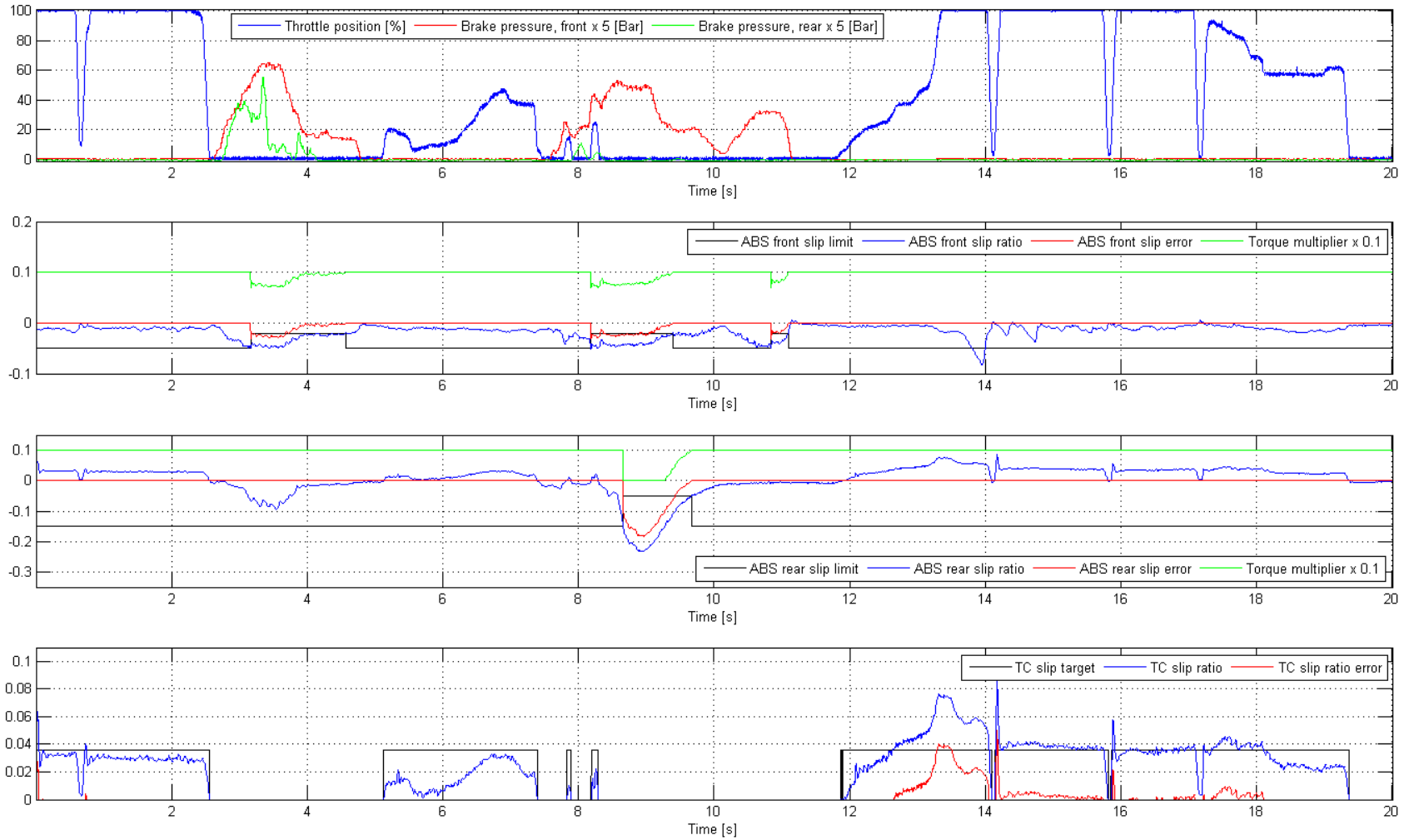


Figure 4.40: Crash avoidance strategies

## 4.14 Model computational performance

The model was coded first in Matlab and then in C. Coding in C was done directly, without the use of a cross-compiler, so as to optimise performance. Efficient matrix arithmetic functions were written and Eqn. (4.37) is solved using Cholesky decomposition. This is possible because the matrix  $K$  is symmetric and positive definite, and Cholesky decomposition [46] was found to outperform LU decomposition [46] by around 5% in this application. The specifications for the

---

Operating system	Windows 8 Pro
Processor	Intel® Core™ i5-3210M CPU
Processor speed	2.5 GHz
Installed RAM	8.00 GB
Operating system type	64-bit
Compiler	Visual C++® 6.0
Compiler type	32-bit

---

Table 4.11: Operating system and compiler specifications

machine and compiler are given in Table 4.11. The model runs between five and six times faster than real time and could therefore be used as an observer in an embedded control application.

# Chapter 5

## The Tyre Model

The tyres contribute significantly to the overall bike behaviour. This chapter begins by outlining the important tyre characteristics and introduces the necessary terminology. It explains the rationale for the chosen tyre model and explains that model in detail. The tyre model equations are given in Appendix A.

### 5.1 Introduction

The tyres are treated as force and torque generating entities rather than as constraints. That means that the tyres deform and slip relative to the road surface so as to produce the forces and torques that keep the bike in dynamic equilibrium.

The sign convention used in the tyre model is the one adopted by Pacejka and is shown in Fig. 5.1. It is similar to the SAE convention, defined in SAE J670 - Vehicle Dynamics Terminology [47], except that the direction of slip angle is reversed and the direction of vertical force  $F_z$  is reversed. Note that although the direction of  $F_z$  is reversed, the direction of the  $z$  axis is not, so positive  $F_z$  acts in the negative  $z$  direction, i.e. upwards. It follows from this convention that the longitudinal force  $F_x$ , lateral force  $F_y$ , overturning moment  $M_x$  and aligning moment  $M_z$  act in the directions shown in Fig. 5.2. The details of this figure are explained further in the following sections.

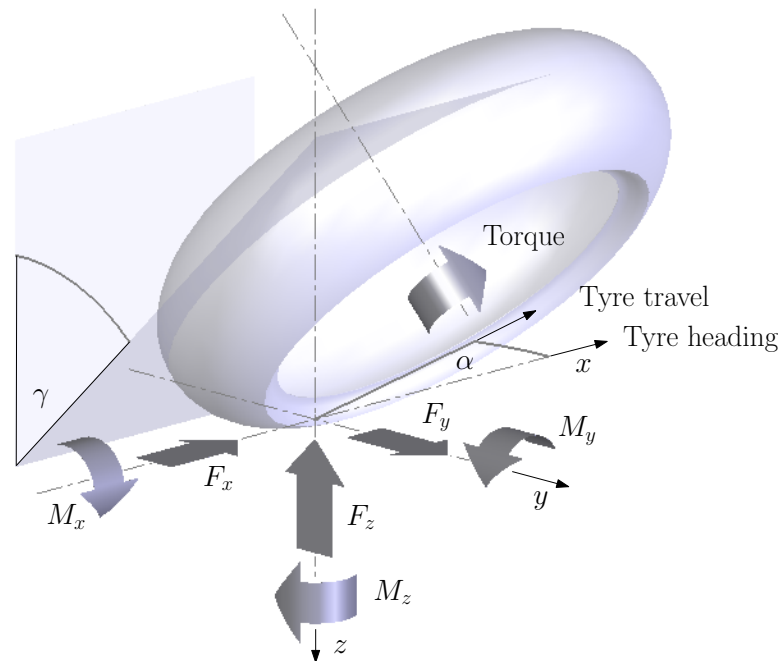


Figure 5.1: Forces and moments acting on a tyre in the Pacejka co-ordinate system

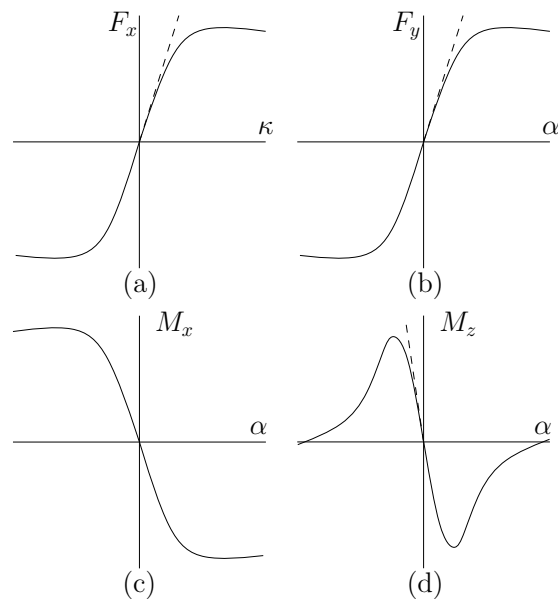


Figure 5.2:  $F_x$ ,  $F_y$ ,  $M_x$  and  $M_z$  vs. longitudinal slip  $\kappa$  and lateral slip  $\alpha$ .

## 5.2 Tyre characteristics and terminology

This section details the characteristics of the motorcycle tyre that are important to the model, and the various terms used to describe them. The tyre tread, or more specifically the contact patch, is the part of the tyre in contact with the

ground, and the material is generically referred to as rubber. The rubber used in tyres is a viscoelastic material usually consisting of both natural rubber and synthetic polymers. The term viscoelastic refers to the fact that when deformed, the rubber exhibits both elastic and viscous properties. This character creates hysteresis that in turn produces grip, as described in Section 5.2.1.

### 5.2.1 Grip

Grip refers to the physical effects, namely indentation and adhesion, that create horizontal force at the tyre contact patch. Indentation requires three factors in order to generate grip; macro-roughness on the ground (on the order of 1 to 10mm), hysteretic rubber and periodic constraint. Fig. 5.3 shows a typical stress-strain hysteresis curve for a viscoelastic material. Clearly the forces are greater during the compression phase than during release. When a tyre tread slips across a rough surface, the indentations subject each part of the contact patch to periodic compression and release. As shown in Fig. 5.4, the hysteresis of the rubber causes greater force to be exerted on the parts of the tread which are undergoing compression, than on those being released. The cumulative effect is a net force exerted on the tyre in the opposite direction to slip.

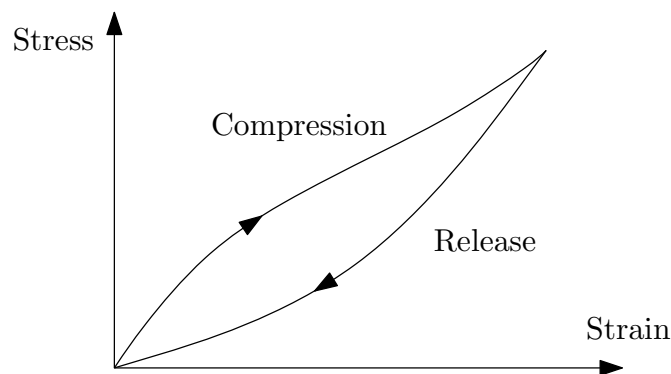


Figure 5.3: Hysteresis in a viscoelastic material

The dominant physical effect contributing to grip is not indentation, but adhesion, which accounts for about 75 to 80% of grip in dry conditions. Adhesion is in turn composed of hysteretic forces due to micro-roughness (on the order of  $10\mu\text{m}$  to 1mm), and Van der Waals force. This is an intermolecular force which,

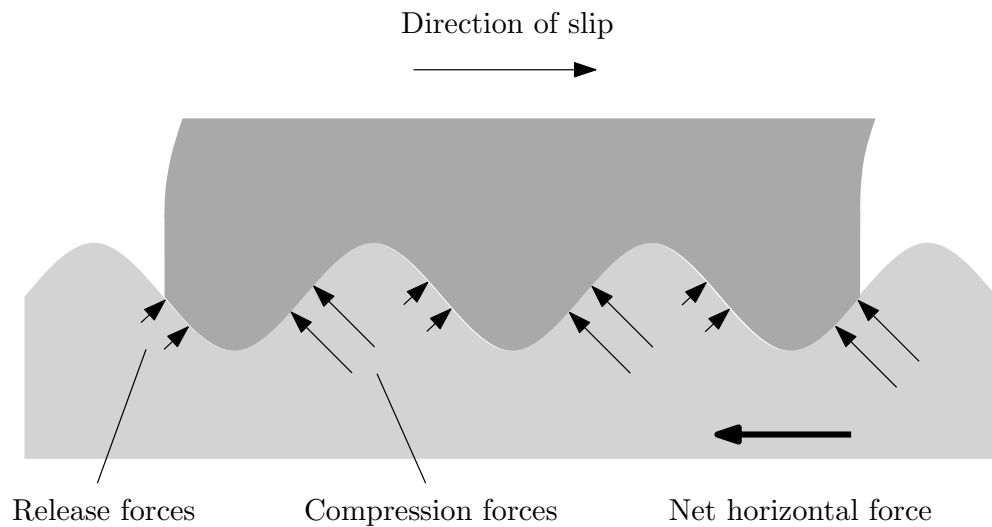


Figure 5.4: Viscoelastic material slipping across an indented surface

although weak in comparison to chemical bonds, generates a high net force due to the large number of molecular interactions. It is effective only at distances of less than around  $100\mu\text{m}$ , so even a thin film of water or dust is enough to disrupt the effect.

The general nature of the relationship between horizontal force and slip is shown in Fig. 5.2 (a) and (b), where (a) represents the longitudinal direction and (b) the lateral direction. The Magic Formula tyre model, which is covered in Section 5.3, describes these relationships in detail, along with the moments that act on the tyre.

### 5.2.2 Tyre radius

In general, a tyre is considered to have an unloaded radius, a loaded radius and an effective rolling radius as shown in Fig. 5.5. The unloaded radius  $R_0$  is sometimes called the free radius. The following definitions of the loaded radius  $R_l$  and the effective rolling radius  $R_e$  are provided in SAE J670 - Vehicle Dynamics Terminology [47].  $R_l$  is the distance from the centre of the tyre contact patch to the wheel centre, measured in the wheel plane. For a free rolling wheel,  $R_e$  is defined as the ratio of forward velocity of the wheel,  $V_x$ , to the free rolling angular

velocity,  $\Omega_0$ .

$$R_e = \frac{V_x}{\Omega_0} \quad (5.1)$$

It is clear from Fig. 5.5 that  $R_l < R_e < R_0$ .

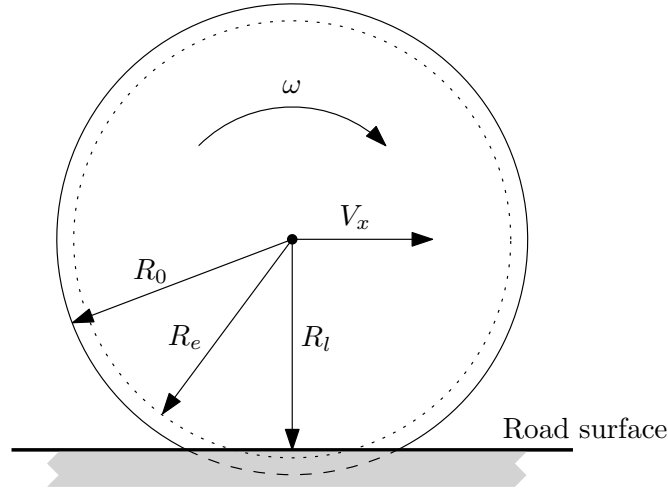


Figure 5.5: Tyre radius

### 5.2.3 Vertical force $F_z$

$F_z$  is the force exerted on the tyre by the ground in the direction normal to the ground plane. In this thesis, the ground plane is assumed to be horizontal, so  $F_z$  acts vertically upwards as shown in Fig. 5.1.

### 5.2.4 Longitudinal force $F_x$

$F_x$  is the force exerted by the ground on the tyre in the positive  $x$  direction, as shown in Fig. 5.1. It is the longitudinal shear force generated by longitudinal slip of the contact patch relative to the ground, and is a function of longitudinal slip  $\kappa$ , lateral slip  $\alpha$ , camber angle  $\gamma$  and vertical force  $F_z$ , i.e.

$$F_x = F_x(\kappa, \alpha, \gamma, F_z)$$

The full formula is given in Eqn. (A.1) in Appendix A.

$F_x$  does not act instantaneously but is subject to a distance-dependent first order lag. The ‘distance constant’ is a characteristic of the tyre, known as the relaxation length, which is the distance the tyre needs to roll in order for  $F_x$  to reach 63% of its final value. The relaxation length is analogous to the time constant in a first order time-dependent system and in fact, this is how it is implemented in the motorcycle model. At a given speed, the relaxation length is converted to a time constant and a first order differential equation is used to calculate  $F_x$ . This behaviour is covered in more detail in Section 5.2.16.

### 5.2.5 Lateral force $F_y$

$F_y$  is the force exerted by the ground on the tyre in the positive  $y$  direction, as shown in Fig. 5.1. Like  $F_x$ , it is a function of longitudinal slip  $\kappa$ , lateral slip  $\alpha$ , camber angle  $\gamma$  and vertical force  $F_z$ , i.e.

$$F_y = F_y(\kappa, \alpha, \gamma, F_z)$$

Eqn. (A.2) gives the Magic Formula equation for  $F_y$  in the general case where the tyre is subject to both lateral and longitudinal slip. The key components of  $F_y$  are shear force due to side slip of the contact patch relative to the ground, and so-called camber thrust due to the camber angle of the tyre. Fig. 5.6 shows a comparison of the range of slip and camber angles for cars and motorcycles, similar to that shown in Tezuka et al. [38]. In cars,  $F_y$  is predominantly due to side slip-induced shear force, and camber thrust is much less important. In motorcycles, the roles are practically reversed. As with  $F_x$ ,  $F_y$  is subject to a distance-dependent first order lag and this dynamic behaviour is covered in more detail in Section 5.2.16.

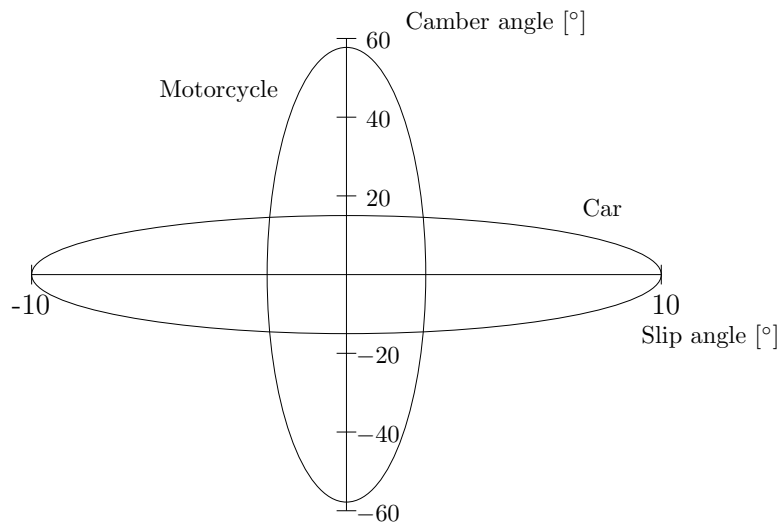


Figure 5.6: Slip and camber angle comparison for bikes and cars

### 5.2.6 Camber thrust force

Camber thrust is the lateral force due to the camber angle of the tyre. There is no separate equation for it in the Magic Formula tyre model. Instead, Eqn. (A.2) includes the effect of both side slip and camber angle. Camber thrust force can be isolated by evaluating Eqn. (A.2) twice; once with the actual value of camber and once with camber set to zero, and subtracting the results. The effect of camber thrust is illustrated in Fig. 5.7, which plots lateral force  $F_y$  against slip angle  $\alpha$  at two camber angles,  $0^\circ$  and  $50^\circ$ . Vertical force  $F_z$  is set at 1500 N, so at  $50^\circ$  camber angle,  $F_y \approx F_z \tan(50) = 1788 \text{ N}^\ddagger$  represents the lateral force generated by centripetal acceleration, which must be balanced by lateral tyre force to achieve equilibrium. The horizontal reference line in Fig. 5.7 indicates this value, and the vertical reference lines show where it cuts the two graphs. Without camber, a slip angle of  $6.2^\circ$  would be needed to achieve equilibrium, but at  $50^\circ$  camber, a slip angle of only  $1.7^\circ$  is sufficient. This shows that camber thrust greatly reduces the slip angle needed to achieve a given lateral force. The other effects evident in Fig. 5.7 are that camber angle increases the maximum lateral force that can be generated by the tyre, but shifts the peak force to a much lower slip angle.

<sup>‡</sup> Equilibrium is affected by other factors such as the overturning and gyroscopic moments.

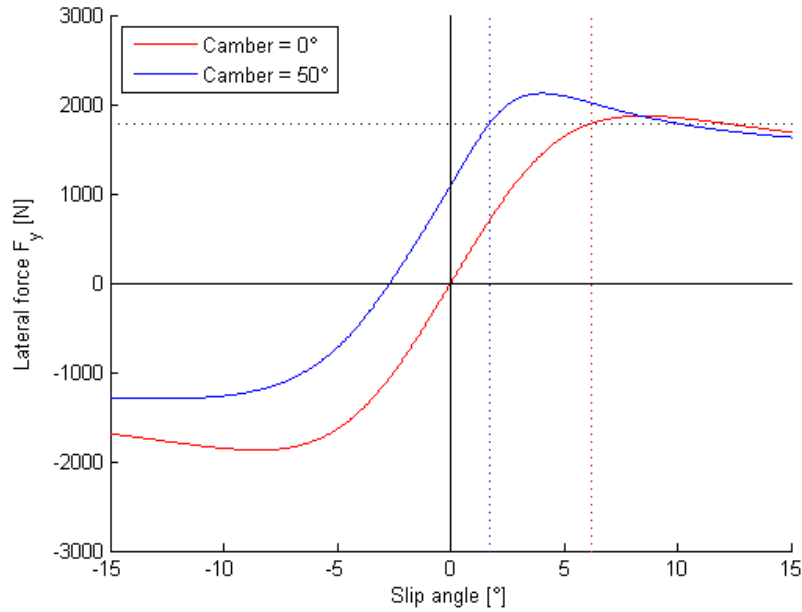


Figure 5.7: The effect of camber thrust on lateral force

### 5.2.7 Pneumatic trail $t$

Lateral force  $F_y$  is not distributed uniformly along the length of the contact patch, but predominantly towards the rear. This means that  $F_y$  appears to act through a point some distance behind the centre of the contact patch. This distance is known as the pneumatic trail  $t$ , and the formula is given in Eqn. (A.7).

### 5.2.8 Overturning moment $M_x$

On motorcycles, the overturning moment  $M_x$  arises because the tyre contact patch is displaced laterally due to camber angle. The vertical force  $F_z$  acting through the contact patch is therefore applied some distance inboard of the central plane of the wheel. In a thin disc tyre model,  $F_z$  is applied at the wheel central plane so the overturning moment is needed to compensate for the lateral offset of  $F_z$ . In the current model on the other hand,  $F_z$  is applied at the actual contact patch and the overturning moment is an automatic consequence to the lateral offset of the contact patch. [27] The formula for  $M_x$  is given in Eqn. (A.4), but for the reason just explained, it is not used in the model.

### 5.2.9 Rolling resistance moment $M_y$

The formula for the rolling resistance moment  $M_y$  is given in Eqn. (A.5). It acts in the opposite direction to wheel rotation. No parameters were available for  $M_y$  so it is set to zero in the model.

### 5.2.10 Aligning moment $M_z$

In Section 5.2.7, it was explained that  $F_y$  acts through a point a distance  $t$  behind the centre of the contact patch, where  $t$  is the pneumatic trail. This creates a moment  $M_z$  acting on the tyre about the  $z$  axis, in the direction shown in Fig. 5.2. Like  $F_x$  and  $F_y$ ,  $M_z$  is a function of longitudinal and lateral slip, camber angle and vertical force, so:

$$M_z = M_z(\kappa, \alpha, \gamma, F_z)$$

The full formula is given in Eqn. (A.6).  $M_z$  acts in the direction that tends to align the wheel with its direction of travel, and is called the aligning, or sometimes self-aligning moment. Because  $M_z$  is generated as a result of  $F_y$ , it too is subject to the distance-dependent lag which is described in detail in Section 5.2.16. Because the model uses correctly shaped tyres rather than disc wheels and because  $F_y$  is applied at the correct point, taking pneumatic trail into account, the aligning moment is automatically included in the model. All results, including model validation in Sections 7.4.1 and 7.4.2 were obtained with  $M_x = M_y = M_z = 0$ .

### 5.2.11 Longitudinal slip

SAE J670 - Vehicle Dynamics Terminology[47] defines longitudinal slip ratio as:

$$\kappa = \frac{\Omega - \Omega_0}{\Omega_0}$$

where  $\Omega$  is the angular velocity of the wheel and  $\Omega_0$  is the angular velocity of a free rolling wheel. Pacejka refers to the longitudinal slip ratio simply as the longitudinal slip and that term will be used here. Substituting  $\Omega_0$  from Eqn. (5.1)

gives:

$$\kappa = \frac{\Omega R_e - V_x}{V_x} \quad (5.2)$$

If the longitudinal slip velocity  $V_{sx}$  is defined as  $V_{sx} = V_x - \Omega R_e$ , then Eqn. (5.2) becomes:

$$\kappa = \frac{\Omega R_e - V_x}{V_x} = -\frac{V_{sx}}{V_x} \quad (5.3)$$

The physical meaning of  $V_{sx}$  is the average speed at which an element of tyre tread, when in contact with the ground, slips in the  $x$  direction relative to the ground. Note from the definition of  $V_{sx}$  that when  $\Omega R_e > V_x$ , then  $V_{sx}$  is negative, as one would expect.

### 5.2.12 Lateral slip

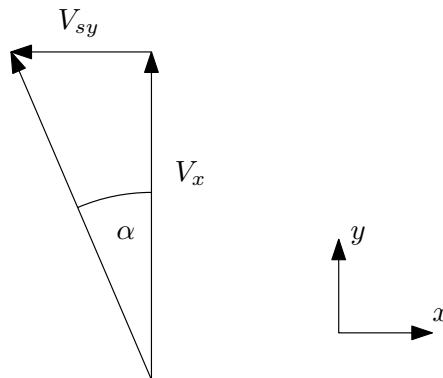


Figure 5.8: Slip angle

Rather than using the slip angle  $\alpha$  as an input quantity, Pacejka [44] defines the lateral slip  $\alpha^*$  as the tangent of the slip angle<sup>†</sup>, as shown in Eqn (5.4), noting that it is better to use this definition in the case of large slip angles or backward running. This expresses lateral slip in a similar form as the definition of

longitudinal slip in Eqn. (5.3).

$$\alpha^* = \tan(\alpha) \operatorname{sgn}(V_x) = -\frac{V_{sy}}{|V_x|} \quad (5.4)$$

### 5.2.13 Stiffness

Fig. 5.2 (a) shows the longitudinal force  $F_x$  plotted against longitudinal slip  $\kappa$  where lateral slip  $\alpha = 0$ , i.e. pure longitudinal slip. The longitudinal slip stiffness  $K_{x\kappa}$  is defined as the slope of this curve at  $\kappa = 0$  and is indicated by a dashed line. Fig. 5.2 (b) shows lateral force  $F_y$  plotted against slip angle  $\alpha$  where the longitudinal slip  $\kappa = 0$ . The lateral slip stiffness, or cornering stiffness  $K_{y\alpha}$ , is defined as the slope of this curve at  $\alpha = 0$ , as indicated by the dashed line. Fig. 5.2 (d) shows aligning moment  $M_z$  plotted against slip angle  $\alpha$ , for  $\kappa = 0$ . The aligning stiffness of the tyre is defined as minus the slope of this curve at  $\alpha = 0$ , i.e. minus the slope of the dashed line. Camber stiffness is the rate of change of camber thrust with camber angle at zero camber angle. [49]

### 5.2.14 Turn slip

Turn slip contributes to  $F_x$ ,  $F_y$  and  $M_z$ , and is defined as:

$$\varphi_t = -\frac{\dot{\psi}}{V_c} = -\frac{1}{R} \quad (5.5)$$

where  $\dot{\psi}$  is the yaw rate,  $V_c (> 0)$  is the velocity of the tyre contact point, and  $R$  is the turn radius. The equality  $\varphi_t = -\frac{1}{R}$  is valid only if the slip angle,  $\alpha$  is constant or zero [44]. The MF-Tire/MF-Swift 6.2 Equation Manual [48] states that turn slip was added to the Magic Formula to represent, for example, the aligning moment occurring when twisting the tyre at a standstill. Eqn. (5.5) shows that the effect of turn slip decreases at higher speeds and larger turn radii, so while it is a significant factor in the analysis of truck and aircraft tyres, which

---

<sup>†</sup> The MF-Tire / MF-Swift 6.2 Equation Manual [48] uses the actual slip angle  $\alpha$ , denoting it as  $\alpha_F$  in the model equations. For small slip angles,  $\alpha^* \approx \alpha$ .

experience large changes in yaw angle at low speed, it is generally not used when modelling motorcycle tyres, and is not included in this model.

### 5.2.15 Ply-steer

The formulas for side force  $F_y$  and aligning torque  $M_z$  in Appendix A contain terms that produce non-zero values for straight-ahead running, i.e. when slip angle  $\alpha = 0$ . These terms account for asymmetry in the tyre construction. The asymmetry may be due to the outer tread having a slightly conical shape or due to the arrangement of the layers of fabric, called plies, within the tyre. This self-steering phenomenon is known as ply-steer. [50]

### 5.2.16 Dynamic behaviour

The dynamic behaviour of  $F_x$  and  $F_y$  was mentioned in Sections 5.2.4 and 5.2.5. To re-cap, these forces are not instantaneous, but each is subject to a distance-dependent first order lag. The ‘distance constant’ is known as the relaxation length, and is the distance the tyre must roll in order for the force to reach 63% of its final value. Although relaxation length is sometimes spoken of as though it were a single quantity, the relaxation lengths  $\delta_x$  and  $\delta_y$  for longitudinal and lateral forces are not necessarily the same. The MF-Tyre / MF-Swift 6.2 formulas for longitudinal and lateral relaxation length are Eqns. 5.12 and 5.16.

Cossalter and Lot 2010 [25], showed how an expression for  $\delta_x$  may be derived by equating longitudinal slip shear force with the elastic force needed to deflect the tyre carcass in that direction. This is useful in understanding how dynamic behaviour arises in the tyre, so it is derived in full here using the current symbols and conventions. Note that while Cossalter and Lot use  $\xi$  to symbolise angular deformation of the tyre, it is used here to denote longitudinal deformation, i.e. the angular deformation multiplied by the effective rolling radius. This makes the formula for longitudinal relaxation length compatible with MF-Tyre / MF-Swift

6.2, and ensures continuity between the expressions for  $\delta_x$  and  $\delta_y$ .

$$F_x = F_{slip}(\kappa, \alpha^*, \gamma, F_z) \approx K_{x\kappa}\kappa \quad (5.6)$$

$$F_x = F_{elastic}(\xi, \gamma) \approx C_x\xi \quad (5.7)$$

where  $\xi$  is the longitudinal elastic deformation of the tyre. So:

$$F_{slip}(\kappa, \alpha^*, \gamma, F_z) - F_{elastic}(\xi, \gamma) = 0 \quad \text{or} \quad K_{x\kappa}\kappa - C_x\xi = 0$$

From Eqn. (5.3), the instantaneous longitudinal slip is

$$\kappa = \frac{\Omega R_e - V_x}{V_x} = -\frac{V_{sx}}{V_x}$$

This equation is modified to include the longitudinal deformation of the tyre,  $\xi$ , to get:

$$\kappa = \frac{\Omega R_e - V_x - \dot{\xi}}{V_x} = -\frac{V_{sx} + \dot{\xi}}{V_x} \quad (5.8)$$

Substituting the second part of Eqn. (5.8) into (5.6) gives:

$$F_x = -K_{x\kappa} \left( \frac{V_{sx} + \dot{\xi}}{V_x} \right) = K_{x\kappa} \frac{-V_{sx}}{V_x} - K_{x\kappa} \frac{\dot{\xi}}{V_x} \quad (5.9)$$

Let the steady state value of longitudinal slip be:

$$\kappa_0 = \frac{-V_{sx}}{V_x}$$

and let the longitudinal force due to the steady state slip be:

$$F_{xs} = K_{x\kappa}\kappa_0 \quad (5.10)$$

Rearranging Eqn. (5.7) and taking the time derivative yields:

$$\dot{\xi} = \frac{\dot{F}_x}{C_x} \quad (5.11)$$

Substitute Eqns. (5.10) and (5.11) into (5.9) to get:

$$F_x = F_{xs} - K_{x\kappa} \frac{\dot{F}_x}{C_x V_x} \quad \text{or}$$

$$\frac{K_{x\kappa}}{C_x V_x} \dot{F}_x + F_x = F_{xs}$$

The solution to this ordinary differential equation (ODE) is

$$F_x(t) = F_{xs} + (F_0 - F_{xs})e^{-t/\tau} \quad \text{where} \quad \tau = \frac{K_{x\kappa}}{C_x V_x}$$

and  $F_0$  is the force at  $t = 0$ . Time is distance over speed so let  $\tau = \frac{\delta_x}{V_x}$ , giving:

$$\delta_x = \frac{K_{x\kappa}}{C_x} \quad (5.12)$$

The relaxation length  $\delta_x$  may also be expressed in terms of the slip and deflection of the tyre. From Eqns. (5.6) and (5.7),

$$K_{x\kappa}\kappa = C_x\xi \quad \text{so} \quad \frac{K_{x\kappa}}{C_x} = \frac{\xi}{\kappa} \quad \text{so} \quad \delta_x = \frac{\xi}{\kappa}$$

The expression for  $\delta_y$  is derived in a similar way, as follows.

$$F_y = F_{slip}(\kappa, \alpha^*, \gamma, F_z) \approx K_{y\alpha}\alpha^* \quad (5.13)$$

$$F_y = F_{elastic}(\zeta, \gamma) \approx C_y\zeta \quad (5.14)$$

where  $\zeta$  is the lateral elastic deformation of the tyre. So:

$$F_{slip}(\kappa, \alpha^*, \gamma, F_z) - F_{elastic}(\zeta, \gamma) = 0 \quad \text{or} \quad K_{y\alpha}\alpha^* - C_y\zeta = 0$$

From Eqn. (5.4) and assuming that  $V_x > 0$ , the instantaneous lateral slip is:

$$\alpha^* = -\frac{V_{sy}}{V_x}$$

This equation is modified to include lateral deflection. Note the similarity to the

second part of Eqn. (5.8).

$$\alpha^* = -\frac{V_{sy} + \dot{\zeta}}{V_x} \quad (5.15)$$

Substitute Eqn. (5.15) into (5.13) to get:

$$\begin{aligned} F_y &= -K_{y\alpha} \frac{V_{sy} + \dot{\zeta}}{V_x} \\ &= K_{y\alpha} \frac{-V_{sy}}{V_x} - K_{y\alpha} \frac{\dot{\zeta}}{V_x} \end{aligned}$$

Similar to the previous derivation, let  $F_{ys} = K_{y\alpha} \frac{-V_{sy}}{V_x}$  be the steady state value of  $F_y$  due to lateral slip. Rearranging Eqn. (5.14) and taking the first derivative yields:

$$\dot{\zeta} = \frac{\dot{F}_y}{C_y}$$

Then:

$$\begin{aligned} F_y &= F_{ys} - K_{y\alpha} \frac{\dot{F}_y}{C_y V_x} \\ \frac{K_{y\alpha}}{C_y V_x} \dot{F}_y + F_y &= F_{ys} \end{aligned}$$

The solution to the ODE is

$$F_y(t) = F_{ys} + (F_{y0} - F_{ys})e^{-t/\tau} \quad \text{where} \quad \tau = \frac{K_{y\alpha}}{C_y V_x}$$

and  $F_{y0}$  is the lateral force at  $t = 0$ . As time is distance over speed, let:

$$\tau = \frac{\delta_y}{V_x} \quad \text{so} \quad \delta_y = \frac{K_{y\alpha}}{C_y} \quad (5.16)$$

The relaxation length  $\delta_y$  may also be expressed in terms of the slip and deflection

of the tyre. From Eqns. (5.13) and (5.14)

$$K_{y\alpha}\alpha^* = C_y\zeta \quad \text{so} \quad \frac{K_{y\alpha}}{C_y} = \frac{\zeta}{\alpha^*} \quad \text{so} \quad \delta_y = \frac{\zeta}{\alpha^*}$$

### 5.3 The Magic Formula tyre model

The Magic Formula tyre model began as an empirical static model and development was done in a co-operative effort by the Delft University of Technology, TU-Delft, and Volvo Car Corporation. The dynamic behaviour of the tyre was added to the model by Pacejka and Besselink in 1997 [36]. It is now well established and is undergoing continuous development. It is used to represent tyre force and moment curves, using more than 150 parameters to characterise the tyre. The history of the Magic Formula is summarised as follows:

- 1987: The first version of the Magic Formula was published by Bakker et al. [32].
- 1989: ‘Monte Carlo’ version. Bakker et al. [33].
- 1993: ‘Version 3’. Pacejka and Bakker [34].
- 1993: Michelin introduced horizontal force generation at combined longitudinal and lateral slip. Bayle et al. [51].
- 1996: The Dutch organisation for applied research, TNO, implemented the Magic Formula in commercial software, MF-Tyre 5.0. [48]
- 1997: Pacejka and Besselink 1997 [36] introduced a relatively simple model for longitudinal and lateral transient behaviour. This version was known as ‘Delft Tyre ‘97’.
- 1998: De Vries and Pacejka adapted the Magic Formula model to be more versatile and cover the larger camber angle range needed for motorcycle tyres. [37]
- 2010: Besselink et al. [52] added the effect of inflation pressure to the Magic Formula.

- 2013: MF-Tyre / MF Swift 6.2 is the current version at time of writing. [48]

The force and moment curves are described by means of two main formulas, one based on the sine function and the other on cosine.

### 5.3.1 The sine formula

The following sine formula is used to describe asymmetric tyre characteristics [36]:

$$Y = D \sin(C \arctan(Bx - E(Bx - \arctan(Bx)))) + S_v \quad \text{where } x = X + S_h$$

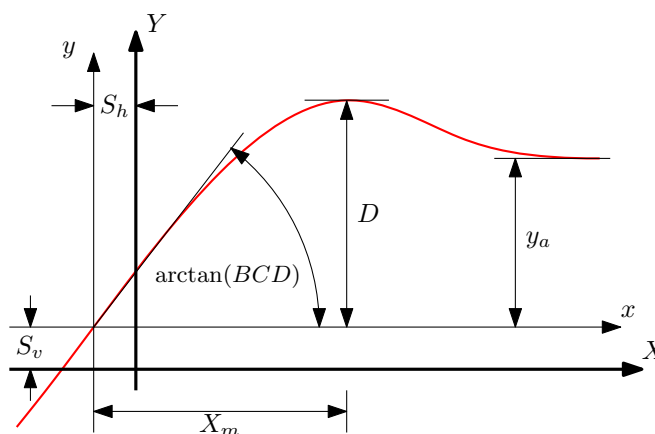


Figure 5.9: The curve produced by the sine formula

- $X$ : Input variable, e.g.  $\kappa$  or  $\alpha$ .
- $Y$ : Output variable, e.g.  $F_x$  or  $F_y$ .
- $B$ : Stiffness factor that controls the slope at  $x = 0$ . This slope  $BCD$  is known as the ‘stiffness’, so when  $C$  and  $D$  are fixed, the slope may be adjusted by  $B$ .
- $C$ : Shape factor that controls stretching in the  $x$  direction.
- $D$ : Peak value.
- $E$ : Curvature factor  $E = \frac{BX_m - \tan(\pi/2C)}{BX_m - \arctan(BX_m)}$  affects the shape of the curve and the position of  $x_m$  if it exists.  $E$  can be made dependent on the sign of  $x$  by making  $E = E_0 + \Delta E \cdot \text{sign}(x)$ .

- $S_h$ : Horizontal shift.
- $S_v$ : Vertical shift.
- $X_m$ : Value of  $x$  at which peak value is reached.
- $y_a$ : Asymptotic value at large values of  $x$ .  $y_a = D \sin\left(\frac{2\pi}{C}\right)$

Fig. 5.10 shows the versatility of the sine formula by using it to represent both  $F_y$  and  $M_z$  as functions of slip angle  $\alpha$ .

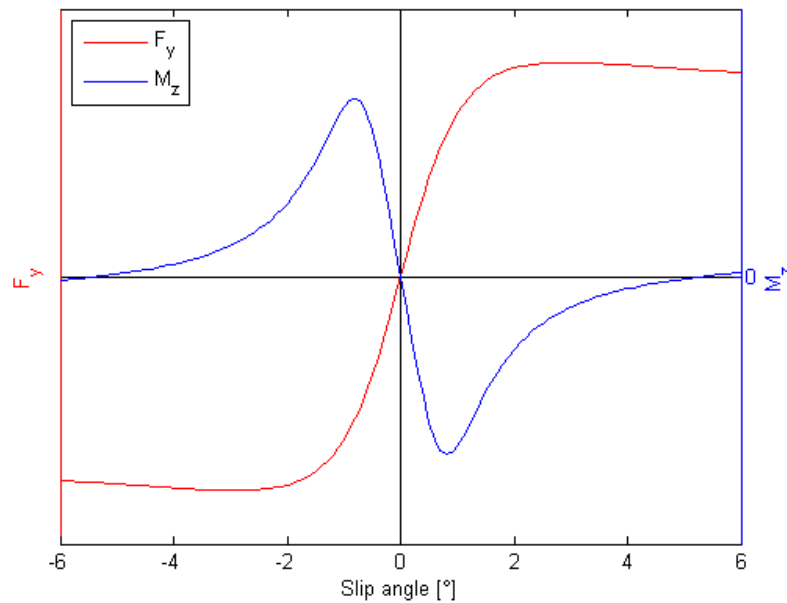


Figure 5.10:  $F_y$  and  $M_z$  versus slip angle  $\alpha$  with  $\kappa = 0$

### 5.3.2 The cosine formula

The cosine formula is used to describe symmetric tyre characteristics as shown in Fig. 5.11. It features in the combined slip equations where both  $\alpha$  and  $\kappa$  are non-zero, and is also used to represent the decay of pneumatic trail with slip angle. The formula is as follows [36]:

$$Y = D \cos(C \arctan(Bx - E(Bx - \arctan(Bx)))) \quad \text{where } x = X + S_H$$

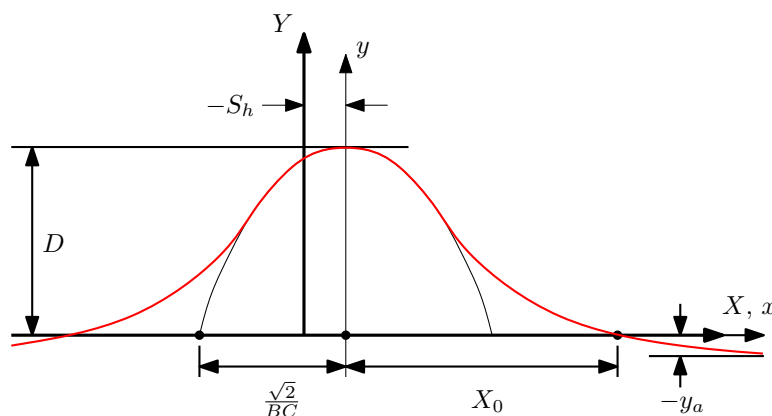


Figure 5.11: The curve produced by the cosine formula

- $X$ : Input variable, e.g.  $\alpha$ .
- $Y$ : Output variable, e.g. pneumatic trail,  $t$ .
- $B$ : Determines the shape at the peak as shown by the parabola in Fig. 5.11.
- $C$ : Shape factor  $C = \frac{2}{\pi} \arccos\left(\frac{y_a}{D}\right)$  determines the level of the horizontal asymptote.
- $D$ : Peak value.
- $E$ : Factor  $E = \frac{BX_0 - \tan(\pi/2C)}{BX_0 - \arctan(BX_0)}$  changes the shape at larger values of  $x$ .
- $S_h$ : Horizontal shift.
- $X_0$ : Value of  $x$  at which  $Y = 0$ .
- $y_a$ : Minus the asymptotic value at large values of  $X$ .

### 5.3.3 Magic Formula inputs and outputs

Fig. 5.12 shows the inputs and outputs of the Magic Formula tyre model. For the reason explained in Section 5.2.14, turn slip is not used as an input.  $F_z$  is the vertical force exerted on the tyre by the ground,  $\kappa$  and  $\alpha^*$  are longitudinal and lateral slip respectively. The other inputs are the tyre camber angle  $\gamma$ , the forward velocity of the wheel,  $V_x$  and the tyre inflation pressure  $P$ . The model outputs are the forces  $F_x$  and  $F_y$ , and the moments  $M_x$ ,  $M_y$  and  $M_z$ . All of the inputs

and outputs are explained in previous sections. As explained in Sections 5.2.8 and 5.2.10, because the actual tyre profile and pneumatic trail are used when applying forces to the wheel,  $M_x$  and  $M_z$  arise implicitly in the model and do not need to be applied explicitly, as would be the case if the wheels were modelled as thin discs.  $M_y$  is not included because no parameters were available.

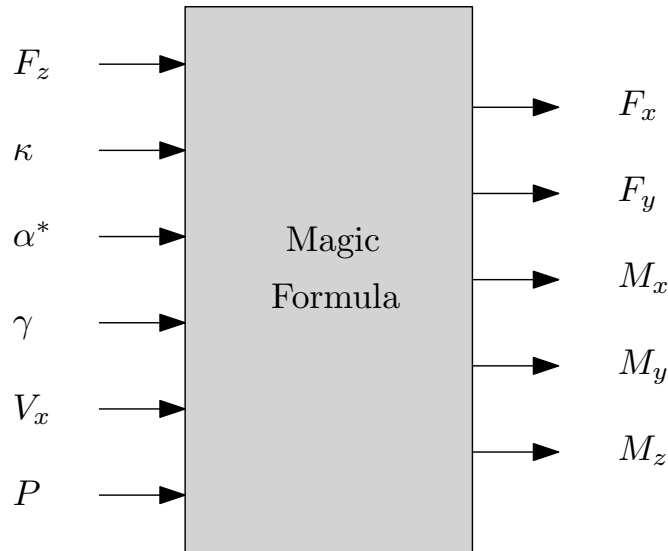


Figure 5.12: The Magic Formula inputs and outputs

The Magic Formula equations are given in Appendix A. All parameters used in the equations, other than the input and output parameters shown in Fig. 5.12, are defined and explained in Appendix A, making it a self-contained ‘black box’, represented by the block in Fig. 5.12.

## 5.4 Magic Formula parameters

The tyres used were Dunlop Sportmax GP Racer D211 120/70 ZR17 front and 180/55 ZR17 rear, on 3.5” and 5.5” wheel rim widths respectively. These are the sizes recommended by Dunlop for the 2004 model CBR600RR. The D211 tyres are road legal ‘super-sport’ tyres, designed for track-day use, and competition where the rules stipulate that road legal tyres must be used. Unfortunately, no Magic Formula parameters were available for these tyres, so they needed to be estimated as realistically as possible.

The principle source for the tyre parameters is Sharp et al. [27], which in turn uses data from [37] and [53]. Parameters are available for three tyre sizes. Parameters for longitudinal force,  $F_x$ , are available for a 160/70 tyre. Parameters for lateral force,  $F_y$ , and aligning moment,  $M_z$  are available for the 160/70 tyre but also for a 120/70 and a 180/55 tyre. Very fortunately, 120/70 and a 180/55 are the sizes of the tyres used in testing for this project. The tyres referenced in Sharp et al. will be referred to by their sizes while the tyres used in this project will be referred to simply as ‘front’ and ‘rear’. Fig. 5.13 shows the character of  $F_x$ ,  $F_y$ , and pneumatic trail for the front and rear tyres at the same non-zero camber angle. The pneumatic trail is calculated in the equations for  $M_z$  in Section A.5, and is included in the model.

The following procedure was used to complete the tyre models. The parameters from Sharp et al. were used, with the longitudinal force parameters from the 160/70 tyre being used for both the front and rear tyres. Then, by comparing graphs of  $F_x$  and  $F_y$  to known tyres, the parameters were adjusted by the minimum amount to achieve what was judged to be a realistic character for the super-sport tyres used in the project. It can be seen in Tables 5.1 to 5.4 that the adjustments to the parameters were relatively few, and perhaps surprisingly, the longitudinal force parameters for the 160/70 tyre did not require much adjustment for the roles of the 120/70 front and 180/55 rear super-sport tyres.

Assumptions made by Sharp et al. [27] are carried over here. The tyres are assumed to be symmetric and all shifts are zero, so for the  $F_x$  calculation,  $S_{Hx\alpha} = 0$ , for the  $F_y$  calculation,  $S_{Hy\kappa} = S_{Vy\kappa} = 0$ . It is assumed that loss of longitudinal force due to side slip is unaffected by camber, so  $r_{Bx3} = 0$ . All  $\lambda$  scale factors, e.g.  $\lambda_{Cx}$  etc. are 1.

### 5.4.1 Refining the tyre parameters

The parameters derived above are a viable starting point but they cannot be expected to be an accurate representation of the actual tyres used. Fig. 5.14 illustrates this very well, as it shows a comparison of the estimated and measured steering angle versus roll angle, using these parameters. Positive values of roll

Parameter	Value	Description
$p_{Cx1}$	1.50	Value from 160/70 tyre, adjusted
$p_{Dx1}$	1.44	Value from 160/70 tyre, adjusted
$p_{Dx2}$	-0.20	Value from 160/70 tyre, adjusted
$p_{Dx3}$	0.10	Variation of friction, $\mu_x$ , with camber
$p_{Ex1}$	0.0263	Value from 160/70 tyre
$p_{Ex2}$	0.27056	Value from 160/70 tyre
$p_{Ex3}$	-0.0769	Value from 160/70 tyre
$p_{Ex4}$	0.50	Value from 160/70 tyre, adjusted
$p_{Kx1}$	20.00	Value from 160/70 tyre, adjusted
$p_{Kx2}$	-4.233	Value from 160/70 tyre
$p_{Kx3}$	0.3369	Value from 160/70 tyre
$r_{Bx1}$	13.476	Value from 160/70 tyre
$r_{Bx2}$	8.00	Value from 160/70 tyre, adjusted
$r_{Cx1}$	1.1231	Value from 160/70 tyre

Table 5.1: Non-zero parameters for front tyre  $F_x$ . No data for 120/70 tyre

Parameter	Value	Description
$p_{Cy1}$	1.6	Value from 120/70 tyre, adjusted
$p_{Cy2}$	0.86765	Value from 120/70 tyre
$p_{Dy1}$	1.45	Value from 120/70 tyre, adjusted
$p_{Ey1}$	-1.5	Value from 120/70 tyre, adjusted
$p_{Ey2}$	-3.2068	Value from 120/70 tyre
$p_{Ey4}$	-3.998	Value from 120/70 tyre
$p_{Ky1}$	-22.841	Value from 120/70 tyre, negated
$p_{Ky2}$	2.1578	Value from 120/70 tyre
$p_{Ky3}$	0.2	
$p_{Ky4}$	2.0	
$p_{Ky5}$	-0.22882	Value from 120/70 tyre
$p_{Ky6}$	-0.69677	Value from 120/70 tyre, negated
$p_{Ky7}$	-0.03077	Value from 120/70 tyre
$p_{Vy3}$	-0.5	
$r_{By1}$	5.00	Value from 120/70 tyre, adjusted
$r_{By2}$	8.1697	Value from 160/70 tyre
$r_{By3}$	-0.05914	Value from 160/70 tyre
$r_{Cy1}$	1.0533	Value from 160/70 tyre
$r_{Vy5}$	1.00	

Table 5.2: Non-zero parameters for front tyre  $F_y$

Parameter	Value	Description
$p_{Cx1}$	1.50	Value from 160/70 tyre, adjusted
$p_{Dx1}$	1.50	Value from 160/70 tyre, adjusted
$p_{Dx2}$	-0.20	Value from 160/70 tyre, adjusted
$p_{Dx3}$	0.10	Variation of friction, $\mu_x$ , with camber
$p_{Ex1}$	0.0263	Value from 160/70 tyre
$p_{Ex2}$	0.27056	Value from 160/70 tyre
$p_{Ex3}$	-0.0769	Value from 160/70 tyre
$p_{Ex4}$	0.50	Value from 160/70 tyre, adjusted
$p_{Kx1}$	25.94	Value from 160/70 tyre
$p_{Kx2}$	-4.233	Value from 160/70 tyre
$p_{Kx3}$	0.3369	Value from 160/70 tyre
$r_{Bx1}$	13.476	Value from 160/70 tyre
$r_{Bx2}$	11.354	Value from 160/70 tyre
$r_{Cx1}$	1.1231	Value from 160/70 tyre

Table 5.3: Non-zero parameters for rear tyre  $F_x$ . No data for 180/55 tyre

Parameter	Value	Description
$p_{Cy1}$	1.50	Value from 180/55 tyre, adjusted
$p_{Cy2}$	0.61397	Value from 180/55 tyre
$p_{Dy1}$	1.56	Value from 180/55 tyre, adjusted
$p_{Ey1}$	-0.94635	Value from 160/70 tyre
$p_{Ey2}$	-1.669	Value from 180/55 tyre
$p_{Ey4}$	-4.288	Value from 180/55 tyre
$p_{Ey5}$	2.00	Value from 180/55 tyre, adjusted
$p_{Ky1}$	-26.601	Value from 160/70 tyre, negated
$p_{Ky2}$	1.6935	Value from 180/55 tyre
$p_{Ky3}$	0.29113	
$p_{Ky4}$	2.00	
$p_{Ky5}$	0.18708	Value from 180/55 tyre
$p_{Ky6}$	-1.10	Value from 180/55 tyre, negated and adjusted
$p_{Ky7}$	0.013293	Value from 180/55 tyre
$p_{Vy3}$	-0.5	
$r_{By1}$	7.7856	Value from 160/70 tyre
$r_{By2}$	8.1697	Value from 160/70 tyre
$r_{By3}$	-0.05914	Value from 160/70 tyre
$r_{Cy1}$	1.0533	Value from 160/70 tyre
$r_{Vy5}$	1.00	

Table 5.4: Non-zero parameters for rear tyre  $F_y$

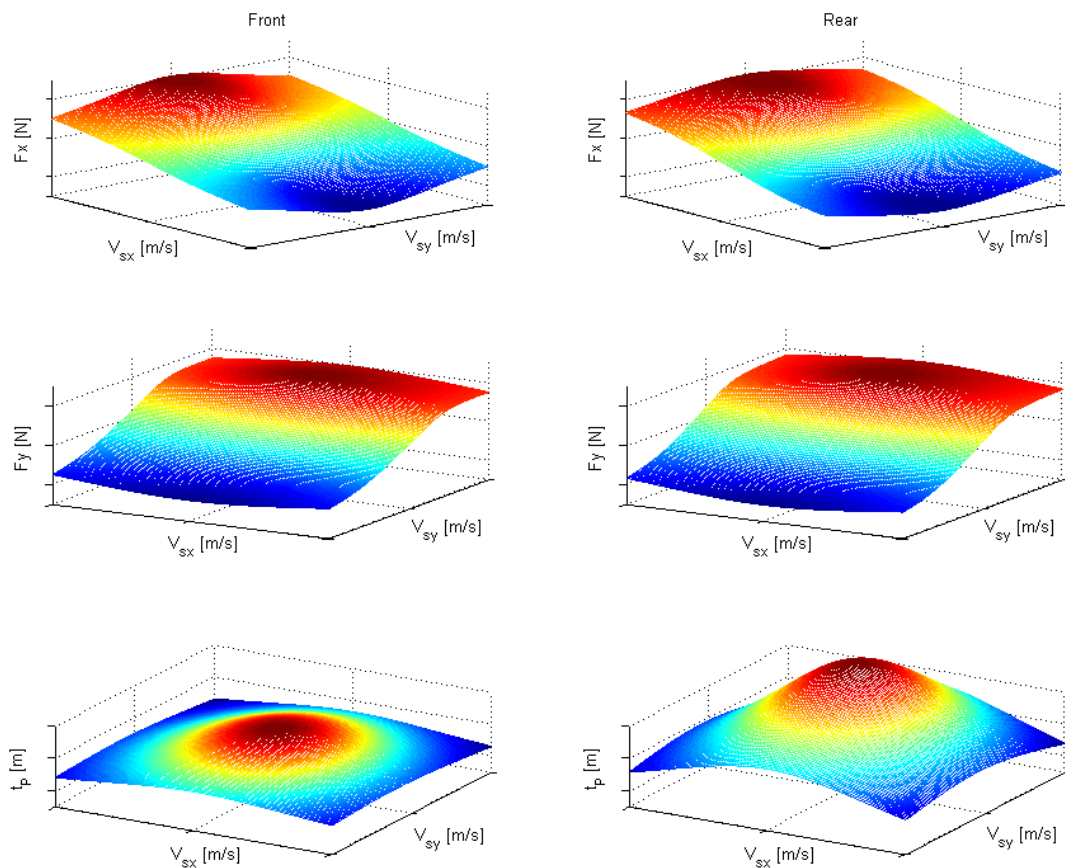


Figure 5.13: Comparison of front and rear tyre character

angle mean the bike is leaned to the right and positive values of steering angle mean the bike is steered to the left. It can be seen that apart from the very slow right-hand corner, which stands apart in the lower right area of the plots, the measured steady state steering angle in the faster corners is approximately  $0.15^\circ$  in the opposite direction to the turn. In other words, at maximum lean in a right hand corner, the bars are turned  $0.15^\circ$  to the left. The estimated steering angle, on the other hand, is approximately  $2^\circ$  to the right. It appears that in order to generate the lateral force required to maintain dynamic equilibrium, the model needs to create a steering angle that differs significantly from the real value.

Steering behaviour is closely connected with the characteristics of both tyres. This is examined in Sections 7.5 and 7.6. It may be the case that the front tyre model does not generate sufficient lateral force from camber thrust and needs to make up the deficit in slip-generated force. It was decided to use the error in steering angle to tune the tyre parameters. An error function was devised which

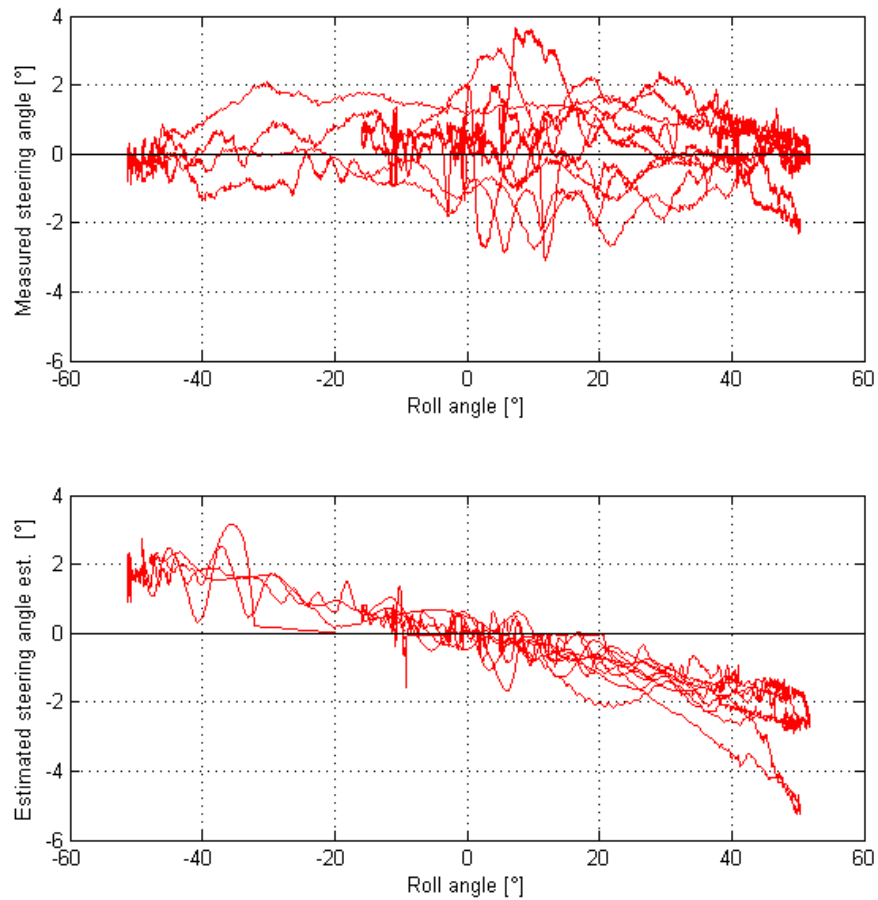
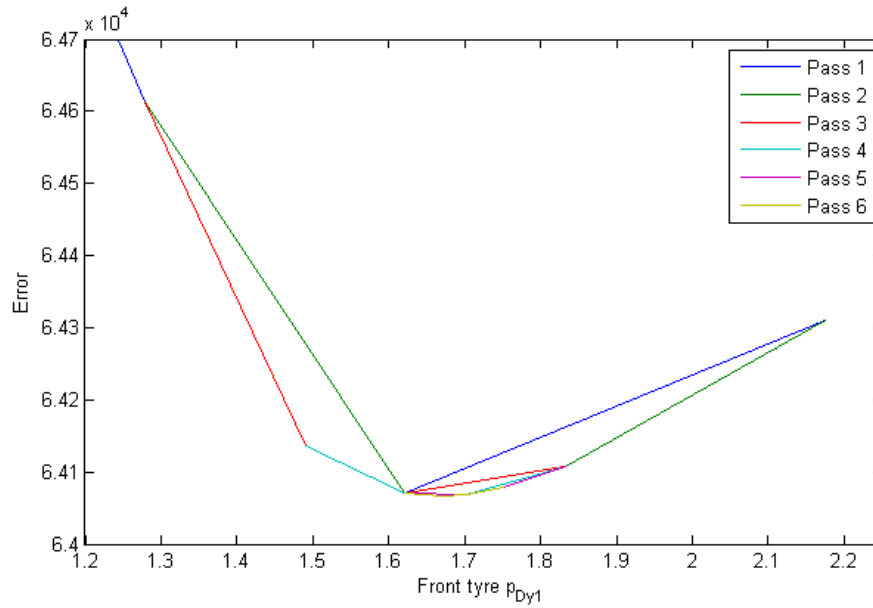


Figure 5.14: Steering angle vs. roll angle using initial set of tyre parameters

consisted of the weighted difference between measured and estimated values for steering, front suspension and rear suspension. Suspension position was included in the error function to prevent anomalous behaviour from creeping in as the tyre parameters were altered. The error was minimised using the ‘golden section’ optimisation method for each lateral force tyre parameter. Fig. 5.15 illustrates the optimisation process for the front tyre parameter  $p_{Dy1}$ , which determines lateral friction  $\mu_y$  at nominal vertical force  $F_z$ . The initial value is 1.45, as shown in Table 5.2. The lower and upper initial values chosen to bracket the optimum value were 0.5 and 1.5 times the initial value, or 0.725 and 2.175. A tolerance of 0.05 was set, and the optimisation algorithm made six passes. The optimal value was found to be  $p_{Dy1} = 1.671$ . The optimisation process was carried out in a similar way for the other lateral force parameters for both tyres.

When the optimisation procedure was finished, the estimated steering angle was as shown in Fig. 5.16. The steering behaviour at maximum lean is now

Figure 5.15: Optimisation of front tyre  $p_{Dy1}$ 

predicted well by the model for both fast and slow corners. This procedure is not expected to reproduce the actual parameter set for the tyres. There are many parameter configurations which will give similar results for steering angle and suspension position. It is merely a way of adjusting a set of parameters that is known to be only approximate, in order to make the behaviour closer to the real tyres.

	Original	Modified	
Front $p_{Cy1}$	1.60	0.80	Cy from the Magic Formula
Front $p_{Dy1}$	1.45	1.67	Lateral friction, $\mu_y$
Front $p_{Ey1}$	-1.50	-2.25	Lateral curvature $E_y$ at nominal $F_z$
Front $p_{Ey2}$	-3.21	-1.60	Variation of $E_y$ with $F_z$
Front $p_{Ey4}$	-4.00	-6.00	Variation of $E_y$ with camber
Front $p_{Ky1}$	-22.84	-50.00	Cornering stiffness $K_{y\alpha}$ scaling factor
Front $p_{Ky2}$	2.16	1.00	Load at which $K_{y\alpha}$ reaches max. value
Front $p_{Ky6}$	-0.70	-0.90	Camber stiffness scaling factor
Front $p_{Vy3}$	-0.50	-0.56	Variation of shift $S_{Vy\gamma}$ with camber
Rear $p_{Ky2}$	1.69	1.60	Load at which $K_{y\alpha}$ reaches max. value
Rear $p_{Ky6}$	-1.10	-0.75	Camber stiffness scaling factor

Table 5.5: Modified  $F_y$  tyre parameters

The modified parameters are shown in Table 5.5. The resulting steering behaviour is shown in Fig. 5.16 for one lap of Nutts Corner ridden by Jeremy

McWilliams, [54] and in Fig. 5.17 for one lap of Mondello Park ridden by the writer during preliminary validation. The steering angle at maximum roll angle now corresponds well with the measured values on both race tracks for both fast and slow corners. Much of the steering movement around the upright position in the upper plot in Fig. 5.16 is missing from the estimated data in the lower plot, but the model assumes a completely flat road surface and the suspension graphs in Chapter 7 show a lot of suspension movement due to the topography of the track. Jeremy's input to the steering in Nutts Corner is clearly greater in reality. There is also a good correlation between the recorded and estimated steering angle in Fig. 5.17. The large steering movements around the upright position visible on Jeremy's data are absent because direction changes by a novice rider are much more tentative.

The relationship between steering and roll angle in Fig. 5.17 is clearly different from that in Fig. 5.16. This may be due to the fact that, not having ridden on a race track in many years, the writer has the habit, common among novice riders, of not shifting his weight to the inside on approaching a corner and then keeping his body too upright while in the corner. The shift in mass centre between professional and novice riders is one of the key differences between them.

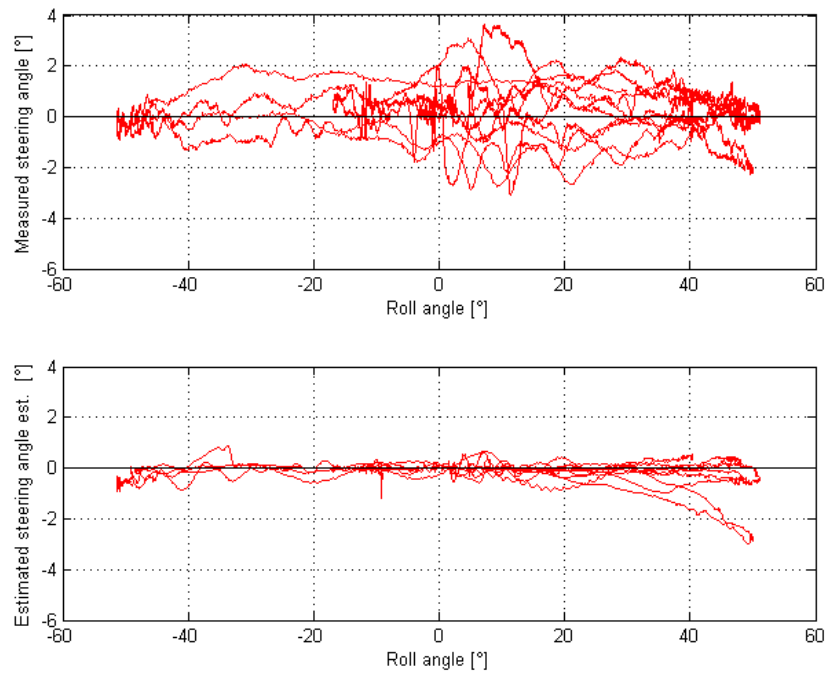


Figure 5.16: Steering angle vs. roll angle in Nutts Corner using adjusted set of tyre parameters

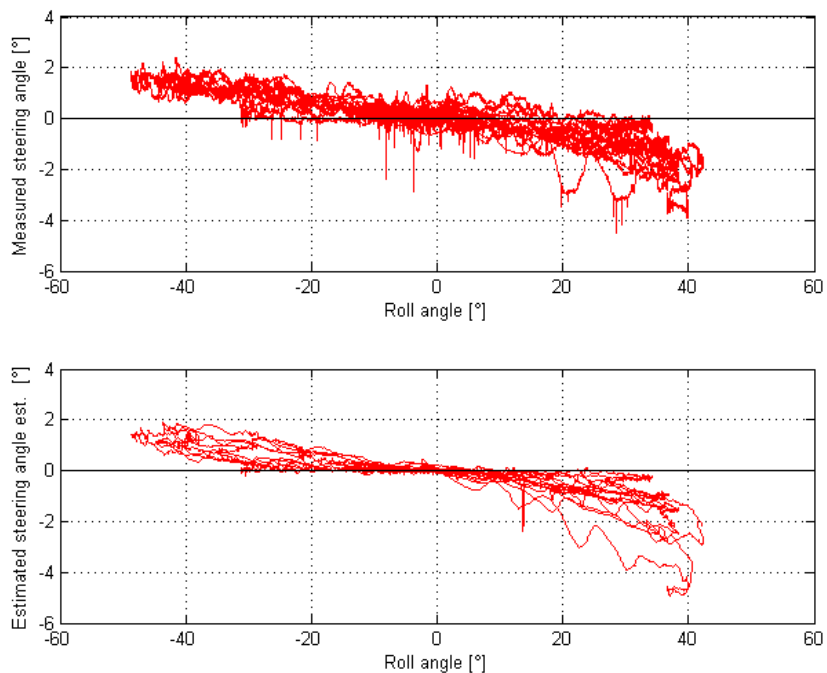


Figure 5.17: Steering angle vs. roll angle in Mondello Park using adjusted set of tyre parameters

## 5.5 Tyre profile

The co-ordinates, in the wheel local reference frame, of the tyre to ground contact point must be available as a function of wheel camber angle, so the tyre profiles

had to be measured. This was done by fixing a number of small pieces of card together as a template, so that each edge was at a tangent to the tyre profile as shown in Fig. 5.18. The co-ordinates of the tangent points were transferred to graph paper as shown in Fig. 5.19, and measured. This photo also shows the orientation of the  $y$  and  $z$  axes in the tyre local co-ordinate system. The marks labelled  $A$  are the end points of the tread and are used to align and centre the template. The measured points are shown in Table 5.6. Using a tape measure, the centre-line circumference of the front and rear tyres were found to be 1905 mm and 2013 mm respectively, corresponding to unloaded rolling radii of 303.2 mm and 320.4 mm respectively. The  $z$  co-ordinates in Table 5.6 are relative to the edge of the tread and must be combined with the rolling radius to find their true values. As none of the measured tangent points happen to be on the centre line, a sensible  $z$  value was chosen visually on the centre line of the tyre ( $y = 0$ ). These were  $z = 49.5$  for the front and  $z = 56.0$  for the rear. As the measured tangent points are asymmetrical, they were mirrored to effectively double the number of measurements on each side of the tyre, thereby reducing the measurement error. This resulted in the values shown in the left-hand pair of columns in Tables 5.7 and 5.8.



Figure 5.18: Card template on front tyre

Front		Rear	
y	z	y	z
-59.5	0.0	-92.0	0.0
-54.0	13.5	-81.5	15.5
-35.5	37.5	-64.0	34.5
-14.5	48.5	-46.0	46.0
10.5	48.5	-22.0	54.0
32.0	41.0	4.0	56.0
50.0	23.0	26.0	53.0
59.5	0.0	43.5	47.0
		61.0	36.5
		82.0	14.0
		92.0	0.0

Table 5.6: Measured tyre profile tangent points

Measured		Profile fitting function and absolute error					
y	z	Circle	Error	Ellipse	Error	Poly.	Error
0.0	303.2	303.1	0.082	303.2	0.000	303.5	0.292
10.5	302.2	302.2	0.000	302.3	0.074	302.5	0.310
14.5	302.2	301.3	0.845	301.4	0.778	301.6	0.572
32.0	294.7	294.0	0.733	294.0	0.731	294.3	0.389
35.5	291.2	291.6	0.414	291.6	0.397	292.0	0.775
50.0	276.7	276.7	0.002	276.6	0.120	275.7	0.957
54.0	267.2	269.9	2.733	269.8	2.584	268.0	0.850
59.5	253.7	253.7	0.000	253.7	0.000	253.5	0.164
			4.809			4.683	4.308

Table 5.7: Front tyre profile, measured and fitted

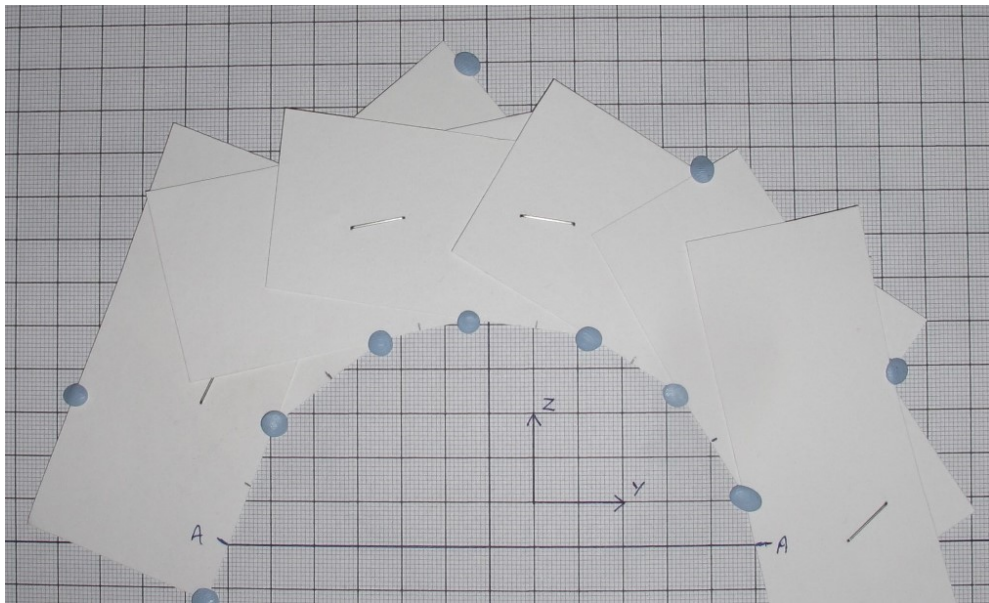


Figure 5.19: Transferring tyre profile tangent points to graph paper

Once the tyre profile had been measured, a function was needed to describe the tyre profile as accurately as possible. Three candidate functions were compared; a semicircle, a semi-ellipse and a polynomial. The formulas for the semicircle and semi-ellipse are as follows, with the parameters as shown in Fig. 5.20.

$$z = \sqrt{r^2 - y^2} + c \quad \text{semicircle}$$

$$z = \frac{b}{a} \sqrt{a^2 - y^2} + c \quad \text{semi-ellipse}$$

These functions were fitted to the measured data by optimising the parameters

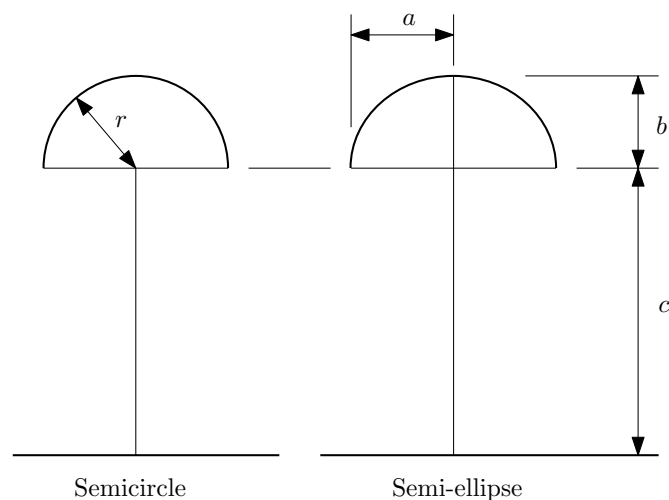


Figure 5.20: Tyre profile semicircle and semi-ellipse

Measured		Profile fitting function and absolute error					
y	z	Circle	Error	Ellipse	Error	Poly.	Error
0.0	320.4	321.4	0.990	320.7	0.271	320.4	0.023
4.0	320.4	321.3	0.910	320.6	0.195	320.3	0.043
22.0	318.4	318.9	0.533	318.3	0.060	318.3	0.040
26.0	317.4	317.9	0.541	317.4	0.000	317.5	0.097
43.5	311.4	311.4	0.000	311.2	0.186	311.4	0.057
46.0	310.4	310.1	0.256	310.0	0.371	310.2	0.158
61.0	299.9	300.5	0.651	301.0	1.111	300.6	0.733
64.0	298.9	298.1	0.764	298.7	0.148	298.2	0.727
81.5	279.9	279.1	0.784	281.2	1.288	279.5	0.370
82.0	278.4	278.4	0.001	280.5	2.138	278.9	0.480
92.0	264.4	260.1	4.293	264.4	0.000	264.3	0.040
		9.724		5.767		2.767	

Table 5.8: Rear tyre profile, measured and fitted

$a$ ,  $b$ ,  $c$  and  $r$ , using the ‘golden section’ method [55] to minimise the overall error in  $z$ . The fitted  $z$  values along with their errors, and the overall error in  $z$  for these functions are shown in Tables 5.7 and 5.8.

A sixth order polynomial was found to work well and, because the tyre profile is symmetrical, only even terms are needed. This has the form:

$$z = f(y) = a_1y^6 + a_2y^4 + a_3y^2 + a_4 \quad (5.17)$$

The coefficients  $a_1 \dots a_4$  were found using the least squares curve fitting method on the measured data in Tables 5.7 and 5.8, with the data mirrored about the centre line of the tyre to represent the complete profile. The fitted values and their errors are shown in the right-hand pair of columns in those tables and the overall error in  $z$  is shown at the bottom. In Table 5.7, for the front tyre, it is clear from the overall  $z$  errors that all three functions fit the measured data more-or-less equally well, which implies that the tyre profile is approximately semi-circular. The rear tyre data in Table 5.8, on the other hand, shows a marked difference in the overall  $z$  error for the three functions, with the polynomial giving the best quality fit. This implies, within the margin for measurement error, that the rear tyre profile is more complex than a semi-ellipse. Fig. 5.21 shows the measured

points for both the front and rear tyres, along with the fitted functions. The plot verifies that all three function types can model the front tyre quite well, but the rear tyre shows an increase in radius, i.e. a flattening of the profile, near the edge of the tyre that cannot be modelled well by either a semicircle or a semi-ellipse. In fact, the semicircle function gives a noticeably poor fit overall. It was therefore decided to proceed using the polynomial function.

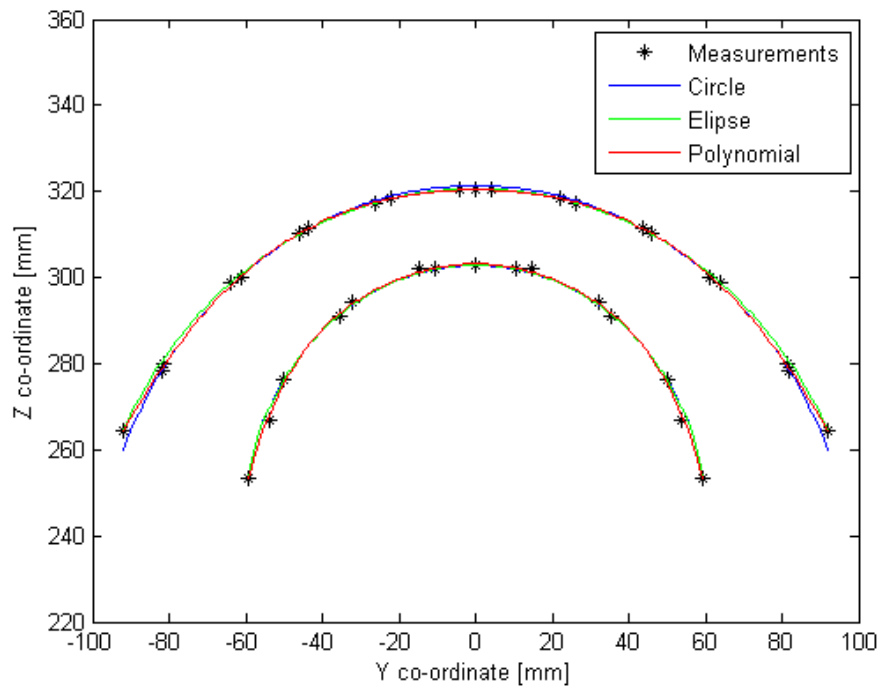


Figure 5.21: Tyre profile measurements and fitted functions

The camber angle is the tangent to the tyre profile at any point, or in other words, the rate of change of  $z$  with respect to  $y$ , i.e.

$$\gamma = \frac{dz}{dy} = 6a_1y^5 + 4a_2y^3 + 2a_3y$$

Now,  $z$  and  $\gamma$  can be expressed in terms of  $y$ , so it is possible to create an array of  $y$  values and calculate arrays of corresponding  $z$  and  $\gamma$  values. The curve fitting procedure can now be repeated to find polynomials describing the co-ordinates  $y$

and  $z$  in terms of  $\gamma$ , as follows:

$$y = b_1\gamma^5 + b_2\gamma^3 + b_3\gamma \quad (5.18)$$

$$z = c_1\gamma^6 + c_2\gamma^4 + c_3\gamma^2 + c_4 \quad (5.19)$$

Note that  $y$  is asymmetrical and uses only odd terms while  $z$  is symmetrical and uses only even terms. Eqn. (5.18) is plotted in Fig. 5.22 and Eqn. (5.19) is plotted in Fig. 5.23. It is interesting to note from Fig. 5.23 that with a matched pair of supersport tyres, the vertical height,  $Z$ , of the front and rear are equal at around  $50^\circ$  bank angle. In other words, at the point where the rider is at maximum lean, the tyres do not impose a pitch angle on the bike. For validation, Fig. 5.24 shows

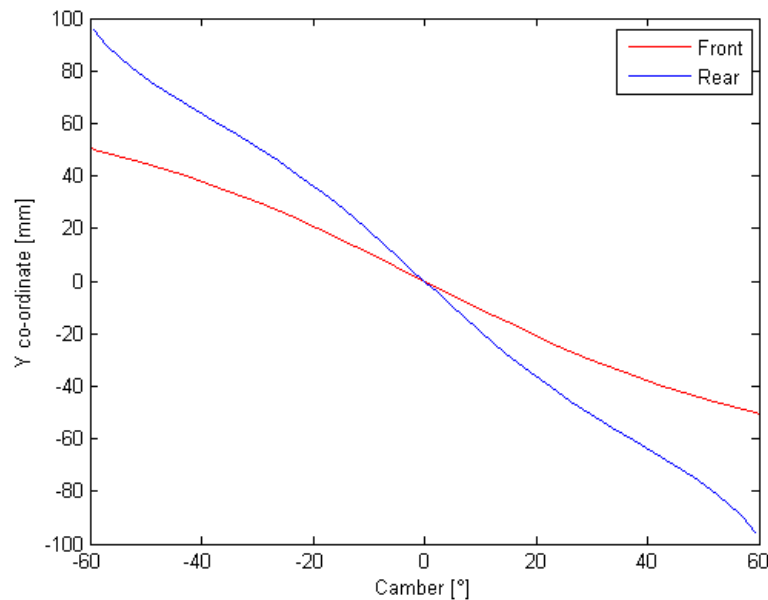


Figure 5.22: Tyre Y co-ordinate versus camber

the polynomials for  $y$  and  $z$  in Eqns. (5.18) and (5.19) plotted against each other and overlaid with the measurement points from Tables 5.7 and 5.8. The results look identical to Fig. 5.21. The coefficients in Eqns. (5.17), (5.18) and (5.19) are shown in Tables 5.9 and 5.10.

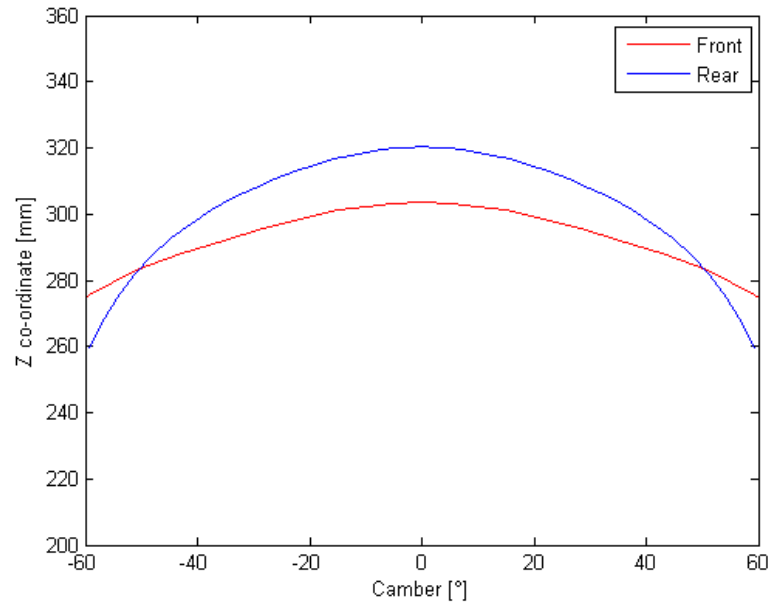
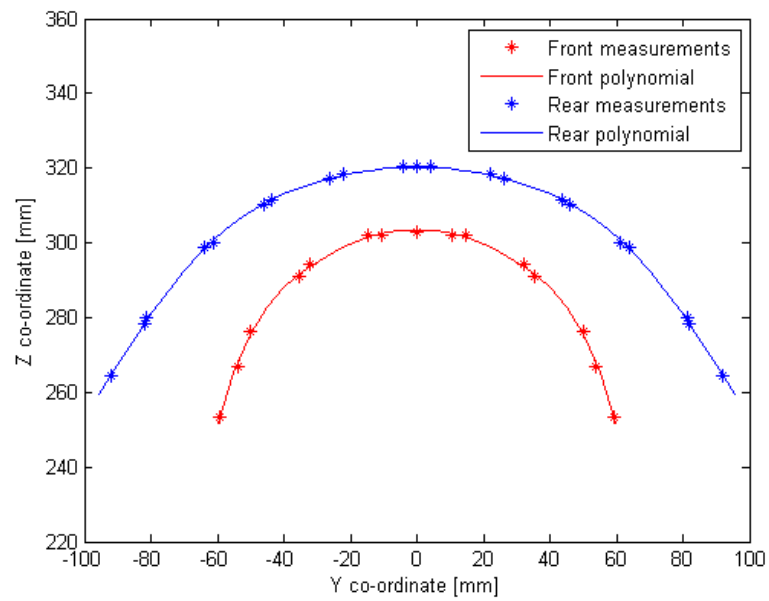


Figure 5.23: Tyre Z co-ordinate versus camber

Figure 5.24: Tyre profile measurements and polynomials in  $\gamma$ 

Coeff.	a	b	c
1	$-5.759 \times 10^5$	$-6.188 \times 10^{-3}$	$-1.320 \times 10^{-2}$
2	$5.839 \times 10^2$	$1.954 \times 10^{-2}$	$2.487 \times 10^{-2}$
3	-8.960	$-6.240 \times 10^{-2}$	$-3.755 \times 10^{-2}$
4	0.3035		0.3034

Table 5.9: Front tyre profile polynomial coefficients

Coeff.	a	b	c
1	$6.406 \times 10^3$	$-3.936 \times 10^{-2}$	$-3.133 \times 10^{-2}$
2	$-3.533 \times 10^2$	$5.961 \times 10^{-2}$	$2.816 \times 10^{-2}$
3	-4.093	-0.1109	$-5.060 \times 10^{-2}$
4	0.3204		0.3202

Table 5.10: Rear tyre profile polynomial coefficients

# Chapter 6

## Sensing and Data Logging

This chapter explains how the data used in the thesis was recorded and processed. The data recording hardware, its interface to the motorcycle and the sensors are explained in detail. The data recording configuration and analysis software is also covered.

### 6.1 Introduction

A 2004 model Honda CBR600RR was used to record the data. Although the bike is street legal, the most important data for the thesis was recorded at Nutts Corner race track in Northern Ireland, where the bike was ridden by professional motorcycle racer and test rider Jeremy McWilliams. [54] This allowed the bike to be ridden at a performance level that would be unattainable in other circumstances. ‘Coast-down’ testing was carried out to measure aerodynamic and mechanical drag, and a preliminary validation test was performed by the writer at Mondello Park race circuit to confirm the operation of the bike and data recording equipment. The data recording system was supplied by 2D Debus & Diebold Meßsysteme GmbH, also known as 2D Datarecoding. 2D have been at the forefront of data recording in motorcycle racing since the early 1990s and both their hardware and software are very well suited to motorcycles.

The criteria for choosing the recorded channels are as follows. Wheel torques are important inputs to the dynamic model but it is difficult to measure them

directly on a motorcycle. Negative wheel torque may be estimated from measured brake pressures. Positive rear wheel torque is a function of engine torque and overall drive-train gear ratio. The engine torque is itself a function of throttle position and engine speed so it may be accessed from a table, which is indexed by those measured values. Front and rear wheel angular velocities were recorded as they are used in the controller for the model. Steering, suspension positions and GPS location and speed were recorded for validation purposes. An IMU is attached to the main frame and this provided accelerations and angular velocities on three orthogonal axes. These were used for both control and model validation. On the CBR600RR, the signal for the speedometer is generated by a Hall effect sensor which is triggered by one of the gears on the gearbox output shaft. By comparing the engine speed to the pulse frequency, and knowing the gear ratios, it was found that the sensor takes its reading from the 6th gear wheel. This channel was also recorded for data validation because although the chain drive creates a dead-band non-linearity between the gearbox output shaft and the rear wheel, the output shaft speed is captured at much higher resolution than the four pulses per revolution of the rear wheel speed sensor.

The main track test was carried out at Nutts Corner circuit in dry conditions with Jeremy McWilliams riding the bike. Two runs were made. The first was three timed laps to check the bike and data recording equipment. The second was a run of seven timed laps. The data in the thesis is from two consecutive laps in the second run with lap-times 38.508 and 38.015 seconds respectively.

Coast-down testing is the term used when the bike is allowed to slow down from high speed without using the brakes. This may be done with the clutch disengaged, in which case, engine frictional torque does not contribute to deceleration. Alternatively, the bike may be allowed to decelerate with the clutch engaged so that engine frictional torque is a contributing factor. The effect of engine frictional torque can be isolated by comparing both tests. The coast-down tests were performed on a level piece of road in calm and dry conditions. The tests to isolate engine frictional torque were carried out in fourth gear. The high speed coast-down runs with the clutch disengaged are primarily to estimate aero-

dynamic drag and were performed with the rider presenting the lowest possible frontal area.

## 6.2 Data logging hardware overview

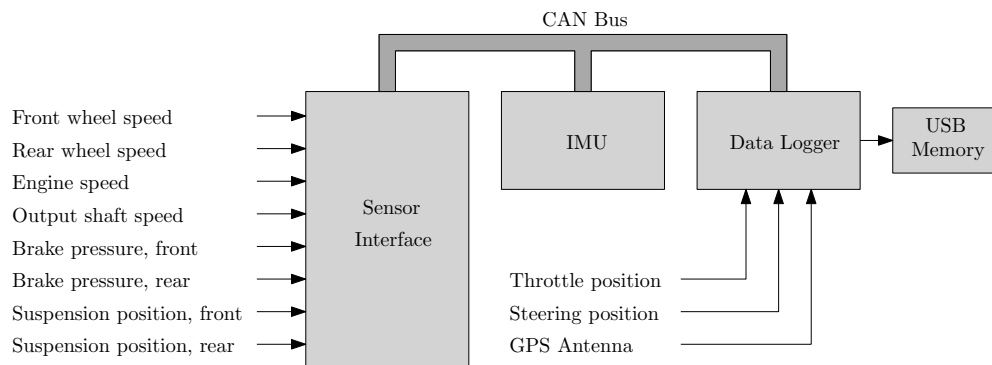


Figure 6.1: Data logger and sensor interface unit

The data recording hardware consists of a data logger, a sensor interface module, and various sensors as shown in Fig. 6.1. The data logger, sensor interface and the IMU are connected by CAN bus. The 2004 CBR600RR does not have a CAN bus, so it was necessary to splice into the bike wiring harness to measure throttle position, engine speed and output shaft speed.

## 6.3 The CAN bus

The CAN bus is ubiquitous in the automotive world. It is a bus standard designed to allow electronic control units to communicate with each other without a host computer. Devices connected to the bus are called nodes, and the nodes broadcast messages that can be ‘heard’ by every other node. The nodes are connected to the bus in wired-AND fashion. This means that if any node is broadcasting a logical 0, the entire bus is in logical 0 state, regardless of how many nodes are broadcasting a logical 1. It is a two wire bus, CAN-H (high) and CAN-L (low), and uses a differential voltage. When the bus is in logical 1 state, both wires are at 2.5 volts. At logical 0, the CAN-H wire goes to 3.75 volts and CAN-L goes to 1.25 volt, creating a differential of 2.5 volts. To prevent reflections on the

cable, the bus is terminated at each end by  $120\Omega$  resistors. These can be set on a 2D CAN module by checking a box in the setting software. The 2D CAN bus conforms to ISO 11898-2 high speed CAN standard [56], and all modules have a default baud rate of 1 Mbaud. The standard CAN data frame consists of the following eight fields:

- 1 bit SOF (start of frame) forces the bus to logical zero to tell all nodes that a message is coming.
- 29 bit CAN ID contains the CAN address of the sender as well as the message priority. Other nodes read this and decide if the message is of interest to them.
- 1 bit RTR (remote transmission request) allows nodes to request messages from other nodes.
- 6 bit CONTROL informs the length of the data in bytes (0 to 8 bytes).
- 0-64 bit DATA contains the transmitted data.
- 16 bit CRC (cyclic redundancy check) checks data integrity.
- 2 bit ACK indicates if the CRC process was successful.
- 7 bit EOF marks the end of the CAN message.

The 64 bit data frame means that each frame can hold data samples from four 16 bit channels, so 2D modules allow data from four channels to be sent in the same data frame, which means they share the same CAN ID. The setting software allows this to be configured in the module that is sending the data. The setting software also configures the data logger to choose which channels to log from the CAN bus, based on their CAN ID and position in the data frame. Data can be placed in the frame using either the ‘big-endian’ or ‘little-endian’ convention. Big and little-endian refers to the order in which bytes are arranged into larger numerical values. Fig. 6.2 shows the data-logger setting dialog that configures a CAN channel to be recorded from the bus. The CAN ID is 0x499 and the data

is expected to be stored in big-endian format in bytes 0 and 1. The channel will be sampled from the CAN bus 800 times per second. The data format when displayed numerically can be set and the data can be filtered if required.

The image shows a configuration window for a CAN channel. It is divided into three main sections: Samplingrate, Parameter, and Display. In the Samplingrate section, the Samplingrate (Hz) is set to 800 and the Resolution is 16 bit. The Parameter section includes an ID field with the value 0x499, a Data field with bits Hi, Lo, 2, 3, 4, 5, 6, and 7, a Data format section with radio buttons for Little Endian (I) and Big Endian (M) (which is selected), and an unchecked checkbox for IEEE 32 bit float. The Display section has a Filter dropdown set to No Filter, a Length input field set to 5, and a Digits after dot input field set to 2.

Figure 6.2: Configuring a CAN channel

## 6.4 The data logger

The data was recorded using 2D's USB stick logger which records all data directly onto a USB memory stick. A download cable is not necessary as the memory stick is unplugged from the logger and plugged directly into the computer. Changing the logger settings can be done either by copying a setting file to the memory stick or by connecting the logger USB socket to the computer by a standard USB cable. The memory stick must be formatted with a proprietary 2D FAT32 file system, using a 2D formatting utility. The maximum size of a stick is limited only by the FAT32 file system, i.e. up to 8 TB. Although it has two 16 bit analog inputs, and on-board GPS, the logger is designed to receive most of the data via the CAN bus. Data is placed on the bus by the sensor interface unit and IMU, and the logger reads the data from the bus at the appropriate sampling rate.

The data logger may be configured to begin recording after a fixed time. Alternatively, a threshold value may be set on any input channel, and recording begins once the threshold has been crossed. A wheel speed threshold may be used

to ensure that recording commences once the bike begins to move. During set-up and testing when the bike is not running, a throttle position threshold allows the user to start the recording manually by simply opening the throttle. Recording continues until power is disconnected from the logger or until the memory is full.



Figure 6.3: Data logger (right) and sensor interface unit (left) installation

## 6.5 The sensor interface module

The wheel speed, brake pressure, suspension, engine speed and output shaft speed measurements are routed to the sensor interface module, which is connected to the data logger by the CAN bus.

### 6.5.1 Analog channels

The 2D data logger and sensor interface unit, use 16 bit analog to digital converter (ADC)s. The maximum sampling rate is the same as the base sampling rate of the logger, which in this case is 800 samples per second. To minimise aliasing, all channels are sampled at the base sampling rate and an average is calculated depending on the selected sampling rate for each channel. Calibration is by means of a multiplier and offset, as shown.

$$Value = Digits * Multiplier + Offset$$

Calibration may be done in the following ways.

- The multiplier and offset are entered directly.
- As above, but the multiplier is entered as a ratio.
- The upper and lower physical values, and upper and lower digits are entered.
- The sensor is moved through its full range and the upper and lower values are set automatically. For example, this is a convenient way to calibrate throttle position.
- The multiplier is set manually and the offset is set by moving the sensor to the zero position and activating a dialog button. This is a convenient way to calibrate suspension position, where the top-out position is set.

Each channel is given a name and dimension, the format for data display is set and a filter may be applied if required. If the analog input is to a module which will place the data on the CAN bus, the CAN address, location in the data frame and byte order are set.

### 6.5.2 Digital channels

The 2D data logger and sensor interface unit do not have any physical digital inputs. Instead, digital channels use analog channels as their source, to which sensors such as Hall effect or inductive sensors are connected. The sensor interface unit has four digital channels which may be used in this way. A digital channel is chosen and the signal source is set to the appropriate analog channel. A checkbox enables an internal  $10\text{ k}\Omega$  pull-up resistor on the analog channel if required. The digital channel may be set to trigger on the rising or falling edge of the signal. Upper and lower comparator threshold settings allow hysteresis to be set. A timeout value may be set to ignore any spurious pulses following the initial signal pulse. 2D expect digital channels to be used most often for wheel speeds and engine speed, so the setting utility is designed to make it easy to configure these two functions. The details are explained in Sections 6.6.1 and 6.6.5. As with analog channels, the digital channel is given a name and dimension, the data format is set, and a filter may be applied if required. If the digital channel is in a module which will place its data on the CAN bus, then the CAN address, location in the data frame and byte order are set.

## 6.6 Recorded channels

The recorded measurements are as follows:

- Engine speed
- Throttle position
- IMU rate gyros and accelerometers
- Front wheel angular velocity
- Rear wheel angular velocity
- Front suspension position
- Rear suspension position

- Steering position
- Front brake pressure
- Rear brake pressure
- Gearbox output shaft speed
- GPS position and speed

### 6.6.1 Engine speed

The CBR600RR determines the crankshaft position by means of two inductive sensors, one on the crankshaft and one on the exhaust camshaft. The crankshaft sensor is excited by a toothed wheel with twelve evenly spaced teeth, which are oriented accurately with respect to crankshaft position. This is shown in Fig. 6.4. The camshaft sensor provides a reference pulse to indicate whether the engine position is in the  $0^\circ$  to  $360^\circ$  or  $360^\circ$  to  $720^\circ$  range, and to notify the engine control unit (ECU) that the following crankshaft pulse denotes the reference crankshaft position. The crankshaft sensor signal is routed to an analog input on the sensor interface unit. Fig. 6.5 shows how an engine speed channel is configured on the 2D system. A digital channel is chosen and the source is set to the analog engine speed channel. Upper and lower comparator threshold settings allow hysteresis. A timeout value may be set to ignore any spurious pulses following the signal pulse. The number of pulses on the toothed wheel are set, in this case twelve. If the toothed wheel revolves at engine speed, the circumference parameter is set to 1. If the toothed wheel revolves at half engine speed, as in the case of a camshaft, the circumference is set to 2. The sample rate is chosen and the data display format is set. A filter may be applied if required. The CAN parameters are also set.

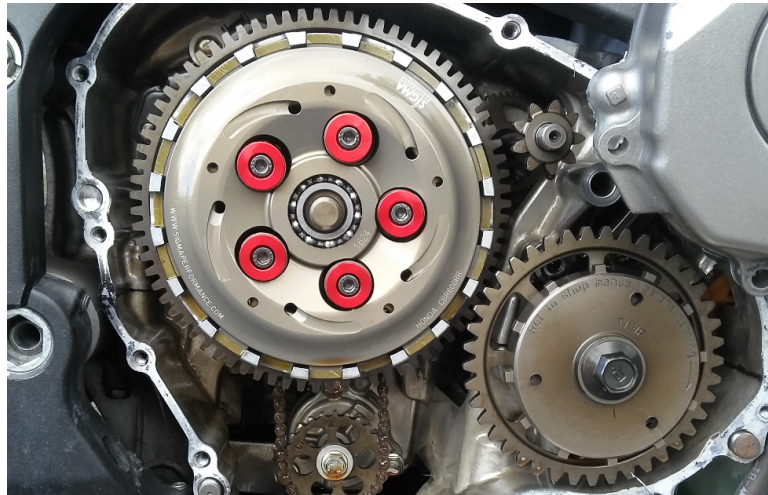


Figure 6.4: CBR600RR crankshaft trigger wheel, bottom right (12 pulses per revolution). The back-torque limiting clutch is also shown.

Samplingrate	
Samplingrate (Hz)	200
Resolution	16 bit
Parameter	
Circumference (mm)	1
Pulses	12
Timeout (µsec)	0
Digital threshold	50
Source channel	RPM_analog (Ch 3)
Lower trigger border (%)	25 <-> 16384 Digits
Upper trigger border (%)	75 <-> 49151 Digits
Display	
Filter	No Filter
Length	5 *****
Digits after dot	0

Figure 6.5: Engine speed channel setting

### 6.6.2 Throttle position

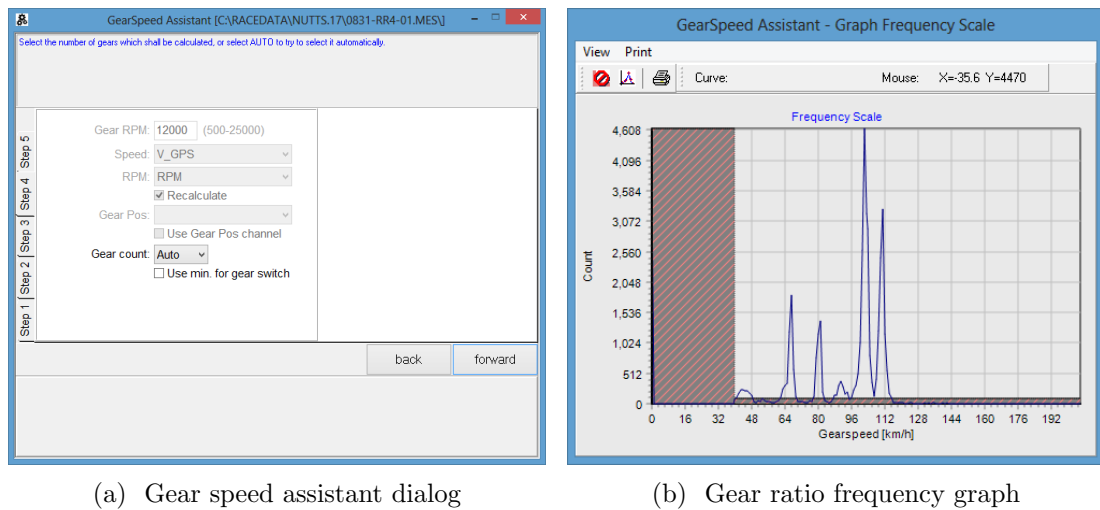
Throttle position is measured by a rotary potentiometer on the throttle body and the signal is routed to the ECU. The signal wire was spliced and routed to an analog channel input on the data logger. The channel was calibrated using the 2D setting software. For channels with clearly defined upper and lower limits, the software provides a function whereby the sensor is moved through its full range and the limits are set automatically.

### 6.6.3 Gear position

Rear wheel torque is the engine torque divided by the primary, gearbox and final drive gear ratios, as shown in Table 6.1. The selected gearbox ratio at every point in time must therefore be known. The CBR600RR does not have a gear position sensor, so a gear position channel is calculated using the ‘gear speed assistant’ feature of the 2D software. This calculates the ratio between engine speed and vehicle speed at every sampling interval. The vehicle speed channel can be chosen as a wheel speed or, as in this case, GPS speed. The user selects a value of engine speed for which the calculation will be done, in this case, 12,000 rpm. The speed ratio must take on discrete values depending on which gear is engaged and these are used to calculate a gear position channel. Fig. 6.6 shows the dialog and frequency graph of the gear speed assistant. The horizontal axis of the frequency graph is vehicle speed as measured by GPS. The vertical axis is the frequency at which engine speed matches the chosen value.

	Drive	Driven
1 <sup>st</sup>	12	32
2 <sup>nd</sup>	16	31
3 <sup>rd</sup>	18	29
4 <sup>th</sup>	22	31
5 <sup>th</sup>	23	29
6 <sup>th</sup>	24	28
Primary	36	76
Final	14	42

Table 6.1: Gear ratios (number of teeth)



(a) Gear speed assistant dialog

(b) Gear ratio frequency graph

Figure 6.6: The 2D gear speed assistant

### 6.6.4 The inertial measurement unit

The IMU houses three accelerometers and three rate gyros, mounted orthogonally. The axis orientation is shown in Fig. 6.7. Gyro orientation uses the right-hand rule, i.e. if an axis is grasped with the right hand, with the thumb pointing in the positive direction, then the fingers point in the positive direction of rotation. Each sensor is sampled internally at 1600 Hz, and a moving average is calculated depending on the selected sampling rate, so for example, if the user selects a sampling rate of 100 Hz, then every 16 samples are averaged. In the test data, the sampling rate is 800 Hz, which is the highest sampling rate possible. This was chosen to allow maximum scope for any necessary post-processing, i.e. filtering.

The mounting bracket for the headlight and instrument assembly was chosen as the location for the IMU. This is fixed rigidly to the main frame. A support bracket for the IMU was designed using computer-aided design (CAD) software, as shown in Fig. 6.8. The internal angle in the IMU support bracket was chosen as follows. The bike was suspended with the wheels equidistant above level ground, as shown in Fig. 6.9. A spirit level and clinometer were used to measure the angle of the bike bracket to the horizontal. The IMU support bracket was 3D printed by Maynooth University Library, using maximum infill to create a solid block. Various measures were tested to minimise the effect of engine vibration, which particularly affected the vertical accelerometer. Fig. 6.10 shows the IMU

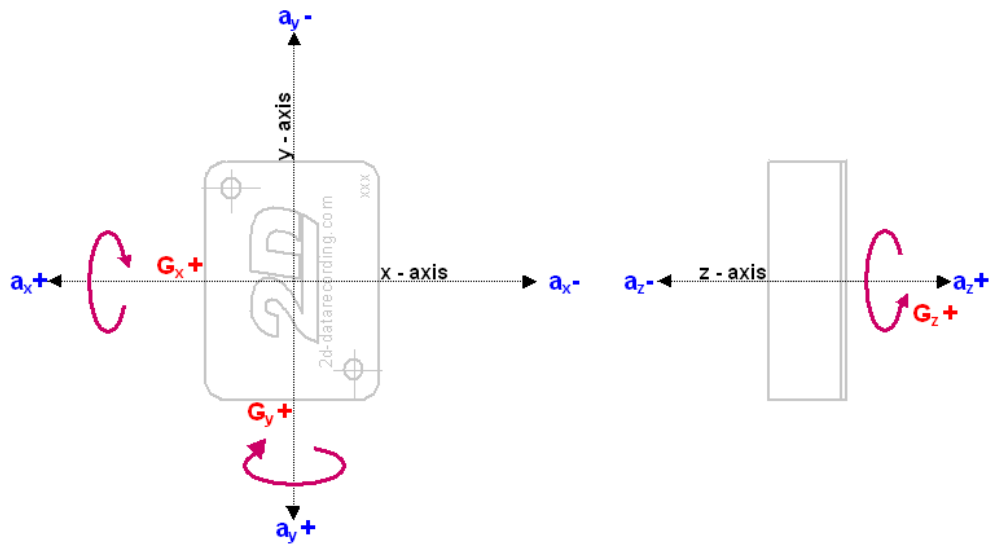


Figure 6.7: Orientation of IMU axes. Figure courtesy of 2D Datarecording

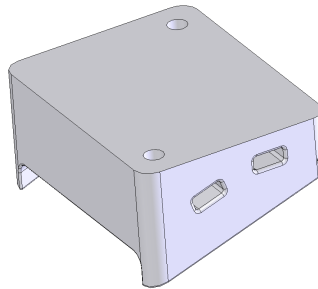


Figure 6.8: IMU mounting bracket



Figure 6.9: Preparation for IMU mounting

mounted on a block of Sorbothane viscoelastic material which is often used as a vibration damper. This arrangement was unsatisfactory as it introduced ad-

ditional dynamic behaviour of the IMU. The arrangement which minimised the effects of engine vibration was to fill the hollow bike bracket with aluminium-impregnated epoxy resin as shown in Fig. 6.12. This increased the mass and rigidity of the bracket, and reduced its tendency to resonate. The IMU is also shown in Fig. 6.13.

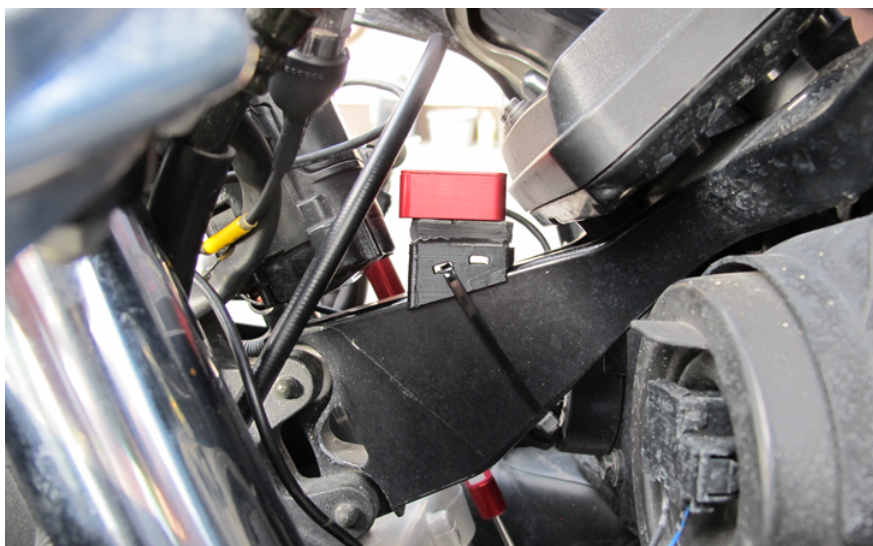


Figure 6.10: The IMU mounted on a Sorbothane pad



Figure 6.11: The IMU final mounting arrangement



Figure 6.12: Aluminium epoxy filler in the instrument mounting bracket



Figure 6.13: IMU and front suspension stroke sensor

### 6.6.5 Front wheel speed

The 2004 CBR600RR is not equipped with anti-lock brakes, so wheel speed sensors are not fitted as standard. The first approach was to source components from a later ABS equipped model. Fig. 6.14. shows a later-model ABS trigger ring fitted. Unfortunately, as the photograph shows, there was insufficient clearance between the ring and the fork leg so this approach had to be abandoned. Instead, it was decided to use the six brake disc mounting bolts to trigger a proximity sensor. A mounting bracket was drawn in CAD, as shown in Fig. 6.15, and plasma-cut from sheet steel to allow a Hall effect sensor to be mounted adjacent to the bolts, as shown in Fig. 6.16. Although the resolution of six pulses per revolution is much lower than the fifty pulses per revolution of the ABS trigger disc, it proved to be more than adequate.



Figure 6.14: Front wheel speed sensor ring from later model

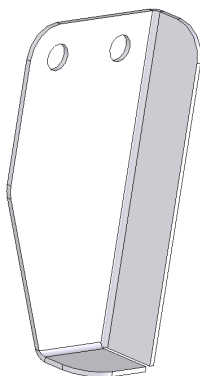


Figure 6.15: Front wheel speed sensor mounting bracket (sheet metal)



Figure 6.16: Front wheel speed sensor

The 2D setting software dialogs for the front wheel speed channel are shown in Fig. 6.17. This is a digital channel, so the analog channel to which the sensor is connected must be selected as the signal source. The nominal wheel circumference and number of pulses per revolution are set. Triggering thresholds and a time-out allow hysteresis to be set, and spurious pulses following the primary pulse to be disregarded. A filter may be applied and the numerical format of the displayed data may be set.

The image shows two dialog boxes for configuring a front wheel speed (FWS) channel.   
 Dialog (a) 'General dialog tab' includes:   
 - Name: FWS   
 - Dimension: km/h   
 - Short cut:   
 - Channel-Type: Digital   
 - Channel-Mode:   
 - Recording:    
 - Use table:    
 - Internal linearization:    
 - Auto zero:    
 - Alarm enabled:    
 - Error-info enabled:    
 - Turned on:    
 - Use extension for formula:    
 - Pullup active:    
 - Use rising edge:    
 - High voltage sensor:    
 - Fixpoint calibration:    
 - Hide parameters:    
 - 2 Wire current sensor:    
 Dialog (b) 'Parameters dialog tab' includes:   
 - Samplingrate:   
 - Samplingrate (Hz): 200   
 - Resolution: 16 bit   
 - Parameter:   
 - Circumference (mm): 1882   
 - Pulses: 6   
 - Timeout (usec): 0   
 - Digital threshold: 50   
 - Source channel: FWS\_analog (Ch 1)   
 - Lower trigger border (%): 1 <-> 655 Digits   
 - Upper trigger border (%): 10 <-> 6554 Digits   
 - Display:   
 - Filter: No Filter   
 - Length: 5   
 - Digits after dot: 2

(a) General dialog tab

(b) Parameters dialog tab

Figure 6.17: Front wheel speed channel setting

### 6.6.6 Rear wheel speed

As in the case of front wheel speed, it proved impossible to fit ABS wheel speed components from a later model bike, so the four rear brake disc mounting bolts are used to trigger a proximity sensor, as shown in Fig. 6.18. A bracket to mount the Hall effect sensor was welded to the existing rear brake mounting bracket. As in the case of front wheel speed, this resolution proved to be more than adequate. Configuration of the rear wheel speed channel is similar to the front wheel speed as explained in Section 6.6.5.



Figure 6.18: Rear wheel speed and rear brake pressure sensors

### 6.6.7 Front suspension position

The front suspension stroke sensor is a linear potentiometer and a reference voltage of 5v is supplied by the sensor interface unit. The sensor is fitted to the left-hand fork leg, as shown in Figs. 6.20 and 6.13. The upper end is mounted to the fork clamp using a small metal bracket. The lower bracket shown in Fig. 6.19 was drawn in CAD, and 3D printed by Maynooth University Library. Maximum infill was used to create a solid part that could be used structurally in this role. The bracket locates in a groove in the lower fork leg and is secured by adhesive and a cable tie. The stroke of the sensor is 150 mm and the ADC is 16 bit, so when calibrating the sensor, the multiplier is set to  $\frac{150}{2^{16}-1}$ . The offset is set by suspending the bike with the wheel off the ground and activating a dialog button to ‘zero’ the channel.



Figure 6.19: 3D printed brackets

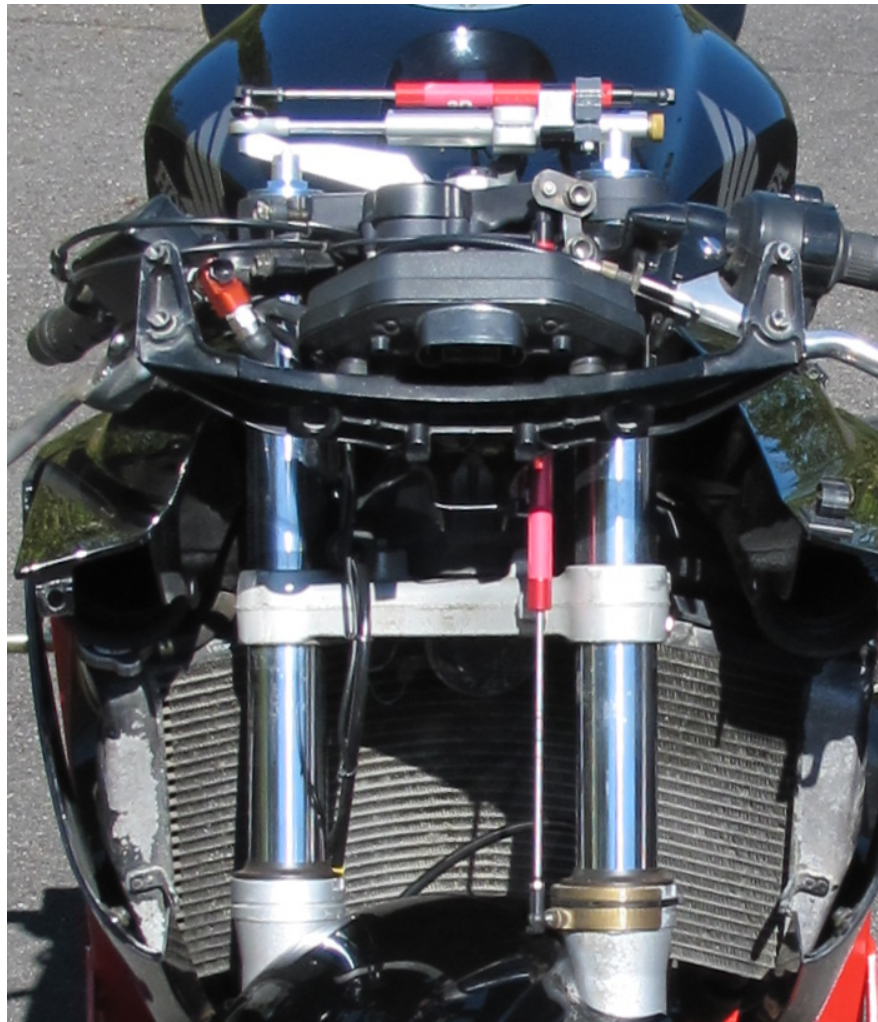


Figure 6.20: Front suspension stroke sensor mounted on left-hand fork leg. Steering and front brake pressure sensors are also shown

### 6.6.8 Rear suspension position

The rear suspension stroke sensor is a linear potentiometer and is shown in Fig. 6.21. A reference voltage of 5v is supplied by the sensor interface unit. The signal from the sensor must provide two measurements; swing-arm angle, which is a state variable in the model, and shock absorber position, which is needed to calculate the spring and damping forces. Ideally, the stroke sensor would be mounted on the shock absorber and measure its stroke directly. However, the shock absorber installation on the CBR600RR is not spacious, so this was impossible. Instead, it is mounted as shown in Fig. 6.22, and the geometry was measured with the suspension fully extended.  $A$  is the length of the stroke sensor with the suspension fully extended:  $A = 241$  mm,  $B = 485$  mm, and  $C = 370$  mm. The swing-arm angle and shock absorber length at full extension of the suspension are known from the bike geometry, and the angle change of the swing-arm from the fully extended position is easily calculated from the stroke sensor displacement. The swing-arm angle to the horizontal\* is created as a calculated channel in post-processing. This measurement is the state variable  $q_2$ . The shock absorber displacement is created as a calculated channel using the geometry of the rear suspension linkage as shown in Fig. 6.23.

The rear stroke sensor was calibrated in a similar way to the front, as described in Section 6.6.7. The sensor stroke is 75 mm and the ADC is 16 bit, so the multiplier is  $\frac{75}{2^{16}-1}$ . The zero-travel position is calibrated with the wheel off the ground, i.e. with the rear suspension fully extended. As with the front stroke sensor, the channel is ‘zeroed’ using a dialog button in the calibration software.

---

\* This refers to the horizontal in reference frame  $A$ , i.e. the reference frame which is aligned with the main frame of the bike.



Figure 6.21: Rear suspension stroke sensor

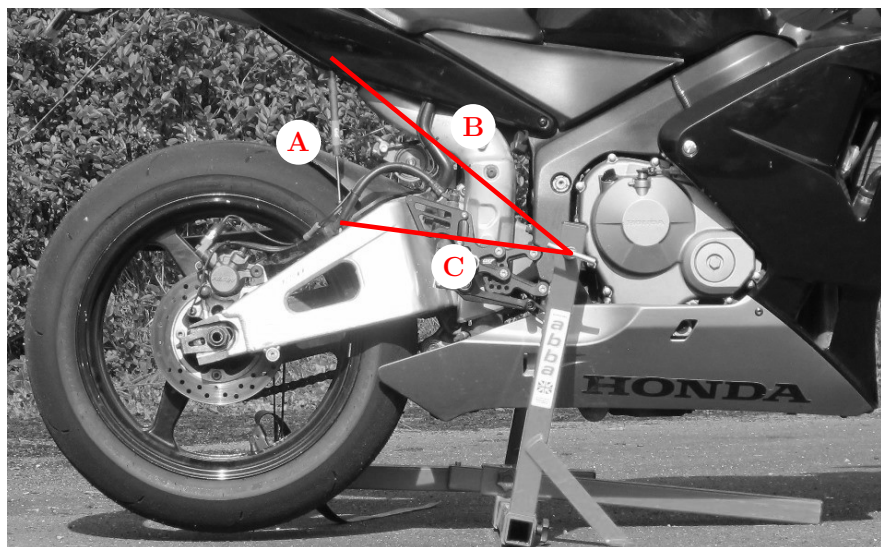
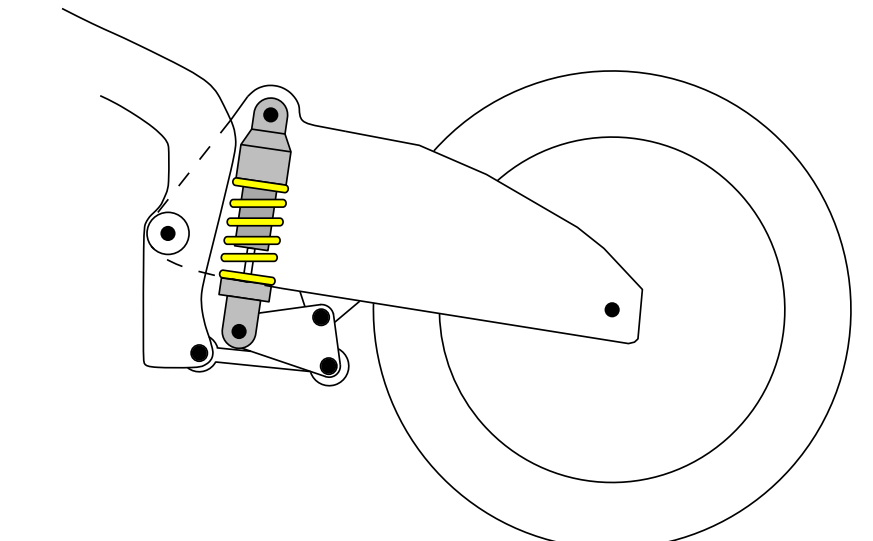


Figure 6.22: Rear stroke sensor geometry



---

Figure 6.23: The Unit Pro-link rear suspension system

### 6.6.9 Steering angle

The steering position is measured using a similar 75 mm stroke sensor mounted on the steering damper, as shown in Fig. 6.24. The mounting bracket shown in Fig. 6.19 was drawn in CAD and 3D printed by Maynooth University Library with solid infill, so that it could be used as a structural part. The sensor calibration is identical to the rear stroke sensor except that the channel is zeroed with the steering in the straight ahead position. The mounting geometry of the steering damper is used to convert the linear stroke to steering angle in post-processing.



Figure 6.24: Steering sensor in place on the steering damper

### 6.6.10 Brake pressures

Front and rear hydraulic brake pressures are measured using pressure sensors with a range of 0 to 100 Bar. The sensor installations are shown in Figs. 6.25 and 6.18. The calibration multiplier for both pressure sensors are  $\frac{100}{2^{16}-1}$  and the offset is zero. The relationship between brake pressures and wheel torques could be calculated with reference to brake disc swept area and brake pad friction coefficients if available, but in fact proportional constants were found by matching deceleration rates, after other factors such as aerodynamic and mechanical drag had been established.



Figure 6.25: Front brake pressure sensor

### 6.6.11 Calculating wheel torques

Rear wheel drive torque is calculated from engine torque and gear position, which are described in Sections 4.7 and 6.6.3. Front and rear wheel braking torque are estimated from front and rear brake pressure as described in Section 6.6.10.

### 6.6.12 GPS

The GPS channels are primarily used for data validation. The GPS position is used to validate the vehicle X and Y positions calculated by the model. The GPS speed channel has a low sample rate and is lagged with respect to actual vehicle speed, but nevertheless is a useful reference when setting up the wheel speed channels. Front wheel speed is affected by wheelies and rear wheel speed by tyre slip, especially on corner entry. GPS speed has the advantage that it is unaffected by these and it was chosen as the speed channel when calculating the gear position, as explained in Section 6.6.3.



Figure 6.26: The GPS Antenna mounted on the tail unit

## 6.7 Coast-down testing

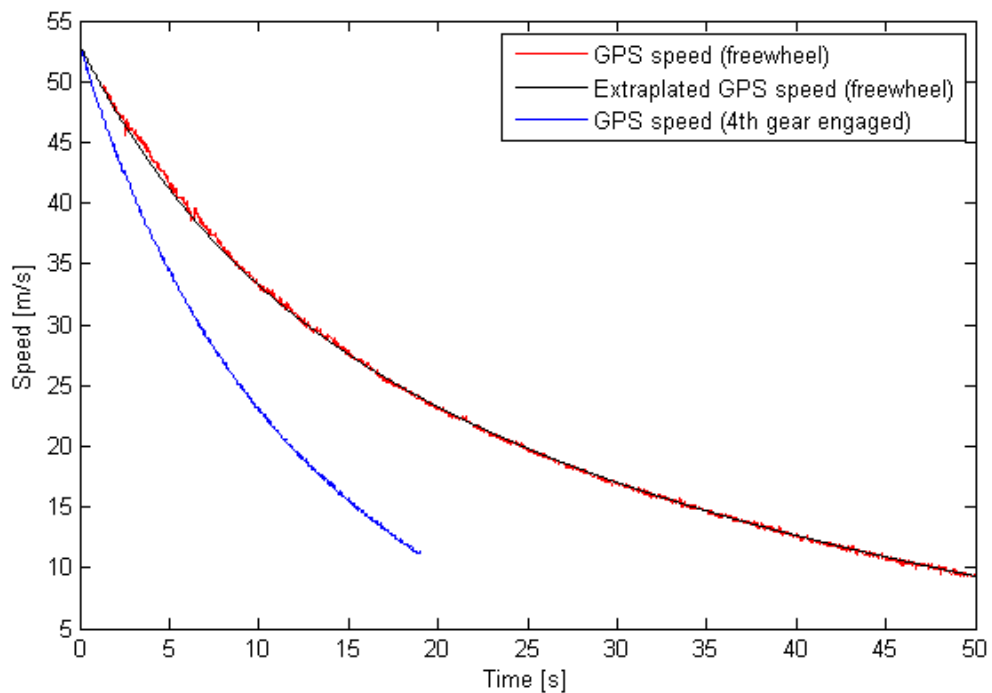


Figure 6.27: Coast-down test speeds

Two coast-down tests were carried out, one in 4<sup>th</sup> gear with the clutch engaged, beginning at maximum engine speed of 14,000 rpm and ending at 3,000 rpm, and the other coast-down test in a similar road speed range but with the clutch disengaged. Comparing acceleration data from the two tests allows engine negative

torque to be differentiated from other sources of drag and evaluated with respect to engine speed. This gives the closed-throttle torque curve, which when combined with the full throttle torque curve, allows the engine torque to be estimated over the full range of throttle position and engine speed. To remove any possibility of clutch slip in the 4<sup>th</sup> gear test, the torque limiting clutch was removed, and the standard one fitted. Fig. 6.27 shows the coast-down speeds plotted against time. The freewheel test began at a slightly lower speed than intended, partly due to space considerations, as the bike decelerates over a much greater distance. It was therefore necessary to extrapolate the speed to a higher value to match the speed range of the 4<sup>th</sup> gear test. A second order polynomial in road speed was fitted to the freewheel speed and then extrapolated to match the maximum speed of the other test. Fitting a function to the data has the advantage that it avoids numerically differentiating a noisy speed signal. Fig. 6.27 shows an anomaly in the freewheel speed at around 4 seconds. This is probably due to a slight change in riding position. This data was used to obtain a torque map for the engine, as explained in Section 4.7. The freewheel coast-down test was used to calibrate the aerodynamic parameters.

## 6.8 Data formatting

The 2D system stores recorded data in a proprietary format for use in the 2D Analyser application. This incorporates a comprehensive set of analysis tools and the user can write calculation scripts to create new calculated channels. However, as the model would be prototyped in Matlab, it was decided to do all postprocessing in Matlab rather than in 2D Analyser. Recorded data was exported at a sample rate of 800 Hz in comma-separated value (CSV) format, that is easily read by Matlab.

# Chapter 7

## Model Validation and Analysis

### 7.1 Introduction

In this chapter, using data recorded during testing, the behaviour of the model is compared to that of the actual bike. Then, the response of the model to various test inputs is examined. The system modes are examined using the root locus technique. Testing consisted of coast-down tests to determine the effects of drag, a preliminary validation of the data recording equipment by the writer at Mondello Park and a test session at Nutts Corner race track with Jeremy McWilliams [54] riding the bike.

### 7.2 Coast-down test

Two coast-down tests were performed, as described in Section 6.7; one where the throttle was closed at maximum engine speed in 4<sup>th</sup> gear and the bike was allowed to slow down under the influence of engine braking, and a freewheel test in a similar road speed range with the clutch disengaged. Section 4.7 explains how the difference in negative acceleration between the two tests was used to calculate the negative engine torque with the throttle closed. Section 4.5.5 explains how the data from the freewheel coast-down test was used to calculate the effects of drag. The first step in validating the model is to simulate the freewheel coast-down test. In addition to analysing drag, the data from the freewheel test is useful in other

ways. By comparing modelled and measured suspension position, and minimising the error, the coefficient of lift and the position of the aerodynamic centre of pressure may be estimated. This is analogous to how these parameters would be calculated in a wind-tunnel, albeit using load cells in a controlled environment. At lower road speeds where aerodynamic forces have less effect, the error in suspension position may be used to verify suspension parameters. Fig. 7.1 shows the measured and modelled road speed and suspension position. The coefficient of aerodynamic lift and the centre of pressure have been optimised so as to minimise the error in suspension position. Fig. 7.2 shows the measured and modelled road

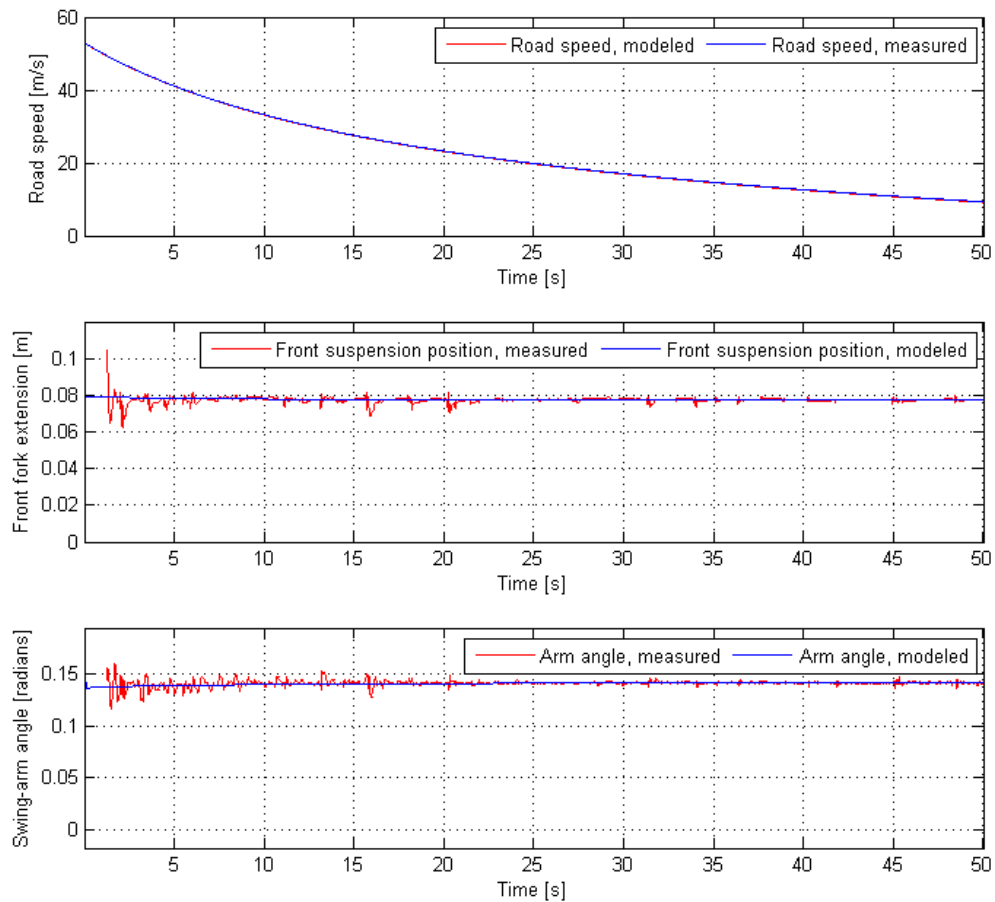


Figure 7.1: Freewheel coast-down speeds and suspension positions, measured and modelled.

speed and suspension position for the 4<sup>th</sup> gear coast-down test. The closed-throttle negative engine torque is assumed to be linearly related to engine speed, so the torque values at minimum and maximum engine speed were adjusted to obtain the match in road speed shown in the upper plot. Once this was done, the

modelled front and rear suspension positions were a close match for the recorded positions, as shown in the second and third plots, with the front position being around 2 mm low at high deceleration rates.

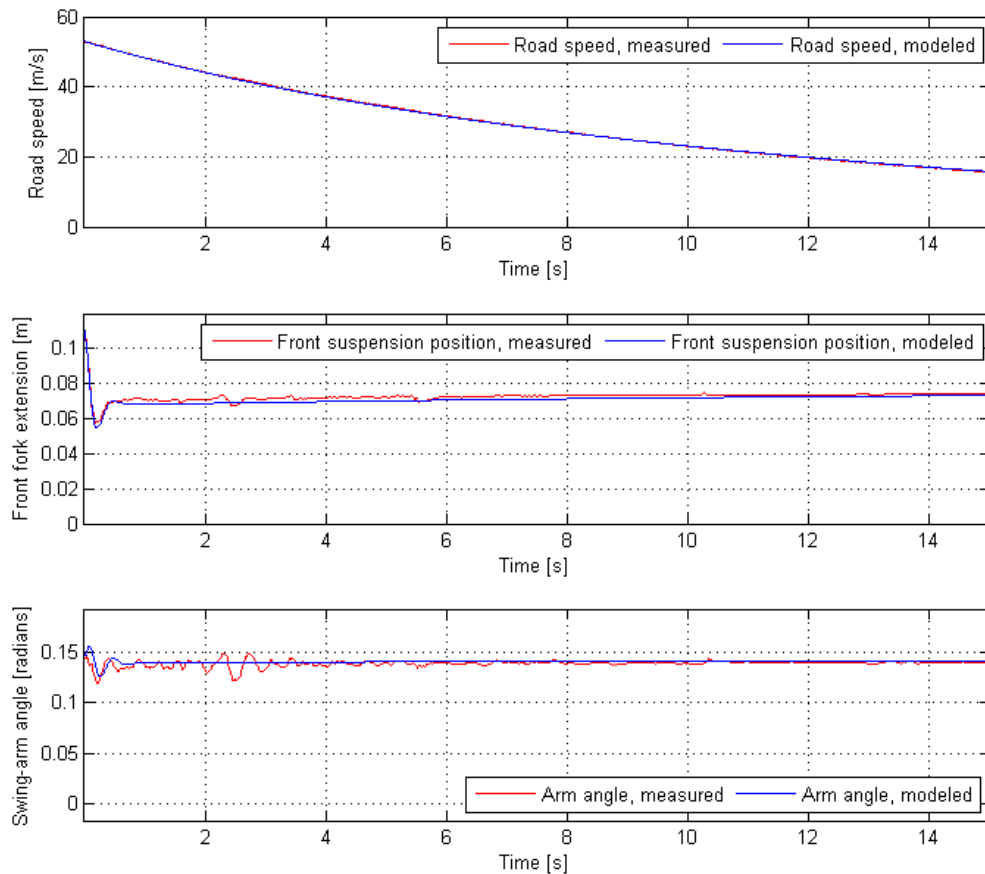


Figure 7.2: 4<sup>th</sup> gear coast-down speeds and suspension positions, measured and modelled.

## 7.3 Race circuit tests

In this Section, the behaviour of the model is compared to the bike behaviour on the track. The data used is primarily that recorded at Nutts Corner race circuit with the bike ridden by Jeremy McWilliams, but data from the preliminary validation test at Mondello Park is also included. Plots of steering angle versus roll angle for both tests are shown in Section 5.4.1.

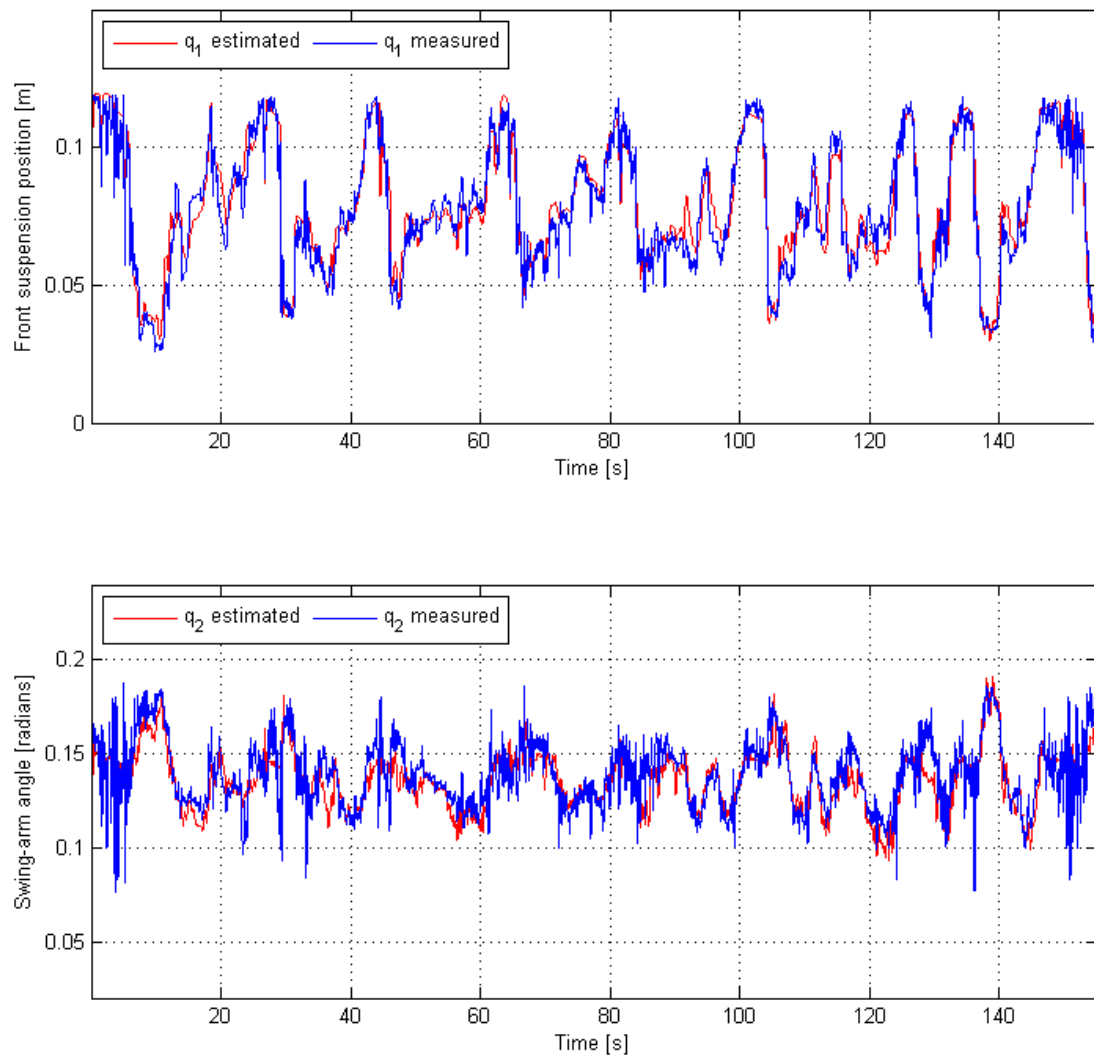


Figure 7.3: Estimated and recorded suspension data for one lap of Mondello Park

### 7.3.1 Preliminary validation in Mondello Park

The purpose of this test was to ensure that the bike and data recording system were working as expected, so as to avoid problems at the important Nutts Corner test. Testing was carried out in dry conditions at Mondello Park race circuit and data for a little over one lap is shown. There is some overlap because the plots begin at the start of the ‘pit’ straight and ending at the end of the pit straight on the following lap. Mondello is quite a bumpy circuit and this can be seen in the recorded suspension data. A map of Mondello Park, including elevation, is shown in Fig. 7.7.

Recorded and estimated suspension data is shown in Fig. 7.3, where  $q_1$  is the position of the front fork and  $q_2$  is the swing-arm angle. While there is a lot of

measured suspension movement which does not appear on the estimated data, the correlation between recorded and estimated data is good. Much of this extra movement is apparent at the beginning and end of the plot, which corresponds to the bumpy pit straight. When compared to Jeremy's suspension data in Fig. 7.4, the suspension neither extends nor compresses to the same extent. Novice riders underestimate the forces that the tyres can withstand and ride well within the performance limits of the bike.

### 7.3.2 Testing at race speed in Nutts Corner

The main track test was carried out at Nutts Corner circuit in dry conditions with Jeremy McWilliams riding the bike. The circuit map is shown in Fig. 7.8, overlaid with two consecutive laps of GPS data recorded on the bike. The GPS mapping was performed by Seán O'Kane using ArcGIS version 10.2.2. The recorded GPS points were converted to a continuous line and displayed using WGS1984 as its geographic coordinate system (the same as the original GPS points), and IRENET95 Irish Transverse Mercator (ITM) as the projected coordinate system. Fig. 7.4 shows the comparison between estimated and recorded suspension data for one lap of Nutts Corner, where  $q_1$  is the front fork position and  $q_2$  is the swing-arm angle. Nutts Corner has an elevation change of approximately eight metres with somewhat abrupt local gradient changes, as can be seen in Fig. 7.9. The crests and troughs give rise to vertical accelerations which are not modelled, creating a difference between estimated and measured suspension travel in some places. It is to be expected that lower frequency suspension movement is created by the dynamics of the system, but the plots show that much of the high frequency movement too is generated by the system dynamics, as the model has no 'knowledge' of road irregularities.

Fig. 7.5 shows a comparison of the estimated and recorded wheel speeds over a period of 40 seconds. Wheel speeds in metres per second are shown because the front and rear wheel angular velocities are not directly comparable due to the different tyre profiles. The upper plot shows the front wheel speed and the second plot shows the rear. The plots were created with the wheel speed Kalman

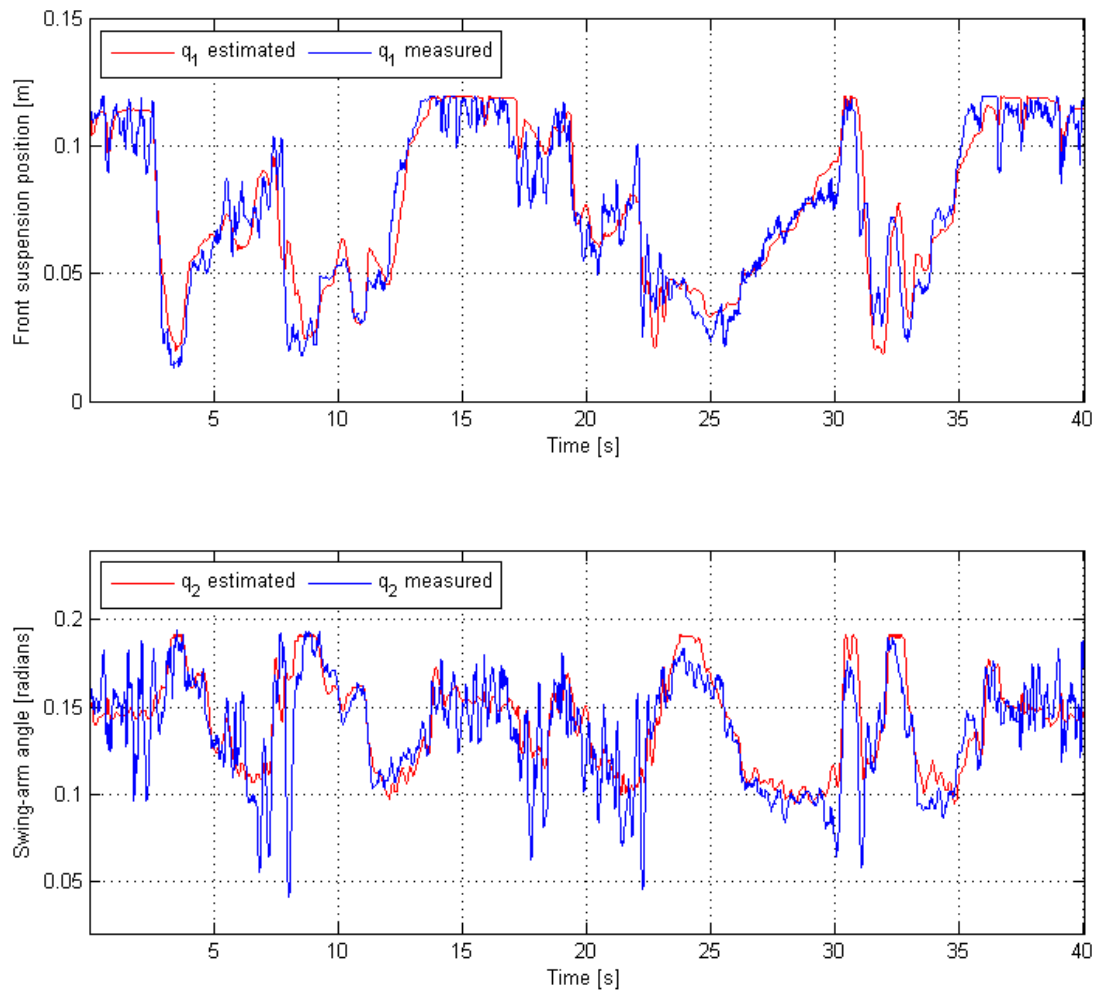


Figure 7.4: Estimated and recorded suspension data for one lap of Nutts Corner

filter disabled, so the wheel speed estimation is open loop, with no influence from the measurements. The estimated front wheel speed matches the recorded data well at high frequency, with small variations appearing similarly in both. The wheelie at 36 seconds has an effect on the estimated front wheel speed but it appears as though the wheel retains some contact with the ground, as it does not decelerate freely. The second plot shows the measured and estimated rear wheel speeds. The estimated bike speed is included for comparison. At around 3, 9 and 24 seconds, the rear wheel locks on braking, with the example at 9 seconds being the most pronounced. The model behaves in a very similar way to the real bike in these situations. Where it does not follow so well is where the real bike appears to experience wheel spin. At 12 seconds, when the bike accelerates in first gear, the rear wheel over-rotates until around 14 seconds, when it begins

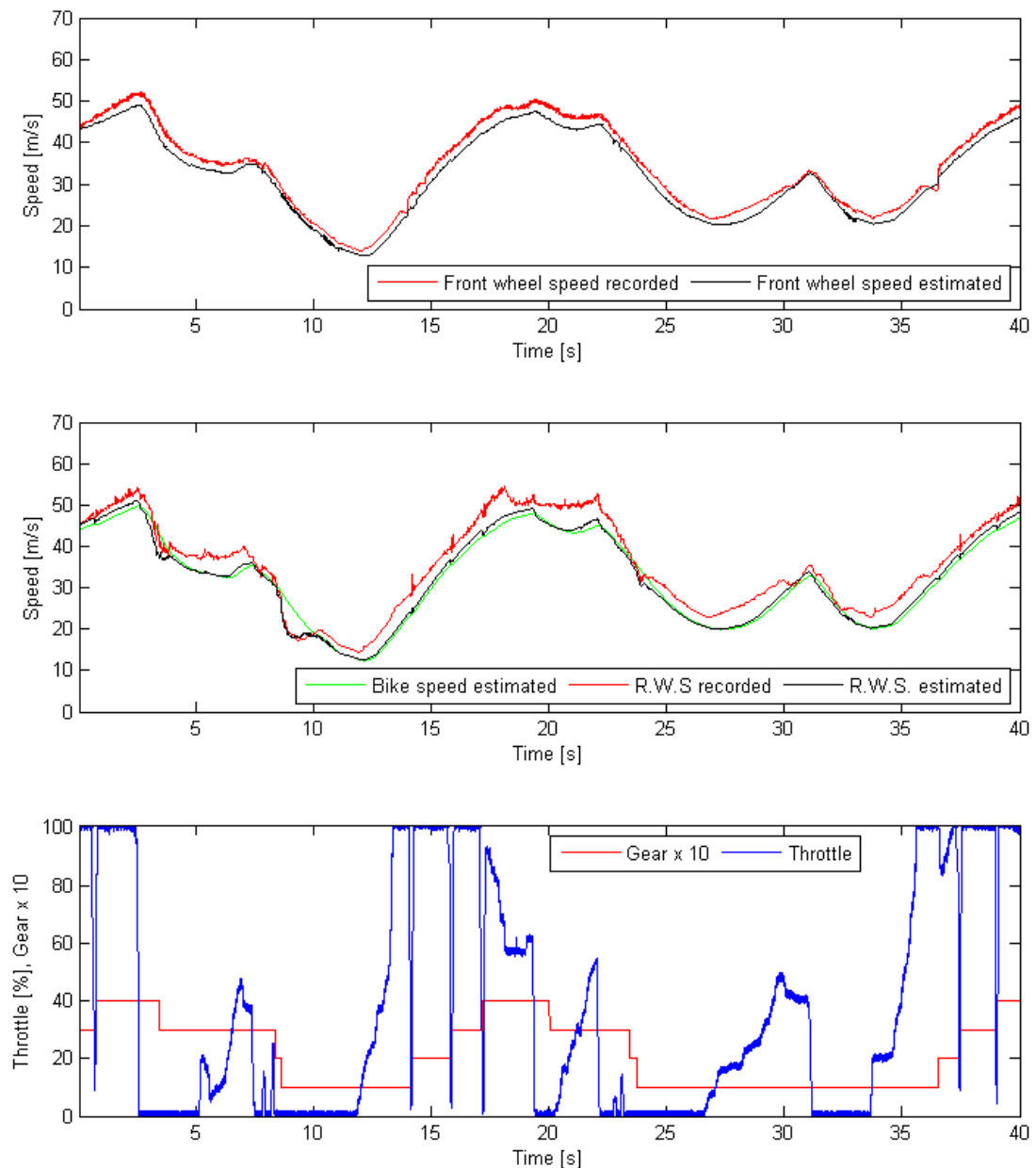


Figure 7.5: Estimated and recorded wheel angular velocity

to grip. This is even more evident at around 35 seconds, where wheel spin ends abruptly, causing the bike to wheelie. At 30 seconds, the rider closes the throttle a little, ending wheel spin. The effect of the sudden torque change at up-shifts is apparent on both the recorded and estimated rear wheel speed, though more so on the recorded data.

Fig. 7.6 shows the comparison of the rate gyro estimated and recorded data. The estimated rate gyro data is constructed as explained in Section 4.11. The plots show that the estimated value of  $\omega_1$  tracks the recorded value much more

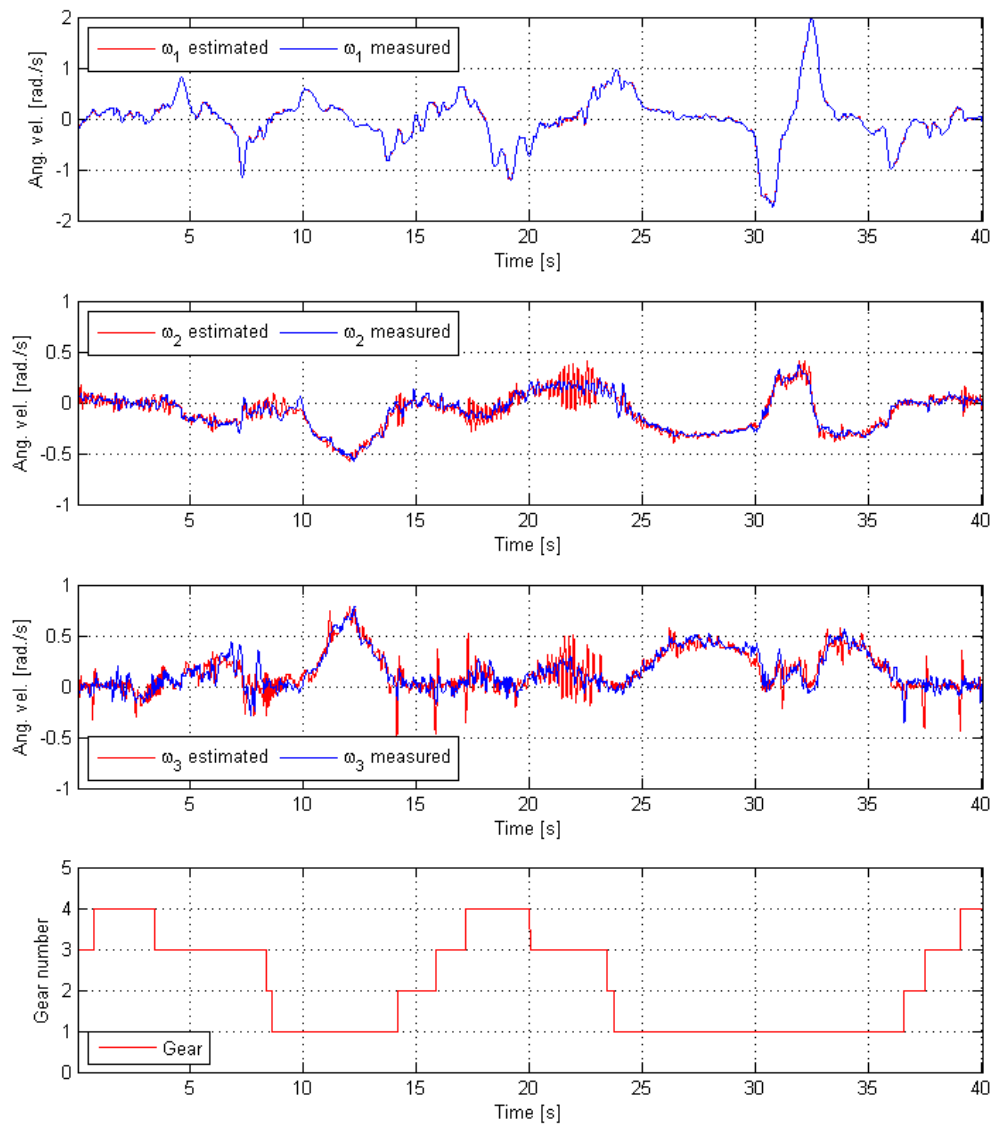


Figure 7.6: Estimated and recorded rate gyro data

closely than either  $\omega_2$  or  $\omega_3$ . This is because the gain  $g_1$  in Fig. 4.37 is higher than  $g_2$  or  $g_3$ , which is due, in turn, to the fact that engine speed is present to a greater extent in  $\omega_2$  and  $\omega_3$  measurements than in  $\omega_1$ . This was explained in Section 4.6. Another factor in choosing the gains was to minimise drift in estimated roll angle while avoiding excessively high values of steering torque, which can induce high frequency vibration in the model. The large impulses visible on  $\omega_3$ , particularly on the estimated plot, are due to gear-change induced pitch. As the rider cuts torque by closing the throttle, there is a negative spike in  $\omega_3$ , followed by a positive spike as the rider re-applies torque and the main frame resumes its attitude. The torque disturbance during up-shifts creates a brief ‘ringing’ in estimated  $\omega_3$ .

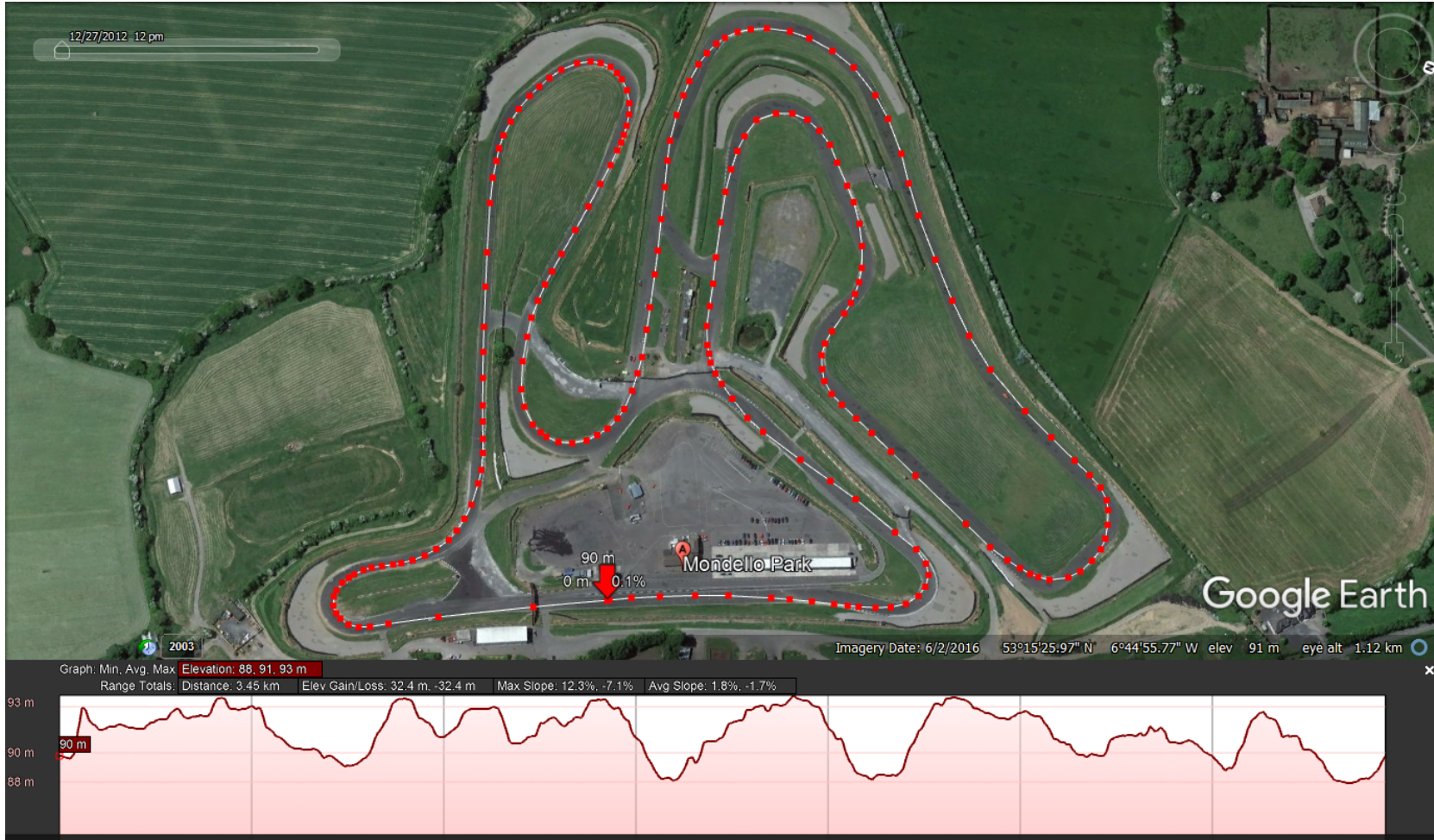


Figure 7.7: Google Earth map of Mondello Park circuit, showing elevation change



Figure 7.8: Nutts Corner race circuit, Antrim, showing two lap GPS trace

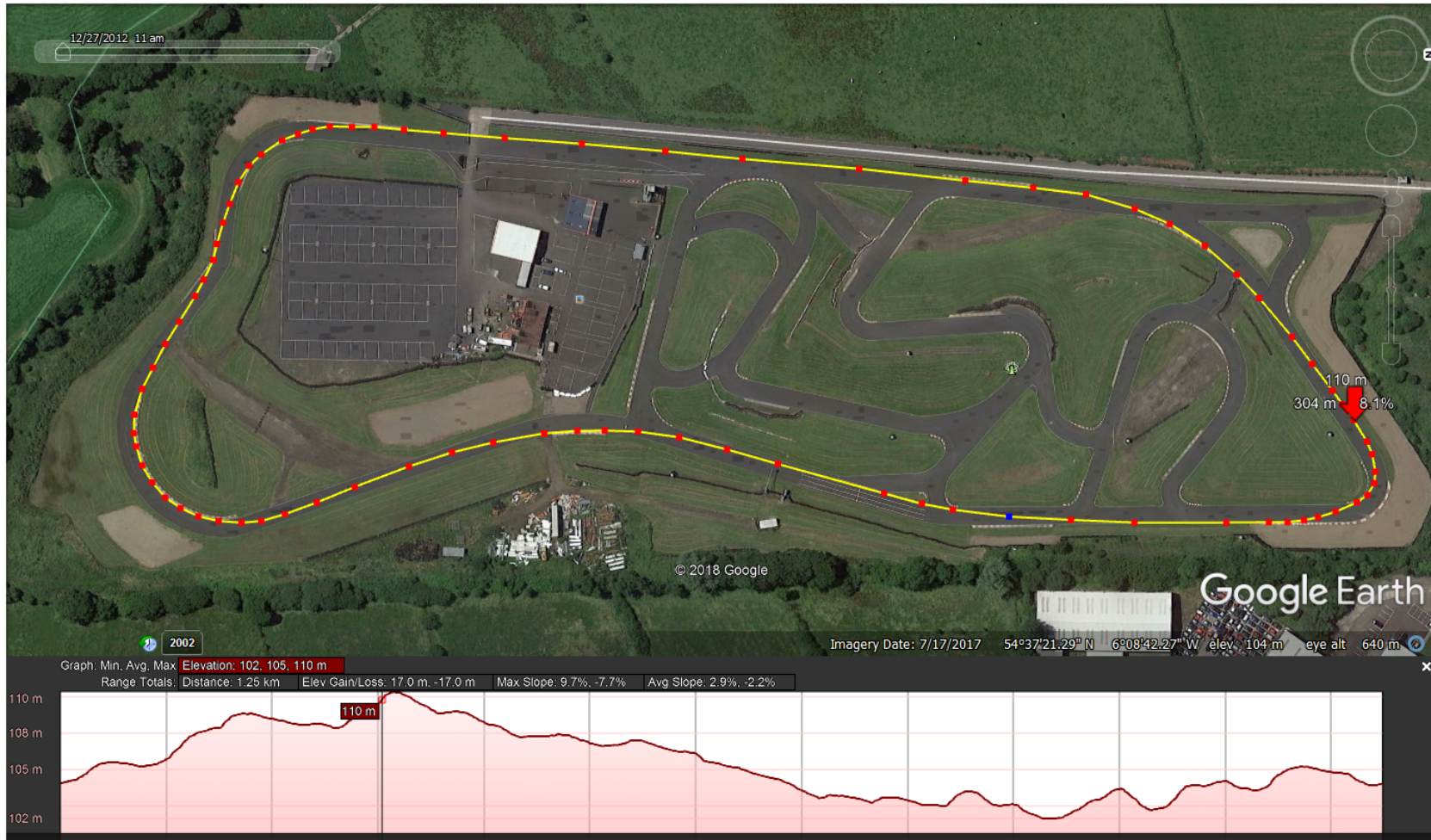


Figure 7.9: Google Earth map of Nutts Corner circuit, showing elevation change

## 7.4 Turning behaviour

For these tests, which are performed by the model only, road speed is regulated by a PI controller, using rear wheel torque as the input. The gains are low, so the dynamics of the speed controller are not apparent in the response of the bike.

### 7.4.1 Steady state turning

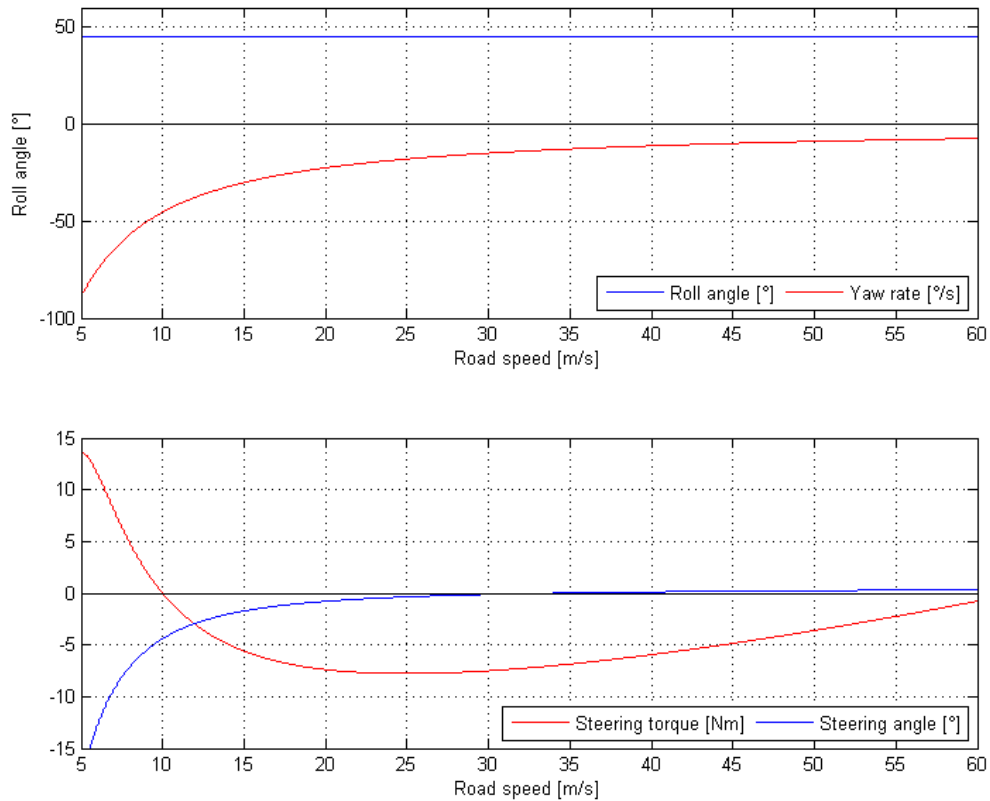


Figure 7.10: Yaw rate, steering torque and steering angle vs. road speed at  $45^\circ$  roll angle

Fig. 7.10 shows how the motorcycle behaves at a constant roll angle of  $45^\circ$  over a road speed range of 5 to 60  $m/s$ . Yaw rate is equal to centripetal acceleration, which is constant in this case, divided by road speed, so at low speed, the magnitude of the yaw rate increases greatly. At low speed, the steering torque needed to maintain a constant roll angle is in the opposite direction to the turn. That is, in a right-hand turn as shown, the steady state steering torque is to the left. As the speed increases, the steering torque drops to zero and then changes sign. It is now entering the speed region where the bike is self-stabilising. The

auto-stable condition continues to above 60  $m/s$  but at some point above that speed, the motorcycle will again enter a region of instability. The speed range of the auto-stable region depends on the parameters of the machine and tyres.

### 7.4.2 Roll angle change

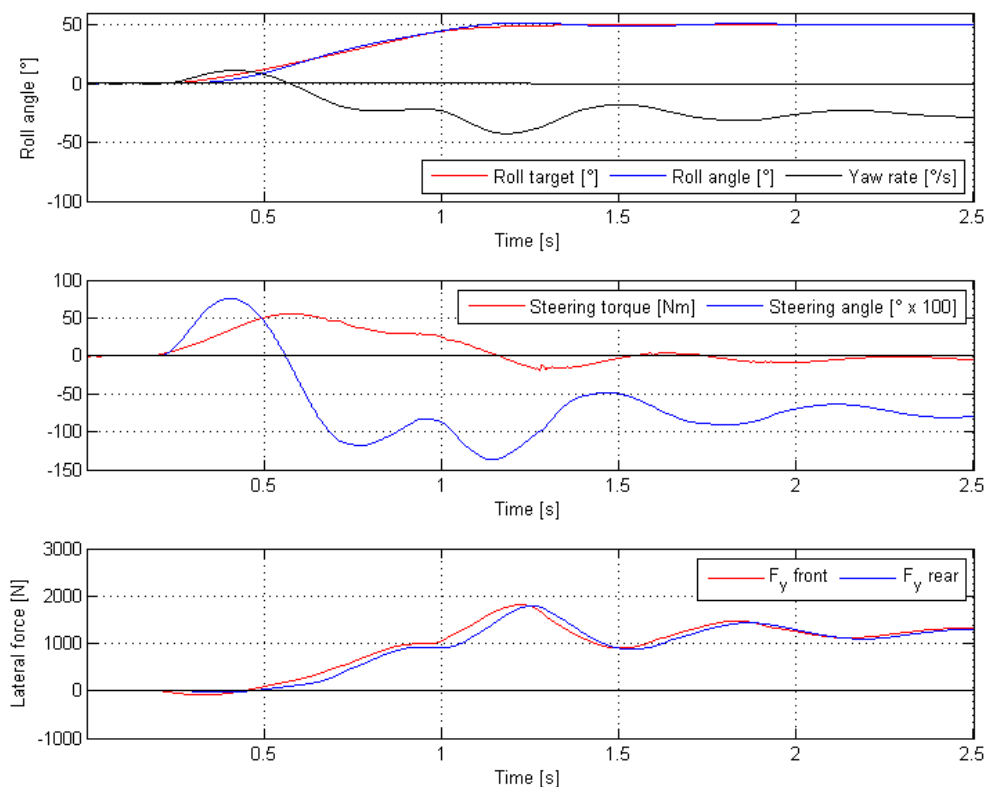


Figure 7.11: Roll angle driven from 0 to 50° at 20  $m/s$

The control input for roll angle is steering torque. In a step response test, the difference between the set point and the output can be very high initially. There is a limit to how much steering torque the motorcycle and tyres can handle, so it is a good idea to limit the steering torque in some way. In this case, the rate of change of the set-point was limited to 1.2 radians per second. The limiting factor was that at higher roll rates, the rear suspension would reach full extension for a short time, introducing significant non-linear behaviour. The roll rate limiter was followed by a first order low pass filter with a time constant  $\tau = 0.15$  seconds, so as to keep the bandwidth of the input signal low relative to that of the model.

The response to a change in roll angle from 0 to 50° at a road speed of 20

$m/s$  is shown in Fig. 7.11. This takes place within the auto-stable region, as explained above. The first plot shows the roll target, roll angle and yaw rate. The second plot shows the steering torque and steering angle. The turn to the right is initiated at  $t = 0.2 s$  by applying steering torque to the left. This steers the front wheel to the left, creating a torque about the longitudinal axis that causes the bike to roll to the right. At  $t = 0.56 s$ , the steering angle changes direction creating a torque about the longitudinal axis that opposes the roll rate and arrests the roll at the desired roll angle. This behaviour is known as counter-steer. The steering angle settles at approximately  $-0.8^\circ$ . As the final roll angle is reached, the steering torque changes sign and settles at approximately  $-7 \text{ Nm}$ . The third plot shows the tyre lateral force. The front tyre lateral force is negative initially due to counter-steer, but then changes sign after the turn is initiated.

## 7.5 Turning radius

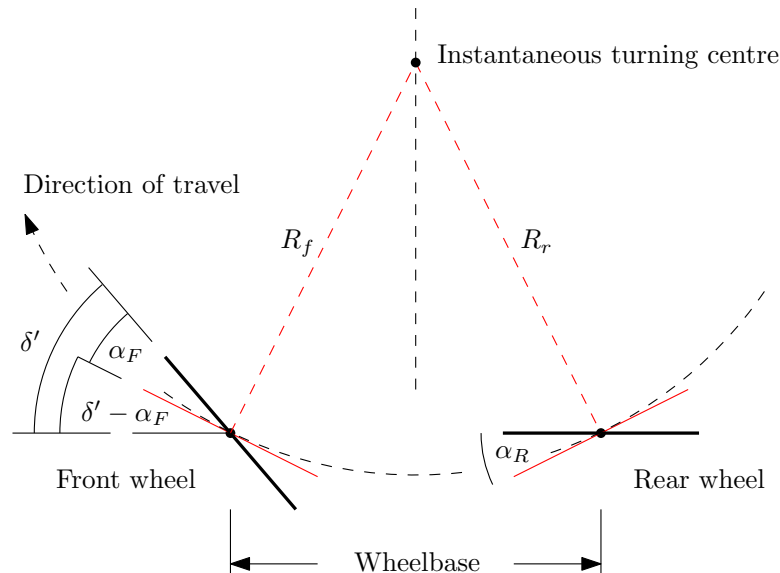


Figure 7.12: Balanced turning

Figure 7.12 shows the projection of the steering geometry onto the ground during steady state turning. This is in fact a special case where the tyre contact points are equidistant from the instantaneous turning centre. The orientation of the tyres is indicated by heavy black lines. The circular path along which

both tyre contact points move is shown by a dashed line, and the solid red lines indicate the instantaneous directions of motion of the tyre contact points. These are tangential to the circular path and at right angles to the dashed red radial lines to the turn centre. The front and rear slip angles are  $\alpha_F$  and  $\alpha_R$  respectively, and  $\delta'$  is the kinematic steering angle, which is the steering angle  $\delta$  projected onto the ground plane, as explained in Section 4.4. To achieve a particular level of turning, riders perform three\* main actions; they control the forward speed of the bike, they modify the turning radius by shifting the lateral position of the centre of mass and, using the handlebars, they control the instantaneous direction in which the front contact point moves. In other words, they control the direction of the solid red line passing through the front tyre contact point in Fig. 7.12. It is the angle of this line to the line connecting the contact points, i.e.  $\delta' - \alpha_F$ , along with the corresponding angle at the rear,  $\alpha_R$ , that determines how the bike will turn. The angle  $\delta' - \alpha_F$  is ultimately what the rider controls with the handlebars.

From Fig. 7.13 it is easy to derive the position of the instantaneous turn centre:

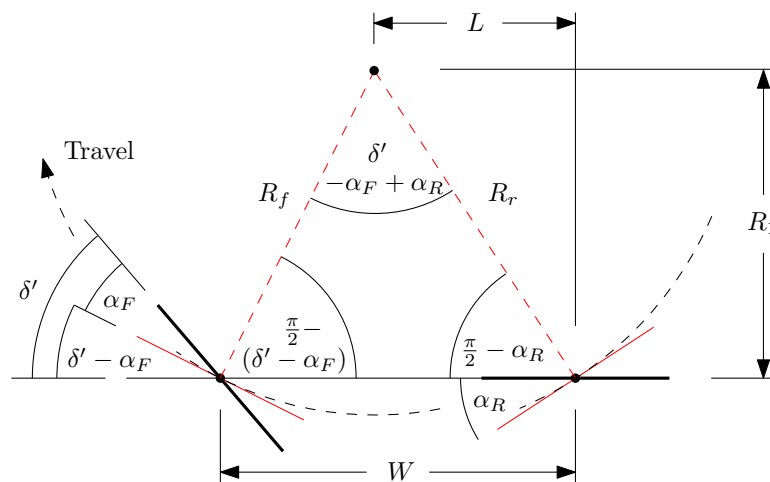


Figure 7.13: Turning radius

$$\frac{R_f}{\sin\left(\frac{\pi}{2} - \alpha_R\right)} = \frac{W}{\sin(\delta' - \alpha_F + \alpha_R)}$$

$$R_f = \frac{W \cos \alpha_R}{\sin(\delta' - \alpha_F + \alpha_R)}$$

\* Of course, the rider can do many other things such as induce oversteer by powering or braking the rear wheel.

Also:

$$\begin{aligned}
\sin\left(\frac{\pi}{2} - (\delta' - \alpha_F)\right) &= \frac{R_1}{R_f} \\
R_1 &= R_f \cos(\delta' - \alpha_F) \\
&= \frac{W \cos \alpha_R \cos(\delta' - \alpha_F)}{\sin(\delta' - \alpha_F + \alpha_R)} \\
&= \frac{W \cos \alpha_R \cos(\delta' - \alpha_F)}{\sin(\delta' - \alpha_F) \cos \alpha_R + \cos(\delta' - \alpha_F) \sin \alpha_R} \\
&= \frac{W}{\frac{\sin(\delta' - \alpha_F) \cos \alpha_R}{\cos \alpha_R \cos(\delta' - \alpha_F)} + \frac{\cos(\delta' - \alpha_F) \sin \alpha_R}{\cos \alpha_R \cos(\delta' - \alpha_F)}} \\
&= \frac{W}{\frac{\sin(\delta' - \alpha_F)}{\cos(\delta' - \alpha_F)} + \frac{\sin \alpha_R}{\cos \alpha_R}} \\
R_1 &= \frac{W}{\tan(\delta' - \alpha_F) + \tan \alpha_R} \tag{7.1}
\end{aligned}$$

Note that the wheels are treated as discs and the lateral offset of the tyre contact points due to roll angle is ignored. This result emphasises that, with regard to turning, the front slip angle  $\alpha_F$  is inseparable from the kinematic steering angle  $\delta'$ .  $L$  is found to be:

$$L = R_1 \sin \alpha_R$$

It can also be stated that the turning radius of the bike centre of mass is:

$$R_2 = \frac{v}{\omega} \tag{7.2}$$

where  $R_2$  is the distance from the centre of mass to the instantaneous turn centre,  $v$  is the forward velocity and  $\omega$  is the angular velocity. It is interesting to compare  $R_1$  and  $R_2$  using the steady state values of the roll angle change test in Section 7.4.2. The values were obtained after 10 seconds in order to allow the system to reach a steady state;  $W = 1.3789m$ ,  $\delta' = -18.4653 \times 10^{-3}$  radians,  $\alpha_F = -1.5401 \times 10^{-3}$  radians,  $\alpha_R = -14.4216 \times 10^{-3}$  radians,  $v = 20.0$  m/s,  $\omega = -0.4571998$  radians/s, resulting in:  $R_1 = -44.0$  m and  $R_2 = -43.7$  m. The difference is 0.3 m and the lateral offset of the combined centre of mass rela-

tive to the contact patches is approximately 0.5 m, which makes the actual error approximately 0.2 m.

Changing parameters, such as the lateral offset of the main frame mass centre, or using a rear tyre in the front, changes the turning radius, but the agreement between the two methods of calculation remains similar, or in some cases better than the example above. Likewise with different road speeds. This close agreement is a useful partial validation of the model.

## 7.6 The effect of changing the slip angle

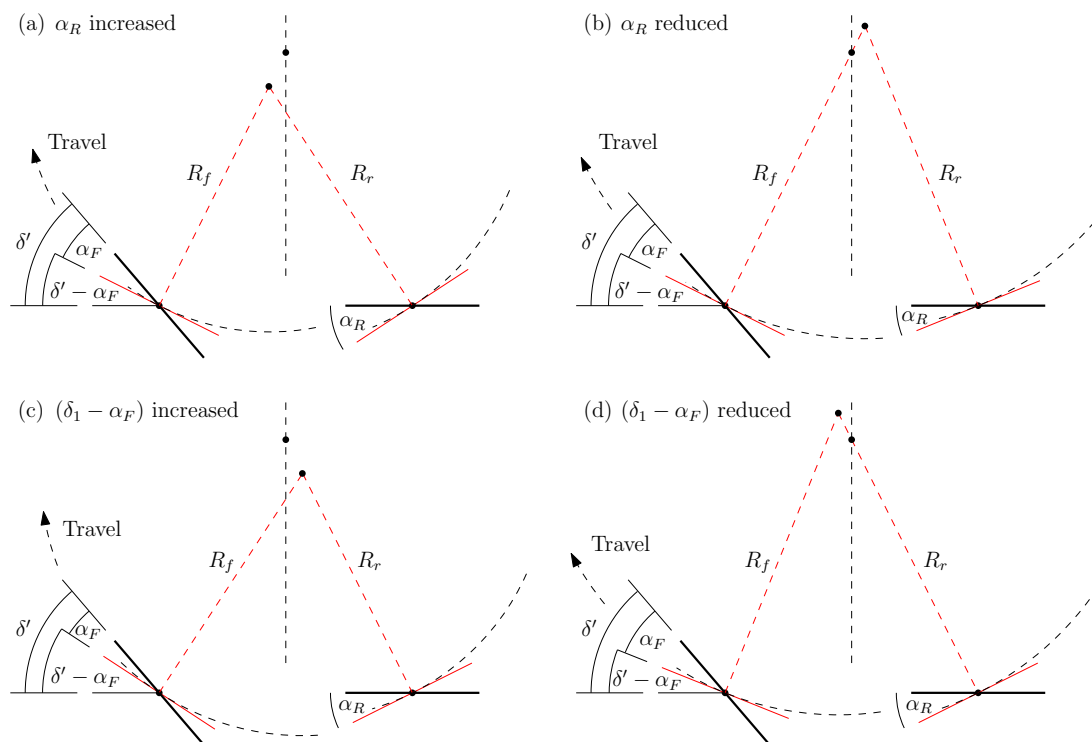


Figure 7.14: The effect of changes in slip angle

Fig. 7.14 investigates what happens when the front and rear slip angles change. The instantaneous turn centre from Fig. 7.12 is shown as a reference. The turning radius is reduced by increasing either  $\alpha_R$  or  $\delta' - \alpha_F$ , and vice versa. Increasing  $\alpha_R$  or reducing  $\delta' - \alpha_F$  moves the instantaneous turning centre forward and vice versa.

## 7.7 Tracking the bike position

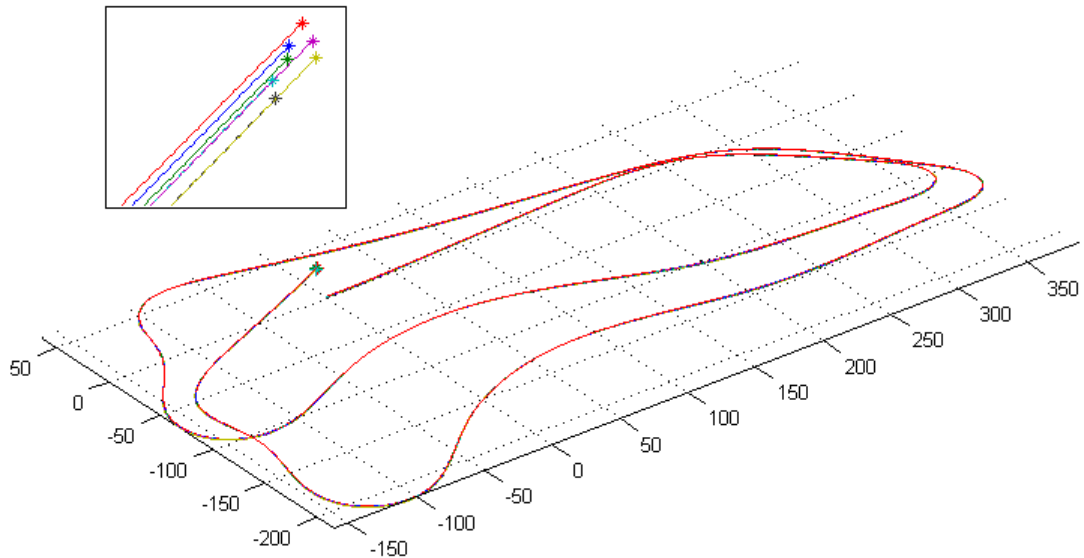


Figure 7.15: 3D map of bike trajectory for two laps, with zoomed inset

Fig. 7.15 shows the three dimensional trajectory of the bike for two laps. The drift in the  $X$  and  $Y$  position and in yaw can be seen. Seven points on the bike from Table 4.1 are tracked in this diagram; front and rear axles  $G$  and  $D$ , front and rear tyre contact points  $S$  and  $T$ , swing-arm pivot  $P$ , steering head point  $H$  and the main frame mass centre  $A$ . These points on the bike in its final position can be seen magnified in the inset. Fig. 4.37 shows the same data in two dimensions, overlaid with the recorded GPS data. It can be seen that the inertially estimated path follows the GPS path well for one or two corners and the drift becomes greater as time goes on.

## 7.8 Root locus analysis

The continuous time state space representation of the bike model is:

$$\dot{x} = Ax + Bu_{in} + Rw \quad (4.38)$$

where\*:

$$u = \begin{bmatrix} F_{fwx} & F_{fwy} & F_{fwz} & F_{rwx} & F_{rwy} & F_{rwz} & F_{lift} & F_{drag} & F_{fork} & T_{mfy} & T_{mfz} & T_{say} & T_{fwx} & T_{fwy} & T_{fwz} & T_{rwx} & T_{rwy} & T_{rwz} & T_{steer} & g \end{bmatrix}^T$$

For the purposes of root locus analysis, the non-linear term  $Rw$  will not be used so Eqn. (4.38) becomes:

$$\dot{x} = Ax + Bu_{in} \quad (7.3)$$

In Section 4.5, it was explained that suspension and tyre forces are not included in the  $A$  matrix but are instead calculated outside the motorcycle model and applied as inputs in the input vector,  $u$ . This means that  $A$  contains no information on tyre or suspension dynamics, so the poles of the system cannot be determined from  $A$  alone, and some other means must be found to calculate them. The tyre and suspension forces contained in the input vector are non-linear functions of the state variables, but for the purposes of root locus analysis they were linearised as follows. Let:

$$u = K_{in}x + u' \quad (7.4)$$

where  $K_{in}$  is a 21 x 22 matrix in which each row corresponds to an element of the input vector and contains coefficients of the state variables. Therefore, each input becomes a linear combination of the state variables plus a possible offset, which resides in the new vector  $u'$ . Eqn. (7.3) becomes:

$$\begin{aligned} \dot{x} &= Ax + BK_{in}x + Bu' \\ &= (A + BK_{in})x + Bu' \end{aligned}$$

The eigenvalues of  $A + BK_{in}$  are the system poles. Each row of  $K_{in}$  may be generated by first running the model using training data, and recording the state and input vectors. Then, the Matlab multiple linear regression function *regress()*

---

\* The input vector is detailed in Table 4.9

is used for each element of the input vector to obtain a set of coefficients that allows that input to be expressed as a function of the state vector. In fact, only the tyre force inputs needed to be generated in this way because the suspension forces are linearised and approximated by spring and damping constants in the  $K_{in}$  matrix.

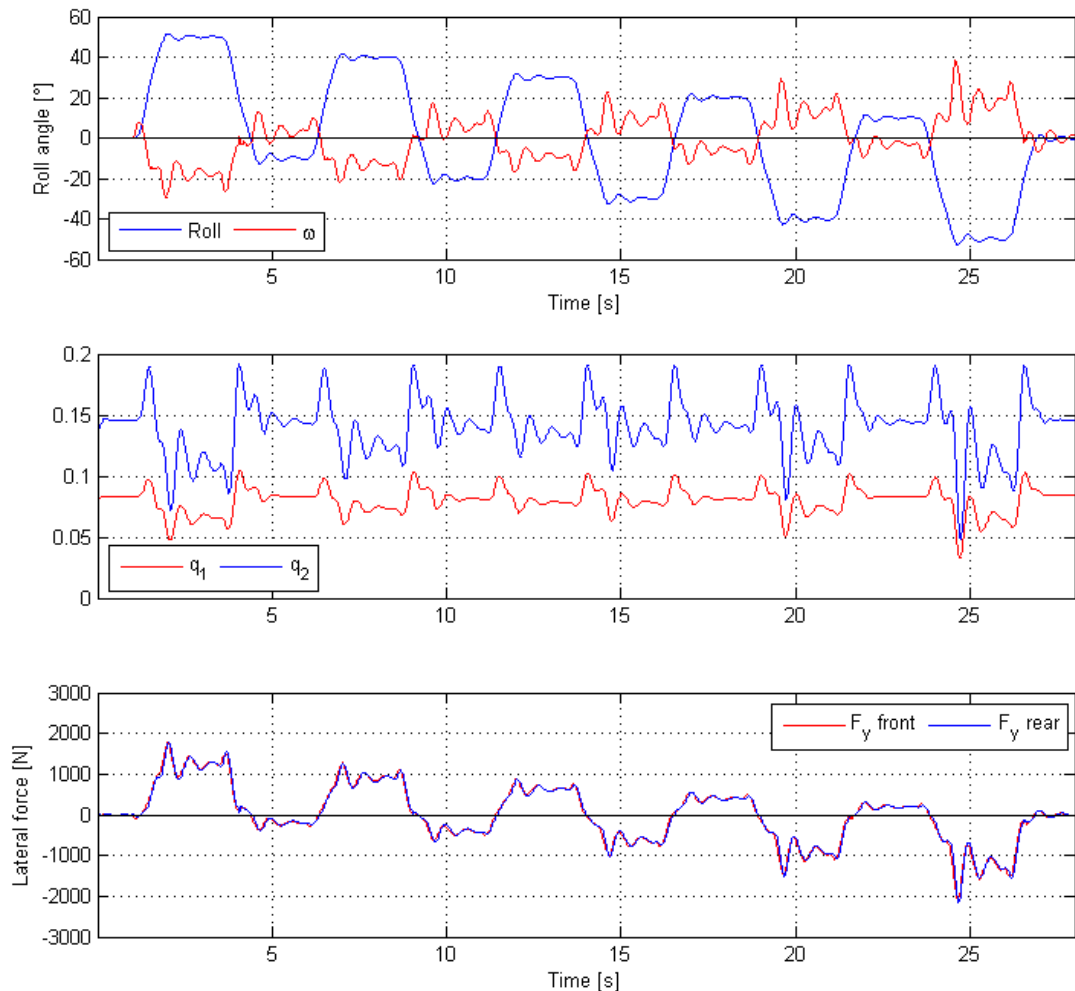


Figure 7.16: Training data used to build the  $K_{in}$  matrix

Fig. 7.16 shows the training data where the roll angle is periodically changed and the system allowed to settle. The set of state variables included in the training set was experimented with. Finally, it was decided to use only roll angle,  $q_9$ . This gave good steady state accuracy although the transient response is not predicted well. However, the root locus tests are performed using very slow parameter changes. The result of estimating  $F_y$  as a function of roll angle is shown in Fig. 7.17, where the estimated and actual values of  $F_y$  for the front and rear tyres

are plotted as the roll angle increases in steps. At low and medium roll angle, the estimated value  $F_y$  is satisfactory.

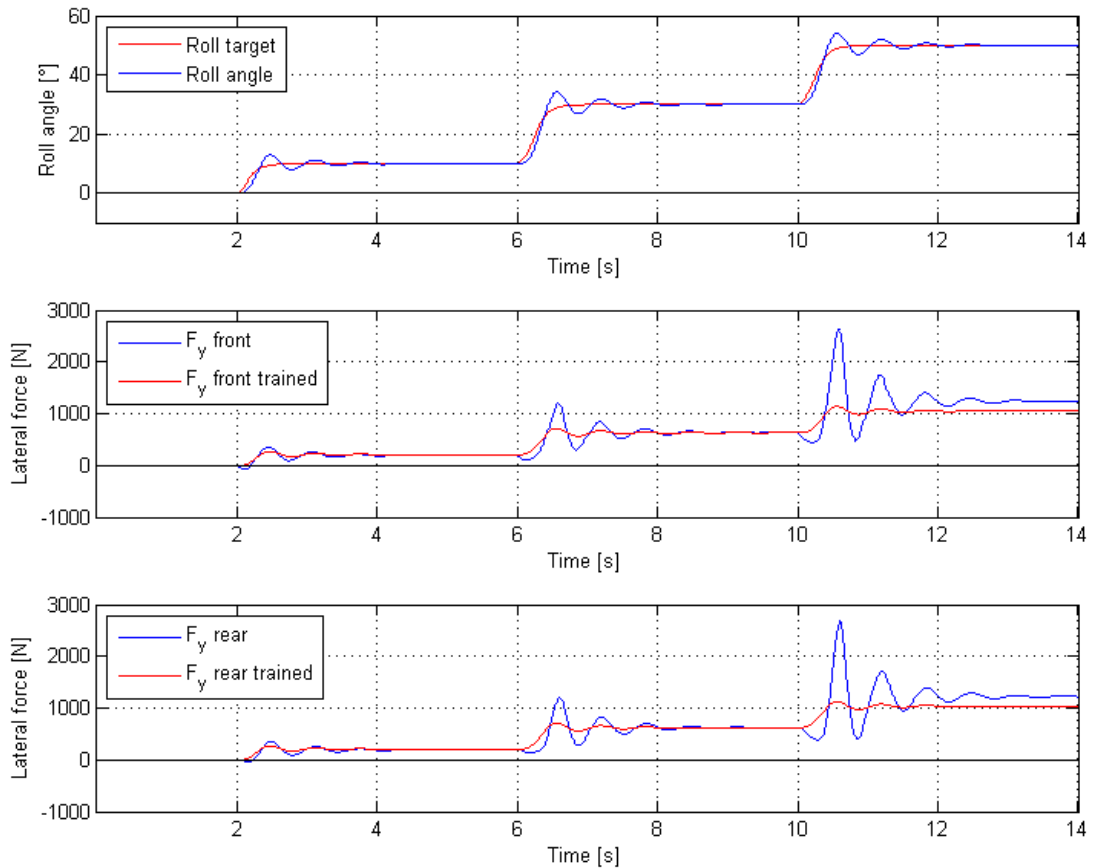


Figure 7.17: Testing the tyre lateral force generated by the trained system

The root locus plots show the oscillatory modes of the system. Note that the real and imaginary axes are not to the same scale. Fig. 7.18 shows the root locus for straight running as road speed is increased from 3 to 60  $m/s$ , with squares marking 3  $m/s$  and diamonds marking 60  $m/s$ . The wheel hop, wobble and suspension modes are largely independent of road speed, with natural frequencies of 17.4 Hz, 8.7 to 8.9 Hz and 2.6 to 2.8 Hz respectively. Weave begins as an undamped oscillatory mode close to the imaginary axis with a frequency of 1.5 Hz, and the frequency and damping factor increase as road speed increases, reaching a maximum damping factor of 0.3 at 29.5  $m/s$  and 2.6 Hz. As road speed continues to increase above 29.5  $m/s$ , so does the weave frequency, but the damping factor decreases, until at 60  $m/s$ , the frequency is 5.2 Hz and the damping factor is 0.17.

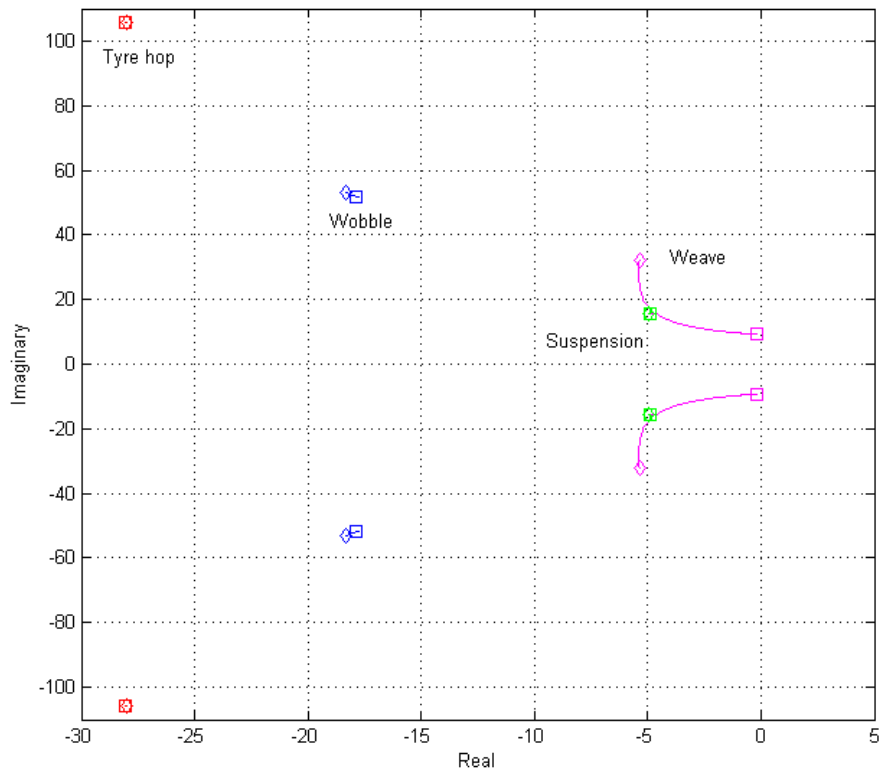
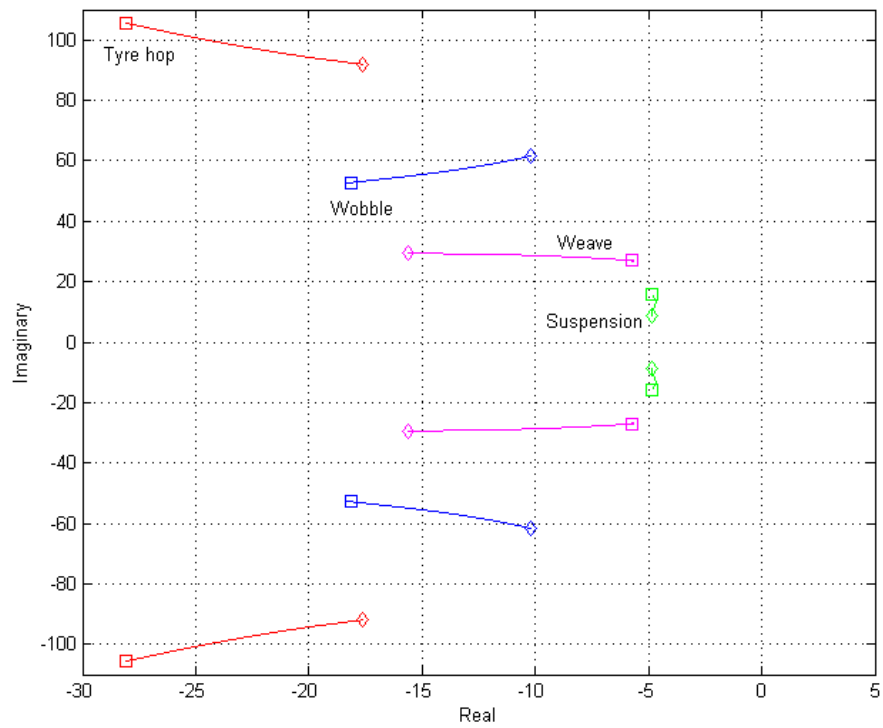


Figure 7.18: Root locus with bike upright for road speed from 3 to 60  $m/s$

Fig. 7.19 shows the root locus at a constant speed of 50  $m/s$  as the roll angle increases from 0 to 50°. Squares indicate 0° and diamonds 50°. As roll angle increases, wheel hop frequency decreases from 17.4 to 14.9 Hz and the damping factor decreases from 0.26 to 0.19. Wobble frequency remains relatively constant, beginning at 8.9 Hz, and increasing to 9.9 Hz at 50° roll angle, as the damping factor decreases from 0.33 to 0.16. Weave frequency increases from 4.4 to 5.3 Hz and the damping factor increases from 0.21 to 0.47. The suspension mode frequency decreases from 2.6 Hz when upright to 1.6 Hz at 50° roll as the damping factor increases from 0.30 to 0.48.

Figure 7.19: Root locus at 50  $m/s$ , with roll angle from 0 to 50°

# Chapter 8

## Application Examples

One of the applications of a high fidelity model is estimation of unmeasurable quantities such as tyre shear force. These estimated quantities may then be used as performance criteria in choosing motorcycle parameters. This is demonstrated by a practical example, using the recorded data from Nutts Corner.

### 8.1 Estimation of unmeasurable quantities

One of the primary uses of the motorcycle model is estimation of unmeasurable quantities. Fig. 8.1 was produced using the initial tyre parameters before they were adjusted as described in Section 5.4.1. The first plot shows the roll angle of the bike for one lap of Nutts Corner circuit. The second plot shows the front and rear lateral forces. The third plot shows the lateral forces normalised with respect to vertical load and the fourth plot shows the tyre slip angles. It is useful to examine the plots from about 22 seconds to 31 seconds as the bike enters and exits a long corner. As the bike begins to lean over, the front tyre lateral force increases in magnitude more quickly than the rear, but the normalised force plot shows that the normalised front and rear lateral forces increase in a much more similar way to each other. This means that the rider is applying lateral force only to the extent allowed by the vertical load. A high front lateral force may be applied on corner entry because the action of braking has transferred weight onto the front tyre. As the brakes are released, and the weight transfer

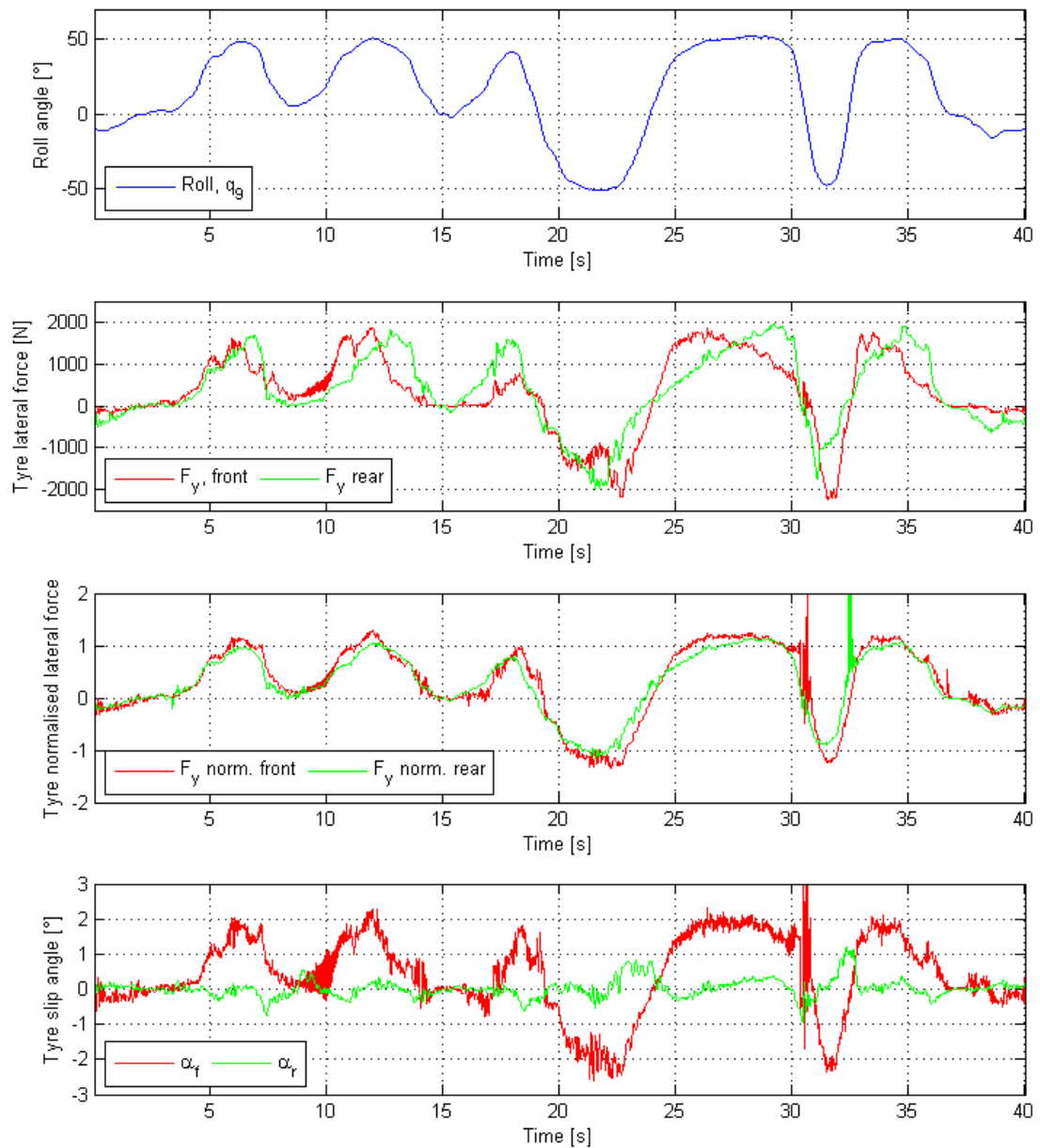


Figure 8.1: Roll angle, tyre lateral shear force (actual and normalised) and slip angle. Data from Nutts Corner with initial tyre parameter set.

to the front decreases, the front lateral force also decreases, until in mid-corner, where the vertical load is shared more-or-less equally between the front and rear tyres, the lateral forces come together. From this point, the rider is accelerating, causing the weight to be transferred to the rear tyre, which can now withstand greater lateral force. As the weight is transferred away from the front tyre, the front lateral force must decrease. The fourth plot in Fig. 8.1 shows that much of the front lateral force is due to the high slip angle of the front tyre. This

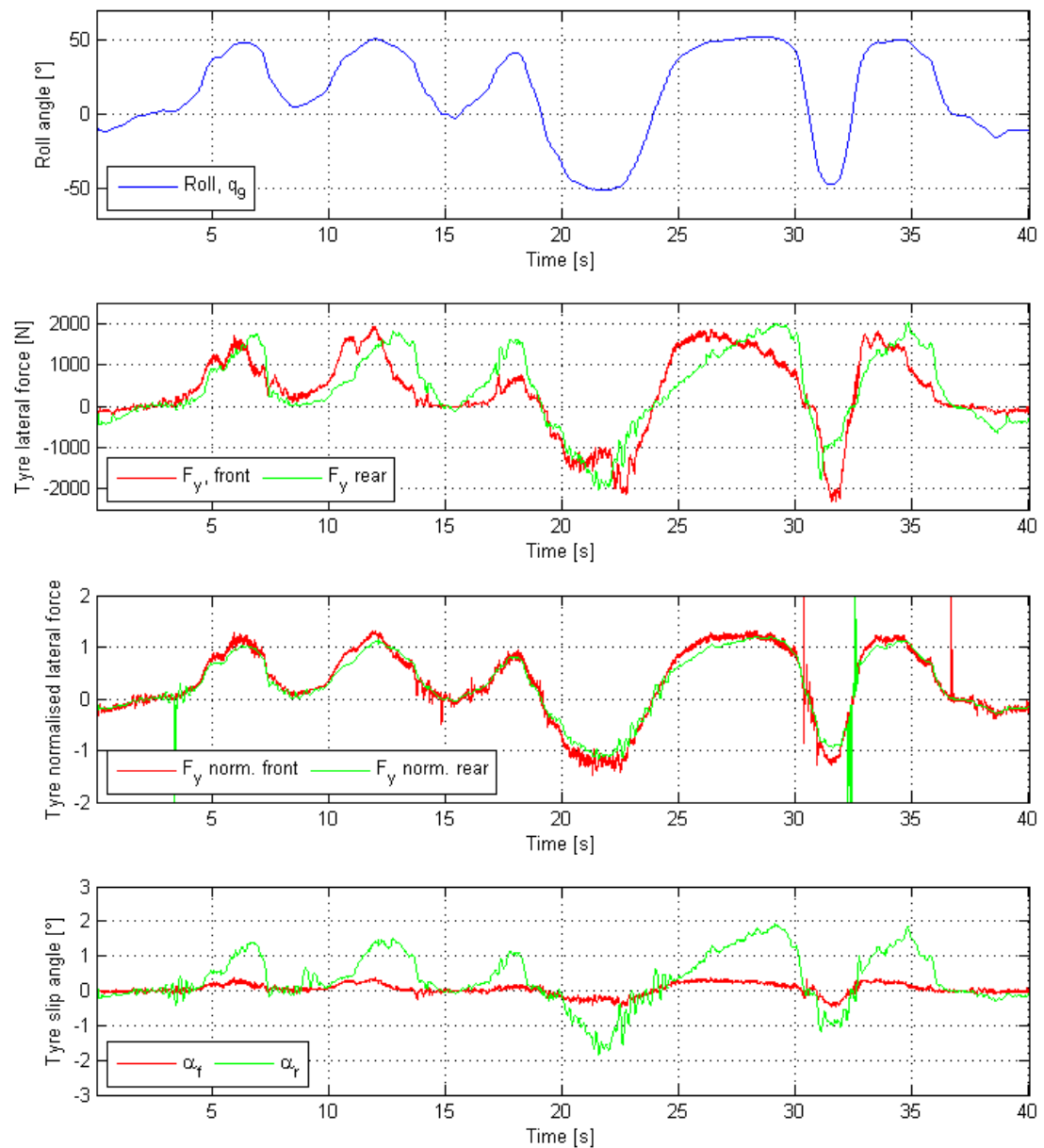


Figure 8.2: Roll angle, tyre lateral shear force (actual and normalised) and slip angle. Data from Nutts Corner with modified tyre parameter set.

contrasts with the fourth plot in Fig. 8.2. This plot was produced using the final tyre parameter set as described in Section 5.4.1. In this case, the tyre lateral force and normalised lateral force have not changed a great deal, but the slip angle behaviour is quite different. The front tyre slip angle remains quite low and the rear tyre slip angle builds progressively through the corner, reaching a peak as the rider accelerates out of the turn. The final tyre parameters are not the definitive parameters for the tyres used; these were not available, but

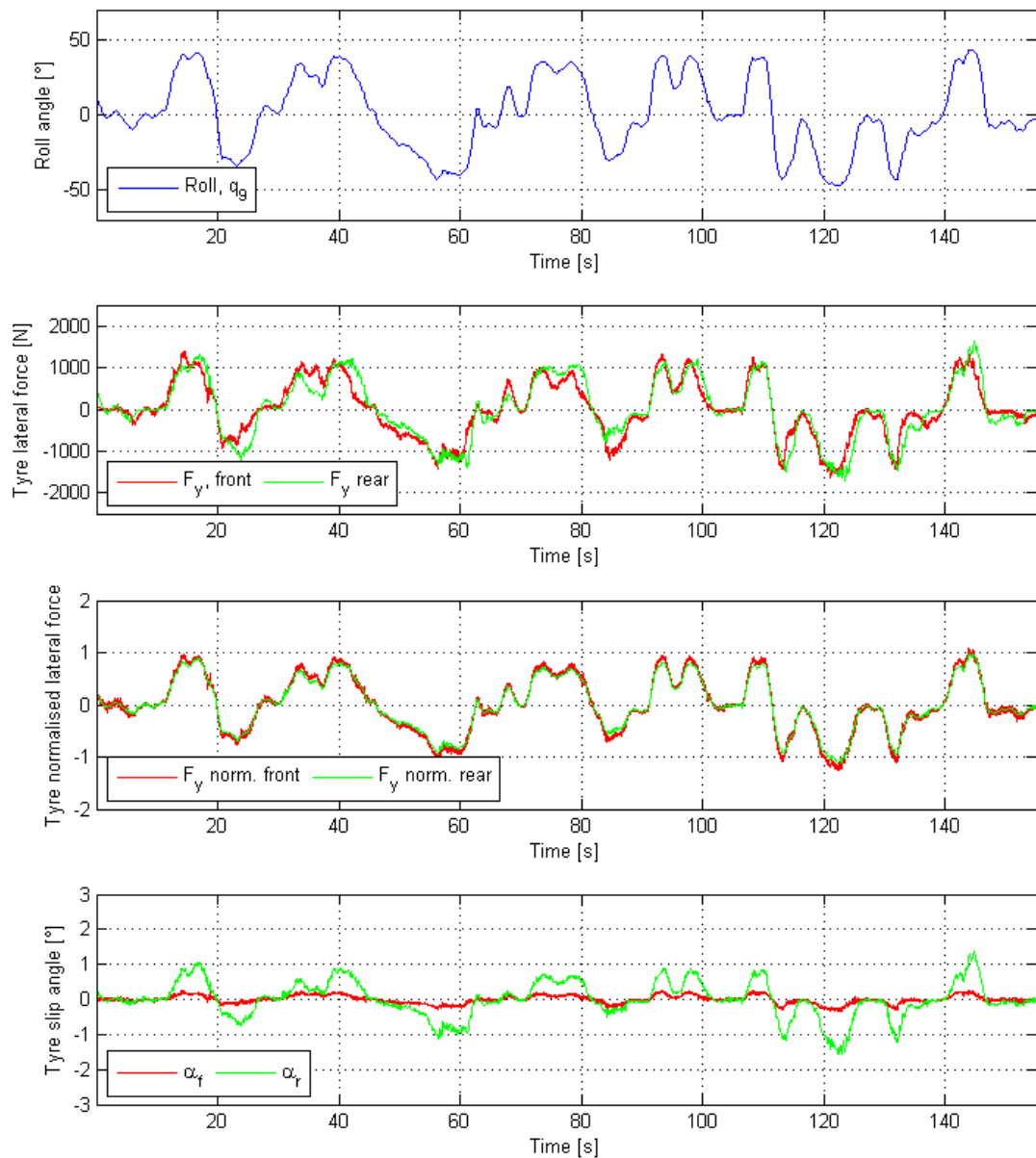


Figure 8.3: Roll angle, tyre lateral shear force (actual and normalised) and slip angle. Data from Mondello Park with final tyre parameter set.

they are modified from the initial parameter set so as to obtain good correlation between the measured and recorded steering and suspension data. The contrast between Figs. 8.1 and 8.2 shows the profound effect of the tyre model parameters on estimated forces and slip angles. In order to have accurate data, it is really necessary to have the actual parameters for the tyres used. Fig. 8.3 shows similar plots from the preliminary validation test in Mondello Park, using the final tyre parameters. The roll angle, lateral forces and slip angles are much lower than for the Nutts Corner data, and this shows the great difference between a professional

and novice rider.

## 8.2 Evaluating parameter changes

Whether at the design stage or when choosing settings for racing, it is useful to be able to evaluate the likely outcome of changes to motorcycle or tyre parameters without having to test them on the road or track. Track testing is expensive and risky, and a screening process for potential changes before they go on the bike will accelerate development. Often, a parameter change may be so small that it will not be noticed by a rider, and simulation may be the only way to investigate if it makes a small step in some particular direction.

This is illustrated by the following example. The normalised front tyre lateral force is one limiting factor when trying to achieve maximum performance. If the maximum value, or the time spent at close to the maximum value is reduced for a given lap-time, then the front tyre is less likely to slide and the margin for safety is increased. Two bike settings are compared: the actual setting used at Nutts Corner circuit to record the data, and the same setting with one chain link removed. This shortens the swing-arm length by 15.875 mm ( $\frac{5}{8}$ " ), and this would be a very noticeable change for the rider. Shortening the swing-arm would be expected to place more weight on the rear of the bike, potentially reducing rear wheel spin. This parameter change will be evaluated using three criteria:

- Does the change actually increase the rear tyre normal load, as expected?
- Does this result in reduced rear wheel longitudinal slip?
- What is the effect on normalised front tyre lateral force?

The upper plot in Fig. 8.4 is a histogram of the rear tyre normal force  $F_z$  for one lap of Nutts Corner circuit. It compares  $F_z$  for the standard setting with that of the modified setting, i.e. the shorter swing-arm. The lower plot shows the difference in  $F_z$  between the modified and standard setting. The area of interest is the upper range of force, around 2,500 N, where the bike is accelerating hard with most or all of the weight on the rear wheel. The bike with the modified

setting clearly spends more time in this range than does the standard setting, confirming that the shorter swing-arm has increased the rear tyre load. The

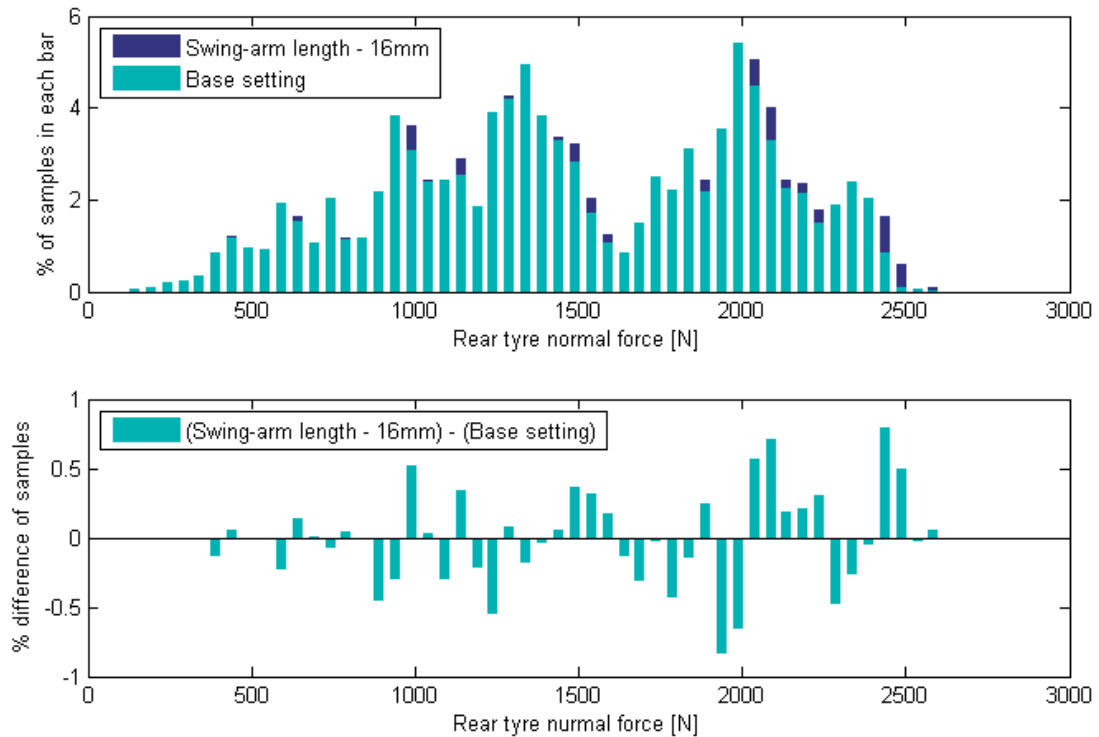


Figure 8.4: Histogram of rear tyre normal force

upper plot in Fig. 8.5 shows the positive rear tyre slip ratio for both settings, and the lower plot shows the difference. The difference in slip ratio is more marked than the force difference, with the modified setting achieving the same maximum slip, but spending much less time in the higher slip range. This confirms the premise that shortening the swing-arm length would reduce slip. The upper plot in Fig. 8.6 shows the histogram of normalised front tyre lateral force for both settings. As noted previously, a lower value is desirable from the point of view of safety. However, although the maximum value is similar, the shorter swing-arm setting shows a marked increase in the amount of time spent in the highest part of the range.

The analysis shows that shortening the swing-arm would be expected to increase the load on the rear tyre on acceleration, thereby reducing wheel spin, but that the front tyre will spend more time close to the limit of lateral adhesion. In other words, the likelihood of crashing due to ‘losing the front’ goes up. Further

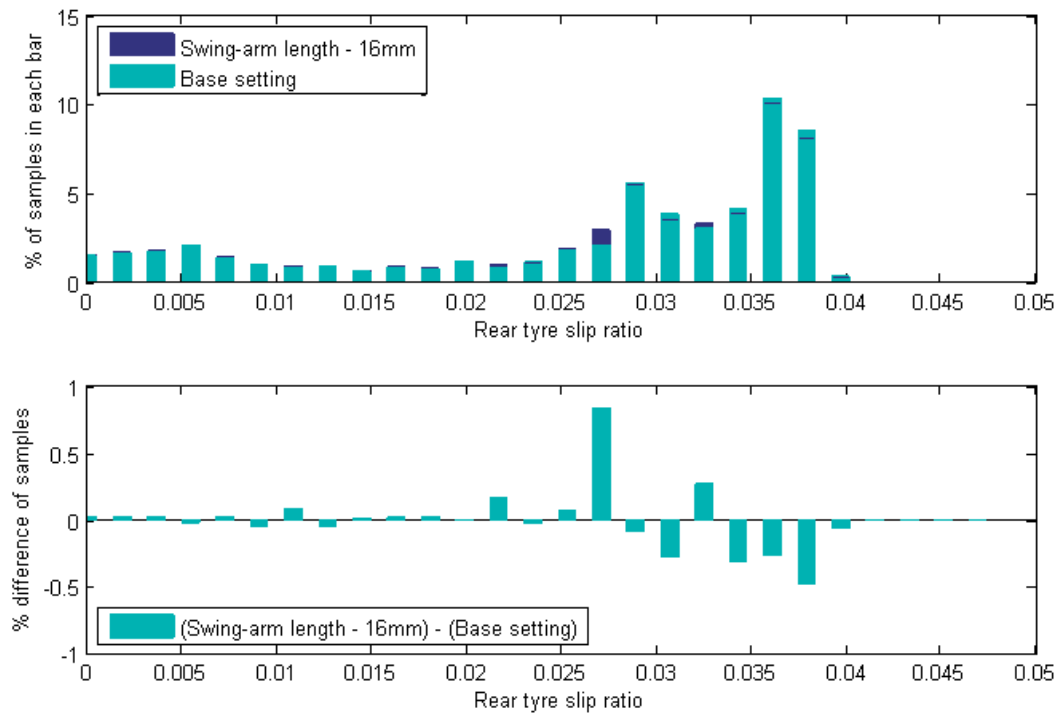


Figure 8.5: Histogram of rear tyre slip ratio

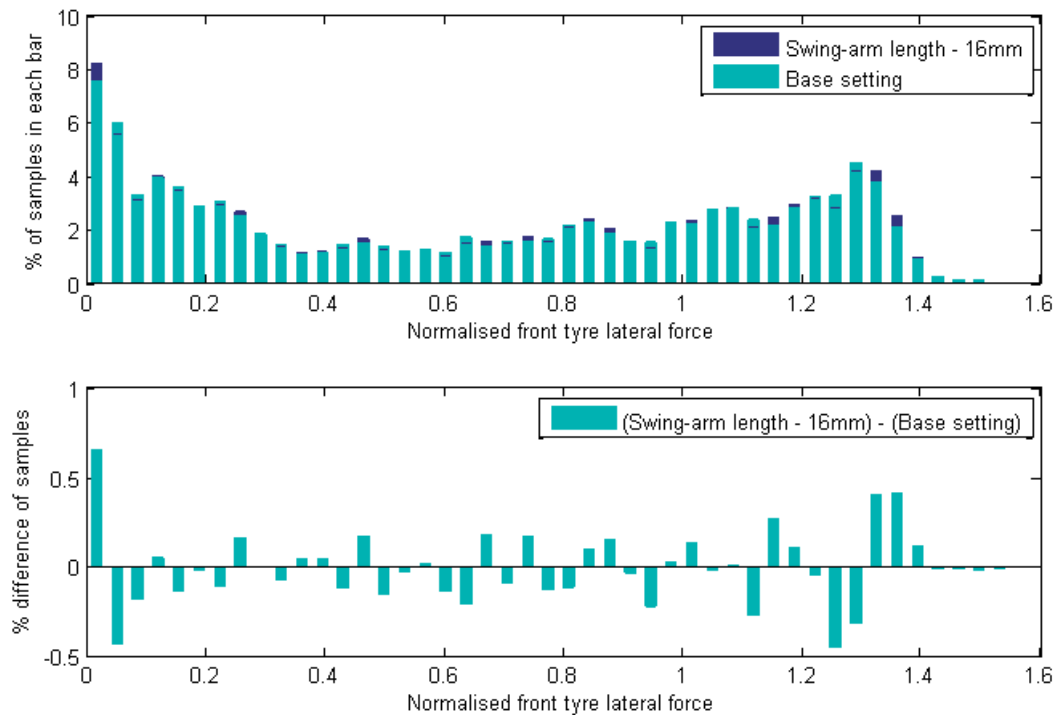


Figure 8.6: Histogram of normalised front tyre lateral force

simulation may result in a setting that mitigates the disadvantage, and the level of detail may be increased by separating the analysis into phases, such as corner entry and exit.

# Chapter 9

## Conclusions

### 9.1 Introduction

One point is worth mentioning with regard to modelling the motorcycle and tyres. The system is continuously in dynamic equilibrium. The tyres are always slipping relative to the ground, generating exactly the right forces and moments to balance the inertial forces and moments experienced by the bike and rider. Although it is possible to test parts of the model in isolation, there comes a time when the entire model must remain in dynamic equilibrium. At that time, everything must work or nothing does. It is difficult to explain the satisfaction experienced when, after countless computational crashes, the bike model finally crashes like a real motorcycle for the first time.

### 9.2 The model

The equations of motion were formulated using Kane's equations. This method was chosen over others because it is highly structured and avoids calculations which are necessary in other techniques. It turned out to be a good choice, as many corrections have to be made during development, and Kane's equations were very manageable even with a relatively complex system.

The objective was to create a model that is linear to the greatest extent possible without losing fidelity. It was possible to linearise many relationships

because they were already very nearly linear, while others, such as roll angle, could not be linearised. Non-linear forces such as those created by the suspension and tyres were treated as non-linear inputs, creating a Hammerstein structure. Certain non-linear terms in the equations of motion were included as an extension to the linear model, while very small non-linear terms were discarded.

Kane's method also allows velocities and accelerations anywhere in the model to be calculated easily, including the rotation rates and accelerations at the IMU location. The IMU rate gyro channels are simulated in the system  $C$  matrix and the simulated accelerometer channels are likewise available in the model. This 'virtual IMU' allows validation of the inertial behaviour of the bike, and in fact the steering controller is driven by the error between the actual rate gyros and the virtual ones. The velocity calculations provide the actual bike speed, and allow the front and rear tyre slip ratios to be calculated relative to each axle speed rather than being the ratio of wheel speeds.

The tyre model used is MF Tyre / MF Swift version 6.2, which is the latest version of the Magic Formula model at the time of writing. The equations for combined longitudinal and lateral slip were used. The tyre lateral force was divided into force due to sideslip and camber thrust for separate analysis, and this allows the point at which counter-steer ends to be identified. As a starting point, tyre parameters from Sharp et al. [27] were used, but these were modified using the golden section optimisation method to minimise the difference between recorded and estimated measurements for steering and suspension. Although good correlation between measured and estimated data was achieved in this way, it cannot produce the definitive parameter set for the tyres. The great difference in slip angle behaviour between the initial and final tyre parameters shows that in order to produce definitive values for slip angle, the tyre parameters for the actual tyres used would be needed.

## 9.3 Utility of the model

The motorcycle model can provide real time estimated values for unmeasurable quantities such as actual vehicle speed, tyre forces and slip angles, which may be used in engine management and vehicle stability strategies. At the time of writing, these strategies tend to operate independently of each other, but in the future it is likely that they will come under the control of an overall vehicle management system.

The model also has wide applicability in simulation. The job of a race engineer can be summarised as constrained optimisation. The race time, i.e. the time from the start of the race to the finish must be minimised, and all decisions leading up to and during a race weekend tend towards that end. The constraints include the range of settings available, tyre type and quantity, and of course time on track. The possibility that the setting is converging to some locally optimal configuration while missing the globally optimal setting is a constant concern and there is rarely enough time to make a big setting change and re-optimize the new configuration. By using the model to optimise parameters with respect to certain criteria, for example lateral front tyre force, it is possible to search for globally optimal settings.

One use of the model is as an aid to understanding. Many times, particularly when the model was close to completion, an apparent error would instead turn out to be ‘not seeing the full picture’ initially with regard to the physics. For example, when building the simulations for the coast-down tests in Chapter 7, the entire drag force, non-aerodynamic as well as aerodynamic, was applied to the centre of pressure, just to ensure that the negative acceleration was as expected. The bike slowed down less than expected and checking the input vector showed positive longitudinal shear forces at the tyre contact patches. Also, the wheels were over-rotating slightly with respect to road speed. Because the wheels have rotational inertia, a moment must act on them if they are to slow down, and this moment is due to the shear force created by tyre longitudinal slip, which depends on the slight over-rotation of the wheel. This brought the understanding that the tyre longitudinal shear forces are an important part of the non-aerodynamic

force in Eqn. (4.7), but not before asking the question “Why are the wheels going faster than the bike?”.

When data is available from track testing with tyres whose parameters are unknown, the model may be used to estimate the unknown parameters to some extent, using optimisation methods. While it is not possible to say, based on the work in this thesis, to what degree the resulting parameters are correct, it can be stated that they improve the match between measured and estimated data. In order to begin the optimisation process, a set of feasible tyre parameters is needed as a starting point.

## 9.4 Future work

In Section 4.6, the effect of engine vibration on the IMU channels was addressed. A better mounting location and or method must be found for the IMU before further testing is carried out. Two IMUs mounted in different locations on the bike may provide redundancy.

Additional degrees of freedom may be added to the model. These may be introduced to allow flex in the frame and swing-arm about various axes. Two additional degrees of freedom may also be used to allow lateral deflection of the tyre contact patches. However, for this to be useful, a good deal would need to be known about the tyre spring and damping rates in this direction.

Section 8.2 shows how proposed changes to parameters may be evaluated prior to testing the motorcycle. This approach may be extended by adding an optimisation algorithm so that a number of parameters may be optimised simultaneously with respect to certain criteria. These may be similar to the criteria chosen in Section 8.2.

The model may be modified to explore suspension configurations other than telescopic forks, for example, the BMW Telelever system. By driving the conventional and alternative models with the same functions and recorded data, a performance comparison may be carried out using similar performance criteria to those described in Chapter 8. This process is not confined to already realised

systems. A model can be formulated around a purely mathematical idea; for example, linking the front and rear suspension in some way. Then if the simulation shows some potential advantage, an effort may be made to design a physical system.

On high powered motorcycles especially, the engine and engine management system have a profound effect on chassis and tyre dynamics. When combined with accurate engine and drivetrain models, the motorcycle model is an ideal tool to develop and test engine management strategies.

Testing on race tracks is becoming ever more heavily proscribed, due to noise and other environmental restrictions. Lap optimisation is now in common use in the four wheel world and is a future application for the motorcycle model. Accurate lap simulation would require a very detailed topographical map of the circuit, but tools such as LIDAR (light detection and ranging) and UAVs (unmanned aerial vehicles) are readily available.

# Bibliography

- [1] R. L. Huston, *Multibody Dynamics*. Butterworth-Heinemann, 1990.
- [2] J. P. Meijaard, J. M. Papadopoulos, A. Ruina, and A. L. Schwab, “Linearized dynamics equations for the balance and steer of a bicycle: a benchmark and review,” *Proceedings of the Royal Society*, vol. 463, 2007.
- [3] R. S. Hand, “Comparisons and stability analysis of linearized equations of motion for a basic bicycle model,” Master’s thesis, Cornell University, 1988.
- [4] W. J. M. Rankine, “On the dynamical principles of the motion of velocipedes,” *Engineer* 28 (1869), pp. 79,129,153,175 and 29 (1870), p. 2.
- [5] A. Sharp, *Bicycles and Tricycles: An Elementary Treatise on Their Design and Construction*. Longman, 1896. (Reprinted as: *Bicycles and Tricycles: A Classic Treatise on Their Design and Construction*. Mineola, NY: Dover, 1977.).
- [6] F. J. W. Whipple, “The stability of the motion of a bicycle,” *Quarterly Journal of Pure and Applied Mathematics*, vol. 30, pp. 312–348, 1899.
- [7] E. Carvallo, “Théorie du mouvement du monocycle et de la bicyclette,” *Journal de l’École polytechnique*, vol. 5, pp. 119–188, 1900.
- [8] E. Carvallo, “Théorie du mouvement du monocycle. part 2: Théorie de la bicyclette,” *Journal de l’École polytechnique*, vol. 6, pp. 1–118, 1901.
- [9] A. L. Schwab and J. P. Meijaard, “A review on bicycle dynamics and rider control,” *Vehicle System Dynamics: International Journal of Vehicle Mechanics and Mobility*, vol. 51, no. 7, pp. 1059–1090, 2013.

- 
- [10] R. S. Sharp, "The stability and control of motorcycles," *Journal of Mechanical Engineering Science*, vol. 13, no. 5, pp. 316–329, 1971.
- [11] S. Timoshenko and D. H. Young, *Advanced Dynamics*. New York: McGraw Hill, 1948.
- [12] H. Bouasse, *Cours de mécanique, part 2*. Ch. Delagrave, 1910.
- [13] D. J. Limebeer and R. S. Sharp, "Bicycles, motorcycles and models," *IEEE Control Systems Magazine*, pp. 34–61, October 2006.
- [14] R. S. Sharp and D. J. N. Limebeer, "A motorcycle model for stability and control analysis," *Multibody System Dynamics*, vol. 6, no. 2, p. 123142, 2001.
- [15] C. Juden, "Shimmy," *Cycletouring*, pp. 208–209, June-July 1988.
- [16] R. S. Sharp, "The influence of frame flexibility on the lateral stability of motorcycles," *Journal of Mechanical Engineering Science*, vol. 15, no. 2, pp. 117–120, 1974.
- [17] K. R. Cooper, "The effects of aerodynamics on the performance and stability of high speed motorcycles," *Proceedings of the Second AIAA Symposium on Aerodynamics of Sports and Competition Automobiles, Los Angeles*, vol. 16, p. 165184, 1974.
- [18] R. D. Roland, "Computer simulation of bicycle dynamics," *Proceedings of the Symposium on Mechanics and Sport, AMSE*, vol. 4, pp. 35–83, 1973.
- [19] J. P. Lynch and R. D. Roland, "Computer animation of a bicycle simulation," *AFIPS '72 (Fall, part I): Proceedings of the December 5-7, 1972, fall joint computer conference, part 1*, 1972.
- [20] R. S. Sharp and E. J. Alstead, "The influence of structural flexibilities on the straight-running stability of motorcycles," *Vehicle System Dynamics*, vol. 9, pp. 327–357, 1980.

- 
- [21] P. T. J. Spierings, “The effects of lateral fork flexibility on the vibrational modes of straight running single track vehicles,” *Vehicle System Dynamics*, vol. 10, pp. 21–35, 1981. Issue 1.
- [22] C. Koenen and H. B. Pacejka, “Vibrational modes of motorcycles in curves,” *Proc. International Motorcycle Safety Conference, Motorcycle Safety Foundation, Washington D.C.*, vol. 2, pp. 501–543, 1980.
- [23] C. Koenen and H. B. Pacejka, “The influence of frame elasticity, simple rider body dynamics, and tyre moments on free vibrations of motorcycles in curves.,” *Proc. 7th IAVSD Symposium on Dynamics of Vehicles on Roads and on Railway Tracks.*, pp. 53–65, 1981.
- [24] C. Koenen, *The dynamic behaviour of motorcycles when running straight ahead and when cornering*. PhD thesis, Delft University of Technology, 1983.
- [25] V. Cossalter and R. Lot, “A motorcycle multi-body model for real time simulations based on the natural coordinates approach,” *Vehicle System Dynamics*, vol. 37, no. 6, pp. 423–447, 2002.
- [26] R. S. Sharp, “Vibrational modes of motorcycles and their design parameter sensitivities,” *Vehicle NVH and Refinement, Proc. Int. Conf. Birmingham Mech. Eng.*, pp. 107–121, 1994.
- [27] R. S. Sharp, S. Evangelou, and D. J. N. Limebeer, “Advances in the Modelling of Motorcycle Dynamics,” *Multibody System Dynamics*, vol. 12, pp. 251–283, 2004.
- [28] S. A. Evangelou, D. J. N. Limebeer, and M. Tomas-Rodriguez, “Suppression of burst oscillations in racing motorcycles,” *Transactions of the ASME, Journal of Applied Mechanics*, 2010.
- [29] H. Fromm, “Sideslip and guiding characteristics of the rolling wheel,” *Bericht über die Sitzung Flattern und Rollverhalten von Fahrwerken am 16./17. Oktober 1941 in Stuttgart. NACA Technical Memorandum 1365*, pp. 191–216.

- 
- [30] H. Sakai, “Effect of main factors on dynamic properties of motorcycle tires,” *SAE paper 79025, Society of Automotive engineers*, 1979.
- [31] L. Segel and R. Wilson, “Requirements for describing the mechanics of tyres used on single track vehicles,” *Proceedings of IUTAM Symposium, Delft, Swets & Zeitlinger, Amsterdam*, 1976.
- [32] E. Bakker, L. Nyborg, and H. B. Pacejka, “Tyre modeling for use in vehicle dynamics studies,” *SAE Paper 870421, Society of Automotive Engineers*, 1986.
- [33] E. Bakker, H. B. Pacejka, and L. Lidner, “A new tyre model with application in vehicle dynamics studies,” *SAE Paper 890087, 4th Auto Technologies Conference, Monte Carlo*, 1989.
- [34] H. B. Pacejka and E. Bakker, “The magic formula tyre model, tyre models for vehicle dynamic analysis,” *Proceedings of the 1st International Colloquium on Tyre Model for Vehicle Dynamics Analysis*, pp. 1–18, 1993.
- [35] J. S. Loeb, D. A. Günther, H. H. Chen, and J. R. Ellis, “Lateral stiffness, cornering stiffness and relaxation length of the pneumatic tyre,” *SAE Paper 900129, Society of Automotive engineers*, 1990.
- [36] H. B. Pacejka and I. J. M. Besselink, “Magic formula tyre model with transient properties,” *Proceedings of the Berlin Tyre Colloquium, Vehicle System Dynamics Supplement 27, Swets & Zeitlinger, Lisse*, pp. 145–155, 1997.
- [37] E. J. H. de Vries and H. B. Pacejka, “Motorcycle tyre measurements and models,” *Vehicle System Dynamics*, vol. 29, no. 1, pp. 280–298, 1998.
- [38] Y. Tezuka, H. Ishii, and S. Kiyota, “Application of the magic formula tire model to motorcycle manoeuvrability analysis,” *JSAE Review*, vol. 22, no. 3, pp. 305–310, 2001.
- [39] H. B. Pacejka, *Tyre and Vehicle Dynamics*. Elsevier, second ed., 2006.

- 
- [40] D. H. Weir and J. W. Zellner, "Lateral-directional motorcycle dynamics and rider control," *SAE Paper 780304*, Society of Automotive Engineers, 1978.
- [41] T. R. Kane and A. L. David, *Dynamics, Theory and Applications*. McGraw-Hill, 1985.
- [42] M. Roithmayr, Carlos and H. Hodges, Dewey, *Dynamics, Theory and Application of Kane's Method*. Cambridge University Press, 2016.
- [43] A. Case, "A brief synopsis of Kane's method." [www.iosrjournals.org/iosr-jmce/papers/vol6-issue4/B0640713.pdf](http://www.iosrjournals.org/iosr-jmce/papers/vol6-issue4/B0640713.pdf).
- [44] H. B. Pacejka, *Tyre and Vehicle Dynamics*. Elsevier, third ed., 2012.
- [45] "OptimumG, Vehicle Dynamics Solutions." [https://s3.amazonaws.com/static.optimumg.com/wp-content/uploads/2012/04/power\\_response.png](https://s3.amazonaws.com/static.optimumg.com/wp-content/uploads/2012/04/power_response.png).
- [46] W. H. Press, S. A. Teukolsky, W. T. Vetterling, and B. P. Flannery, *Numerical Recipes*. Cambridge University Press, 3 ed., 2007.
- [47] "SAE J670 - Vehicle Dynamics Terminology, SAE Vehicle Dynamics Standards Committee," 2008.
- [48] "MF-Tyre / MF-Swift 6.2 Equation manual." [www.delft-tyre.nl/](http://www.delft-tyre.nl/), Copyright © 2013 TNO.
- [49] W. F. Milliken and D. L. Milliken, *Race Car Vehicle Dynamics*. Society of Automotive Engineers (SAE), 1995.
- [50] *General Approach of Tyre*. Dufournier Technologies, 2016.
- [51] P. Bayle, J. F. Forissier, and S. Lafon, "A new tyre model for vehicle dynamics simulation," *Automotive Technology International*, 1993.
- [52] I. J. M. Besselink, A. J. C. Schmeitz, and H. B. Pacejka, "An improved Magic Formula / Swift Tyre model that can handle inflation pressure changes," *Vehicle System Dynamics*, vol. 48, no. 1, pp. 337–352, 2010.

- [53] H. B. Pacejka, *Tyre and Vehicle Dynamics*. Butterworth Heinemann, Oxford, 2002.
- [54] “Jeremy McWilliams, Wikipedia article.” [https://en.wikipedia.org/wiki/Jeremy\\_McWilliams](https://en.wikipedia.org/wiki/Jeremy_McWilliams).
- [55] J. Kiefer, “Sequential minimax search for a maximum,” *Proceedings of the American Mathematical Society*, vol. 4, no. 3, pp. 502–506, 1953.
- [56] “ISO 11898-1:2015, Road Vehicles – Controller Area Network (CAN), International Organization for Standardization.”

# Appendices

# Appendix A

## Magic Formula Equations

The equations in this appendix are in accordance with MF-Tyre / MF-Swift 6.2 [48], which at the time of writing is the most up-to-date version of the Magic Formula tyre model. The following variables are used throughout the equations,

$$\begin{aligned}df_z &= \frac{F_z - F_{z0}}{F_{z0}} && \text{Vertical force increment} \\ dp_i &= \frac{P - P_0}{P_0} && \text{Inflation pressure increment} \\ F'_{z0} &= \lambda_{Fz0} F_{z0} && \text{Scaled nominal force}\end{aligned}$$

where  $F_z$  is the vertical force,  $F_{z0}$  is the nominal vertical force,  $P$  is the inflation pressure,  $P_0$  is the nominal inflation pressure, and  $\lambda_{Fz0}$  is a non-dimensional constant parameter representing the scale factor of nominal load. The equations in the following sections contain many parameters like  $\lambda_{Fz0}$ , and these are listed after each set of equations. It is the values of these parameters that define the characteristics of a particular tyre.

### A.1 Longitudinal force $F_x$

The longitudinal force is given by:

$$F_x = F_{x0} G_{x\alpha} \tag{A.1}$$

In the absence of side slip,  $G_{x\alpha} = 1$ , so  $F_x = F_{xo}$ .

### A.1.1 Longitudinal force (pure longitudinal slip, $\kappa \neq 0$ , $\alpha = 0$ )

$$F_{xo} = D_x \sin(C_x \arctan(B_x \kappa_x - E_x(B_x \kappa_x - \arctan(B_x \kappa_x)))) + S_{Vx}$$

$$\kappa_x = \kappa + S_{Hx}$$

$$C_x = p_{Cx1} \lambda_{Cx} \quad (> 0)$$

$$D_x = \mu_x F_z \zeta_1 \quad (> 0)$$

$$\mu_x = (p_{Dx1} + p_{Dx2} df_z)(1 + p_{px3} dp_i + p_{px4} dp_i^2)(1 - p_{Dx3} \gamma^2) \lambda_{\mu x}$$

$$E_x = (p_{Ex1} + p_{Ex2} df_z + p_{Ex3} df_z^2)(1 - p_{Ex4} \operatorname{sgn}(\kappa_x)) \lambda_{Ex} \quad (\leq 1)$$

$$K_{x\kappa} = F_z (p_{Kx1} + p_{Kx2} df_z) \exp(p_{Kx3} df_z)(1 + p_{px1} dp_i + p_{px2} dp_i^2)$$

$$B_x = \frac{K_{x\kappa}}{(C_x D_x + \varepsilon_x)}$$

$$S_{Hx} = (p_{Hx1} + p_{Hx2} df_z) \lambda_{Hx}$$

$$S_{Vx} = F_z (p_{Vx1} + p_{Vx2} df_z) \lambda_{Vx} \lambda_{\mu x} \zeta_1$$

The constants are:

$p_{Cx1}$  : Shape factor for longitudinal force.

$p_{Dx1}$  : Longitudinal friction,  $\mu_x$ , at nominal  $F_z$ .

$p_{Dx2}$  : Variation of longitudinal friction,  $\mu_x$ , with load,  $F_z$ .

$p_{Dx3}$  : Variation of longitudinal friction,  $\mu_x$ , with camber,  $\gamma$ .

$p_{Ex1}$  : Longitudinal curvature at nominal  $F_z$ .

$p_{Ex2}$  : Variation of longitudinal curvature with load,  $F_z$ .

$p_{Ex3}$  : Variation of longitudinal curvature with load squared,  $F_z^2$ .

$p_{Ex4}$  : Factor in longitudinal curvature while driving.

$p_{Hx1}$  : Horizontal shift,  $S_{Hx}$ , at nominal  $F_z$ .

$p_{Hx2}$  : Variation of horizontal shift,  $S_{Hx}$ , with load,  $F_z$ .

$p_{Kx1}$  : Longitudinal slip stiffness at nominal  $F_z$ .

$p_{Kx2}$  : Variation of longitudinal slip stiffness with load,  $F_z$ .

$p_{Kx3}$  : Exponent in longitudinal slip stiffness with load,  $F_z$ .

$p_{px1}$  : Linear pressure effect on longitudinal slip stiffness.

$p_{px2}$  : Quadratic pressure effect on longitudinal slip stiffness.

$p_{px3}$  : Linear pressure effect on longitudinal friction.

$p_{px4}$  : Quadratic pressure effect on longitudinal friction.

$p_{Vx1}$  : Vertical shift at nominal  $F_z$ .

$p_{Vx2}$  : Variation of vertical shift with load,  $F_z$ .

$\lambda_{Cx}$  : Scale factor of  $F_x$  shape factor.

$\lambda_{Ex}$  : Scale factor of  $F_x$  curvature factor.

$\lambda_{Hx}$  : Scale factor of  $F_x$  horizontal shift.

$\lambda_{Vx}$  : Scale factor of  $F_x$  vertical shift.

$\lambda_{\mu x}$  : Scale factor of  $F_x$  peak friction coefficient.

$\zeta_1$  : Turn slip parameter ( = 1 when turn slip is not used).

$\varepsilon_x$  : Small quantity to avoid singularity.

### A.1.2 Longitudinal force (combined slip, $\kappa \neq 0$ , $\alpha \neq 0$ )

In the realistic situation where the tyre has both longitudinal and side slip,  $G_{x\alpha}$  in Eqn. (A.1) is not equal to 1, but is given by:

$$G_{x\alpha} = \frac{\cos(C_{x\alpha} \arctan(B_{x\alpha}\alpha_s - E_{x\alpha}(B_{x\alpha}\alpha_s - \arctan(B_{x\alpha}\alpha_s))))}{\cos(C_{x\alpha} \arctan(B_{x\alpha}S_{Hx\alpha} - E_{x\alpha}(B_{x\alpha}S_{Hx\alpha} - \arctan(B_{x\alpha}S_{Hx\alpha}))))}$$

$$\alpha_s = \alpha^* + S_{Hx\alpha}$$

$$B_{x\alpha} = (r_{Bx1} + r_{Bx3}\gamma^2) \cos(\arctan(r_{Bx2}\kappa))\lambda_{x\alpha}$$

$$C_{x\alpha} = r_{Cx1}$$

$$E_{x\alpha} = r_{Ex1} + r_{Ex2}df_z$$

$$S_{Hx\alpha} = r_{Hx1}$$

The constants are:

$r_{Bx1}$  : Slope factor for combined slip  $F_x$  reduction.

$r_{Bx2}$  : Variation of slope  $F_x$  reduction with  $\kappa$ .

$r_{Bx3}$  : Influence of camber on stiffness for  $F_x$  combined slip.

$r_{Cx1}$  : Shape factor for combined slip  $F_x$  reduction.

$r_{Ex1}$  : Curvature factor of combined slip  $F_x$ .

$r_{Ex2}$  : Curvature factor of combined slip  $F_x$  with load.

$r_{Hx1}$  : Shift factor for combined slip  $F_x$  reduction.

$\lambda_{x\alpha}$  : Scale factor of  $\alpha$  influence on  $F_x$ .

## A.2 Lateral force $F_y$

The lateral force is given by:

$$F_y = G_{y\kappa} F_{yp} + S_{Vy\kappa} \quad (\text{A.2})$$

In the absence of longitudinal slip,  $G_{y\kappa} = 1$  and  $S_{Vy\kappa} = 0$ , so  $F_y = F_{yp}$ .

### A.2.1 Lateral force (pure side slip, $\kappa = 0$ , $\alpha \neq 0$ )

$$F_{yp} = D_y \sin(C_y \arctan(B_y \alpha_y - E_y (B_y \alpha_y - \arctan(B_y \alpha_y)))) + S_{Vy} \quad (\text{A.3})$$

$$\alpha_y = \alpha^* + S_{Hy}$$

$$B_y = \frac{K_{y\alpha}}{C_y D_y + \varepsilon_y}$$

$$C_y = p_{Cy1} \lambda_{Cy}$$

$$D_y = \mu_y F_z \zeta_2$$

$$\mu_y = (p_{Dy1} + p_{Dy2} df_z)(1 + p_{py3} dp_i + p_{py4} dp_i^2)(1 - p_{Dy3} \gamma^2) \lambda_{\mu y}$$

$$E_y = (p_{Ey1} + p_{Ey2} df_z)(1 + p_{Ey5} \gamma^2 - (p_{Ey3} + p_{Ey4} \gamma) \text{sgn}(\alpha_y)) \lambda_{Ey} \quad (\leq 1)$$

$$K_{y\alpha} = p_{Ky1} F'_{z0} (1 + p_{py1} dp_i) \sin \left( p_{Ky4} \arctan \left( \frac{F_z}{(p_{Ky2} + p_{Ky5} \gamma^2) F'_{z0} (1 + p_{py2} dp_i)} \right) \right) \\ \cdot (1 - p_{Ky3} |\gamma|) \lambda_{Ky\alpha} \zeta_3$$

$$S_{Hy} = (p_{Hy1} + p_{Hy2} df_z) \lambda_{Hy} + \frac{K_{y\gamma 0} \gamma - S_{Vy\gamma}}{K_{y\alpha}} \zeta_0 + \zeta_4 - 1$$

$$S_{Vy} = F_z (p_{Vy1} + p_{Vy2} df_z) \lambda_{Vy} \lambda_{\mu y} \zeta_2 + S_{Vy\gamma}$$

$$S_{Vy\gamma} = F_z (p_{Vy3} + p_{Vy4} df_z) \gamma \lambda_{Ky\gamma} \lambda_{\mu y} \zeta_2$$

$$K_{y\gamma 0} = (p_{Ky6} + p_{Ky7} df_z) F_z \lambda_{Ky\gamma} (1 + p_{py5} dp_i)$$

The constants are:

$p_{Cy1}$  : Shape factor for lateral force.

$p_{Dy1}$  : Lateral friction,  $\mu_y$ , at nominal  $F_z$ .

$p_{Dy2}$  : Variation of lateral friction,  $\mu_y$ , with load,  $F_z$ .

$p_{Dy3}$  : Variation of lateral friction,  $\mu_y$ , with squared camber,  $\gamma^2$ .

$p_{Ey1}$  : Lateral curvature at nominal  $F_z$ .

$p_{Ey2}$  : Variation of lateral curvature with load,  $F_z$ .

$p_{Ey3}$  : Zero order camber dependency of curvature.

$p_{Ey4}$  : Variation of lateral curvature with camber,  $\gamma$ .

$p_{Ey5}$  : Camber curvature coefficient.

$p_{Hy1}$  : Horizontal shift,  $S_{Hy}$ , at nominal  $F_z$ .

$p_{Hy2}$  : Variation of horizontal shift,  $S_{Hy}$ , with load,  $F_z$ .

$p_{Ky1}$  : Maximum value of stiffness,  $\frac{K_{y\alpha}}{F_{z0}}$

$p_{Ky2}$  : Load at which  $K_{y\alpha}$  reaches maximum value.

$p_{Ky3}$  : Variation of  $\frac{K_{y\alpha}}{F_{z0}}$  with camber.

$p_{Ky4}$  : Peak stiffness variation with camber squared.

$p_{Ky5}$  : Lateral stiffness dependency on camber.

$p_{Ky6}$  : Camber stiffness factor.

$p_{Ky7}$  : Load dependency of camber stiffness factor.

$p_{py1}$  : Pressure effect on cornering stiffness magnitude.

$p_{py2}$  : Pressure effect on location of cornering stiffness peak.

$p_{py3}$  : Linear pressure effect on lateral friction.

$p_{py4}$  : Quadratic pressure effect on lateral friction.

$p_{py5}$  : Influence of inflation pressure on camber stiffness.

$p_{Vy1}$  : Vertical shift in  $\frac{S_{Vy}}{F_z}$  at nominal load,  $F_{z0}$ .

$p_{Vy2}$  : Variation of shift in  $\frac{S_{Vy}}{F_z}$  with load,  $F_z$ .

$p_{Vy3}$  : Variation of shift in  $\frac{S_{Vy}}{F_z}$  with camber,  $\gamma$ .

$p_{Vy4}$  : Variation of shift in  $\frac{S_{Vy}}{F_z}$  with camber and load.

$\lambda_{Cy}$  : Scale factor of  $F_y$  shape factor.

$\lambda_{Ey}$  : Scale factor of  $F_y$  curvature factor.

$\lambda_{Hy}$  : Scale factor of  $F_y$  horizontal shift.

$\lambda_{Ky\alpha}$  : Scale factor of cornering stiffness.

$\lambda_{Ky\gamma}$  : Scale factor of camber stiffness.

$\lambda_{Vy}$  : Scale factor of  $F_y$  vertical shift.

$\lambda_{\mu y}$  : Scale factor of  $F_y$  peak friction coefficient.

$\zeta_0, \zeta_2 \dots \zeta_4$  : Turn slip parameters ( = 1 when turn slip is not used).

$\varepsilon_y$  : Small quantity to avoid singularity.

### A.2.2 Lateral force (combined slip, $\kappa \neq 0$ , $\alpha \neq 0$ )

Where the tyre has both longitudinal and side slip,  $G_{y\kappa} \neq 1$  and  $S_{Vy\kappa} \neq 0$ .

$$S_{Vy\kappa} = D_{Vy\kappa} \sin(r_{Vy5} \arctan(r_{Vy6} \kappa)) \lambda_{Vy\kappa}$$

$$D_{Vy\kappa} = \mu_y F_z (r_{Vy1} + r_{Vy2} df_z + r_{Vy3} \gamma) \cos(\arctan(r_{Vy4} \alpha^*)) \zeta_2$$

$$G_{y\kappa} = \frac{\cos(C_{y\kappa} \arctan(B_{y\kappa} \kappa_s - E_{y\kappa} (B_{y\kappa} \kappa_s - \arctan(B_{y\kappa} \kappa_s))))}{\cos(C_{y\kappa} \arctan(B_{y\kappa} S_{Hy\kappa} - E_{y\kappa} (B_{y\kappa} S_{Hy\kappa} - \arctan(B_{y\kappa} S_{Hy\kappa}))))}$$

$$\kappa_s = \kappa + S_{Hy\kappa}$$

$$B_{y\kappa} = (r_{By1} + r_{By4} \gamma^2) \cos(\arctan(r_{By2} (\alpha^* - r_{By3}))) \lambda_{y\kappa}$$

$$C_{y\kappa} = r_{Cy1}$$

$$E_{y\kappa} = r_{Ey1} + r_{Ey2} df_z$$

$$S_{Hy\kappa} = r_{Hy1} + r_{Hy2} df_z$$

The constants are:

$$r_{Vy1} : \kappa \text{ induced side force } \frac{S_{Vy\kappa}}{\mu_y F_z} \text{ at } F_{z0}.$$

$$r_{Vy2} : \text{Variation of } \frac{S_{Vy\kappa}}{\mu_y F_z} \text{ with load, } F_z.$$

$$r_{Vy3} : \text{Variation of } \frac{S_{Vy\kappa}}{\mu_y F_z} \text{ with camber, } \gamma.$$

$$r_{Vy4} : \text{Variation of } \frac{S_{Vy\kappa}}{\mu_y F_z} \text{ with slip angle, } \alpha.$$

$$r_{Vy5} : \text{Variation of } \frac{S_{Vy\kappa}}{\mu_y F_z} \text{ with slip ratio, } \kappa.$$

$$r_{Vy6} : \text{Variation of } \frac{S_{Vy\kappa}}{\mu_y F_z} \text{ with } \arctan(\kappa).$$

$r_{By1}$  : Slope factor for combined slip  $F_y$  reduction.

$r_{By2}$  : Variation of slope  $F_y$  reduction with slip angle,  $\alpha$ .

$r_{By3}$  : Shift term for  $\alpha$  in slope  $F_y$  reduction.

$r_{By4}$  : Influence of camber on stiffness of  $F_y$  combined slip.

$r_{Cy1}$  : Shape factor for combined slip  $F_y$  reduction.

$r_{Ey1}$  : Curvature factor of combined slip  $F_y$ .

$r_{Ey2}$  : Curvature factor of combined slip  $F_y$  with load.

$r_{Hy1}$  : Shift factor for combined slip  $F_y$  reduction.

$r_{Hy2}$  : Shift factor for combined slip  $F_y$  reduction with load.

$\lambda_{y\kappa}$  : Scale factor of  $\kappa$  influence on  $F_y$ .

$\lambda_{Vy\kappa}$  : Scale factor of  $\kappa$  induced ply-steer. See Section 5.2.15.

### A.3 Overturning moment $M_x$

The MF-Tyre / MF-Swift 6.2 Equation manual [48] provides two alternative equations for  $M_x$ . One is described as being useful for “special motorcycle tyres”.

The tyres used to obtain the test data were Dunlop Sportmax GP Racer D211s.

As these are high performance tyres intended for racetrack use, this version of the equation was chosen.

$$M_x = R_0 \lambda_{Mx} (F_y (q_{sx13} + q_{sx14} |\gamma|) - F_z q_{sx12} \gamma |\gamma|) \quad (\text{A.4})$$

$R_0$  is the unloaded tyre radius. The constants are:

$q_{sx12}$  : Camber squared induced overturning moment.

$q_{sx13}$  : Lateral force induced overturning moment.

$q_{sx14}$  : Lateral force induced overturning moment with camber.

$\lambda_{Mx}$  : Scale factor for overturning moment.

## A.4 Rolling resistance moment $M_y$

$$\begin{aligned}
M_y = & -R_0 F_{z0} \lambda_{My} \\
& \cdot \left( q_{sy1} + q_{sy2} \frac{F_x}{F_{z0}} + q_{sy3} \left| \frac{V_x}{V_0} \right| + q_{sy4} \left( \frac{V_x}{V_0} \right)^4 + q_{sy5} \gamma^2 + q_{sy6} \frac{F_z}{F_{z0}} \gamma^2 \right) \\
& \cdot \left( \left( \frac{F_z}{F_{z0}} \right)^{q_{sy7}} \left( \frac{P}{P_0} \right)^{q_{sy8}} \right)
\end{aligned} \tag{A.5}$$

The constants are:

$V_0$  : Reference velocity.

$q_{sy1}$  : Rolling resistance moment coefficient.

$q_{sy2}$  : Rolling resistance moment dependence on  $F_x$ .

$q_{sy3}$  : Rolling resistance moment dependence on speed  $V_x$ .

$q_{sy4}$  : Rolling resistance moment dependence on  $V_x^4$ .

$q_{sy5}$  : Rolling resistance moment dependence on  $\gamma^2$ .

$q_{sy6}$  : Rolling resistance moment dependence on  $\gamma^2$  and load  $F_z$ .

$q_{sy7}$  : Rolling resistance moment dependence on load.

$q_{sy8}$  : Rolling resistance moment dependence on inflation pressure.

$\lambda_{My}$  : Scale factor for rolling resistance moment.

## A.5 Aligning moment $M_z$

$$M_z = -tG_{y\kappa 0}F_{y0} + M_{zr} + sF_x \quad (\text{A.6})$$

where  $G_{y\kappa 0}F_{y0}$  is  $G_{y\kappa}F_{yp}$  in Eqn. (A.2) evaluated at  $\gamma = 0$ .

$$t = D_t \cos(C_t \arctan(B_t \alpha_{t,eq} - E_t(B_t \alpha_{t,eq} - \arctan(B_t \alpha_{t,eq})))) \cos(\alpha^*) \quad (\text{A.7})$$

$$B_t = (q_{Bz1} + q_{Bz2}df_z + q_{Bz3}df_z^2)(1 + q_{Bz4}\gamma + q_{Bz5}|\gamma|) \frac{\lambda_{Ky\alpha}}{\lambda_{\mu y}}$$

$$C_t = q_{Cz1}$$

$$D_t = F_z(q_{Dz1} + q_{Dz2}df_z)(1 - p_{pz1}dp_i)(1 + q_{Dz3}\gamma + q_{Dz4}\gamma^2) \frac{R_0}{F_{z0}} \lambda_t \zeta_5$$

$$E_t = (q_{Ez1} + q_{Ez2}df_z + q_{Ez3}df_z^2) \cdot \left( 1 + (q_{Ez4} + q_{Ez5}\gamma) \left( \frac{2}{\pi} \right) \arctan(B_t C_t \alpha_t) \right)$$

$$s = \left( s_{sz1} + s_{sz2} \left( \frac{F_y}{F_{z0}} \right) + (s_{sz3} + s_{sz4}df_z)\gamma \right) R_0 \lambda_s$$

$$M_{zr} = D_r \cos(\zeta_7 \arctan(B_r \alpha_{r,eq}))$$

$$D_r = F_z R_0 \lambda_{\mu y} \cos(\alpha^*) (q_{Dz6} + q_{Dz7}df_z) \lambda_r \zeta_2 + (q_{Dz8} + q_{Dz9}df_z) \gamma \lambda_{Kz\gamma} \\ (1 + p_{pz2}dp_i) \zeta_0 + (q_{Dz10} + q_{Dz11}df_z) \gamma |\gamma| \lambda_{Kz\gamma} \zeta_0 - \zeta_8 + 1$$

$$B_r = \left( q_{Bz9} \frac{\lambda_{Ky\alpha}}{\lambda_{\mu y}} + q_{Bz10} B_y C_y \right) \zeta_6$$

$$\alpha_{r,eq} = \arctan \sqrt{\tan^2(\alpha_t) + \left( \frac{K_{x\kappa}}{K_{y\alpha}} \right)^2 \kappa^2 \cdot \text{sgn}(\alpha_t)}$$

$$\alpha_{t,eq} = \arctan \sqrt{\tan^2(\alpha_t) + \left( \frac{K_{x\kappa}}{K_{y\alpha}} \right)^2 \kappa^2 \cdot \text{sgn}(\alpha_r)}$$

$$\alpha_r = \alpha^* + S_{Hy} + \frac{S_V y}{K_{y\alpha}}$$

$$\alpha_t = \alpha^* + S_{Ht}$$

$$S_{Ht} = q_{Hz1} + q_{Hz2}df_z + (q_{Hz3} + q_{Hz4}df_z)\gamma$$

The constants are:

$q_{Bz1}$  : Slope factor for pneumatic trail  $B_t$  at nominal load  $F_{z0}$ .

$q_{Bz2}$  : Variation of slope factor for pneumatic trail  $B_t$  with load.

$q_{Bz3}$  : Variation of slope factor for pneumatic trail  $B_t$  with load squared.

$q_{Bz4}$  : Variation of slope factor for pneumatic trail  $B_t$  with camber.

$q_{Bz5}$  : Variation of slope factor for pneumatic trail  $B_t$  with absolute camber.

$q_{Cz1}$  : Shape factor for  $C_t$  for pneumatic trail.

$q_{Dz1}$  : Peak pneumatic trail  $D_t$ .

$q_{Dz2}$  : Variation of peak pneumatic trail  $D_t$  with load.

$q_{Dz3}$  : Variation of peak pneumatic trail  $D_t$  with camber.

$q_{Dz4}$  : Variation of peak pneumatic trail  $D_t$  with camber squared.

$q_{Ez1}$  : Pneumatic trail curvature  $E_t$  at nominal load  $F_{z0}$ .

$q_{Ez2}$  : Variation of pneumatic trail curvature  $E_t$  with load.

$q_{Ez3}$  : Variation of pneumatic trail curvature  $E_t$  with load squared.

$q_{Ez4}$  : Variation of pneumatic trail curvature  $E_t$  with sign of  $\alpha_t$ .

$q_{Ez5}$  : Variation of  $E_t$  with camber and sign of  $\alpha_t$ .

$q_{Hz1}$  : Pneumatic trail horizontal shift  $S_{ht}$  at  $F_{z0}$ .

$q_{Hz2}$  : Variation of  $S_{ht}$  with load.

$q_{Hz3}$  : Variation of  $S_{ht}$  with camber.

$q_{Hz4}$  : Variation of  $S_{ht}$  with camber and load.

$q_{Bz9}$  : Slope factor  $B_r$  of residual torque  $M_{zr}$ .

$q_{Bz10}$  : Slope factor  $B_r$  of residual torque  $M_{zr}$ .

$p_{pz1}$  : Linear pressure effect on pneumatic trail.

$p_{pz2}$  : Influence of inflation pressure on residual aligning moment.

$q_{Dz6}$  : Peak residual torque  $D_r$ .

$q_{Dz7}$  : Variation of  $D_r$  with load.

$q_{Dz8}$  : Variation of  $D_r$  with camber.

$q_{Dz9}$  : Variation of  $D_r$  with camber and load.

$q_{Dz10}$  : Variation of  $D_r$  with camber squared.

$q_{Dz11}$  : Variation of  $D_r$  with camber squared and load.

$s_{sz1}$  : Nominal value of  $\frac{s}{R_0}$ : effect of  $F_x$  on  $M_z$ .

$s_{sz2}$  : Variation of  $\frac{s}{R_0}$  with  $\frac{F_y}{F_{z0}}$ .

$s_{sz3}$  : Variation of  $\frac{s}{R_0}$  with camber.

$s_{sz4}$  : Variation of  $\frac{s}{R_0}$  with load and camber.

$\lambda_r$  : Scale factor of offset of residual torque.

$\lambda_s$  : Scale factor of moment arm of  $F_x$ .

$\lambda_t$  : Scale factor of peak of pneumatic trail.

$\lambda_{Kz\gamma}$  : Scale factor of camber stiffness.

$\lambda_{Ky\alpha}$  : Scale factor of cornering stiffness.

$\zeta_5 \dots \zeta_8$  : Turn slip parameters ( = 1 when turn slip is not used).

## A.6 Relaxation behaviour

The relaxation lengths for longitudinal and lateral forces are  $\delta_x$  and  $\delta_y$  respectively, and the expressions are derived in Section 5.2.16.

$$\delta_x = \frac{K_{x\kappa}}{C_x} \quad (5.12)$$

$$\delta_y = \frac{K_{y\alpha}}{C_y} \quad (5.16)$$

$$C_x = C_{x0}(1 + p_{cfx1}df_z + p_{cfx2}df_z^2)(1 + c_{fx3}dp_i)$$

$$C_y = C_{y0}(1 + p_{cfy1}df_z + p_{cfy2}df_z^2)(1 + c_{fy3}dp_i)$$

where  $K_{x\kappa}$  and  $K_{y\alpha}$  are the longitudinal and lateral slip stiffness of the tyre at the nominal vertical force and inflation pressure. See Section 5.2.13 for definitions.

$C_x$  and  $C_y$  are the elastic longitudinal and lateral stiffness respectively of the tyre.

The constants are:

$p_{cfx1}$  : Tyre overall longitudinal stiffness vertical deflection dependency linear term.

$p_{cfx2}$  : Tyre overall longitudinal stiffness vertical deflection dependency quadratic term.

$p_{cfx3}$  : Tyre overall longitudinal stiffness pressure dependency.

$p_{cfy1}$  : Tyre overall lateral stiffness vertical deflection dependency linear term.

$p_{cfy2}$  : Tyre overall lateral stiffness vertical deflection dependency quadratic term.

$p_{cfy3}$  : Tyre overall lateral stiffness pressure dependency.

# Index

- 2D Datarecording , 152–178
- Acceleration expressions, 90–99
- Alstead, E. J., 10
- Anti-lock braking, 112–113
- ArcGIS, 183
- Bouasse, H., 8
- C programming language, 106, 115
- CAN bus, 154–156
- Capsize mode, 8
- Cartesian co-ordinates, 20
- Carvallo, Emmanuel, 7
- Chain force, 49–50
- Channel
  - analog, 158
  - brake pressure, 175–176
  - digital, 159
  - engine speed, 160–161
  - front suspension position, 170–171
  - front wheel speed, 167–169
  - gear position, 162
  - rear suspension position, 172–175
  - rear wheel speed, 169–170
  - steering angle, 175
  - throttle position, 161
  - wheel torques, 176
- Cholesky decomposition, 115
- Coast-down testing, 177–178
- Computational performance, 115
- Constraints, 7, 8, 13, 14, 33–37, 116
- Controller
  - road speed, 107–110
  - roll angle, 107–110
- Cooper, K. R., 10
- Cornell Aeronautical Laboratory, 10
- Cossalter and Lot 2002 model, 11
- Counter-steer, 7, 65, 192
- Crankshaft, 50
- Data logger, 156–157
- Degrees of freedom, 8–10, 13, 21, 34–37, 212
- Drag, 51–55
  - aerodynamic, 53–54
  - coefficient, 54
- Engine torque, 62–63
- Generalised co-ordinates, 13, 19, 21, 23, 26, 28–30, 34, 37–41, 64, 65, 75, 77, 80, 89–91, 100
- Generalised speeds, 19, 21, 23, 29, 30, 34, 37–38, 89, 90, 101
- Gyroscopic torque, 50

- 
- Hand, R. S., 6
- Inertial Measurement Unit (IMU), 56–62, 153, 154, 156, 160, 163–165, 210, 212
- Juden, C., 9
- Kalman filter, 108
- Kane’s equations, 19, 29, 33, 44, 89, 99–106, 209, 210
- Koenen, C., 11
- Lagrange’s equations, 9, 13, 19, 26, 33
- Limebeer, David J. N., 8, 9, 11, 12, 17
- LU decomposition, 115
- Main frame, 64
  - pitch angle, 67–74
  - roll angle, 87, 93
  - x position, 75
  - y position, 85–86
  - yaw angle, 81–85, 87
  - z position, 76–78
- Mathematica, 97, 106
- Matlab, 106, 115
- Meijaard, J. P., 6, 7
- Mondello Park, 142, 152, 179, 181, 182, 202, 205
- Motion variables, *see* Generalised speeds
- Multibody system, 19–34
- Newton’s Equations, 19, 23, 33
- Nutts Corner, 87, 141, 142, 152, 153, 179, 181–183, 190, 202, 205, 206
- Pacejka, H. B., 11
- Partial angular velocity, 21
- Partial velocity, 21
- Perl, 106
- Rankine, W.J. M., 7
- Reference frame, 19–21, 23, 24, 30, 33, 38–44, 57, 58, 68, 69, 75, 76, 80, 87, 91, 93, 94, 97, 107, 143, 172
- Rider body position, 55–62
- Right hand rule, 20
- Roland, Douglas, 10
- Runge-Kutta, 10
- Sampling rate, 88–89
- Schwab, A. L., 7
- Schwinn Bicycle Company, 10
- Sensor
  - brake pressure, 175–176
  - front suspension position, 170–171
  - front wheel speed, 167–169
  - GPS, 176
  - IMU, 163–165
  - interface module, 158
  - rear suspension position, 172–175
  - rear wheel speed, 169–170
  - steering angle, 175
  - throttle position, 161
- Sharp and Limebeer 2001 model, 11
- Sharp, Archibald, 7
- Sharp, Robin S., 8–12, 17, 18
- Spierings, P. T. J., 10

- 
- Suspension force, 45–49
  - Suspension mode, 199, 200
  - Taylor series, 71, 72, 87, 92
  - Timoshenko, S., 8
  - Timoshenko-Young model, 8
  - Traction control, 111
  - Trail, 80–81
  - Tyre, 116–149
    - aligning moment, 15–18, 116, 124, 126, 136, 231
    - aligning stiffness, 126
    - camber stiffness, 126, 227, 234
    - camber thrust, 121–123
    - cornering stiffness, 14, 15, 126, 227, 229, 234
    - grip, 118
    - lateral force, 12, 15–18, 116, 121–123, 126, 127, 130, 136, 225–230, 234
    - lateral slip stiffness, *see* cornering stiffness
    - longitudinal force, 12, 15, 116, 120–121, 126, 127, 136, 221, 222, 224, 234
    - longitudinal slip, 8, 12, 15, 17, 116, 120, 121, 124, 126–128, 132, 134, 222–225, 228, 234
    - longitudinal slip stiffness, 16, 17, 126, 223, 234
    - longitudinal force, 128
    - magic formula, 16–18, 119, 121, 122, 126, 131–136, 221
    - overturning moment, 12, 15, 17, 18, 116, 122, 123, 229–230
    - ply steer, 127
    - pneumatic trail, 8, 16, 17, 35, 123, 124, 133, 134, 136, 232–234
    - profile, 143–149
    - radius, 119
      - free, 119
      - loaded, 119
      - rolling, 119
      - unloaded, 119
    - relaxation length, 9, 16, 17, 121, 127, 129, 130, 234
    - side slip, 8, 17, 18, 117, 120–122, 124–126, 129, 130, 132, 134, 136, 222, 224–228
    - turn slip, 126–127, 134, 223, 228, 234
  - Velocity expressions, 90–99
  - Weave mode, 8, 199, 200
  - Wheel hop mode, 199, 200
  - Wheelbase, 78–80
  - Whipple model, 7
  - Whipple, Francis John Welsh, 6, 7
  - Wobble mode, 8, 10, 199, 200
  - Young, D. H., 8